Copyright Statement

This copy of the thesis has been supplied on condition that anyone who consults it is understood to recognise that its copyright rests with its author and that no quotation from the thesis and no information derived from it may be published without the author's prior consent.

UNIVERSITY OF PLYMOUTH

THE LATTICE BOLTZMANN METHOD FOR FLOWS WITH SLIP AND NO-SLIP BOUNDARIES

by

SEEMAA ABDULSATTAR MOHAMMED

A thesis submitted to the University of Plymouth

in partial fulfilment for the degree of

DOCTOR OF PHILOSOPHY

School of Computing, Electronics and Mathematics

January 2019

Acknowledgments

First and foremost I would like to to express my sincere thanks to my supervisors Dr David Graham and Dr Timothy Reis for their patience, support and guidance throughout my PhD studies. They have made themselves available and offered assistance even at the busiest of times. Their help has been greatly appreciated.

I would like to give my thanks to all the staff at the School of Computing, Electronics and Mathematics and Doctoral college for their help with all the little things that keep everything running smoothly.

Special thanks are extended to Dr H.J.H. Clercx and Dr Duncan Sutherland for their generosity in sharing their knowledge when i contact them .

My deepest gratitude are due to my parents, my dear husband, Rasool, my son, Mohammed, my sisters and brother, and all my family for their continuous love, tolerance, encouragement, and prayers that always kept me going.

Finally, I would like to thank the Higher committee for Education Development in Iraq (HCEDiraq) for their support throughout my PhD studies.

Seemaa Abdulsattar Mohammed

At no time during the registration for the degree of *Doctor of Philosophy* has the author been registered for any other University award without prior agreement of the Doctoral College Quality Sub-Committee.

Work submitted for this research degree at the University of Plymouth has not formed part of any other degree either at the University of Plymouth or at another establishment.

A programme of advanced study was undertaken, which included *taught modules taken, other as relevant*

- What is LaTex? (14 November 2014).

- Introduction to EndNote (4 December 2014).

- math3510 fluid dynamics (Term1 2014).

- math3510 fluid dynamics(Term2 2015).

- latex getting start (9 February 2015).

- introduction to qualitative research(10 February 2015).

- UK Consortium on Mesoscale Engineering Sciences Workshop (UKCOMES) (12-13 December 2016).

- Supporting Assessment, Learning and Teaching Workshop (SALT) (10th January 2017).

<u>*Publications:*</u>

- S. Mohammed and T. Reis. Using the lid-driven cavity flow to validate moment-based boundary conditions for the lattice Boltzmann equation. *Arch. Mech. Eng.*, 64(1): 57–74, 2017.

- S. Mohammed, D. Graham, and T. Reis. Assessing moment-based boundary conditions for the lattice Boltzmann equation: A study of dipole-wall collisions. *Comput. Fluids.*, 2018.

- S. Mohammed, D. Graham, and T. Reis. The effect of Navier-slip boundary on dipole wall collision by using moment-based boundary conditions. *In progress.*

Presentations at conferences:

- 8th European Postgraduate Turbulence conference. 4th-9th July 2016 Warsaw, Poland.

- EGL workshop on applied and numerical mathematics. 8th-9th June 2017 University of Greenwich, Greenwich, UK.

- BAMC conference 2018. 26th-29th March 2018 University of St Andrews, Scotland, UK

Word count of main body of thesis: 55057

Signed: _____

Date: _____

The Lattice Boltzmann method For Flows With Slip and No-slip Boundaries

Seemaa Abdulsattar Mohammed

Abstract

This thesis assesses and extends a modern method to study the physics of simple and complex flows by using the lattice Boltzmann method (LBM). With the moment-based boundary conditions, different problems with no-slip and slip boundaries are simulated. The moment method is based on the specification of the appropriate hydrodynamic moments of LBM.

Throughout this thesis, distinct collision operators of D2Q9 LBM are presented and examined; the models include the Bhatnager-Gross-Krook (BGK), multiple relaxation time (MRT) and a special case of the last model which is two relaxation times (TRT-LBM). Simple numerical simulations are given and the LBM proved its accuracy when it is compared with other numerical methods.

The accuracy of the LBM with the no-slip and slip moment-based boundary conditions is examined numerically by studying the dipole wall collision flow. The two relaxation times lattice Boltzmann model is used to simulate this flow and the results are compared with other numerical methods. Our implementation shows excellent agreement with other numerical results. The vorticity generation on the wall shows interesting behaviour after the dipole collides with no-slip wall. The angle of the incidence effects the behaviour of the dipole after the wall collision, the dissipation of the energy and the growth of the enstrophy.

Throughout this thesis the impact of the slip length and Reynolds number on the dipole wall collision is studied. By applying the Navier-slip condition with moment boundary conditions the behaviour of the flow changes and the dissipation of the energy is affected by slip length and the peaks of the enstrophy decreases with higher slip lengths.

The dissipation of the energy and its relation to the enstrophy over dipole wall collision are also investigated for different types of boundaries and angles. The theoretical and the numerical investigation shows that the presence of the wall modifies this relation. Moreover, the dissipation of the energy in the absence and the existence of the viscosity effect are studied. Finally, an analysis is done of the stress field of the LBM by using the same boundary conditions for simple flow.

Contents

7   Analysis of the stress field computed by the lattice Boltzmann equation   **196**

8   General conclusions and future work   **216**

A   flowcharts of LBM simulation   **221**

Bibliography   **224**

List of Figures

List of Tables

Chapter 1

Fluid flow

Introduction

Computational fluid dynamics (CFD) is a branch of fluid dynamics which includes a study of various natural phenomena in real life by simulating the governing equations numerically. The governing equations for the Navier-Stokes equations have been utilized to describe the motions of fluids for over 150 years [27, 46]. In CFD, numerous numerical methods are used to approximate the Navier-Stokes equations, like the finite difference method, finite element method, finite volume and spectral method. All these methods are established methods for discretising the macroscopic Navier-Stokes equations. In contrast to the other computational methods, another approach which is considered a link between the microscopic models and the continuum macroscopic equations is used to solve the governing equations is the lattice Boltzmann method. In this thesis the lattice Boltzmann method will be applied with accurate conditions to simulate simple and complex flows. In this chapter, some fundamental concepts of conservation laws are expressed. The equation of motion will be found from the momentum equation. A brief description of macroscopic boundary conditions and boundary layer theory are given in this chapter. Some explanation about the kinetic theory will be given followed by an introduction to the lattice Boltzmann method. The motivation for, and outline of, the thesis are listed.

1.1 Macroscopic description

In this scale, the fluids are described as a continuum. In classic physics, the macroscopic behaviour is used to simulate the fluid in large scales. In a closed and arbitrary volume V, we can derive the continuity and momentum equations which lead to the Navier-Stokes equations.

1.1.1 The continuity equation

In a closed and arbitrary volume V that is bounded by surface S, one can derive the mass equation from the following integral form [90]

$$\frac{\partial}{\partial t} \int_V \rho \, dV + \int_S \rho \mathbf{n} \cdot \mathbf{u} \, dS = 0, \tag{1.1}$$

where the first term describes the rate of change of mass in a volume V, while the second term represents the mass flux through the control boundary S. $\mathbf{n}$ is the unit vector normal to the surface that points out from the inside to the outside of V. The density ρ and the fluid velocity vector $\mathbf{u}$ depend on time t and position $\mathbf{x}$. By using the Leibniz rule ($\frac{\partial}{\partial t} \int_V \rho \, dV = \int_V \frac{\partial \rho}{\partial t} \, dV$) and the Gauss's divergence theorem, ($\int_V \nabla \cdot A \, dV = \int_S A \cdot \mathbf{n} \, dS$), equation (1.1) becomes

$$\int_V \left(\frac{\partial \rho}{\partial t} + \nabla \cdot (\rho \mathbf{u}) \right) dV = 0. \tag{1.2}$$

By assuming all the integrals are continuous and for any value of V, the integrand vanishes as follows

$$\frac{\partial \rho}{\partial t} + \nabla \cdot (\rho \mathbf{u}) = 0. \tag{1.3}$$

Equation (1.3) is called the continuity equation. For incompressible flow where the density is constant, the continuity equation is reduced to

$$\nabla \cdot \mathbf{u} = 0. \tag{1.4}$$

1.1.2 The momentum equation

The momentum equation can be described in a volume V that is not changing with time. Newtons second law indicated that [66, 73]

$$\frac{\partial}{\partial t} \int_V \rho \mathbf{u} \, dV + \int_S \rho (\mathbf{n} \cdot \mathbf{u}) \mathbf{u} \, dS = \int_V \mathbf{F} dV + \int_S \mathbf{n} \cdot \boldsymbol{\sigma} \, dS, \tag{1.5}$$

where $\mathbf{F} = \rho \mathbf{G}$ is the body force and $\boldsymbol{\sigma}$ is the stress tensor. Again by using the divergence theorem, the integration of equation (1.5) combines over volume V

$$\int_V \left(\frac{\partial}{\partial t} (\rho \mathbf{u}) + \nabla \cdot (\rho \mathbf{u} \mathbf{u}) \right) dV = \int_V \left(\mathbf{F} + \nabla \cdot \boldsymbol{\sigma} \right) dV, \tag{1.6}$$

and for an arbitrary fixed volume V, the integrands of equation (1.6) must be equal

$$\frac{\partial}{\partial t} (\rho \mathbf{u}) + \nabla \cdot (\rho \mathbf{u} \mathbf{u}) = \mathbf{F} + \nabla \cdot \boldsymbol{\sigma}. \tag{1.7}$$

By using the dot product properties

$$\nabla \cdot (\rho \mathbf{u} \mathbf{u}) = \nabla \cdot (\rho \mathbf{u}) + \rho \mathbf{u} \cdot \nabla \mathbf{u}, \tag{1.8}$$

and by applying the continuity equation (1.4), we get the momentum equation

$$\rho \frac{\partial \mathbf{u}}{\partial t} + \rho \mathbf{u} \cdot \nabla \mathbf{u} = \mathbf{F} + \nabla \cdot \boldsymbol{\sigma}, \tag{1.9}$$

where the left-hand side is the convection of the fluid while the right side represents the diffusion and external force.

In Newtonian fluids the stress tensor in index notation takes the form as

$$\sigma_{\alpha\beta} = -P\delta_{\alpha\beta} + \mu D_{\alpha\beta}, \tag{1.10}$$

where P is the pressure, μ is the dynamic viscosity of the fluid, $\delta_{\alpha\beta}$ is the Kronecker delta function

$$\delta_{\alpha\beta} = \begin{cases} 1, & \text{if } \alpha = \beta, \\ 0, & \text{if } \alpha \neq \beta, \end{cases} \tag{1.11}$$

and $D_{\alpha\beta}$ is the strain tensor, which is defined as

$$D_{\alpha\beta} = \left(\frac{\partial u_\alpha}{\partial x_\beta} + \frac{\partial u_\beta}{\partial x_\alpha} \right). \tag{1.12}$$

Substituting equation (1.10) and (1.12) into equation (1.9) yields the equation of motion in Newtonian incompressible flow which is called the Navier-Stokes equations

$$\frac{\partial \mathbf{u}}{\partial t} + \mathbf{u} \cdot \nabla \mathbf{u} = -\frac{1}{\rho}\nabla P + \nu\nabla^2\mathbf{u} + \mathbf{G},$$
$$\nabla \cdot \mathbf{u} = 0 \tag{1.13}$$

where $\nu = \mu/\rho$ is the kinematic viscosity. The importence of viscosity is characterised by the non-dimensional Reynolds number. Reynolds number is defined as $Re = UL/\nu$ where L and U are the characteristics length and velocity, respectively.

In the macroscopic approach, the Navier-Stokes equations describe the motion of the fluids as a continuum in a hydrodynamic length and time scales. These partial differential equations are non-linear and difficult to solve, except under specific assumptions, like in unidirectional channel flow. Therefore, accurate and functional numerical methods with correct conditions are needed to approximate this system of equations.

1.2   Boundary conditions

Boundary conditions are a vital part of any numerical method for fluid flow since they are part of the physical problem and they have an effect on the stability of the numerical algorithm. In computational fluid dynamics, the velocity, pressure or the stress will be specified at the boundary [46]. In the macroscopic approach, boundary conditions are generally divided into three different types: Dirichlet boundary conditions, Neumann boundary conditions and Robin boundary conditions. With Dirichlet conditions, the velocity at a boundary will be specified to a constant value. Neumann boundary conditions can be introduced as the gradient derivative of the velocity at the wall. If the fluid at the boundary is moving with the same velocity as the boundary, then the condition is called the no-slip boundary condition. The free-slip boundary condition is an example of Neumann boundary conditions where the gradient velocity that results from equation (1.12) at the wall is specified as zero. The combination between the Dirichlet and Neumann boundary conditions is called the Robin boundary condition. The partial-slip or Navier-Maxwell slip boundary condition is an example of the Robin condition. In special applications, for instance at micro-fluids, the velocity at the wall is changing where the slip boundary conditions are applied. The slip velocity at the wall is represented by the shear stress from equation (1.12) where the amount of the slip is described by the magnitude of small length called the slip length. Note that, if the slip length is very small, then the fluid mimics the no-slip boundary conditions. Nevertheless, at a very big slip length, the wall faces a very small amount of friction and the fluid will slip at the boundary without significant resistance from the surface.

Moreover, if the particles from the boundary move to the opposite side of the flow and re-enter from it, then there is another type of the condition, named the periodic boundary conditions. In this work different types of boundary conditions will be studied and will be implemented for various kinds of flows.

1.2.1 Boundary layer theory

The flow at very high Reynolds numbers acts approximately as an ideal flow in the region away from the boundary. However, the viscous effects are confined to the region near the wall, because the fluid has to stick to the wall, especially at no-slip walls. As a result, very high velocity gradient in the area near the boundary will appear which induces a layer from the solid boundary called the boundary layer. The study of the boundary layer expanded from incompressible laminar flow, then it was developed to include the turbulent flow [101]. The boundary layer (BL) at complex or turbulent flows detaches from the boundary and produces complicated patterns.

D'Alembert declared a paradox in 1752 which states that any object moves in an infinite fluid without any friction effect or drag. In 1904 Prandtl introduced a theory called boundary layer or frictional layer theory [92]. This theory illustrated that at higher Reynolds numbers the flow can be split into two regimes. The first one is located in the bulk flow where the friction is neglected. The second regime is placed near the boundary where a very thin layer appears and the viscosity effect is taken into consideration.

The thickness of the boundary layer δ in a laminar flow can be found from the ratio of advective part to the viscous term in Navier-Stokes equation [73], where

$$
\begin{aligned}
Re_{\text{BL}} \simeq & \frac{(\mathbf{u} \cdot \nabla \mathbf{u})}{(\nu \nabla^2 \mathbf{u})} \sim \frac{U^2/L^2}{\nu U/\delta^2} \\
= & \frac{\delta^2}{L^2} Re.
\end{aligned}
\tag{1.14}
$$

The boundary layer is distinguished by the passing from the mainstream domain to the area near the boundary where the viscosity is dominated in that region. The estimation of the thickness of the boundary layer demands the assumption that the appropriate Reynolds number for the flow is around one [100], which yields

$$
\delta \sim \sqrt{\frac{\nu L}{U}} = \frac{L}{\sqrt{Re}}.
\tag{1.15}
$$

Moreover, at higher Reynolds numbers, the thickness of the boundary layer will be much smaller than the characteristic length of the flow.

1.3 The kinetic description

There is another approach that can be used to predict the behaviour of the fluid flow which was established by the physicist Ludwig Boltzmann [8]. In this approach, fluids are described as a large number of particles and molecules which interact with each other. These particles are described in terms of the microscopic distribution functions. In the kinetic theory, the distribution function f gives the number of particles with a velocity $\mathbf{c}$ at time t and position $\mathbf{x}$ where $\mathbf{x} \in \mathbb{R}^D$, $\mathbb{K} = \mathbb{R}^D \times \mathbb{R}^D$ is the phase space where all the positions and momentum variables exist and D is the number of the dimension. The time evolution of the distribution function can be written without a force term [15]

$$\partial_t f + \mathbf{c} \cdot \nabla f = \Omega(f), \tag{1.16}$$

where $f = f(\mathbf{x}, \mathbf{c}, t)$ is a probability distribution function and $\partial_t = \frac{\partial}{\partial t}$ and $\mathbf{c}$ is the particle's velocity. The right-hand side is the collision operator where the distribution functions change their values because of the collisions of the particles. The simplest collision operator is the Bhatnagar-Gross-Krook model (BGK) [7] which reads

$$\Omega(t) = -\frac{1}{\tau}(f - f^{(0)}), \tag{1.17}$$

where τ is the relaxation time that controls the rate at which the distribution functions reach their equilibrium. $f^{(0)}$ is Maxwell Boltzmann distribution function, which is defined as [15]

$$f^{(0)} = \frac{\rho}{(2\pi RT)^{(D/2)}} \exp\left(-\frac{(\mathbf{c} - \mathbf{u})^2}{2RT}\right), \tag{1.18}$$

where ρ is the density, R is the Boltzmann constant and T is the Temperature. The mass, momentum and energy of the macroscopic approach can be computed by using the probability distribution function as

$$\text{Density} \qquad \rho = \int f(\mathbf{x}, \mathbf{c}, t) d\mathbf{c}, \qquad (1.19a)$$

$$\text{Momentum} \qquad \rho \mathbf{u} = \int \mathbf{c} f(\mathbf{x}, \mathbf{c}, t) d\mathbf{c}, \qquad (1.19b)$$

$$\text{Kinetic Energy per unit volume} \quad \rho E = \frac{1}{2} \int |\mathbf{c} - \mathbf{u}|^2 f(\mathbf{x}, \mathbf{c}, t) d\mathbf{c}, \qquad (1.19c)$$

where E is the energy and $|\mathbf{c} - \mathbf{u}|$ is the particular velocity [14, 15, 45].

By using the suitable multiscale method, one can get the continuum equations and the hydrodynamic moments from the kinetic Boltzmann equation. The Chapman-Enskog expansion provides a multiscale expansion of the distribution function f and time t derivative by using a small parameter τ. This parameter is proportional to the Knudsen number Kn. The Knudsen number $Kn = \ell_f / L_f$ is a ratio between the mean free path ℓ_f and a typical hydrodynamic length scale L_f, where $L_f \gg \ell_f$ for handling the fluid as a continuum. So, the distribution function is expanded around its equilibrium as

$$f = f^0 + \tau f^{(1)} + \tau^{(2)} f^{(2)} + ..., \qquad (1.20)$$

and the time derivative is expanded as follows

$$\frac{\partial}{\partial_t} = \frac{\partial}{\partial_{t_0}} + \tau \frac{\partial}{\partial_{t_1}} + \tau^2 \frac{\partial}{\partial_{t_2}} + ... \qquad (1.21)$$

With the first-order of truncation, the Navier-Stokes equations (1.13) are recovered from the continuous Boltzmann equation, for more details see [14]. From the higher order truncation of τ, there are additional stress terms of Burnett type which will appear [15, 108]. The influence of the stress for the higher order truncation is investigated in Chapter 7.

1.4   Introduction to the lattice Boltzmann method

The lattice Boltzmann method (LBM) is considered an alternative to the traditional computational methods to simulate fluid flow problems. Conversely, to the other computational methods that discretise the governing equations directly, the LBM features a simplified mesoscopic scope of fluid flow to recover the Navier-Stokes equations in the macroscopic frame [46]. The characteristics of the LBM make it an attractive method of computational fluid dynamics for the following reasons. Firstly, the LBM features linear, constant coefficient advection similar to the kinetic Boltzmann equation, whereas the Navier-Stokes equations involve non-linear convection (non-linear convection terms dominate at high Reynolds numbers and are difficult to discretise). Secondly, in this model the pressure is calculated efficiently by using an equation of state unlike other numerical methods which compute solutions to the Navier-Stokes equations and often find it through a Poisson solver. Thirdly, it is easy to apply different types of boundary conditions in complex geometries with LBM. Fourthly, the method is readily parallelizable. This feature allows faster simulation of large computational flows. So, because of these reasons, it can be said that the LBM is a competitive and advantageous method compared to the other computational fluid methods.

The lattice Boltzmann method originally advanced to overcome shortcomings of the lattice gas cellular automaton (LGCA). In 1973 Hardy, de Pazzis and Pomeau [49] introduced the first model of LGCA, named HPP-LGCA. This model expressed the motion and the interactions between the particles in the fluid. The HPP model achieved mass and momentum conservation, but it was unable to recover the Navier Stokes equations. In 1986 Frisch, Hasslacher and Pomeau [38] introduced another model of LGCA called the FHP model, which is based on similar principle on HPP, namely, mass and momentum conservation and simplification of particle dynamics. However, the authors increased the number of degrees of freedom to improve the symmetry properties and recover the correct equation of motion in the macroscopic limit. Despite the efficiency of LGCA, it suffered from some drawbacks including statistical

noise [78]. In 1988 McNamara and Zanetti [82] proposed a method to solve statistical noise problems in LGCA. They replaced the (Boolean) occupation variable with a probability distribution function to create the first lattice Boltzmann equation (LBE) [103]. In 1989 Higuera and Jimenez [54] linearised the LBE around its equilibrium to simplify the LBM and improve computational efficiency. Later, several researchers [93, 16] proposed a simple collision operator based on the previous operator with a single relaxation time, called the Bhatnager-Gross-Krook model (LBGK). More recently; the LBM was derived from a velocity-space truncation of the Boltzmann equation with a BGK-collision operator [51, 102].

Despite the popularity of the BGK-LBM, it is well-known that its stability suffers at small values of τ (high Reynolds number flows) [29, 1]. D'Humieres [32] introduced the multiple relaxation time (MRT) model, and such models have been shown to significantly enhance the stability of LBM algorithms with only a little extra computational overhead [68, 29, 67, 96]. A specific and simplified MRT collision operator is the two relaxation time (TRT) model.

As mentioned before, the LBM can accurately and simply incorporate complicated boundary conditions in complicated flows. Therefore the choice of the appropriate and accurate boundary conditions is the key to successful fluid flow numerical simulation.

1.5 Motivation for this thesis

The first purpose of this thesis is to present the lattice Boltzmann method with accurate boundary conditions for fluid dynamics flows and to highlight some advantages and disadvantages of this method. The efficiency of the boundary conditions affects the accuracy of LBM. The presented boundary conditions, so-called "Moment-based Method", are based on applying conditions directly onto the moments of the LBM [4]. The moment-based implementation discussed here uses only hydrodynamic moments to satisfy boundary conditions and may be viewed as a direct extension of the method first proposed by Noble *et al* [88] for simpler lattices [84]. By using the moment

method, no-slip and Navier-Maxwell slip boundary conditions can be imposed in less complicated ways on any problem with flat walls. The moment method has already been applied to diffusive slip [5], natural convection problems [1], lid cavity fluid flow [84], the slip-flow regime [95], and wetting phenomena in multiphase flow [48], and reported very favourable results.

In viscous fluid, the interaction between the vortex and the boundary has a significant impact on the development of the flow. The evolution of the sequence of vortices resulting from wall collision makes this flow an excellent benchmark to validate any numerical method [89]. The basic contribution of this thesis is to study the validation of LBM with moment-based boundary conditions. To do that, the dipole rebounds from the no-slip solid wall are studied and compared with benchmarking data of [19, 71]. The investigation of Latt and Chopard [71] is expanded to include the study for higher Reynolds numbers to show the accuracy of moment boundary conditions compared with bounce-back method. Moreover, in this thesis a new physics of dipole collisions with solid walls at an angle of 45° are introduced for intermediate and higher Reynolds numbers.

The other main strand of this work is showing the significant impact of the slip length on dipole wall collisions together with higher Reynolds numbers and various angles of collisions by using Navier-slip condition with moment method. Latterly, Farge *et al* [35] studied the energy dissipation of normal dipole wall collision in the limit of vanishing viscosity by using the volume penalisation method repeated by Sutherland *et al* [105]. Here, the same study is carried out by using the LBM with moment-based boundary conditions for normal wall collisions, extending the study to include oblique dipole wall collision. In the bounded domain, the relationship between the dissipation of the energy and growth of the enstrophy at the wall is investigated, where the no-slip then slip walls acts as a provider of the enstrophy. This relationship confirms the finding from our study of dipole wall collision for slip and no-slip boundaries where the dissipation of the energy decreases by increasing the Reynolds numbers.

Finally, this thesis gives a detailed analysis of the stress tensor for unidirectional flow by

using the LBM and shows the contribution of the Navier-slip condition with moment-based boundary conditions in this analysis.

1.6   Outline of the thesis

Since the examination of the moment-based boundary conditions with the more accurate model of the lattice Boltzmann method is the main function of this work, the arrangement of the thesis is as follows:

In **Chapter 2** the essential principle of LGCA is introduced, then how it leads to developing the idea of the lattice Boltzmann method is discussed. Three collision operators are discussed: the BGK, MRT and a special one of MRT which is the TRT model. The derivation of the Navier-Stokes equations from a discrete Boltzmann equation are presented in this chapter. Also we illustrate the method based on Grad's approximation to find the general formula of the explicit second-order lattice Boltzmann equation.

In **Chapter 3** a review of various approaches of boundary conditions is held. Then the local second-order boundary conditions are presented, called 'moment-based boundary conditions'. An analytic solution of LBE is demonstrated with some numerical analysis. Some benchmark simulations are presented to validate the moment method with different models of LBM.

In **Chapter 4** a dipole wall collision flow is solved numerically with no-slip moment conditions and compared with benchmark data. Subsequently, slip conditions are applied to the same flow in **Chapter 5** and the role of the slip length is described in the same investigation.

To give a better understanding to the behaviour of the dipole wall collision with the slip and no-slip cases the relation between the dissipation of the energy and the growth of the enstrophy is shown in **Chapter 6**. Then the scale of these quantities according to the thickness of boundary layer is studied.

In **Chapter 7** the observation of [94] about the limitation of the moment method for the channel flow is analysed; then this study is extended to the slip boundary

conditions. A conclusion and suggestions for future work are discussed in **Chapter 8**.

Chapter 2

Lattice Boltzmann Method (LBM)

A theoretical background of lattice Boltzmann method is discussed in this chapter including the lattice gas cellular automata (LGCA). The LGCA is considered the ancestor of the the lattice Boltzmann method. The BGK-LBE can be found alternatively by using Grad's approach [45] by projecting the distribution functions on the Hermite polynomials. From this model, a detailed explanation of the hydrodynamic and non-hydrodynamic moments that depends on the probability distribution function are given. From the discrete Boltzmann equation, the Navier-Stokes equations will be recovered. As well as the BGK model, the multiple relaxation times model (MRT-LBE) will be introduced. Following Bennett [4], via Chapman-Enskog expansion, the minimum number of velocities to recover the Navier-Stokes equations for one and two dimensional lattice Boltzmann models are shown.

2.1 The Lattice Gas Cellular Automata (LGCA)

Numerous methods have been used to simulate the Navier Stokes equations, such as the finite difference method, the finite element method, Smooth-Particle Hydrodynamics (SPH) and lattice Gas Cellular Automata (LGCA). Our theme in this section will be the LGCA, which is a simple method to simulate flow based on simplified microscopic behaviour of fluid particles. We will explain the first model of LGCA which is the HPP

model. Inasmuch as this model cannot fully recover the Navier Stokes equations we will introduce another model of LGCA named the FHP model. Finally, we will show the development of this method leads to a more appropriate computational tool for fluid flow which is the lattice Boltzmann equation model [97].

2.1.1 The HPP model

Lattice Gas Cellular Automata is a numerical method customized by imitating the behaviour of molecules when they interact with each other in a gas and it was originally inspired by Cellular Automata, which are finite individual cells with discrete states related with their nearest neighbours [109, 112]. The LGCA began with Hardy, Pomeau and de Pazzis in 1973 when they introduced a new two dimensional model which is called by the first letters of their names: HPP model [112]. In the HPP model, each node is connected with its four nearest neighbours by discrete vectors $\mathbf{c}_i$, $i = 1, 2, 3, 4$ [37]. As shown in Figure 2.1, the four velocities in the HPP model are

$$\mathbf{c}_i = \left\{ (1, 0), (0, 1), (-1, 0), (0, -1) \right\}.$$
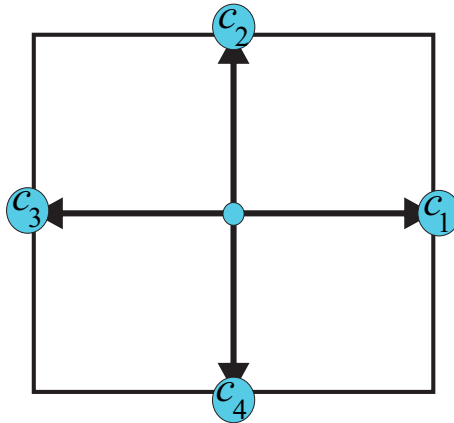
Figure 2.1: The HPP lattice.

This method is summarised as follows: particles stream from a node with position vector $\mathbf{x}$ along one of the four directions to a neighbor node $\mathbf{x}+\mathbf{c}_i$, see Figure 2.1. When they arrive they collide and change their momentum according to some pre-determined collision rules. In this model, the particles that collide rotate 90° and move to the site

that depends on their momentum, as shown in Figure 2.2, [77, 112].
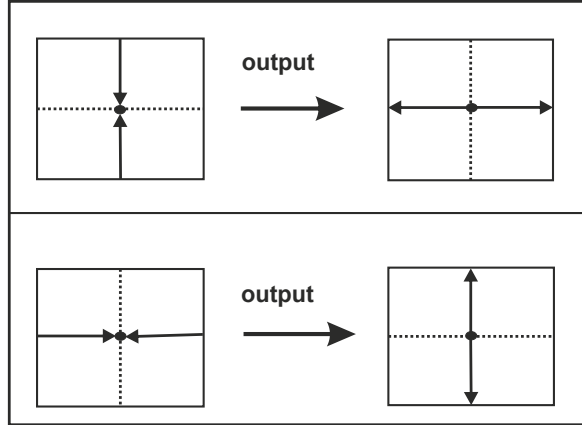
Figure 2.2: Two particles hit each other when they reach a new node and change their direction by $90°$ in the HPP model.

The occupation Boolean variables $n_i(\mathbf{x}, t), i = 1, 2, 3, 4$, are defined as the number of particles in each node $\mathbf{x}$ where $n_i = 1$ for the existence of a particle at the node with velocity c_i and $n_i = 0$ otherwise. So the microscopic behaviour of LGCA can be written as

$$n_i(\mathbf{x} + \mathbf{c}_i \Delta t, t + \Delta t) - n_i(\mathbf{x}, t) = N_i(\mathbf{n}(\mathbf{x}, t)),\qquad(2.1)$$

where N_i denotes the collision rules. The density at each node can be calculated from the presence of the particles as follows

$$\rho = \sum_{i=1}^{4} n_i,\qquad(2.2)$$

and the momentum at each node is

$$\rho \mathbf{u} = \sum_{i=1}^{4} n_i \mathbf{c}_i.\qquad(2.3)$$

The left-hand side of equation (2.1) represents the streaming of the particles at each node while the collision operator $N_i(\mathbf{n}(\mathbf{x}, t))$, $\mathbf{n} = (n_1, n_2, n_3, n_4)$, for HPP model is

defined by

$$N_i(\mathbf{n}) = n_{i+1}n_{i+3}\widetilde{n}_i\widetilde{n}_{i+2} - n_i n_{i+2}\widetilde{n}_{i+1}\widetilde{n}_{i+3}, \tag{2.4}$$

where $\widetilde{n}_i = 1 - n_i$. The collision operator $N_i(\mathbf{n})$ is constructed to conserve mass and momentum

$$\sum_i N_i(\mathbf{n}) = 0, \tag{2.5}$$

$$\sum_i \mathbf{c}_i N_i(\mathbf{n}) = 0. \tag{2.6}$$

By using equations (2.5), (2.6) and summing equation (2.1) over i we obtain:

$$\sum_i n_i(\mathbf{x} + \mathbf{c}_i\Delta t, t + \Delta t) = \sum_i n_i(\mathbf{x}, t). \tag{2.7}$$

Similarly, by multiplying the equation (2.1) by $\mathbf{c}_i$ and summing over i we will get the conservation of momentum

$$\sum_i \mathbf{c}_i n_i(\mathbf{x} + \mathbf{c}_i\Delta t, t + \Delta t) = \sum_i \mathbf{c}_i n_i(\mathbf{x}, t). \tag{2.8}$$

2.1.1.1   Evaluation of mean occupation numbers

The analysis of the LGCA method is started by taking the ensemble average of the occupation numbers $f_i = \langle n_i \rangle, i = 1, 2, 3, 4$. f_i is the probability of finding the particles in a given node in the direction of $\mathbf{c}_i$. The mean occupation number is used to find the macroscopic density by summing the probability distribution functions at each node

$$\rho(\mathbf{x}, t) = \sum_{i=1}^{4} f_i(\mathbf{x}, t), \tag{2.9}$$

and we calculate the momentum by summing the product of the probability with the velocity vector

$$\rho u_\alpha(x, t) = \sum_{i=1}^{4} f_i(\mathbf{x}, t) c_{i\alpha}, \tag{2.10}$$

Similarly, the momentum flux tensor is defined to be

$$\Pi_{\alpha\beta} = \sum_{i=1}^{4} f_i(\mathbf{x}, t) c_{i\alpha} c_{i\beta}, \tag{2.11}$$

where α and β are the Cartesian components of the velocity ($\alpha, \beta = x$ or y) and $\mathbf{u}$ is the velocity of the fluid. Since the symmetry properties are important in the recovery of the Navier Stokes equations from LGCA, we confirm that the HHP model has second-order isotropy defined by Hardy *et al.* [49]

$$\sum_i c_{i\alpha} = 0,$$
$$\sum_i c_{i\alpha} c_{i\beta} = 2\delta_{\alpha\beta}, \tag{2.12}$$

where $\delta_{\alpha\beta}$ is the Kronecker delta function defined in equation (1.11) while the isotropy will be discussed in Section 2.3.2.

2.1.1.2 Equilibrium distribution function and Euler's equation

To find the equilibrium state of the assemble average of the occupation numbers, we expand the equilibrium function $f_i^{(0)}$ up to order two in velocity where the magnitude of velocity $u = |\mathbf{u}|$ is assumed to be small. By using the equations (2.9), (2.10) and (2.12), the equilibrium distribution function of the HHP model can be shown to be [46, 97]:

$$f_i^{(0)} = W \left[1 + 2u_\alpha c_{i\alpha} + 2\frac{1 - 2W}{1 - W} \left(c_{i\alpha} c_{i\beta} - \frac{1}{2}\delta_{\alpha\beta} \right) u_\alpha u_\beta \right] + O(u^3), \tag{2.13}$$

where $W = \rho/4$ is the density per link.

To get the macroscopic Navier-Stokes equations, a Taylor expansion is applied to equation (2.1). Then using Chapman-Enskog expansion, (we will explain this expansion in Section 2.3.1), the momentum equation

$$\partial_t(\rho u_\alpha) + \partial_\alpha(\Pi_{\alpha\beta}) = 0, \tag{2.14}$$

is obtained, and

$$\Pi_{\alpha\beta}^{(0)} = \begin{cases} 2W\left[1 + \frac{1-2W}{1-W}(2u_\alpha - u^2)\right], & \text{if } \alpha = \beta \\ 0. & \text{if } \alpha \neq \beta \end{cases} \tag{2.15}$$

However according to [97, 37], the tensor in equation (2.15) should be isotropic if it is invariant in all directions. This tensor is not invariant so Galilean invariance is broken. This means the tensor $\Pi_{\alpha\beta}$ will not be sufficient to recover the Euler equation or Navier Stokes equations.

2.1.2 The FHP model

Although the HPP model has been used to simulate the fluid behaviour in a simple way, obstacles in this model exist. From equation (2.12), we saw that the HPP has only two orders of isotropy, however the discrete kinetic model needs fourth-order isotropy to recover the Navier Stokes equations, see Section 2.5.3. Furthermore, because of the nature of the collision principle in this model, it is difficult to apply periodic boundary conditions [77]. Moreover, the main problem in this model is the statistical noise at microscopic behaviour.

In 1986 three authors, Frisch, Hasslacher and Pomeau, designed a new model for LGCA [38], named by the first letters of their names FHP. In FHP model the center node is connected with its six closer neighbours by the lattice vector $\mathbf{c}_i, i = 1, ..., 6$, (see Figure 2.3), where $\mathbf{c}_i$ are given by:

$$\mathbf{c}_i = \left(\cos \frac{\pi}{3} i, \sin \frac{\pi}{3} i \right).$$

Note that $|\mathbf{c}_i| = 1$ for all i.
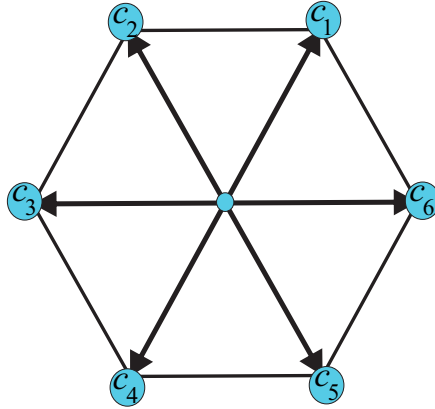
Figure 2.3: FHP lattice.

The main difference between HPP and FHP models is the increase in the number of lattice vectors. In addition, the following first three orthogonality relationships are found:

$$\sum_i c_{i\alpha} = 0, \tag{2.16}$$

$$\sum_i c_{i\alpha} c_{i\beta} = 3\delta_{\alpha\beta}, \tag{2.17}$$

$$\sum_i c_{i\alpha} c_{i\beta} c_{i\gamma} = 0. \tag{2.18}$$

The consequence is to enable the FHP-LGCA to recover the correct Euler and Navier Stokes equations [112].

During the streaming step the particles move from node $\mathbf{x}$ to the new position $\mathbf{x} + \mathbf{c}_i$. In the collision step and contrast of HHP model which have a one possible rotation as we mentioned before, there are two possible rotations for FHP model. One way, two incoming particles will have head-on collision and rotate by $(\pi/3)$ or $(-\pi/3)$ with probability $p = 0.5$ and $1 - p$ respectively, as shown in Figure 2.4. Another possibility

of the collision in this model is three particles having head-on collision with an angle of $2\pi/3$ and modify their direction by rotating $(\pi/3)$ only, see Figure 2.4. In each collision step the mass and momentum must be conserved where the mass and momentum can be calculated as in equations (2.2) and (2.3) but summing with six directions of n_i in each node. As in HPP model, FHP has a formula for equation (2.1) with the following collision rule:

$$
\begin{aligned}
N_i(\mathbf{n}) = {} & n_{i+1}n_{i+3}n_{i+5}\tilde{n}_i\tilde{n}_{i+2}\tilde{n}_{i+4} \\
& -n_i n_{i+2}n_{i+4}\tilde{n}_{i+1}\tilde{n}_{i+3}\tilde{n}_{i+5} \\
& +\kappa n_{i+1}n_{i+4}\tilde{n}_i\tilde{n}_{i+2}\tilde{n}_{i+3}n_{i+5} \\
& +(1-\kappa)n_{i+2}\tilde{n}_{i+5}\tilde{n}_i\tilde{n}_{i+1}\tilde{n}_{i+3}\tilde{n}_{i+4} \\
& -n_i\tilde{n}_{i+3}\tilde{n}_{i+1}\tilde{n}_{i+2}\tilde{n}_{i+4}\tilde{n}_{i+4},
\end{aligned}
\tag{2.19}
$$

where $\kappa(\mathbf{x},t)$ is a Boolean variable which takes the values 0 or 1, depending on the direction of the rotation [77, 37]. $\mathbf{n} = (n_1, n_2, n_3, n_4, n_5, n_6)$ is the Boolean occupation numbers.
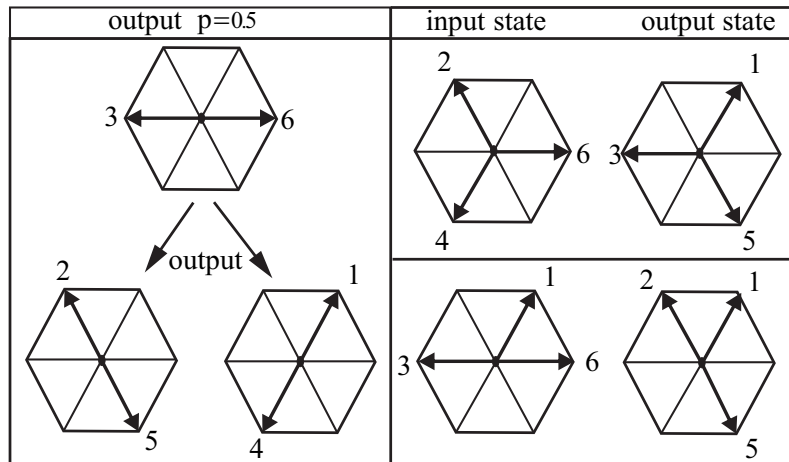
Figure 2.4: The probability of head-on collisions in the FHP model.

Despite the significant improvements of FHP model over the HPP model, the statistical noise problem still exists. This is because of the fluctuation in the calculation

of the average of the occupation numbers [112, 109]. In LGCA, it is difficult to extend the simulations to three dimensions because of the geometry and the collision principle of these models also the simulation at higher Reynolds number is very complicated [78, 103]. So to avoid these drawbacks, an alternative method is used to solve the hydrodynamics flow problems.

2.2 Theory of lattice Boltzmann Method

To overcome the disadvantages of LGCA, in 1988 McNamara and Zanetti [82] proposed a new technique to solve the problems of the previous models and preserve the conservation laws at the same time. The general idea of the McNamara and Zanetti [82] method is summarised by replacing the occupation variables with a velocity distribution function, as we saw in the previous section. So by taking the assemble average of LGCA $f_i = \langle n_i \rangle$, the lattice Boltzmann equation was created.

2.2.1 BGK-Lattice Boltzmann method

By taking the ensemble average of LGCA as $f_i(\mathbf{x}, t) = \langle n_i(\mathbf{x}, t) \rangle$, equation (2.1) yields:

$$f_i(\mathbf{x} + \mathbf{c}_i \Delta t, t + \Delta t) - f_i(\mathbf{x}, t) = \langle N_i(\mathbf{n}(\mathbf{x}, t)) \rangle, \quad i = 1, ..., b \qquad (2.20)$$

$f_i(\mathbf{x}, t)$ is the probability distribution function where each node has b numbers of these functions which depend on the number of lattice velocities in each model. The hydrodynamic quantities are obtained by taking discrete moments of f_i as follows:

$$\text{Density} \qquad \rho = \sum_{i=1}^{b} f_i, \qquad (2.21)$$

$$\text{Momentum} \qquad \rho \mathbf{u} = \sum_{i=1}^{b} f_i \mathbf{c}_i, \qquad (2.22)$$

$$\text{Momentum flux} \qquad \mathbf{\Pi} = \sum_{i=1}^{b} f_i \mathbf{c}_i \mathbf{c}_i. \tag{2.23}$$

The left-hand side of equation (2.20) is the streaming step. This step can be described as the propagation of particles from node to a nearest neighbour according to its velocity vectors $\mathbf{c}_i$ in time Δt. After the streaming step the collision step will start. In this step, the distribution functions are updated according to the right-hand side of the equation (2.20). Because of the complications caused by the ensemble average in the simulation, two authors, named Higura and Jimenez in 1989 [54], linearised the collision step about its equilibrium $f_i^{(0)}$ where $f_i = f_i^{(0)} + \tau f_i^{(1)} + \tau^2 f_i^{(2)} + ...$, [14]

$$N_i(\mathbf{f}) = N_i(f_i^{(0)}) + \sum_j \frac{\partial N_i(f^{(0)})}{\partial f_j}(f_j - f_j^{(0)}) + \frac{1}{2}\sum_{j,k} \frac{\partial N_i^2(f^{(0)})}{\partial f_j \partial f_k}(f_j - f_j^{(0)})(f_k - f_k^{(0)}) + ...,$$
$$\tag{2.24}$$

where $\mathbf{f} = (f_1, ... f_b)$. At the equilibrium state when $f_i = f_i^{(0)}$ the collision term will vanish such that $N_i(f_i^{(0)}) = 0$. Truncating equation (2.24) at second-order of N_i, the last equation will simplify to

$$N_i(\mathbf{f}) \approx \sum_j \frac{\partial N_i(f^{(0)})}{\partial f_j}(f_j - f_j^{(0)}). \tag{2.25}$$

Defining $M_{ij} = \partial N_i(f^{(0)})/\partial f_j$, we get

$$N_i(\mathbf{f}) = \sum_j M_{ij}(f_j - f_j^{(0)}). \tag{2.26}$$

If we assume the distribution functions will relax to their equilibrium with a specific single relaxation time τ then [7],

$$M_{ij} = -\frac{1}{\tau}\delta_{ij}, \tag{2.27}$$

where δ_{ij} is the Kronecker delta function defined in equation (1.11). Thus the lattice Bhatnagar-Gross-Krook model (LBGK) can be written as

$$f_i(\mathbf{x} + \mathbf{c}_i \Delta t, t + \Delta t) - f_i(\mathbf{x}, t) = -\frac{1}{\tau}(f_i - f_i^{(0)}). \tag{2.28}$$

The collision term of the lattice Boltzmann equation will conserve the mass and momentum and fulfill the following constrains

$$\sum_{i=1}^{b} f_i = \sum_{i=1}^{b} f_i^{(0)}, \tag{2.29}$$

$$\sum_{i=1}^{b} f_i \mathbf{c}_i = \sum_{i=1}^{b} f_i^{(0)} \mathbf{c}_i. \tag{2.30}$$

Subsequently, the streaming and colliding steps can be expressed separately in the following equations, (the streaming step shown in Figure 2.5):

$$\text{Collision step:} \quad \tilde{f}_i(\mathbf{x}, t) = f_i(x, t) - \frac{1}{\tau}(f_i - f_i^{(0)}), \tag{2.31}$$

$$\text{Streaming step:} \quad f_i(\mathbf{x} + \mathbf{c}_i \Delta t, t + \Delta t) = \tilde{f}_i(\mathbf{x}, t). \tag{2.32}$$
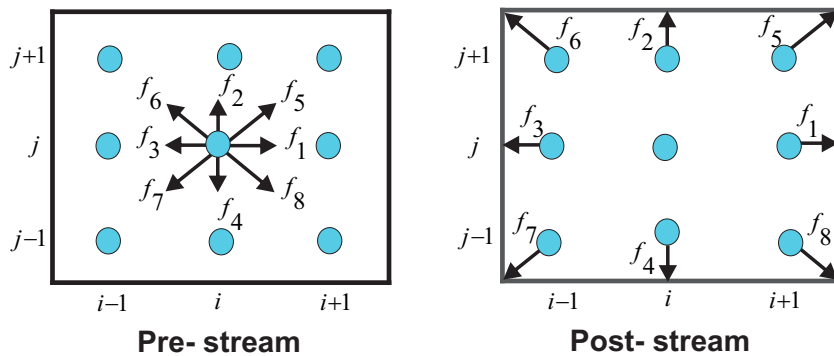
Figure 2.5: An example of the streaming step of D2Q9 LBGK model, see Section 2.3.2.

2.3 Choice of lattice

The lattices used in the lattice Boltzmann method are named DdQq. The letter d is the number of spatial dimensions while q is the number of the lattice velocities. In the next subsections one and two dimensional models with different lattice velocities will be shown.

2.3.1 One dimensional lattice

In this subsection we will present two examples of one dimensional lattice Boltzmann models which are the D1Q2 and D1Q3 models, see Figure 2.6. Here we will show the minimum macroscopic velocities required to recover the Navier Stokes equations by making a comparison between these two models.
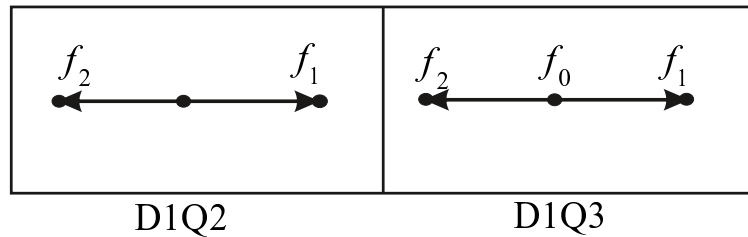
Figure 2.6: One dimensional lattice with two and three velocities.

According to [4] the D1Q2 model does not have enough independent moments to recover the Navier Stokes equations. By taking the second-order Taylor expansion to equation (2.28), we will get one dimension discrete Boltzmann equation (DBE)

$$\partial_t f_i + c_i \partial_x f_i = -\frac{1}{\tau} \left(f_i(x,t) - f_i^{(0)}(x,t) \right), \tag{2.33}$$

where $f_i^{(0)}$ is the equilibrium distribution function for the D1Q2 model and we can find it by using the power series which depends on the density and the velocity as follows:

$$f_i^{(0)} = \rho \omega_i \left(A + B c_{ix} u_x \right), \tag{2.34}$$

where in the D1Q2 model the lattice links have the same length so $w_1 = w_2 = 1/2$. The constants A and B can be found by using the mass conservation from equation (2.29) which yields $A = 1$. Then by using the momentum conservation of equation (2.30), we get $\rho u_x = B\rho u_x$ so $B = 1$.

In the next steps we will try to recover the Navier-Stokes equations. After summing the vectors of equation (2.33) and considering $\sum_i f_i = \rho$ and $\sum_i f_i c_i = \rho u_x$ we get the mass conservation equation

$$\partial_t \rho + \partial_x (\rho u_x) = 0.$$

Then multiply equation (2.33) by c_i and then sum it to get

$$\partial_t (\rho u_x) + \partial_x \rho = 0, \tag{2.35}$$

because $\sum_i f_i c_i c_i = \rho$ in the D1Q2 model. By taking second moments of equation (2.33), we will have another first-order momentum equation. Thus if we continuously apply moments to equation (2.33) we will never obtain the suitable stress tensor to recover the correct macroscopic equation because we do not have enough moments.

However, the D1Q3 model has three velocities including the rest one and this third velocity enables us to recover the Navier Stokes equations. Using the same strategy as in the D1Q2 model we can find $f_i^{(0)}$ for D1Q3 model [60]

$$f_i^{(0)} = w_i \rho (1 + 3 c_i u_x), \tag{2.36}$$

where the weight function for this model is

$$w_i = \begin{cases} 2/3, & \text{if } i = 0, \\ 1/6, & \text{if } i = 1, 2. \end{cases} \tag{2.37}$$

Similarly to D1Q2, summing the vectors of equation (2.33) we get the mass equation

$$\partial_t \rho + \partial_x(\rho u_x) = 0. \tag{2.38}$$

Add the first moment to equation (2.33) to get the momentum equation

$$\partial_t(\rho u_x) + \partial_x \Pi_{xx} = 0, \tag{2.39}$$

where $\Pi_{xx} = \sum_i f_i c_{ix} c_{ix}$ is the second-order moment. Now the second moment of equation (2.33) yields

$$\partial_t \Pi_{xx} + \partial_x Q_{xxx} = -\frac{1}{\tau}(\Pi_{xx} - \Pi_{xx}^{(0)}), \tag{2.40}$$

and from equation (2.36) we can find $\Pi_{xx}^{(0)} = P + \rho u_x^2$, where $P = \rho/3$ is the pressure. $Q_{xxx} = \sum_i f_i c_{ix} c_{ix} c_{ix}$ is the third-order moment. To recover the Navier-Stokes equations, the Chapman-Enskog expansion will be used [15]. Here, multiscale expansions for both time scale and the non conserved tensors are provided by using the small parameter $\tau \approx Kn$. So the following expansion is be applied

$$\partial_t = \partial_{t_0} + \tau \partial_{t_1} + ...,$$
$$\Pi_{xx} = \Pi_{xx}^{(0)} + \tau \Pi_{xx}^{(1)} + ..., \tag{2.41}$$
$$Q_{xxx} = Q_{xxx}^{(0)} + \tau Q_{xxx}^{(1)} + ...,$$

and we truncate equation (2.41) to $O(\tau)$. Substituting it into equation (2.40) yields

$$\partial_{t_0} \Pi_{xx}^{(0)} + \partial_x Q_{xxx}^{(0)} = -\Pi_{xx}^{(1)}. \tag{2.42}$$

Now insert $\Pi_{xx}^{(0)} = P + \rho u_x^2$ and, from equation (2.36), $Q_{xxx}^{(0)} = \rho u_x$ into equation (2.42)

such that

$$\partial_{t_0}(P + \rho u_x^2) + \partial_x(\rho u_x) = -\Pi_{xx}^{(1)}. \tag{2.43}$$

By using equations (2.38) and (2.39), one can find the value of $\Pi_{xx}^{(1)}$ (it will be discussed in detail in Section 2.5):

$$\Pi_{xx}^{(1)} = -\frac{2}{3}\rho\partial_x u_x. \tag{2.44}$$

The final step will be inserting the value of $\Pi_{xx}^{(1)}$ into equation (2.39) which gives us the one dimensional weakly compressible Navier-Stokes equations.

$$\partial_t(\rho u_x) + \partial_x(\rho u_x^2) = -\partial_x P + \partial_x\left(\frac{2\tau\rho}{3}\partial_x u_x\right), \tag{2.45}$$

where $\nu = \tau/3$ is the kinematic viscosity.

To demonstrate that the D1Q3 model is more effective than D1Q2, a code was written using FORTRAN to see the behaviour of the velocity and the density of these models. The code was running until 100 steps to test if the velocity will reach the steady state or not. Periodic boundary conditions are applied to this simulation. The equilibrium distribution function for the D1Q2 and D1Q3 models are used from equations (2.34) and (2.36) respectively. The collision frequency is used $(1/\tau = 1/3)$ while the density was set initially to be

$$\rho = \begin{cases} 2, & \text{if } -10 \leq x < 20, \\ 1, & \text{if } 0 \leq x < 10 \quad \text{or} \quad 20 \leq x \leq 30. \end{cases} \tag{2.46}$$

(a)

(b)

(c)
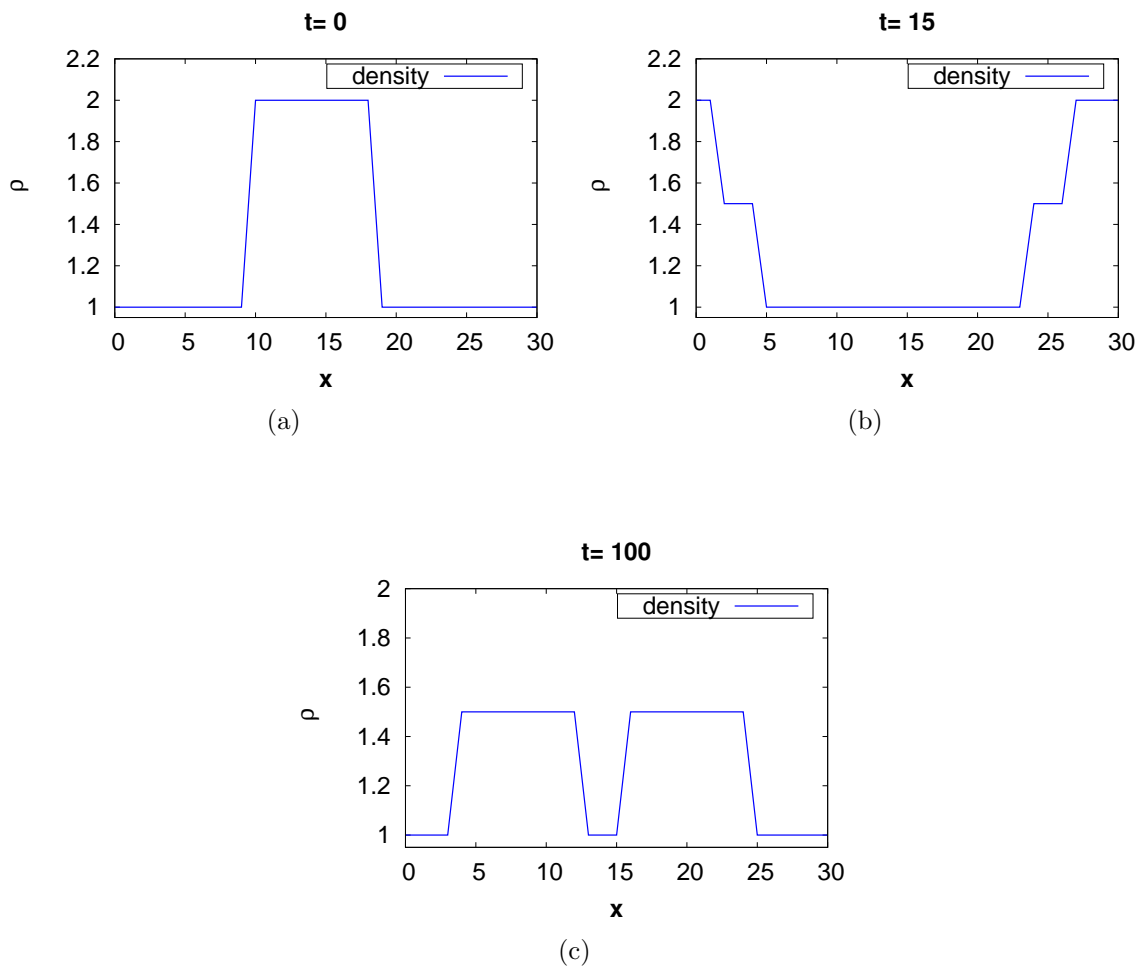
Figure 2.7: The density profile for D1Q2 model

(a)

(b)
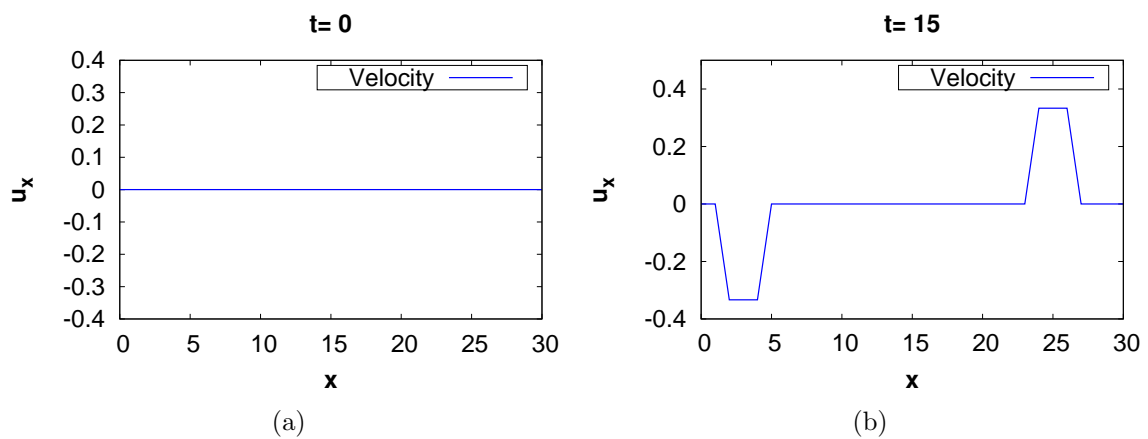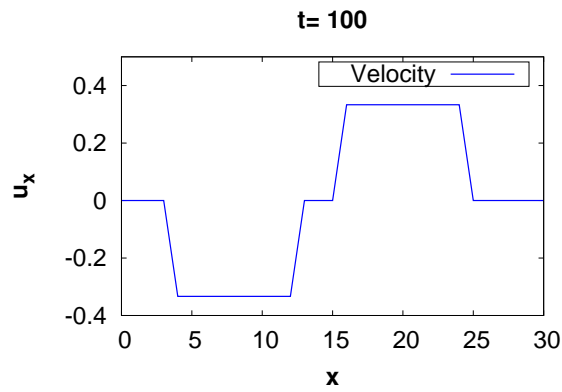
(c)

Figure 2.8: The velocity profile for D1Q2 model.

Figures 2.7 and 2.8 show that the D1Q2 model did not reach the steady state and the velocity was not even close to its equilibrium whatever the time step that we reached. This confirms the analysis of equation (2.35) where the Navier-Stokes equations can not be recovered from this number of microscopic velocities. For D1Q3, from Figures 2.9 and 2.10 we can see from time $t = 15$ the peak velocity is reducing then around $t = 100$ it has approximately reached the steady state where the velocity is zero and density is approximately constant.

(a)

(b)
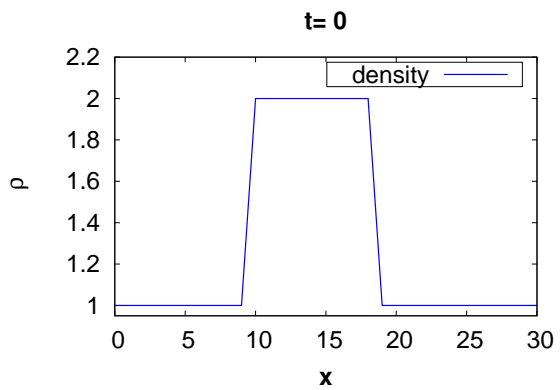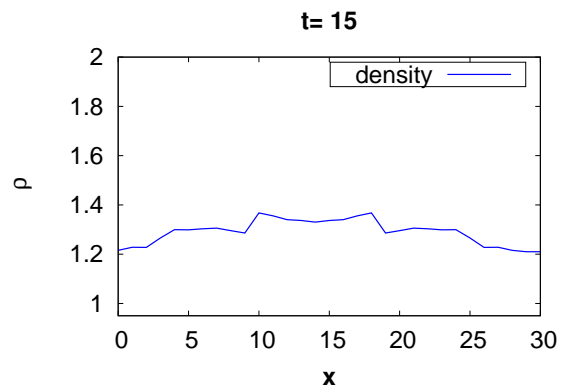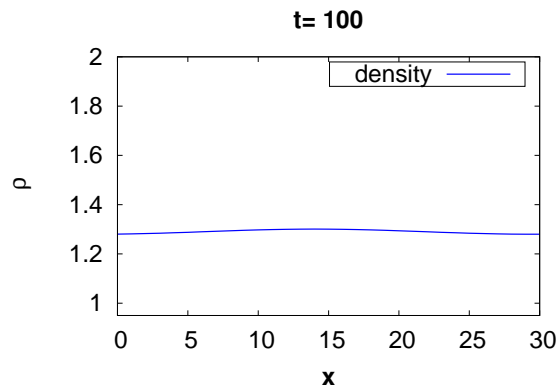
Figure 2.9: The density profile for D1Q3 model
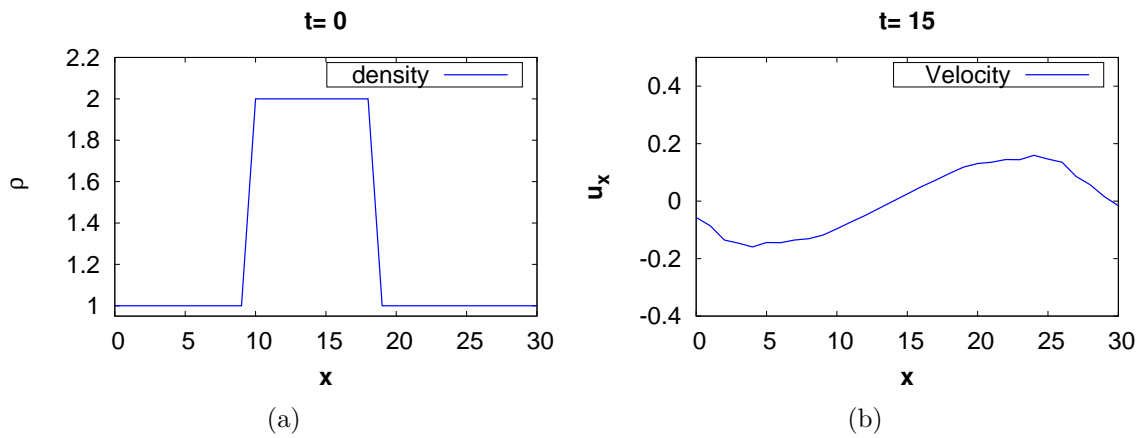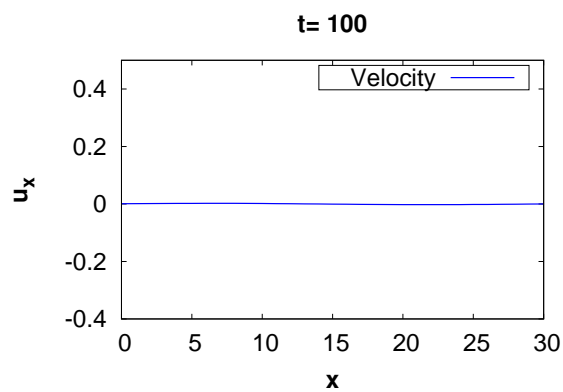
Figure 2.10: The velocity profile for D1Q3 model.

2.3.2 Two dimensional models

The popular choice of lattices in two dimensional models include D2Q5, D2Q7 and D2Q9. In general, the lattice Boltzmann method with a square lattice, like D2Q9, is more common since it is easier in the simulation because of the number of the lattice velocities.

Related with the lattice velocities are weight factors w_i and the speed of sound c_s. These weights are different from one model to another and can be found by using Hermite polynomials [102]. For example in Table 2.1 different values of w_i and speed of sound to different models of lattice Boltzmann method are presented [46]

Model	w_i	c_s^2
D1Q3	2/3	1/3
	1/6	
D2Q5	1/3	1/3
	1/6	
D2Q7	1/2	1/4
	1/12	
D2Q9	4/9	1/3
	1/9	
	1/36	
D3Q15	2/9	1/3
	1/9	
	1/27	

Table 2.1: DdQq models with weights and speed of sound.

In the next chapters we will work with the D2Q9 model. The D2Q9 model has nine velocities including the zero one in the middle of the model, see Figure 2.11, [53]

$$\mathbf{c}_i = \begin{cases} 0, & i = (0,0) \\ \frac{\Delta x}{\Delta t}\left(\cos\frac{(i-1)\pi}{4}, \sin\frac{(i-1)\pi}{4}\right), & i = 1,2,3,4 \\ \sqrt{2}\frac{\Delta x}{\Delta t}\left(\cos\frac{(i-5)\pi}{2}, \sin\frac{(i-5)\pi}{4}\right). & i = 5,6,7,8 \end{cases} \qquad (2.47)$$
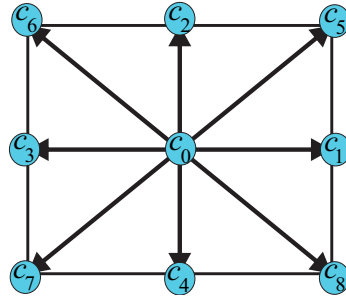
Figure 2.11: D2Q9 scheme

An essential property of the lattice Boltzmann method is isotropy. The isotropy of a tensor is the ability of remaining unchanged under the influence of rotation and reflections. The nth rank of the lattice velocity tensor associated with the discrete weights coefficient w_i is defined as

$$A_{\alpha_1 \alpha_2 ... \alpha_n} = \sum_{i=1}^{b} w_i c_{i\alpha_1} c_{i\alpha_2} ... c_{i\alpha_n}, \qquad (2.48)$$

so to recover the Navier-Stokes equations from D2Q9 lattice Boltzmann model we need fourth-order isotropy tensors, $n = 4$, and this is achieved if the tensors of equation (2.48) are isotropic to order 4. To derive the macroscopic equation, the following fourth-order isotropy should be satisfied

$$\sum_i w_i = 1, \qquad (2.49a)$$

$$\sum_i w_i c_{i\alpha} = 0, \qquad (2.49b)$$

$$\sum_i w_i c_{i\alpha} c_{i\beta} = c_s^2 \delta_{\alpha\beta}, \qquad (2.49c)$$

$$\sum_i w_i c_{i\alpha} c_{i\beta} c_{i\gamma} = 0, \qquad (2.49d)$$

$$\sum_i w_i c_{i\alpha} c_{i\beta} c_{i\gamma} c_{i\delta} = c_s^4 (\delta_{\alpha\beta} \delta_{\gamma\delta} + \delta_{\alpha\gamma} \delta_{\beta\delta} + \delta_{\alpha\delta} \delta_{\beta\gamma}), \qquad (2.49e)$$

where $\delta_{\alpha\beta}$ can be found from equation (1.11).

2.4 Choice of lattice Boltzmann units

In order to solve the physical problems represented by Navier-Stokes equations by lattice Boltzmann method accurately, a suitable system of units should be chosen. According to [69] we can either simulate the problems by discretising the dimensional physical system and convert it to lattice Boltzmann system or we can use a second approach. In this approach we rescale the physical systems into dimensionless systems where length h_0 and time t_0 scales are used. Then we convert this system to the LBM where the time step Δt and space step Δx are used. The Navier-Stokes equations in this approach depends essentially on one dimensionless number called the Reynolds number (Re) so the physical, dimensionless and lattice Boltzmann systems have the same Reynolds number. To explain the second approach clearly, variables in the physical system are denoted by x_p and the dimensionless system are indicated by x_d while the lattice Boltzmann symbolised by x_{lb}. The physical problems in fluids are described by the Navier-Stokes equations. In incompressible viscous fluids where the density $\rho = \rho_0$ is constant the Navier-Stokes equations together with the continuity equation from equation (1.13) in a physical system read

$$
\partial_{t_p}\mathbf{u}_p + (\mathbf{u}_p \cdot \nabla_p)\mathbf{u}_p = -\frac{1}{\rho_{0_p}}\nabla_p P_p + \nu_p \nabla_p^2 \mathbf{u}_p,
$$
$$
\nabla_p \cdot \mathbf{u}_p = 0.
$$
(2.50)

Firstly to convert the physical system to a dimensionless one, introduce the characteristics length h_0 and time t_0 to rescale their physical counterpart with the velocity and the derivatives as

$$
\begin{aligned}
t_d &= \frac{t_p}{t_0}, & h_d &= \frac{h_p}{h_0}, \\
u_p &= \frac{h_0}{t_0}u_d, & P_p &= \rho_0\frac{h_0^2}{t_0^2}P_d, \\
\partial_{t_p} &= \frac{1}{t_0}\partial_{t_d}, & \nabla_p &= \frac{1}{h_0}\nabla_d.
\end{aligned}
$$
(2.51)

As a result of inserting equation (2.51) into equation (2.50), the dimensionless Navier Stokes equations become

$$\partial_{t_d}\mathbf{u}_d + (\mathbf{u}_d \cdot \nabla_d)\mathbf{u}_d = -\frac{1}{\rho_{0_d}}\nabla_d P_d + \frac{1}{Re}\nabla_d^2\mathbf{u}_d,$$

$$\nabla_d \cdot \mathbf{u}_d = 0,$$

$$(2.52)$$

where $Re = h_0^2/t_0\nu$ is the Reynolds number. In this dimensionless system where the unit length and time are used the viscosity will be $\nu = 1/Re$.

Now, convert the dimensionless system to lattice Boltzmann one by using $\Delta x = 1/M$ and $\Delta t = 1/N$, the lattice spacing and lattice time step respectively where M is the number of cells and N is the number of iterations. The dimensionless velocity and viscosity convert to

$$u_d = \frac{\Delta x}{\Delta t}u_{lb},$$

$$\nu_d = \frac{\Delta x^2}{\Delta t}\nu_{lb},$$

$$(2.53)$$

which leads to

$$u_{lb} = \frac{\Delta t}{\Delta x}u_d,$$

$$\nu_{lb} = \frac{\Delta t}{\Delta x^2}\frac{1}{Re}.$$

$$(2.54)$$

But the question is still present, how can we choose the lattice speed $c = \Delta x/\Delta t$. It is obvious from equation (2.54) the velocity depends on the lattice units and the dimensionless velocity determined to be equal to 1 so the following constraint states

$$\|u_{lb}\|_2 = (\Delta t/\Delta x)\|u_d\|_2 \ll c_s^2,$$

$$(2.55)$$

where $\|.\|_2$ is the L_2 norm. Also the velocity in equation (2.55) should not be larger than the speed of sound c_s^2 for compressibility reasons. To obtain accurate results, we make sure the compressibility of the fluid is small. As a result a Mach number, defined as a ratio between the fluid velocity and the speed of sound $Ma = u_{lb}/c_s$, should be

very small where $Ma \ll 1$ is a requirement based on the expansion of $f^{(0)}$. At the same time when we increase the number of the grid points, the numerical error should be reduced. So to reduce the compressibility error and numerical error in the same time, the relation between the time step and space step will be $\Delta t \ll \Delta x$. In the next section we will see how we can derive the lattice Boltzmann equation using special polynomials called Hermite polynomials.

2.5 From Boltzmann equation to discrete Boltzmann equation

Earlier we obtained the lattice Boltzmann equation from LGCA. But in addition to this technique one can derive this equation from the kinetic equation. The non linear continuous Boltzmann equation with an external force term will be used to derive lattice Boltzmann equation such that

$$\frac{\partial f}{\partial t} + \mathbf{c} \cdot \nabla f + \mathbf{g} \cdot \nabla_c f = -\frac{1}{\tau}(f - f^{(0)}), \tag{2.56}$$

where $\nabla_c f$ is the gradient operator with respect to particle velocity and $\mathbf{g}$ is the acceleration value located in the the force term. The Maxwell Boltzmann distribution function $f^{(0)}$ is defined in equation (1.18) where RT in the equation represents the square of the speed of sound c_s^2.

Shan *et al.* [102] presented the procedure to recover the lattice Boltzmann method from the continuous Boltzmann equation. In their derivation, they utilised special polynomials called Hermite polynomials. The hydrodynamic variables can be obtained from the zero, first and second moments from equation (1.19). In the next subsection we will use projections of probability functions onto subspaces of Hermite polynomials in order to get the discrete Boltzmann equation from the continuous Boltzmann equation (2.56) then we will recover the Navier-Stokes equations from this discretization.

2.5.1 Hermite polynomials

A system of conservation mass, momentum, energy flux equations can be found by using equations (1.16), (1.18) and equation (1.19) [31]. That system of equations needs a sufficiently high number of moments to recover the energy flux and the pressure tensor. Grad [45] considered a sufficient 13 moments of the Boltzmann equation by using special polynomials, named Hermite polynomials.

Our goal is to discetise the Boltzmann equation in velocity space to get the Discrete Boltzmann equation (DBE) and its moments in equation (1.19) by using the same technique and follow the procedure of Shan *et al.* [102]. So, by applying the Hermite polynomials and projecting the distribution functions on these polynomials where a suitable truncation order should be considered, the DBE will be found. Hermite polynomials are the best choice because these polynomials are orthogonal and we can obtain the governing equations of lattice Boltzmann equation from the coefficient of Hermite polynomials. Moreover, the Hermite quadrature gives the exact solution to a certain order when we use it to discetise the continuous distribution functions and velocities. So according to Shan *et al.* [102], by projecting the distribution functions on the Hermite polynomials, we will get the discrete Boltzmann equation. First let's define the D-dimensional n^{th} order weighted orthonormal Hermite polynomial as

$$H^{(n)}(\mathbf{c}) = \frac{(-1)^n}{\omega(\mathbf{c})} \nabla^n \omega(\mathbf{c}), \qquad (2.57)$$

where $\omega(\mathbf{c})$ is the weight function specified by

$$\omega(\mathbf{c}) = \frac{1}{(2\pi)^{D/2}} \exp(-c^2/2), \qquad (2.58)$$

so the initial three basic polynomials will be

$$H^{(0)}(\mathbf{c}) = 1, \ H_\alpha^{(1)}(\mathbf{c}) = c_\alpha \ \text{ and } \ H_{\alpha\beta}^{(2)}(\mathbf{c}) = c_\alpha c_\beta - \delta_{\alpha\beta}, \qquad (2.59)$$

where $\delta_{\alpha\beta}$ is the identity matrix. The distribution function are projected on the Hermite orthonormal polynomials as

$$f(\mathbf{x}, \mathbf{c}, t) = \omega(\mathbf{c}) \sum_{n=0}^{\infty} \frac{1}{n!} \mathbf{a}^{(n)}(\mathbf{x}, t) H^{(n)}(\mathbf{c}), \qquad (2.60)$$

where the symmetric coefficient $\mathbf{a}^{(n)}$ is the tensor that is used to define moments of the Boltzmann equation

$$\mathbf{a}^{(n)}(\mathbf{x}, t) = \int f(\mathbf{x}, \mathbf{c}, t) H^{(n)}(\mathbf{c}) d\mathbf{c}. \qquad (2.61)$$

If we apply the zero, first and second rank Hermite polynomials from equation (2.59) into equation (2.61), one can get the essential hydrodynamic quantities

$$\begin{aligned}
\mathbf{a}^{(0)} &= \rho, \\
\mathbf{a}^{(1)} &= \rho\mathbf{u}, \\
\mathbf{a}^{(2)} &= \mathbf{P} + (\rho\mathbf{u}\mathbf{u} - \boldsymbol{\delta}),
\end{aligned} \qquad (2.62)$$

where $\mathbf{P}$ is the second-order moment tensor. Similar to equation (2.62) the coefficients of the Maxwell equilibrium distribution function (1.18) after applying equation (2.59) to it, will be

$$\begin{aligned}
\mathbf{a}_0^{(0)} &= \rho, \\
\mathbf{a}_0^{(1)} &= \rho\mathbf{u}, \\
\mathbf{a}_0^{(2)} &= \rho(\mathbf{u}\mathbf{u} + ((c_s^2 - 1)\boldsymbol{\delta})).
\end{aligned} \qquad (2.63)$$

In order to discretise the velocity space of the continuum Boltzmann equation, the probability distribution function in equation (2.60) should be truncated at order N as

$$f^N(\mathbf{x}, \mathbf{c}, t) = \omega(\mathbf{c}) \sum_{n=0}^{N} \frac{1}{n!} \mathbf{a}^{(n)}(\mathbf{x}, t) H^{(n)}(\mathbf{c}), \qquad (2.64)$$

also the coefficient $\mathbf{a}^{(n)}(\mathbf{x}, t)$ in equation (2.62) can be represented in terms of the truncated f^N , $n = 1, ...N$, as

$$\mathbf{a}^{(n)}(\mathbf{x}, t) = \int f^N(\mathbf{x}, \mathbf{c}, t) H^{(n)}(\mathbf{c}) d\mathbf{c}, \tag{2.65}$$

where both f and H are up to N order. So to get the most accurate evaluation, let's define the $2N$ order polynomial $q(\mathbf{x}, \mathbf{c}, t)$ such that

$$f^N(\mathbf{x}, \mathbf{c}, t) H^{(n)}(\mathbf{c}) = \omega(\mathbf{c}) q(\mathbf{x}, \mathbf{c}, t). \tag{2.66}$$

Then the Gauss-Hermite quadrature defined by

$$\int \omega(\mathbf{c}) f(\mathbf{c}) d\mathbf{c} \cong \sum_{i=1}^{b} \omega_i f(\mathbf{c}_i), \tag{2.67}$$

can be employed so the coefficient $\mathbf{a}^{(n)}$ can be written as

$$\mathbf{a}^{(n)} = \int \omega(\mathbf{c}) q(\mathbf{x}, \mathbf{c}, t) d\mathbf{c} = \sum_{i=1}^{b} \omega_i q(\mathbf{x}, \mathbf{c}_i, t) = \sum_{i=1}^{b} \frac{\omega_i}{\omega(\mathbf{c}_i)} f^N(\mathbf{x}, \mathbf{c}_i, t) H^{(n)}(\mathbf{c}_i), \tag{2.68}$$

where $\mathbf{c}_i$ is the Gauss-Hermite quadrature abscissa and ω_i is the weights function for $(i = 1, ..., b)$.

By using the Gauss-Hermite quadrature from equation (2.67) and in order to match the lattice Boltzmann models, the discrete velocity $\mathbf{c}_i$ should be rescaled. That is because the lattice velocities $\mathbf{c}_i$ is not of unity scale [102]. The coefficient c_s which is defined as the speed of sound will be used as a rescale factor. c_s is different from lattice to another, see Table 2.1. So the rescaled Hermite polynomials have the following formula

$$H_i^{(0)} = 1,$$
$$H_{i\alpha}^{(1)} = c_{i\alpha}, \tag{2.69}$$
$$H_{i\alpha\beta}^{(2)} = c_{i\alpha} c_{i\beta} - c_s^2 \delta_{\alpha\beta},$$

and the rescaled coefficient tensors $\mathbf{a}^n$ have the following formulae

$$\mathbf{a}^{(0)} = \rho,$$
$$\mathbf{a}^{(1)} = \rho\mathbf{u}, \tag{2.70}$$
$$\mathbf{a}^{(2)} = P + \rho(\mathbf{u}\mathbf{u} + (c_s^2\boldsymbol{\delta})),$$

while the rescaled coefficients of the equilibrium function become

$$\mathbf{a}_0^{(0)} = \rho,$$
$$\mathbf{a}_0^{(1)} = \rho\mathbf{u}, \tag{2.71}$$
$$\mathbf{a}_0^{(2)} = \rho(\mathbf{u}\mathbf{u} + c_s^2((c_s^2 - 1)\boldsymbol{\delta})).$$

The continuous Maxwell equilibrium distribution function in equation (1.18) can be expanded up to order two in velocity as

$$f^{(0)}(\mathbf{x}, t) = \omega\rho\left(1 + \mathbf{c}\cdot\mathbf{u} + \frac{1}{2}(\mathbf{c}\cdot\mathbf{u})^2 - \frac{1}{2}\mathbf{u}^2\right) + O(\mathbf{u}^3), \tag{2.72}$$

while the last term of the left-side in equation (2.56) is the force term. By taking the gradient of distribution function defined in equation (2.60) and the definition of Hermite polynomials equation (2.57) [80], we obtain

$$\begin{aligned}
\nabla_c f &= \sum_{n=0}^{\infty} \frac{1}{n!}\mathbf{a}^{(n)}\nabla_c(\omega H^{(n)}), \\
&= \sum_{n=0}^{\infty} \frac{(-1)}{n!}\mathbf{a}^{(n)}\nabla_c^{n+1}\omega, \\
&= -\omega\sum_{n=0}^{\infty} \frac{1}{n!}\mathbf{a}^{(n)}H^{(n+1)}, \\
&= -\omega\sum_{n=1}^{\infty} \frac{1}{n!}n\mathbf{a}^{(n-1)}H^{(n)}. \tag{2.73}
\end{aligned}$$

Let's define the force term $R(\mathbf{c}) = -\mathbf{g} \cdot \nabla_c f$, then equation (2.73) becomes

$$R(\mathbf{c}) = \omega \sum_{n=1}^{\infty} \frac{1}{n!} \mathbf{g} n \mathbf{a}^{(n-1)} H^{(n)}. \tag{2.74}$$

2.5.2 Discrete Boltzmann's equation

The discrete velocity Boltzmann equation can be obtained by using the Gauss-Hermite quadrature (2.67) and applying it to equations (1.19) such that

$$\begin{aligned}
\rho &= \sum_{i=1}^{b} \frac{\omega_i f(\mathbf{x}, \mathbf{c}_i, t)}{\omega(\mathbf{c}_i)}, \\
\rho \mathbf{u} &= \sum_{i=1}^{b} \frac{\omega_i f(\mathbf{x}, \mathbf{c}_i, t) \mathbf{c}_i}{\omega(\mathbf{c}_i)}, \\
\rho \mathbf{u}\mathbf{u} + P &= \sum_{i=1}^{b} \frac{\omega_i f(\mathbf{x}, \mathbf{c}_i, t) \mathbf{c}_i^2}{\omega(\mathbf{c}_i)}.
\end{aligned} \tag{2.75}$$

To simplify the equations let's define

$$f_i(\mathbf{x}, t) = \frac{\omega_i}{\omega(\mathbf{c}_i)} f(\mathbf{x}, \mathbf{c}_i, t) \qquad i = 1, ..., b. \tag{2.76}$$

To complete the discretization of the velocity, the rescaled equilibrium distribution function can be defined according to equations (2.69) and (2.71) as

$$f_i^{(0)}(\mathbf{x}, t) = w_i \sum_{n=0}^{b} \frac{1}{c_s^{2n} n!} \mathbf{a}_0^{(n)}(\mathbf{x}, t) H^{(n)}(\mathbf{c}_i). \tag{2.77}$$

Now applying the values of $a_0^{(n)}$ from equations (2.71) to equation (2.77) and truncating the equilibrium to order two, yields

$$f_i^{(0)}(\mathbf{x}, t) = \omega_i \rho \left(1 + \frac{\mathbf{c}_i \cdot \mathbf{u}}{c_s^2} + \frac{(\mathbf{c}_i \cdot \mathbf{u})^2}{2c_s^4} - \frac{\mathbf{u}^2}{2c_s^2} \right), \tag{2.78}$$

where the Mach number $Ma = u/c_s^2$ in the equilibrium distribution function should be less than one for compressibility reasons.

Now the rescaled force term of the discrete Boltzmann equation is:

$$R_i(\mathbf{x}, t) = \omega_i \sum_{n=1}^{b-1} \frac{1}{n! c_s^{2n}} \mathbf{g} n \mathbf{a}^{(n-1)} H^{(n)}(\mathbf{c}_i). \tag{2.79}$$

Also by applying $\mathbf{a}^{(n)}$ from equation (2.70) to equation (2.79) and truncating the sum to order two, the discrete force term can be written as

$$R_i(\mathbf{x}, t) = \omega_i \rho \left(\frac{\mathbf{c}_i - \mathbf{u}}{c_s^2} + \frac{(\mathbf{c}_i \cdot \mathbf{u}) \mathbf{c}_i}{c_s^4} \right) \cdot \mathbf{g}. \tag{2.80}$$

Note that the form of R_i is designed to recover the Navier-Stokes equations by satisfying the following relations

$$\sum_i R_i = 0,$$
$$\sum_i R_i \mathbf{c}_i = \mathbf{F}, \tag{2.81}$$
$$\sum_i R_i \mathbf{c}_i \mathbf{c}_i = \mathbf{F} \mathbf{u} + \mathbf{u} \mathbf{F},$$

where $\mathbf{F} = \rho \mathbf{g}$. The first constraint in equation (2.81) ensures that mass is conserved and the second constraint is the force term which appears in Navier-Stokes equations. The third constraint guarantees the term $\mathbf{F}$ cancels in the stress tensor of Navier-Stokes equations. Finally, by applying equations (2.78), (2.80) and (2.76) to equation (2.56), the discrete BGK-Boltzmann equation is

$$\frac{\partial f_i}{\partial t} + \mathbf{c}_i \cdot \nabla f_i = -\frac{1}{\tau}(f_i - f_i^{(0)}) + R_i \qquad (i = 1, ..., b). \tag{2.82}$$

2.5.3   Recovery of Navier Stokes equations from discrete Boltzmann equation

To ensure the lattice Boltzmann equation recovers the Navier-Stokes equations, the Chapman-Enskog expansion is used. In this chapter we will use the Einstein's summation convention notation. The zero, first and second moments of equation (2.82) respectively produce the following three equations

$$\partial_t \rho + \partial_\alpha \rho u_\alpha = 0, \tag{2.83}$$

$$\partial_t \rho u_\alpha + \partial_\beta \Pi_{\alpha\beta} = F_\alpha, \tag{2.84}$$

$$\partial_t \Pi_{\alpha\beta} + \partial_\gamma Q_{\alpha\beta\gamma} = -\frac{1}{\tau}(\Pi_{\alpha\beta} - \Pi_{\alpha\beta}^{(0)}) + F_\alpha u_\beta + F_\beta u_\alpha, \tag{2.85}$$

where $\Pi_{\alpha\beta} = \sum_i f_i c_{i\alpha} c_{i\beta}$ is the momentum flux and it relaxes to its equilibrium $\Pi_{\alpha\beta}^{(0)} = \sum_i f_i^{(0)} c_{i\alpha} c_{i\beta}$. $Q_{\alpha\beta\gamma} = \sum c_{i\alpha} c_{i\beta} c_{i\gamma} f_i$ is the third-order moment. Obviously mass and momentum are conserved by Newton's law but the higher order moments are not conserved. Our aim is to find solutions that change slowly over timescales which are longer than the collision time τ. So the Chapman-Enskog expansion is used to expand the time derivative and the non-conserved moments as follows:

$$\partial_t = \partial_{t_0} + \tau \partial_{t_1} + \tau^2 \partial_{t_2} + ..., \tag{2.86}$$

$$\Pi_{\alpha\beta} = \Pi_{\alpha\beta}^{(0)} + \tau \Pi_{\alpha\beta}^{(1)} + \tau^2 \Pi_{\alpha\beta}^{(2)} + ..., \tag{2.87}$$

$$Q_{\alpha\beta\gamma} = Q_{\alpha\beta\gamma}^{(0)} + \tau Q_{\alpha\beta\gamma}^{(1)} + \tau^2 Q_{\alpha\beta\gamma}^{(2)} + ... \tag{2.88}$$

Substituting the expansion of equation (2.86) to $O(\tau)$ into equation (2.83) yields

$$(\partial_{t_0} + \tau \partial_{t_1})\rho + \partial_\alpha \rho u_\alpha = 0. \tag{2.89}$$

At leading order we have

$$\partial_{t_0}\rho + \partial_\alpha \rho u_\alpha = 0, \tag{2.90}$$

Thus from equation (2.89) and equation (2.90) we get $\partial_{t_1}\rho = 0$. Now substitute the expansions of equations (2.86) and (2.87) into equation (2.84) then truncate them to $O(\tau)$ to get

$$(\partial_{t_0} + \tau\partial_{t_1})\rho u_\alpha + \partial_\beta(\Pi^{(0)}_{\alpha\beta} + \tau\Pi^{(1)}_{\alpha\beta}) = F_\alpha. \tag{2.91}$$

Rearranging equation (2.91) as

$$\partial_{t_0}\rho u_\alpha + \tau\partial_{t_1}\rho u_\alpha + \partial_\beta\Pi^{(0)}_{\alpha\beta} + \tau\partial_\beta\Pi^{(1)}_{\alpha\beta} = F_\alpha, \tag{2.92}$$

then truncating the expansion of equation (2.92) to leading order yields

$$\partial_{t_0}\rho u_\alpha + \partial_\beta\Pi^{(0)}_{\alpha\beta} = F_\alpha. \tag{2.93}$$

The next step will be finding the equilibrium stress tensor $\Pi^{(0)}_{\alpha\beta}$ by multiplying equation (2.78) by $c_{i\alpha}c_{i\beta}$ as follows

$$
\begin{aligned}
\Pi^{(0)}_{\alpha\beta} &= \sum_i c_{i\alpha}c_{i\beta}f_i^{(0)} \\
&= \rho\Big[\sum_i w_i c_{i\alpha}c_{i\beta} + \frac{1}{c_s^2}u_\gamma\sum_i w_i c_{i\alpha}c_{i\beta}c_{i\gamma} + \frac{1}{2c_s^4}u_\gamma u_\delta\sum_i w_i c_{i\alpha}c_{i\beta}c_{i\gamma}c_{i\delta} \\
&\quad - \frac{1}{2c_s^2}u_\gamma u_\gamma\sum_i w_i c_{i\alpha}c_{i\beta}\Big], \\
&= \rho\Big[c_s^2\delta_{\alpha\beta} - \frac{u_\gamma u_\gamma}{2}\delta_{\alpha\beta} + \frac{u_\gamma u_\delta}{2}(\delta_{\alpha\beta}\delta_{\gamma\delta} + \delta_{\alpha\gamma}\delta_{\beta\delta} + \delta_{\alpha\delta}\delta_{\beta\gamma})\Big]. \tag{2.94}
\end{aligned}
$$

So the second-order moment of equilibrium function is calculated as

$$\Pi^{(0)}_{\alpha\beta} = P\delta_{\alpha\beta} + \rho u_\alpha u_\beta. \tag{2.95}$$

where $P = c_s^2 \rho$ is the pressure.

By applying the expansion of equations (2.86), (2.87) and (2.88) into equation (2.85) one can get

$$
\begin{aligned}
(\partial_{t_0} + \tau \partial_{t_1})(\Pi_{\alpha\beta}^{(0)} + \tau \Pi_{\alpha\beta}^{(1)}) &+ \partial_\gamma (Q_{\alpha\beta\gamma}^{(0)} + \tau Q_{\alpha\beta\gamma}^{(1)}) \\
&= -\frac{1}{\tau}(\Pi_{\alpha\beta}^{(0)} + \tau \Pi_{\alpha\beta}^{(1)} - \Pi_{\alpha\beta}^{(0)}) + F_\alpha u_\beta + F_\beta u_\alpha,
\end{aligned}
\tag{2.96}
$$

where $Q_{\alpha\beta\gamma}^{(0)} = \sum f_i^{(0)} c_{i\alpha} c_{i\beta} c_{i\gamma}$. Then truncate the expansion of equation (2.96) to leading order to obtain

$$
\partial_{t_0} \Pi_{\alpha\beta}^{(0)} + \partial_\gamma Q_{\alpha\beta\gamma}^{(0)} - F_\alpha u_\beta - F_\beta u_\alpha = -\Pi_{\alpha\beta}^{(1)}.
\tag{2.97}
$$

Now to recover the Navier-Stokes equations, $\Pi_{\alpha\beta}^{(1)}$ needs to be calculated. First, from equation (2.78)

$$
\begin{aligned}
Q_{\alpha\beta\gamma}^{(0)} &= \sum_i f_i^{(0)} c_{i\alpha} c_{i\beta} c_{i\gamma} \\
&= \rho \left[\sum_i w_i c_{i\alpha} c_{i\beta} c_{i\gamma} + \frac{1}{c_s^2} u_\delta \sum_i w_i c_{i\alpha} c_{i\beta} c_{i\gamma} c_\delta \right. \\
&\quad \left. - \frac{1}{2c_s^2} u_\delta u_\delta \sum_i w_i c_{i\alpha} c_{i\beta} c_{i\gamma} + \frac{u_\delta u_\epsilon}{2c_s^4} \sum_i w_i c_\alpha c_\beta c_{i\gamma} c_{i\delta} c_{i\epsilon} \right], \\
&= c_s^2 \rho u_\delta \left[\delta_{\alpha\beta} \delta_{\gamma\delta} + \delta_{\alpha\gamma} \delta_{\beta\delta} + \delta_{\alpha\delta} \delta_{\beta\gamma} \right].
\end{aligned}
\tag{2.98}
$$

Secondly, to find $\Pi_{\alpha\beta}^{(1)}$, we must find $\partial_{t_0} \Pi_{\alpha\beta}^{(0)}$ and $\partial_\gamma Q_{\alpha\beta\gamma}^{(0)}$. So the second term of equation (2.97) is

$$
\begin{aligned}
\partial_\gamma Q_{\alpha\beta\gamma}^{(0)} &= c_s^2 \partial_\gamma \rho u_\delta (\delta_{\alpha\beta} \delta_{\gamma\delta} + \delta_{\alpha\gamma} \delta_{\beta\delta} + \delta_{\alpha\delta} \delta_{\beta\gamma}), \\
&= c_s^2 \delta_{\alpha\beta} \partial_\gamma u_\gamma + c_s^2 \partial_\alpha \rho u_\beta + c_s^2 \partial_\beta \rho u_\alpha,
\end{aligned}
\tag{2.99}
$$

while the partial derivative of equation (2.95) leads to

$$\partial_{t_0} \Pi_{\alpha\beta}^{(0)} = \partial_{t_0} \rho u_\alpha u_\beta + \partial_{t_0} \rho c_s^2 \delta_{\alpha\beta}. \tag{2.100}$$

By using the product rule, we get

$$\partial_{t_0} \Pi_{\alpha\beta}^{(0)} = \rho u_\alpha \partial_{t_0} u_\beta + u_\beta \partial_{t_0} \rho u_\alpha + \partial_{t_0} \rho c_s^2 \delta_{\alpha\beta}, \tag{2.101}$$

and

$$\rho u_\alpha \partial_{t_0} u_\beta = u_\alpha \partial_{t_0} \rho u_\beta - u_\alpha u_\beta \partial_{t_0} \rho. \tag{2.102}$$

Then by inserting equation (2.102) into equation (2.101), we produce

$$\partial_{t_0} \Pi_{\alpha\beta}^{(0)} = u_\alpha \partial_{t_0} \rho u_\beta + u_\beta \partial_{t_0} \rho u_\alpha - u_\alpha u_\beta \partial_{t_0} \rho + c_s^2 \delta_{\alpha\beta} \partial_{t_0} \rho. \tag{2.103}$$

From equations (2.83) and (2.84) we have

$$\partial_{t_0} \Pi_{\alpha\beta}^{(0)} = -u_\alpha \partial_\gamma (\rho u_\beta u_\gamma + \rho c_s^2 \delta_{\alpha\beta}) - u_\beta \partial_\gamma (\rho u_\alpha u_\gamma + \rho c_s^2 \delta_{\alpha\beta})$$
$$+ u_\alpha u_\beta \partial_\gamma \rho u_\gamma - c_s^2 \delta_{\alpha\beta} \partial_\gamma \rho u_\gamma + u_\alpha F_\beta + u_\beta F_\alpha. \tag{2.104}$$

With the same approach we found the following relation

$$\partial_\gamma \rho u_\alpha u_\beta u_\gamma = u_\alpha \partial_\gamma \rho u_\beta u_\gamma + u_\beta \partial_\gamma \rho u_\alpha u_\gamma - u_\alpha u_\beta \partial_\gamma \rho u_\gamma, \tag{2.105}$$

so equation (2.103) becomes

$$\partial_{t_0} \Pi_{\alpha\beta}^{(0)} = -\partial_\gamma \rho u_\alpha u_\beta u_\gamma - c_s^2 u_\alpha \partial_\beta \rho - c_s^2 u_\beta \partial_\alpha \rho - c_s^2 \delta_{\alpha\beta} \partial_\gamma \rho u_\gamma$$
$$+ u_\alpha F_\beta + u_\beta F_\alpha. \tag{2.106}$$

Now adding equation (2.99) and equation (2.106) to equation (2.97) leads to

$$-\Pi_{\alpha\beta}^{(1)} = \partial_{t_0}\Pi_{\alpha\beta}^{(0)} + \partial_\gamma Q_{\alpha\beta\gamma}^{(0)} - F_\alpha u_\beta - F_\beta u_\alpha$$

$$= -\partial_\gamma \rho u_\alpha u_\beta u_\gamma - c_s^2 u_\alpha \partial_\beta \rho - c_s^2 u_\beta \partial_\alpha \rho$$

$$- c_s^2 \delta_{\alpha\beta} \partial_\gamma \rho u_\gamma + c_s^2 \delta_{\alpha\beta} \partial_\gamma u_\gamma + c_s^2 \partial_\beta \rho u_\alpha +$$

$$c_s^2 \partial_\alpha \rho u_\beta + u_\alpha F_\beta + u_\beta F_\alpha - F_\alpha u_\beta - F_\beta u_\alpha. \tag{2.107}$$

So, the final result of equation (2.107) reads

$$\Pi_{\alpha\beta}^{(1)} = -c_s^{(2)}\rho[\partial_\beta u_\alpha + \partial_\alpha u_\beta] + O(Ma^3). \tag{2.108}$$

By equation (2.84),

$$\partial_t(\rho u_\alpha) + \partial_\beta(\Pi^{(0)} + \tau\Pi^{(1)}) = F_\alpha. \tag{2.109}$$

After neglecting $O(Ma^3)$, substituting equation (2.108) into equation (2.109) gives

$$\partial_t(\rho u_\alpha) + \partial_\beta \left(c_s^2 \rho \delta_{\alpha\beta} + \rho u_\alpha u_\beta - \tau c_s^2 \rho(\partial_\alpha u_\beta + \partial_\beta u_\alpha) \right) = F_\alpha. \tag{2.110}$$

Now rearranging the above equation yields

$$\partial_t(\rho u_\alpha) + \partial_\beta c_s^2 \rho \delta_{\alpha\beta} + \partial_\beta \rho u_\alpha u_\beta - \tau c_s^2 \rho \partial_\beta(\partial_\alpha u_\beta + \partial_\beta u_\alpha) = F_\alpha \tag{2.111}$$

So the Navier-Stokes equations can be written as

$$\partial_t \rho \mathbf{u} + \nabla \cdot (\rho \mathbf{u}\mathbf{u}) = -\nabla P + \nabla \cdot [\rho\nu(\nabla \mathbf{u} + \nabla \mathbf{u}^T)] + \mathbf{F} \tag{2.112}$$

where $\nu = c_s^2 \tau$ is the kinematic viscosity.

Furthermore, for small Mach number the density ρ is a constant then from equations

(2.83) and (2.112) one can obtain the incompressible Navier-Stokes equations as

$$\nabla.\mathbf{u} = 0 \tag{2.113}$$

$$\partial_t \mathbf{u} + \mathbf{u} \cdot \nabla \mathbf{u} = -\frac{1}{\rho} \nabla P + \nu \nabla^2 \mathbf{u} + \mathbf{G} \tag{2.114}$$

2.5.4 Discretisation of space and time

To achieve a completely discrete lattice Boltzmann equation, equation (2.82) should be discretised in space and time. Integrate both sides of equation (2.82) from t to $t + \Delta t$ to obtain

$$\int_t^{t+\Delta t} \left(\frac{\partial f_i}{\partial s} + \mathbf{c}_i \cdot \nabla f_i \right) ds = \int_t^{t+\Delta t} \left(-\frac{1}{\tau}(f_i - f_i^{(0)}) + R_i \right) ds. \tag{2.115}$$

The integration of the left-hand side along a characteristic Δt is found exactly while for the right-hand side an approximation is obtained using the trapezoidal rule:

$$f_i(\mathbf{x} + \mathbf{c}_i \Delta t, t + \Delta t) - f_i(\mathbf{x}, t) = -\frac{\Delta t}{2\tau} \left(f_i(\mathbf{x} + \mathbf{c}_i \Delta t, t + \Delta t) - f_i^{(0)}(\mathbf{x} + \mathbf{c}_i \Delta t, t + \Delta t) \right)$$
$$+ \frac{\Delta t}{2} R_i(\mathbf{x} + \mathbf{c}_i \Delta t, t + \Delta t)) - \frac{\Delta t}{2\tau} \left(f_i(\mathbf{x}, t) - f_i^{(0)}(\mathbf{x}, t) \right) + \frac{\Delta t}{2} R_i(\mathbf{x}, t) + O(\Delta t^3). \tag{2.116}$$

The accuracy of equation (2.116) is second-order in time because of the Trapezoidal rule. However, it is implicit system of algebraic equations. So $f_i^{(0)}$ and R_i at the new time step $t + \Delta t$ depend on the moments of ρ and $\mathbf{u}$ at the new time step which are a function of f_i at $t + \Delta t$. That leads to an implicit non-linear equations which are difficult to solve. Alternatively, He *et al.* [52] introduced a change of variables to obtain an explicit scheme

$$\bar{f}_i(\mathbf{x}, t) = f_i(\mathbf{x}, t) + \frac{\Delta t}{2\tau} \left(f_i(\mathbf{x}, t) - f_i^{(0)}(\mathbf{x}, t) \right) - \frac{\Delta t}{2} R_i(\mathbf{x}, t). \tag{2.117}$$

Substitute equation (2.117) into equation (2.116) and after some algebraic steps, the fully discrete lattice Boltzmann equation reads

$$\bar{f}_i(\mathbf{x} + \mathbf{c}_i \Delta t, t + \Delta t) - \bar{f}_i(\mathbf{x}, t) = -\frac{\Delta t}{(\tau + \Delta t/2)} \left(\bar{f}_i(\mathbf{x}, t) - f_i^{(0)}(\mathbf{x}, t) \right)$$
$$+ \frac{\tau \Delta t}{(\tau + \Delta t/2)} R_i. \tag{2.118}$$

The moments of equation (2.118) are obtained easily from equation (2.117). So the zer-order moment

$$\rho = \sum_{i=0}^{8} f_i = \sum_{i=0}^{8} \bar{f}_i, \tag{2.119}$$

while the momentum and the stress tensor of equation (2.118) are obtained as follows

$$\sum_{i=0}^{8} \bar{f}_i \mathbf{c}_i = \rho \mathbf{u} - \frac{\Delta t}{2} \sum_{i=0}^{8} \mathbf{c}_i R_i,$$
$$= \rho \mathbf{u} - \frac{\Delta t}{2} \mathbf{F}, \tag{2.120}$$

$$\sum_{i=0}^{8} \bar{f}_i \mathbf{c}_i \mathbf{c}_i = \frac{(2\tau + 1)}{2\tau} \mathbf{\Pi} - \frac{1}{2\tau} \mathbf{\Pi}^{(0)} - \frac{1}{2} (\mathbf{Fu} + \mathbf{uF}). \tag{2.121}$$

2.6 Multiple Relaxation Time (MRT) lattice Boltzmann method

Despite the advantages of the LBM as we mentioned earlier, some problems of the BGK-LBM model remain. A lack of numerical stability is the main problem since all the particles relax to their equilibrium at the same rate which is not acceptable physically according to Guo and Shu [46]. Moreover, for small relaxation time τ, the discrete distribution functions $\bar{f}_i$ exceed their equilibrium values instead of relaxing toward them quickly which cause a problem in the stability of simulations [29]. To

conquer this drawback a technique which relaxes non-conserved moments at different rates has been proposed. The MRT-LBM was introduced originally by d'Humieres [32] then analysed in detail by Lallemand and Luo [68]. In this work the MRT approach is based on the Hermite polynomials which were introduced by Benzi *et al.* [6]. Because we have used Hermite polynomials the vectors are orthogonal with respect to weighted inner product

$$\langle p, q \rangle = \sum_{i=0}^{8} w_i p_i q_i = 0 \quad for \quad p \neq q, \tag{2.122}$$

where p and q are orthogonal to each other.

The discrete Boltzmann equation can be written in a more general form as

$$\frac{\partial f_i}{\partial t} + \mathbf{c}_i \cdot \nabla f_i = M^{-1} A M (f_i - f_i^{(0)}), \tag{2.123}$$

where A is a diagonal matrix involving the relaxation times. M is $b \times b$ transformation matrix relating moments to distribution functions. The general idea of MRT-LBM is to transform the distribution functions to its moments, then relax the non-conserved moments at different rates. Then we transform the post collision moments back into the distribution basis. So the relationship between the moments and distribution functions can be formed as $\mathbf{m} = M\mathbf{f}$ where $\mathbf{m}$ is a vector of moments and $\mathbf{f}$ is a vector of the nine distribution functions such that

$$\frac{\partial \mathbf{m}}{\partial t} + \mathbf{c}_i \cdot \nabla \mathbf{m} = \mathbf{A}(\mathbf{m} - \mathbf{m}^{(0)}). \tag{2.124}$$

According to the Hermite polynomials the first six row vectors in the transform matrix M give the hydrodynamic variables ρ, $\mathbf{u}$ and the three components of the stress tensor

$\boldsymbol{\Pi}$ as follows

$$
\begin{aligned}
1_i &= (1, 1, 1, 1, 1, 1, 1, 1, 1), \\
c_{ix} &= (0, 1, 0, -1, 0, 1, -1, -1, 1), \\
c_{iy} &= (0, 0, 1, 0, -1, 1, 1, -1, -1), \\
c_{ix}^2 - \frac{1}{3} &= \frac{1}{3}(-1, 2, -1, 2, -1, 2, 2, 2, 2), \\
c_{iy}^2 - \frac{1}{3} &= \frac{1}{3}(-1, -1, 2, -1, 2, 2, 2, 2, 2), \\
c_{ix}c_{iy} &= (0, 0, 0, 0, 0, 1, -1, 1, -1).
\end{aligned}
\tag{2.125}
$$

A lattice with b velocities has b moments, so for D2Q9 model in addition to the six vectors in equations (2.125) there are three non-hydrodynamic orthogonal weighted basis h_i, $h_i c_{ix}$ and $h_i c_{iy}$ such that

$$
\begin{aligned}
h_i &= (1, -2, -2, -2, -2, 4, 4, 4, 4) \\
h_i c_{ix} &= (0, -2, 0, 2, 0, 4, -4, -4, 4), \\
h_i c_{iy} &= (0, 0, -2, 0, 2, 4, 4, -4, -4).
\end{aligned}
\tag{2.126}
$$

Similar to the hydrodynamic moments of equation (2.23), these lattice vectors define three moments, called "ghost moments" introduced by Benzi *et al.* [6]:

$$
\chi = \sum_{i=0}^{8} h_i f_i,
\tag{2.127}
$$

$$
\boldsymbol{\Psi} = \sum_{i=0}^{8} h_i \mathbf{c}_i f_i,
\tag{2.128}
$$

The ghost moments satisfy the following equations from the zero and first-order moments of the discrete Boltzmann equation:

$$\partial_t \chi + \nabla \cdot \boldsymbol{\Psi} = -\frac{1}{\tau_g}(\chi - \chi^0),$$

$$\partial_t \boldsymbol{\Psi} + \nabla \cdot \left(\sum_{i=0}^{8} h_i \mathbf{c}_i \mathbf{c}_i f_i \right) = -\frac{1}{\tau_p} \left(\boldsymbol{\Psi} - \boldsymbol{\Psi}^{(0)} \right), \tag{2.129}$$

where the equilibrium of the ghost variables

$$\chi^{(0)} = \Psi^{(0)} = 0. \tag{2.130}$$

Note that

$$\Psi_x = 6Q_{xyy} - 2\rho u_x, \quad \Psi_y = 6Q_{yxx} - 2\rho u_y,$$

$$\chi = 9S_{xxyy} + \rho - 3(\Pi_{xx} + \Pi_{yy}), \tag{2.131}$$

where $Q_{\alpha\beta\beta}$ and $S_{\alpha\alpha\beta\beta} = \sum_i f_i c_{ix}^2 c_{iy}^2$ are the three basic non-hydrodynamic moments of the D2Q9 model.

In terms of $\bar{f}_i$, the non-conserved moments relax to their equilibria with different collision times. So the three post collisional non-conserved moments of the LBE are

$$\overline{\boldsymbol{\Pi}}^* = \overline{\boldsymbol{\Pi}} - \frac{\Delta t}{\tau_s + \frac{\Delta t}{2}}(\overline{\boldsymbol{\Pi}} - \boldsymbol{\Pi}^{(0)}),$$

$$\overline{\chi}^* = \overline{\chi} - \frac{\Delta t}{\tau_g + \frac{\Delta t}{2}}(\overline{\chi} - \chi^{(0)}), \tag{2.132}$$

$$\overline{\boldsymbol{\Psi}}^* = \overline{\boldsymbol{\Psi}} - \frac{\Delta t}{\tau_p + \frac{\Delta t}{2}}(\overline{\boldsymbol{\Psi}} - \boldsymbol{\Psi}^{(0)}),$$

where the ghost moments that depend on $\bar{f}_i$ are defined as:

$$\overline{\chi} = \sum_{i=0}^{8} h_i \bar{f}_i, \tag{2.133}$$

$$\overline{\boldsymbol{\Psi}} = \sum_{i=0}^{8} h_i \mathbf{c}_i \bar{f}_i, \tag{2.134}$$

The distribution function can be declared in terms of the post collision moments in equation (2.132), [28, 29]

$$\bar{f}_i = w_i \left(\rho + 3(\rho\mathbf{u}) + \frac{9}{2}\left(\overline{\mathbf{\Pi}}^* - \frac{\rho}{3}\mathbf{I}\right) : \left(\mathbf{c}_i\mathbf{c}_i - \frac{1}{3}\mathbf{I}\right)\right) + w_i h_i \left(\frac{1}{4}\overline{\chi}^* + \frac{3}{8}\mathbf{c}_i.\overline{\mathbf{\Psi}}^*\right).$$

$$(2.135)$$

A special implementation of the MRT model is the two relaxation time (TRT) model [42]. In this model, two relaxation times in the collision part of the lattice Boltzmann equation will be used, one for moments with even number of velocities $(\overline{\mathbf{\Pi}}, \overline{\chi})$, and another for the odd ones $(\overline{\mathbf{\Psi}})$. Note that the relaxation process will not be applied to the conservation moments, ρ and $\rho\mathbf{u}$. In our simulation the moments of equation (2.132) relax with different rates. $\overline{\mathbf{\Pi}}$ and $\overline{\chi}$ will collide with one relaxation time $\tau_s = \tau_g$ which depends on the non-dimensional Reynolds number (Re). The odd moments $\overline{\mathbf{\Psi}}$ will relax to another relaxation time that is determined according to specific parameter named ' the magic parameter' Λ. The most important part in this model is how we choose the two relaxation times. One should choose the product of these two relaxation times equal to Λ where $\Lambda = \tau_s\tau_p$. This parameter is very important, because it controls the stability of the method. According to [33, 94] the choice of $\Lambda = \frac{1}{4}$ is the best for numerical stability for the lattice Boltzmann method and its equilibrium state. For bounce-back boundary conditions, $\Lambda = \frac{3}{16}$ will give the exact location of the no-slip wall in the channel flow which is half-way between two grid points. However, $\Lambda = \frac{1}{6}$ is consistent with Lele's compact finite difference schemes [75]. The BGK-LBM effectively assumes all the relaxation times are equal, that means $\tau_s = \tau_p = \tau$. In this thesis, the magic parameter will be fixed to take the value $\Lambda = \frac{1}{4}$.

Chapter 3

Boundary conditions and simple numerical simulations for the LBM

I have explained the streaming and colliding steps of the lattice Boltzmann method, but there is still another important issue to clarify: boundary conditions. In order to determine the boundary conditions for the D2Q9 lattice Boltzmann method, the conditions should be expressed in terms of the probability distribution functions. Various boundary conditions have been introduced for LBM to satisfy slip and no-slip flows. Different implementations have different levels of accuracy. After the streaming step, the nodes at the boundaries have three incoming unknown distribution functions. By applying the boundary conditions, these unknown functions will be determined. From Figure 3.1, the incoming distribution functions, which are dashed lines, are unknown functions, while the dark lines are the known functions. The unknown functions at the boundary can be found by various techniques. One way is by using symmetry conditions which are applied directly to the particle distribution functions at the wall, like in bounce-back methods. On the other hand, a different methodology which is based on the hydrodynamic moments of the LBM has been used to find the unknown distribution functions at a boundary nodes, for instance [4, 88].

This chapter begins with some types of no-slip boundary conditions for flat walls which are explained briefly with respect to $\bar{f}_i$ by ignoring the force term. Then a de-

tailed explanation about one specific boundary condition namely the "moment-based boundary conditions" is given. The analytic solution in time independent unidirectional channel flow of LBM is explained. Then some numerical implementations are given to show the accuracy of the method. Results for Poiseuille flow, Couette flow and cavity flow with some benchmark data are presented for BGK and MRT of lattice Boltzmann models. The Navier-Maxwell slip condition is explained where the measure of slip velocity at the surface depends upon length named slip length. The Navier condition is combined with moment-based boundary conditions to simulate unidirectional channel flow in this chapter, it will be used later to simulate a more complicated flow.
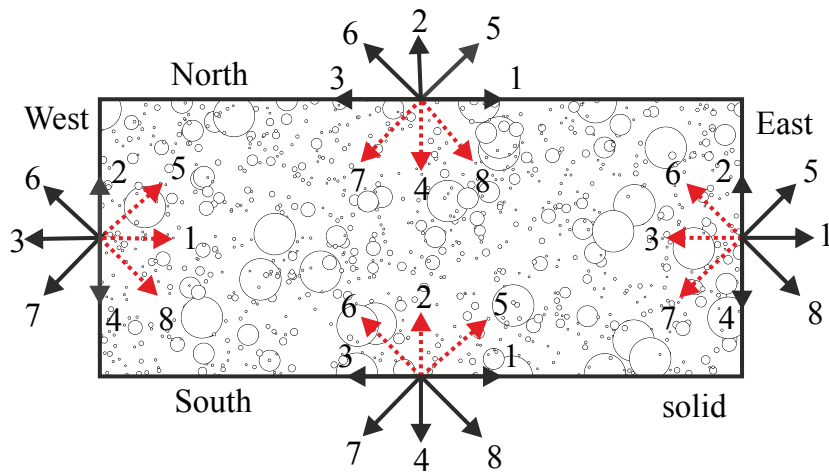
Figure 3.1: Distribution functions at the boundaries. Each number represents the direction of c_i

3.1 Periodic boundary conditions

Periodic boundary conditions are the simplest example of boundary conditions which apply to an infinite repeating flow between the inlet and outlet of the domain. For example, in a channel flow where it is infinitely long, the fluid is driven by internal body force, see Figure 3.1. The particle distribution functions at the east boundary leave their sites and enter at the west boundary. A similar procedure is applied at the west boundary. $\bar{f}_1^{in}$, $\bar{f}_5^{in}$ and $\bar{f}_8^{in}$ are unknown functions at the west boundary and they take their values from the same known function at the east boundary, $\bar{f}_1^{out}$, $\bar{f}_5^{out}$ and

$\bar{f}_8^{out}$. In general periodic conditions can be expressed as

$$\text{West:} \qquad \bar{f}_i(x_0, y, t + \Delta t) = \bar{f}_i(x_L, y - c_{iy}\Delta t, t) \qquad\qquad i = 1, 5, 8, \qquad (3.1)$$

$$\text{East:} \qquad \bar{f}_i(x_L, y, t + \Delta t) = \bar{f}_i(x_0, y - c_{iy}\Delta t, t) \qquad\qquad i = 3, 6, 7, \qquad (3.2)$$

where x_0 and x_L is the nodes at inlet and outlet, respectively [46]. Similar conditions can also be applied to the vertical boundaries.

3.2 Bounce-back boundary conditions

A simple method connecting the interactions between the solid walls and fluid is the bounce-back boundary conditions. Bounce-back is used to implement the no-slip condition for both stationary and moving boundaries. This method states that the distribution functions on the boundary nodes are reflected back to the fluid domain after colliding with the solid boundary [46]. Two ways of implementing bounce-back boundary conditions are commonly used.

The first, is on-grid bounce-back. The particles near the boundary stream towards the boundaries and hit the wall. At the same time step, the known functions reverse their direction back to the fluid field. For example, at the south boundary and after the propagation step, the known functions $\bar{f}_4$, $\bar{f}_7$ and $\bar{f}_8$ reverse their direction. This gives values to the unknown function $\bar{f}_2$, $\bar{f}_5$ and $\bar{f}_6$, as shown in Figure 3.1. To clarify the method and by ignoring the force term, in Figure 3.1 the black lines of distribution function reverse and give their values to the functions in red colours as follows

$$\bar{f}_2 = \bar{f}_4, \ \bar{f}_5 = \bar{f}_7 \ \text{ and } \ \bar{f}_6 = \bar{f}_8. \qquad (3.3)$$

The second implementation of bounce-back conditions is half-way bounce-back. This technique is considered to be a simple and accurate way to apply the boundary conditions [53]. These conditions state that the solid wall is located between two lattice sites and the process happens over two time steps. At the streaming step the

particles propagate towards the solid walls, depending on their lattice velocities. Then they exceed the boundaries and reverse their directions. In the next time step, the streaming starts and the reflected particles return to the fluid domain. For instance, at the south boundary and firstly, the functions stream towards the boundary and pass it to the next lattice site. The known functions $\bar{f}_4$, $\bar{f}_7$ and $\bar{f}_8$ reverse their direction . At time $t + \Delta t$ they stream to the interior nodes then give their values to unknown $\bar{f}_2$, $\bar{f}_5$ and $\bar{f}_6$, see Figure 3.2, such that

$$\bar{f}_2(x, t + \Delta t) = \bar{f}_4(x, t),$$
$$\bar{f}_5(x, t + \Delta t) = \bar{f}_7(x, t),$$
$$\bar{f}_6(x, t + \Delta t) = \bar{f}_8(x, t).$$

(3.4)
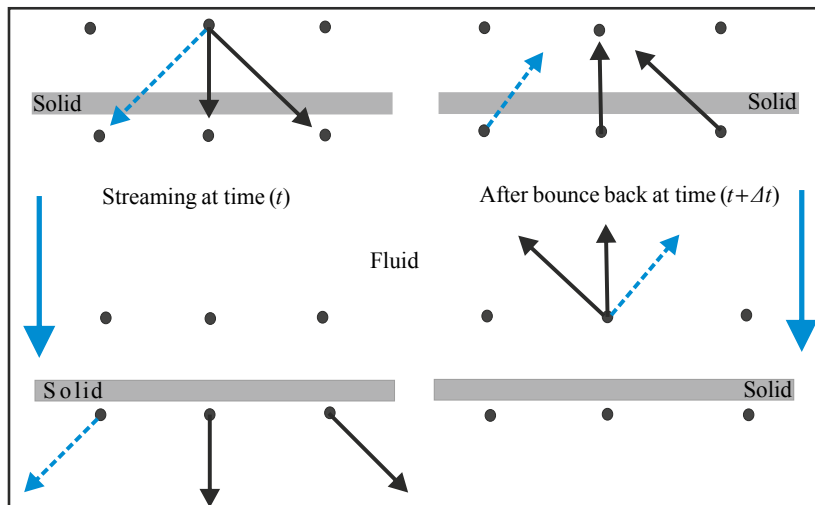
Figure 3.2: Half way bounce back.

Although often efficient and accurate, bounce-back introduces an additional error into the numerical method; a purely artificial slip. This error term is viscosity-dependent and second order in space if the boundary is placed halfway between grid points, and first order otherwise [41, 53, 55]. Bouzidi *et al.* [10] introduced their interpolation scheme for boundary conditions as a generalisation of the bounce back method with linear or quadratic interpolation for flows in complex geometries. Furthermore, Ginzburg and d'Humiereśs [43] presented a general framework for modification of interpolation

using Bouzidi *et al.* and bounce-back methods. In this chapter we will show also that the half way bounce-back is second-order accurate where in our implementations the above conditions will be converted to $\bar{f}_i$.

3.3 Zhou and He boundary conditions

An example of alternative to the bounce-back boundary condition is Zhou and He boundary conditions. Zhou and He [113] presented a form of boundary conditions implementation where the pressure or the velocity are specified at grid points. These boundary conditions are based on the idea of bounce-back of non equilibrium parts of the probability distribution functions. Zhou and He [113] applied this method to the channel flow, as a result they show that the poiseuille flow with half way bounce-back simulation is second order accurate.

Velocity boundary

In velocity boundary conditions the velocities u_x and u_y are imposed. From Figure 3.1, after streaming the north boundary has $\bar{f}_0$, $\bar{f}_1$, $\bar{f}_2$, $\bar{f}_3$, $\bar{f}_5$ and $\bar{f}_6$ as known functions while $\bar{f}_4$, $\bar{f}_7$ and $\bar{f}_8$ are unknown and should be found. By using the bounce-back condition for non equilibrium distribution functions $(\bar{f}_4 - \bar{f}_4^{(0)} = \bar{f}_2 - \bar{f}_2^{(0)})$ which are normal to the wall, one can calculate $\bar{f}_4$ as

$$\bar{f}_4 = \bar{f}_2 - \frac{2}{3}\rho u_y. \tag{3.5}$$

From the momentum equation (2.22), one can write ρu_x and ρu_y as

$$\rho u_x = \bar{f}_1 - \bar{f}_3 + \bar{f}_5 - \bar{f}_6 - \bar{f}_7 + \bar{f}_8, \tag{3.6}$$

and

$$\rho u_y = \bar{f}_2 - \bar{f}_4 + \bar{f}_5 + \bar{f}_6 - \bar{f}_7 - \bar{f}_8. \tag{3.7}$$

Now adding equation (3.6) to equation (3.7), yields

$$\bar{f}_7 = \bar{f}_5 + \frac{1}{2}(\bar{f}_1 - \bar{f}_3) - \frac{1}{6}\rho u_y - \frac{1}{2}\rho u_x. \tag{3.8}$$

And subtracting equation (3.6) from equation (3.7) gives

$$\bar{f}_8 = \bar{f}_6 + \frac{1}{2}(\bar{f}_3 - \bar{f}_1) - \frac{1}{6}\rho u_y + \frac{1}{2}\rho u_x. \tag{3.9}$$

From equation (2.21), by writing the unknown functions in terms of known ones and using equation (3.7), the density is determined as

$$\rho = \frac{1}{1 + u_y} \left[\bar{f}_0 + \bar{f}_1 + \bar{f}_3 + 2(\bar{f}_2 + \bar{f}_6 + \bar{f}_5) \right]. \tag{3.10}$$

Pressure boundary

In the lattice Boltzmann method the pressure is calculated from the density, $P = \rho c_s^2$. At the flow boundary, for example the west boundary, after streaming the three unknown distribution functions $\bar{f}_1$, $\bar{f}_5$ and $\bar{f}_8$ should be found. The velocity u_x is determined by setting $\rho u_y = 0$ and specify $\rho = \rho_{in}$. So from equation (2.21) the unknown function is written in term of known ones as:

$$\bar{f}_1 + \bar{f}_5 + \bar{f}_8 = \rho_{in} - (\bar{f}_0 + \bar{f}_2 + \bar{f}_3 + \bar{f}_4 + \bar{f}_6 + \bar{f}_7), \tag{3.11}$$

and from the momentum equations (3.6) and (3.7) one can get

$$\bar{f}_1 + \bar{f}_5 + \bar{f}_8 = \rho_{in} u_x + (\bar{f}_3 + \bar{f}_6 + \bar{f}_7),$$
$$\bar{f}_5 - \bar{f}_8 = \bar{f}_4 - \bar{f}_2 - \bar{f}_6 + \bar{f}_7. \tag{3.12}$$

From equations (3.11) and (3.12) u_x is equal to

$$u_x = 1 - \frac{\left[\bar{f}_0 + \bar{f}_2 + \bar{f}_4 + 2(\bar{f}_3 + \bar{f}_6 + \bar{f}_7)\right]}{\rho_{in}}. \tag{3.13}$$

Now to find the unknown distribution functions, the bounce back boundary conditions for the non-equilibrium functions will be employed such that $(\bar{f}_1 - \bar{f}_1^{(0)} = \bar{f}_3 - \bar{f}_3^{(0)})$. By substituting the values of $\bar{f}_1^{(0)}$ and $\bar{f}_3^{(0)}$ from equation (2.78) to the above constraint one can have

$$\bar{f}_1 = \bar{f}_3 + \frac{2}{3}\rho_{in}u_x, \tag{3.14}$$

and from equations (3.12) and (3.14) the following is obtained

$$\begin{aligned}
\bar{f}_5 &= \bar{f}_7 - \frac{1}{2}(\bar{f}_2 - \bar{f}_4) + \frac{1}{6}\rho_{in}u_x, \\
\bar{f}_8 &= \bar{f}_6 + \frac{1}{2}(\bar{f}_2 - \bar{f}_4) + \frac{1}{6}\rho_{in}u_x.
\end{aligned} \tag{3.15}$$

For the nodes of north inlet wall and outlet nodes with there corners, the same method can be used.

3.4 Moment-based boundary conditions method with no-slip and inflow boundaries

A different methodology has been used to find the unknown distribution functions at boundary nodes, one that is based on the hydrodynamic moments of the LBM. Noble *et al.* [88] used the hydrodynamic moments to apply no-slip boundary conditions for the 6-point FHP lattice. The approach of Noble *et al.* is not immediately applicable to the now-standard LBM lattices. The FHP model (which is essentially obsolete for simulating fluid flows) has just two unknown functions at a flat boundary while the commonly used D2Q9 lattice has three. Thus a different set of boundary constraints is required. Bennett [4] generalised the ideas of Noble *et al* in what has been dubbed

the "moment-based" method for imposing boundary conditions. The moment-based method is similar in spirit to Noble *et al*'s approach but is far more general in terms of the types of boundary conditions that can be implemented and the lattice stencils they can be applied too. Bennett [4] clarified that the unknown distribution functions from the hydrodynamic and non-hydrodynamic moments at the boundary can be calculated. The basic idea of this method is summarized as following:

Because there are three unknown distribution functions at each boundary aligned with grid points, three linearly independent equations are required. In the moment conditions, three of the following hydrodynamics moments to find these three unknown functions are needed

$$\bar{\rho} = \sum \bar{f}_i = \bar{f}_0 + \bar{f}_1 + \bar{f}_2 + \bar{f}_3 + \bar{f}_4 + \bar{f}_5 + \bar{f}_6 + \bar{f}_7 + \bar{f}_8, \tag{3.16a}$$

$$\rho \bar{u}_x = \sum \bar{f}_i c_{ix} = \bar{f}_1 - \bar{f}_3 + \bar{f}_5 - \bar{f}_6 - \bar{f}_7 + \bar{f}_8, \tag{3.16b}$$

$$\rho \bar{u}_y = \sum \bar{f}_i c_{iy} = \bar{f}_2 - \bar{f}_4 + \bar{f}_5 + \bar{f}_6 - \bar{f}_7 - \bar{f}_8, \tag{3.16c}$$

$$\overline{\Pi}_{xx} = \sum \bar{f}_i c_{ix}^2 = \bar{f}_1 + \bar{f}_3 + \bar{f}_5 + \bar{f}_6 + \bar{f}_7 + \bar{f}_8, \tag{3.16d}$$

$$\overline{\Pi}_{yy} = \sum \bar{f}_i c_{iy}^2 = \bar{f}_2 + \bar{f}_4 + \bar{f}_5 + \bar{f}_6 + \bar{f}_7 + \bar{f}_8, \tag{3.16e}$$

$$\overline{\Pi}_{xy} = \sum \bar{f}_i c_{ix} c_{iy} = \bar{f}_5 - \bar{f}_6 + \bar{f}_7 - \bar{f}_8, \tag{3.16f}$$

$$\overline{Q}_{xxy} = \sum \bar{f}_i c_{ix}^2 c_{iy} = \bar{f}_5 + \bar{f}_6 - \bar{f}_7 - \bar{f}_8, \tag{3.16g}$$

$$\overline{Q}_{xyy} = \sum \bar{f}_i c_{ix} c_{iy}^2 = \bar{f}_5 - \bar{f}_6 - \bar{f}_7 + \bar{f}_8, \tag{3.16h}$$

$$\overline{S}_{xxyy} = \sum \bar{f}_i c_{ix}^2 c_{iy}^2 = \bar{f}_5 + \bar{f}_6 + \bar{f}_7 + \bar{f}_8. \tag{3.16i}$$

Figure 3.1 shows that at the horizontal and vertical walls there are three unknown distribution functions and these three unknowns $\bar{f}_i$ appear in different combinations in equations (3.16). In Tables (3.1) and (3.2) all the groups of the unknown moments have been listed. Moments in different rows are linearly independent. Therefore a constraint (a boundary condition) on one moment from each row should be imposed. Since we are interested in numerically solving the Navier-Stokes equations, it seems sensible to choose the hydrodynamic moments instead of the higher order ones that do

not appear in these equations of motion.

Moments	South boundary	North boundary
$\bar{\rho}, \rho\bar{u}_y, \overline{\Pi}_{yy}$	$\bar{f}_2 + \bar{f}_5 + \bar{f}_6$	$\bar{f}_4 + \bar{f}_7 + \bar{f}_8$
$\rho\bar{u}_x, \overline{\Pi}_{xy}, \overline{Q}_{xyy}$	$\bar{f}_5 - \bar{f}_6$	$\bar{f}_7 - \bar{f}_8$
$\overline{\Pi}_{xx}, \overline{Q}_{xxy}, \overline{S}_{xxyy}$	$\bar{f}_5 + \bar{f}_6$	$\bar{f}_7 + \bar{f}_8$

Table 3.1: Moment combinations for unknown $\bar{f}_i$ at the South and North boundary.

Moments	East boundary	West boundary
$\bar{\rho}, \rho\bar{u}_x, \overline{\Pi}_{xx}$	$\bar{f}_3 + \bar{f}_6 + \bar{f}_7$	$\bar{f}_1 + \bar{f}_5 + \bar{f}_8$
$\rho\bar{u}_y, \overline{\Pi}_{xy}, \overline{Q}_{xxy}$	$\bar{f}_6 - \bar{f}_7$	$\bar{f}_5 - \bar{f}_8$
$\overline{\Pi}_{yy}, \overline{Q}_{xyy}, \overline{S}_{xxyy}$	$\bar{f}_6 + \bar{f}_7$	$\bar{f}_5 + \bar{f}_8$

Table 3.2: Moment combinations for unknown $\bar{f}_i$ at the East and West boundary.

To understand the method, a stationary, no-slip northern wall is taken as an example. The no-slip boundary condition is imposed, $u_x = u_y = 0$ and zero tangential derivative $\partial_T u_T = 0$ where T denotes the tangential component. At the north wall $\bar{f}_4$, $\bar{f}_7$ and $\bar{f}_8$ are unknown functions. Thus in terms of $\bar{f}_i$, from Table 3.1 we will pick $\rho\bar{u}_y$ from the first row, $\rho\bar{u}_x$ from the second one and for the last equation we will use $\overline{\Pi}_{xx}$ and impose upon them. So by neglecting the force term the conditions are

$$
\begin{aligned}
\rho\bar{u}_y &= 0, \\
\rho\bar{u}_x &= 0, \\
\overline{\Pi}_{xx} &= \rho/3,
\end{aligned}
\tag{3.17}
$$

where $\overline{\Pi}_{xx} = \Pi_{xx}^{(0)}$ from the Chapman-Enskog expansion in Section 2.5.3 such that

$$
\begin{aligned}
\overline{\Pi}_{xx} &\approx \overline{\Pi}_{xx}^{(0)} + \tau\overline{\Pi}_{xx}^{(1)} \\
&= \overline{\Pi}_{xx}^{(0)},
\end{aligned}
\tag{3.18}
$$

where $\Pi_{xx}^{(1)} \propto \partial_x u_x$ according to equation (2.108) and since the tangential derivative

$\partial_x u_x$ is equal to zero, $\overline{\Pi}_{xx}^{(1)} = 0$.

By solving the three equations, the unknown functions in the north boundary are:

$$\bar{f}_4 = \bar{f}_1 + \bar{f}_3 + \bar{f}_2 + 2(\bar{f}_5 + \bar{f}_6) - \frac{\rho}{3},$$

$$\bar{f}_7 = \frac{\rho}{6} - \bar{f}_3 - \bar{f}_6, \tag{3.19}$$

$$\bar{f}_8 = \frac{\rho}{6} - \bar{f}_1 - \bar{f}_5.$$

The density ρ at the wall can be constructed from the known distribution functions and the velocity $\rho \bar{u}_y$ at the boundary where $\rho \bar{u}_y = 0$ such that

$$\rho = \bar{f}_0 + \bar{f}_1 + \bar{f}_3 + 2(\bar{f}_2 + \bar{f}_5 + \bar{f}_6) - \rho \bar{u}_y. \tag{3.20}$$

The nodes on the corners need special treatment because there are five unknown distribution functions together in the vertical and horizontal walls [1], as in Figure 3.3. To find these five values, five linearly independent equations from five different constrains will be applied. These five moments are $\rho \bar{u}_x = 0$, $\rho \bar{u}_y = 0$, $\overline{\Pi}_{xx} = \rho/3$ and $\overline{\Pi}_{yy} = \rho/3$ while the fifth moment is the shear stress $\overline{\Pi}_{xy}$. This fifth moment is zero because of the Chapman Enskog expansion

$$\overline{\Pi}_{xy} \approx \overline{\Pi}_{xy}^{(0)} + \tau \overline{\Pi}_{xy}^{(1)},$$

$$= 0, \tag{3.21}$$

since the diagonal derivative of $\overline{\Pi}_{xy}^{(1)} = \rho \bar{u}_x \bar{u}_y = 0$ since the velocities at the wall $\bar{u}_x = \bar{u}_y = 0$. For example the five unknown distribution functions in northwest corner

are found to be:

$$\bar{f}_1 = \frac{2\rho}{3} - \bar{f}_0 - \bar{f}_3,$$

$$\bar{f}_4 = \frac{2\rho}{3} - \bar{f}_0 - \bar{f}_2,$$

$$\bar{f}_5 = \frac{\rho}{6} - \bar{f}_2 - \bar{f}_6, \tag{3.22}$$

$$\bar{f}_7 = \frac{\rho}{6} - \bar{f}_3 - \bar{f}_6,$$

$$\bar{f}_8 = -\frac{2\rho}{3} + \bar{f}_0 + \bar{f}_2 + \bar{f}_3 + \bar{f}_6.$$

also, the ρ is established from known distribution functions at the wall as:

$$\rho = \bar{f}_0 + 2\bar{f}_3 + 4\bar{f}_6 + 2\bar{f}_2. \tag{3.23}$$
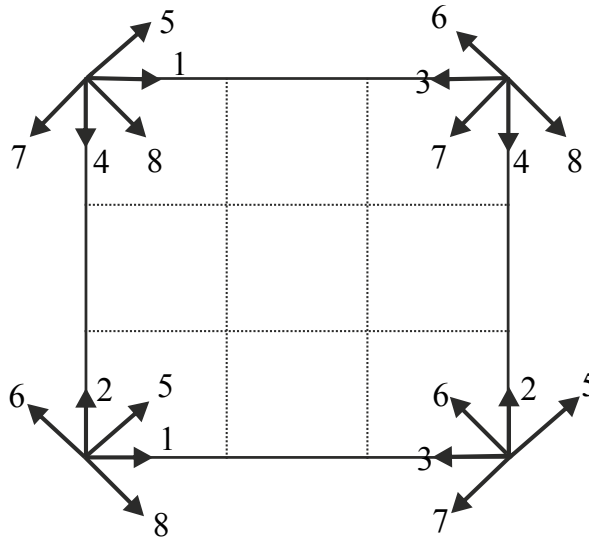
Figure 3.3: Unknown distribution functions at corners.

For inflow open boundaries, the vertical wall will be determined as an example. In Table 3.2, consider the western wall, the three unknown functions are $\bar{f}_1$, $\bar{f}_5$ and $\bar{f}_8$. From the first row the density $\rho = \rho_{in}$ is imposed, $\rho\bar{u}_y$ is selected from the second row

and from the third row $\overline{\Pi}_{yy}$ such that [5]

$$\rho = \rho_{in},$$
$$\rho\overline{u}_y = 0, \tag{3.24}$$
$$\overline{\Pi}_{yy} = P_{in} = \rho_{in}/3,$$

where $P_{in} = \rho_{in}/3$ is the specified pressure at the boundaries. By solving the three equations, the unknown functions at the west boundary are

$$\bar{f}_1 = \frac{2\rho_{in}}{3} - f_0 - f_3,$$
$$\bar{f}_5 = \frac{\rho_{in}}{6} - \bar{f}_2 - \bar{f}_6, \tag{3.25}$$
$$\bar{f}_8 = \frac{\rho_{in}}{6} - \bar{f}_4 - \bar{f}_7.$$

3.5 Analytical solution of lattice Boltzmann equation

In this section the analytic solution of the lattice Boltzmann equation for plane Poiseuille flow will be found. This flow is a unidirectional, laminar, time independent, incompressible and viscous flow between two stationary parallel plates. Many authors use plane Poiseuille flow as a perfect benchmark to examine the accuracy of their numerical methods, because the Navier-Stokes equations have an exact solution in this scenario.

3.5.1 Exact solution of velocity field for LBE

The BGK-Lattice Boltzmann equation in lattice units, with $\Delta t = \Delta x = 1$, is

$$\bar{f}_i(\mathbf{x} + \mathbf{c}_i, t + 1) - \bar{f}_i(\mathbf{x}, t) = -\frac{1}{(\tau + 1/2)}(\bar{f}_i(\mathbf{x}, t) - f_i^{(0)}(\mathbf{x}, t)) + \frac{\tau}{(\tau + 1/2)}R_i(\mathbf{x}, t). \tag{3.26}$$

He *et al.* [53] found an analytic solution of the LBE in Poiseuille flow. Assume the flow is steady and the velocity satisfies

$$\partial_x u_x = 0,$$
$$\partial_x u_y = 0, \tag{3.27}$$
$$\frac{d}{dt} = 0,$$

also the velocity and the distribution function $\bar{f}_i$ depends on y only while the body force pushes the flow towards x direction such that $\mathbf{F} = (\rho G, 0)$. To simplify our notations let's set $(u_x, u_y) = (u, v)$, so by applying the equilibrium distribution function (2.78) and the assumption of equation (3.27) into equation (3.26), the following are obtained

$$\bar{f}_0^j = \frac{4\rho}{9}\left(1 - \frac{3}{2}(u_j^2 + v_j^2)\right) - \frac{4\rho G}{3}u_j, \tag{3.28a}$$

$$\bar{f}_1^j = \frac{\rho}{9}\left(1 + 3u_j + 3u_j^2 - \frac{3}{2}v_j^2\right) + \frac{\tau\rho G}{3}(2u_j + 1), \tag{3.28b}$$

$$\bar{f}_2^j = \frac{\rho}{9(\tau + 1/2)}\left(1 + 3v_{j-1} + 3v_{j-1}^2 - \frac{3}{2}u_{j-1}^2\right) - \frac{\tau\rho G}{3(\tau + 1/2)}u_{j-1}$$
$$+ \frac{\tau - 1/2}{\tau + 1/2}\bar{f}_2^{j-1}, \tag{3.28c}$$

$$\bar{f}_3^j = \frac{\rho}{9}\left(1 - 3u_j + 3u_j^2 - \frac{3}{2}v_j^2\right) + \frac{\tau\rho G}{3}(2u_j - 1), \tag{3.28d}$$

$$\bar{f}_4^j = \frac{\rho}{9(\tau + 1/2)}\left(1 - 3v_{j+1} + 3v_{j+1}^2 - \frac{3}{2}u_{j+1}^2\right) - \frac{\tau\rho G}{3(\tau + 1/2)}u_{j+1}$$
$$+ \frac{\tau - 1/2}{\tau + 1/2}\bar{f}_4^{j+1}, \tag{3.28e}$$

$$\bar{f}_5^j = \frac{\rho}{36(\tau + 1/2)}\left(1 + 3u_{j-1} + 3v_{j-1} + 3u_{j-1}^2 + 3v_{j-1}^2 + 9u_{j-1}v_{j-1}\right)$$
$$+ \frac{\tau\rho G}{12(\tau + 1/2)}(1 + 2u_{j-1} + 3v_{j-1}) + \frac{\tau - 1/2}{\tau + 1/2}\bar{f}_5^{j-1}, \tag{3.28f}$$

$$\bar{f}_6^j = \frac{\rho}{36(\tau + 1/2)}\left(1 - 3u_{j-1} + 3v_{j-1} + 3u_{j-1}^2 + 3v_{j-1}^2 - 9u_{j-1}v_{j-1}\right)$$
$$- \frac{\tau\rho G}{12(\tau + 1/2)}(1 - 2u_{j-1} + 3v_{j-1}) + \frac{\tau - 1/2}{\tau + 1/2}\bar{f}_6^{j-1}, \tag{3.28g}$$

$$\bar{f}_7^j = \frac{\rho}{36(\tau + 1/2)}\left(1 - 3u_{j+1} - 3v_{j+1} + 3u_{j+1}^2 + 3v_{j+1}^2 + 9u_{j+1}v_{j+1}\right)$$

$$- \frac{\tau \rho G}{12(\tau + 1/2)}(1 - 2u_{j+1} - 3v_{j+1}) + \frac{\tau - 1/2}{\tau + 1/2} \bar{f}_7^{j+1}, \tag{3.28h}$$

$$\bar{f}_8^j = \frac{\rho}{36(\tau + 1/2)} \left(1 + 3u_{j+1} - 3v_{j+1} + 3u_{j+1}^2 + 3v_{j+1}^2 - 9u_{j+1}v_{j+1}\right)$$

$$+ \frac{\tau \rho G}{12(\tau + 1/2)}(1 + 2u_{j+1} - 3v_{j+1}) + \frac{\tau - 1/2}{\tau + 1/2} \bar{f}_8^{j+1}, \tag{3.28i}$$

where $\bar{f}_i^j$ symbolises the distribution function at node j. The above components are suitable only in the interior points, $2 \leq j \leq n - 1$, with the south and the north walls located at the nodes $j = 1$ and $j = n$ respectively.

The first order moment of $\bar{f}_i$ in x direction gives

$$\sum_i \bar{f}_i c_{ix} = \rho \bar{u}_j = \rho u_j - \frac{1}{2} \sum_i R_i^j \tag{3.29}$$

$$= \rho u_j - \frac{1}{2} \rho G, \tag{3.30}$$

where ρG is the force term. Then writing the momentum in terms of its components gives:

$$\rho u_j - \frac{1}{2} \rho G = (\bar{f}_1^j - \bar{f}_3^j + \bar{f}_5^j - \bar{f}_6^j + \bar{f}_8^j - \bar{f}_7^j). \tag{3.31}$$

To write the first moment in terms of the velocity at neighbouring nodes, the right-hand side of equation (3.31) should be calculated. By using the components of equations (3.28) for $\bar{f}_i^j$, one can obtain from the first two terms on the right-hand side:

$$(\bar{f}_1^j - \bar{f}_3^j) = \left(\frac{\rho}{9} \left(1 + 3u_j + 3u_j^2 - \frac{3}{2}v_j^2\right) + \frac{\tau \rho G}{3}(2u_j + 1) \right)$$

$$- \left(\frac{\rho}{9} \left(1 - 3u_j + 3u_j^2 - \frac{3}{2}v_j^2\right) + \frac{\tau \rho G}{3}(2u_j - 1) \right),$$

which reduces to,

$$(\bar{f}_1^j - \bar{f}_3^j) = \frac{2}{3}\rho u_j + \frac{2}{3}\tau\rho G. \tag{3.32}$$

The third and fourth terms become:

$$
\begin{aligned}
(\bar{f}_5^j - \bar{f}_6^j) &= \left(\frac{\rho}{36(\tau + 1/2)}(1 + 3u_{j-1} + 3v_{j-1} + 3u_{j-1}^2 + 3v_{j-1}^2 + 9u_{j-1}v_{j-1}) \right. \\
&\quad \left. + \frac{\tau\rho G}{12(\tau + 1/2)}(1 + 2u_{j-1} + 3v_{j-1}) + \frac{\tau - 1/2}{\tau + 1/2}\bar{f}_5^{j-1} \right) - \left(\frac{\rho}{36(\tau + 1/2)} \right. \\
&\quad \left(1 - 3u_{j-1} + 3v_{j-1} + 3u_{j-1}^2 + 3v_{j-1}^2 - 9u_{j-1}v_{j-1} \right) \\
&\quad \left. - \frac{\tau\rho G}{12(\tau + 1/2)}(1 - 2u_{j-1} + 3v_{j-1}) + \frac{\tau - 1/2}{\tau + 1/2}\bar{f}_6^{j-1} \right), \\
&= \frac{\rho}{6(\tau + 1/2)}u_{j-1} + \frac{\rho}{2(\tau + 1/2)}u_{j-1}v_{j-1} + \frac{\tau\rho G}{6(\tau + 1/2)} \\
&\quad + \frac{\tau\rho G}{2(\tau + 1/2)}v_{j-1} + \frac{(\tau - 1/2)}{(\tau + 1/2)}\left(\bar{f}_5^{j-1} - \bar{f}_6^{j-1} \right), \tag{3.33}
\end{aligned}
$$

while the fifth and sixth combined give

$$
\begin{aligned}
(\bar{f}_8^j - \bar{f}_7^j) &= \left(\frac{\rho}{36(\tau + 1/2)} \left(1 + 3u_{j+1} - 3v_{j+1} + 3u_{j+1}^2 + 3v_{j+1}^2 - 9u_{j+1}v_{j+1} \right) \right. \\
&\quad \left. + \frac{\tau\rho G}{12(\tau + 1/2)}(1 + 2u_{j+1} - 3v_{j+1}) + \frac{\tau - 1/2}{\tau + 1/2}\bar{f}_8^{j+1} \right) - \left(\frac{\rho}{36(\tau + 1/2)} \right. \\
&\quad \left(1 - 3u_{j+1} - 3v_{j+1} + 3u_{j+1}^2 + 3v_{j+1}^2 + 9u_{j+1}v_{j+1} \right) \\
&\quad \left. - \frac{\tau\rho G}{12(\tau + 1/2)}(1 - 2u_{j+1} - 3v_{j-1}) + \frac{\tau - 1/2}{\tau + 1/2}\bar{f}_7^{j+1} \right), \\
&= \frac{\rho}{6(\tau + 1/2)}u_{j+1} - \frac{\rho}{2(\tau + 1/2)}u_{j+1}v_{j+1} + \frac{\tau\rho G}{6(\tau + 1/2)} \\
&\quad - \frac{\tau\rho G}{2(\tau + 1/2)}v_{j+1} + \frac{(\tau - 1/2)}{(\tau + 1/2)}(\bar{f}_8^{j+1} - \bar{f}_7^{j+1}). \tag{3.34}
\end{aligned}
$$

Now inserting equations (3.32), (3.33) and (3.34) into equation (3.31) yields

$$
\begin{aligned}
\rho u_j - \frac{1}{2}\rho G &= \frac{2}{3}\rho u_j + \frac{2\tau\rho G}{3} + \frac{\rho}{6(\tau + 1/2)}u_{j-1} + \frac{\rho}{2(\tau + 1/2)}u_{j-1}v_{j-1} \\
&\quad + \frac{\rho}{6(\tau + 1/2)}u_{j+1} - \frac{\rho}{2(\tau + 1/2)}u_{j+1}v_{j+1} + \frac{\tau\rho G}{6(\tau + 1/2)} + \frac{\tau\rho G}{6(\tau + 1/2)}
\end{aligned}
$$

$$+ \frac{(\tau - 1/2)}{(\tau + 1/2)} \left((\bar{f}_5^{j-1} - \bar{f}_6^{j-1}) + (\bar{f}_8^{j+1} - \bar{f}_7^{j+1}) \right),$$

$$= \frac{2}{3}\rho u_j + \frac{2\tau\rho G}{3} + \frac{\rho}{6(\tau + 1/2)}(u_{j-1} + u_{j+1}) + \frac{\rho}{2(\tau + 1/2)}(u_{j-1}v_{j-1} - u_{j+1}v_{j+1})$$

$$+ \frac{\tau\rho G}{3(\tau + 1/2)} + \frac{\tau\rho G}{2(\tau + 1/2)}v_{j-1} - \frac{\tau\rho G}{2(\tau + 1/2)}v_{j+1} + \frac{(\tau - 1/2)}{(\tau + 1/2)}$$

$$\left((\bar{f}_5^{j-1} - \bar{f}_6^{j-1}) + (\bar{f}_8^{j+1} - \bar{f}_7^{j+1}) \right). \tag{3.35}$$

To simplify equation (3.35), $(\bar{f}_5^{j-1} - \bar{f}_6^{j-1}) + (\bar{f}_8^{j+1} - \bar{f}_7^{j+1})$ should be calculated. So, from the first moment of the distribution function $\bar{f}_i$ at node $j - 1$,

$$\rho \bar{u}_{j-1} = \rho u_{j-1} - \frac{1}{2}\rho G = ((\bar{f}_1^{j-1} - \bar{f}_3^{j-1}) + (\bar{f}_5^{j-1} - \bar{f}_6^{j-1}) + (\bar{f}_8^{j-1} - \bar{f}_7^{j-1})),$$

yields,

$$(\bar{f}_5^{j-1} - \bar{f}_6^{j-1}) = \rho u_{j-1} - \frac{1}{2}\rho G - (\bar{f}_1^{j-1} - \bar{f}_3^{j-1}) - (\bar{f}_8^{j-1} - \bar{f}_7^{j-1}). \tag{3.36}$$

Similarly, from the first moment of the distribution function $\bar{f}_i$ at node $j + 1$,

$$\rho \bar{u}_{j+1} = \rho u_{j+1} - \frac{1}{2}\rho G = ((\bar{f}_1^{j+1} - \bar{f}_3^{j+1}) + (\bar{f}_5^{j+1} - \bar{f}_6^{j+1}) + (\bar{f}_8^{j+1} - \bar{f}_7^{j+1})),$$

we get,

$$(\bar{f}_8^{j+1} - \bar{f}_7^{j+1}) = \rho u_{j+1} - \frac{1}{2}\rho G - (\bar{f}_1^{j+1} - \bar{f}_3^{j+1}) - (\bar{f}_5^{j+1} - \bar{f}_6^{j+1}). \tag{3.37}$$

In equation (3.36), $(\bar{f}_8^{j-1} - \bar{f}_7^{j-1})$ at index $j - 1$ can be expressed as

$$(\bar{f}_8^{j-1} - \bar{f}_7^{j-1}) = \frac{\rho}{6(\tau + 1/2)}u_j - \frac{\rho}{2(\tau + 1/2)}u_j v_j + \frac{\tau\rho G}{6(\tau + 1/2)}$$

$$- \frac{\tau\rho G}{2(\tau + 1/2)}v_j + \frac{(\tau - 1/2)}{(\tau + 1/2)}(\bar{f}_8^j - \bar{f}_7^j), \tag{3.38}$$

and in equation (3.37), $(\bar{f}_5^{j+1} - \bar{f}_6^{j+1})$ at index $j + 1$ can be written as

$$(\bar{f}_5^{j+1} - \bar{f}_6^{j+1}) = \frac{\rho}{6(\tau + 1/2)}u_j + \frac{\rho}{2(\tau + 1/2)}u_j v_j + \frac{\tau\rho G}{6(\tau + 1/2)}$$

$$+ \frac{\tau\rho G}{2(\tau + 1/2)}v_j + \frac{(\tau - 1/2)}{(\tau + 1/2)}(\bar{f}_5^j - \bar{f}_6^j). \tag{3.39}$$

By using equations (3.36), (3.37), (3.38) and (3.39), $(\bar{f}_5^{j-1} - \bar{f}_6^{j-1}) + (\bar{f}_8^{j+1} - \bar{f}_7^{j+1})$ can be obtained as follows

$$(\bar{f}_5^{j-1} - \bar{f}_6^{j-1}) + (\bar{f}_8^{j+1} - \bar{f}_7^{j+1}) = (\rho u_{j-1} + \rho u_{j+1}) - (\bar{f}_1^{j-1} - \bar{f}_3^{j-1}) - (\bar{f}_1^{j+1} - \bar{f}_3^{j+1})$$

$$-\frac{\rho}{6(\tau + 1/2)}u_j + \frac{\rho}{2(\tau + 1/2)}u_j v_j - \frac{\tau \rho G}{6(\tau + 1/2)} - \frac{(\tau - 1/2)}{(\tau + 1/2)}$$

$$\left(\bar{f}_8^j - \bar{f}_7^j\right) - \frac{\rho}{6(\tau + 1/2)}u_j - \frac{\rho}{2(\tau + 1/2)}u_j v_j - \frac{\tau \rho G}{6(\tau + 1/2)}$$

$$-\frac{(\tau - 1/2)}{(\tau + 1/2)}\left(\bar{f}_5^j - \bar{f}_6^j\right),$$

which yields,

$$(\bar{f}_5^{j-1} - \bar{f}_6^{j-1}) + (\bar{f}_8^{j+1} - \bar{f}_7^{j+1}) = \frac{1}{3}\rho u_{j-1} + \frac{1}{3}\rho u_{j+1} - \frac{1}{3}\frac{(\tau - 1/2)}{(\tau + 1/2)}\rho u_j - \frac{1}{3(\tau + 1/2)}\rho u_j +$$

$$\frac{(\tau - 1/2)}{2(\tau + 1/2)}\rho G + \frac{2(\tau - 1/2)}{3(\tau + 1/2)}\tau \rho G - \frac{4\tau \rho G}{3} - \rho G - \frac{\tau \rho G}{3(\tau + 1/2)}.$$

$$(3.40)$$

Substituting equation (3.40) into (3.35) gives

$$\rho u_j - \frac{1}{2}\rho G = \frac{2}{3}\rho u_j + \frac{\rho}{6(\tau + 1/2)}(u_{j-1} + u_{j+1}) + \frac{\rho}{2(\tau + 1/2)}$$

$$(u_{j-1}v_{j-1} - u_{j+1}v_{j+1}) + \frac{(\tau - 1/2)}{3(\tau + 1/2)}\rho u_{j-1} + \frac{(\tau - 1/2)}{3(\tau + 1/2)}\rho u_{j+1}$$

$$-\frac{(\tau - 1/2)}{3(\tau + 1/2)^2}\rho u_j - \frac{(\tau - 1/2)^2}{3(\tau + 1/2)^2}\rho u_j + \frac{2\tau \rho G}{3} - \frac{4(\tau - 1/2)}{3(\tau + 1/2)}\tau \rho G$$

$$-\frac{(\tau - 1/2)}{3(\tau + 1/2)^2}\tau \rho G - \frac{(\tau - 1/2)}{(\tau + 1/2)}\rho G + \frac{\tau \rho G}{3(\tau + 1/2)} + \frac{(\tau - 1/2)^2}{2(\tau + 1/2)^2}\rho G$$

$$+\frac{\tau \rho G}{2(\tau + 1/2)}v_{j-1} - \frac{\tau \rho G}{2(\tau + 1/2)}v_{j+1} + \frac{2(\tau - 1/2)^2}{3(\tau + 1/2)^2}\tau \rho G. \qquad (3.41)$$

Simplifying (3.41) gives

$$\frac{u_{j+1}v_{j+1} - u_{j-1}v_{j-1}}{2} = \nu(u_{j+1} + u_{j-1} - 2u_j) + G + \frac{\tau G}{2}(v_{j-1} - v_{j+1}), \qquad (3.42)$$

where $\nu = \tau/3$ is the kinematic viscosity of the fluid.

Now we should show the result of the vertical velocity in y direction

$$\sum_i \bar{f}_i c_{iy} = \rho \bar{v}_j = \rho v_j = (\bar{f}_2^j - \bar{f}_4^j + \bar{f}_5^j + \bar{f}_6^j - \bar{f}_7^j - \bar{f}_8^j). \tag{3.43}$$

From the $\bar{f}_i^j$ components of equations (3.28), and similar to the previous implementation approach, the following can be expressed

$$
\begin{aligned}
(\bar{f}_2^j + \bar{f}_5^j + \bar{f}_6^j) = &\left(\frac{\rho}{9(\tau + 1/2)}(1 + 3v_{j-1} + 3v_{j-1}^2 - \frac{3}{2}u_{j-1}^2) - \frac{\tau \rho G}{3(\tau + 1/2)}u_{j-1} \right. \\
&+ \frac{\tau - 1/2}{\tau + 1/2}\bar{f}_2^{j-1} \Big) + \Big(\frac{\rho}{36(\tau + 1/2)}(1 + 3u_{j-1} + 3v_{j-1} + 3u_{j-1}^2 + 3v_{j-1}^2 \\
&+ 9u_{j-1}v_{j-1}) + \frac{\tau \rho G}{12(\tau + 1/2)}(1 + 2u_{j-1}) + \frac{(\tau - 1/2)}{(\tau + 1/2)}\bar{f}_5^{j-1} \Big) + \\
&\left(\frac{\rho}{36(\tau + 1/2)}\left(1 - 3u_{j-1} + 3v_{j-1} + 3u_{j-1}^2 + 3v_{j-1}^2 - 9u_{j-1}v_{j-1}\right) \right. \\
&\left. - \frac{\tau \rho G}{12(\tau + 1/2)}(1 - 2u_{j-1}) + \frac{(\tau - 1/2)}{(\tau + 1/2)}\bar{f}_6^{j-1} \right).
\end{aligned}
$$

$$\tag{3.44}$$

Rearranging the last equation yields,

$$
\begin{aligned}
(\bar{f}_2^j + \bar{f}_5^j + \bar{f}_6^j) = &\frac{\rho}{6(\tau + 1/2)} + \frac{1}{2(\tau + 1/2)}\rho v_{j-1} + \frac{1}{2(\tau + 1/2)}\rho v_{j-1}^2 \\
&+ \frac{(\tau - 1/2)}{(\tau + 1/2)}(\bar{f}_2^{j-1} + \bar{f}_5^{j-1} + \bar{f}_6^{j-1}).
\end{aligned}
\tag{3.45}
$$

Adding the terms $(\bar{f}_4^j + \bar{f}_8^j + \bar{f}_7^j)$ gives

$$
\begin{aligned}
(\bar{f}_4^j + \bar{f}_8^j + \bar{f}_7^j) = &\left(\frac{\rho}{9(\tau + 1/2)}(1 - 3v_{j+1} + 3v_{j+1}^2 - \frac{3}{2}u_{j+1}^2) - \frac{\tau \rho G}{3(\tau + 1/2)}u_{j+1} \right. \\
&+ \frac{\tau - 1/2}{\tau + 1/2}\bar{f}_4^{j+1} \Big) + \Big(\frac{\rho}{36(\tau + 1/2)}(1 + 3u_{j+1} - 3v_{j+1} + 3u_{j+1}^2 \\
&+ 3v_{j+1}^2 - 9u_{j+1}v_{j+1}) + \frac{\tau \rho G}{12(\tau + 1/2)}(1 + 2u_{j+1}) + \frac{(\tau - 1/2)}{(\tau + 1/2)}\bar{f}_8^{j+1} \Big) \\
&+ \left(\frac{\rho}{36(\tau + 1/2)}\left(1 - 3u_{j+1} - 3v_{j+1} + 3u_{j+1}^2 + 3v_{j+1}^2 + 9u_{j+1}v_{j+1}\right) \right.
\end{aligned}
$$

$$-\frac{\tau \rho G}{12(\tau + 1/2)}(1 - 2u_{j+1}) + \frac{(\tau - 1/2)}{(\tau + 1/2)}\bar{f}_7^{j+1}\Bigg),$$

$$= \frac{\rho}{6(\tau + 1/2)} - \frac{1}{2(\tau + 1/2)}\rho v_{j+1} + \frac{1}{2(\tau + 1/2)}\rho v_{j+1}^2$$

$$+ \frac{(\tau - 1/2)}{(\tau + 1/2)}(\bar{f}_8^{j+1} + \bar{f}_7^{j+1}). \tag{3.46}$$

Inserting equations (3.45) and (3.46) into equation (3.43) leads to

$$\rho v_j = \frac{1}{2(\tau + 1/2)}\rho v_{j-1} + \frac{1}{2(\tau + 1/2)}\rho v_{j+1} + \frac{1}{2(\tau + 1/2)}\rho v_{j-1}^2$$

$$- \frac{1}{2(\tau + 1/2)}\rho v_{j+1}^2 + \frac{(\tau - 1/2)}{(\tau + 1/2)}\Bigg((\bar{f}_5^{j-1} + \bar{f}_6^{j-1} + \bar{f}_2^{j-1})$$

$$- (\bar{f}_7^{j+1} + \bar{f}_8^{j+1} + \bar{f}_4^{j+1})\Bigg) \tag{3.47}$$

In order to find the result of equation (3.47), the value of $((\bar{f}_5^{j-1} + \bar{f}_6^{j-1} + \bar{f}_2^{j-1}) - (\bar{f}_7^{j+1} + \bar{f}_8^{j+1} + \bar{f}_4^{j+1}))$ is required, so the first moment of the distribution function $\bar{f}_i$ at node $j - 1$ will be used first:

$$\rho \bar{v}_{j-1} = \rho v_{j-1} = (\bar{f}_2^{j-1} - \bar{f}_4^{j-1} + \bar{f}_5^{j-1} + \bar{f}_6^{j-1} - \bar{f}_8^{j-1} - \bar{f}_7^{j-1}).$$

Now the above equation is rearranged to obtain

$$(\bar{f}_2^{j-1} + \bar{f}_5^{j-1} + \bar{f}_6^{j-1}) = \rho v_{j-1} + \bar{f}_4^{j-1} + \bar{f}_8^{j-1} + \bar{f}_7^{j-1}. \tag{3.48}$$

The first moment of the distribution function $\bar{f}_i$ at node $j + 1$ gives

$$\rho \bar{v}_{j+1} = \rho v_{j+1} = (\bar{f}_2^{j+1} - \bar{f}_4^{j+1} + \bar{f}_5^{j+1} + \bar{f}_6^{j+1} - \bar{f}_8^{j+1} - \bar{f}_7^{j+1}),$$

rearranging the above equation, yields

$$(\bar{f}_8^{j+1} + \bar{f}_7^{j+1} + \bar{f}_4^{j+1}) = -\rho v_{j+1} + \bar{f}_2^{j+1} + \bar{f}_5^{j+1} + \bar{f}_6^{j+1}. \tag{3.49}$$

In equation (3.48), $(\bar{f}_4^{j-1} + \bar{f}_8^{j-1} + \bar{f}_7^{j-1})$ can be written as

$$
(\bar{f}_4^{j-1} + \bar{f}_8^{j-1} + \bar{f}_7^{j-1}) = \frac{\rho}{6(\tau + 1/2)} - \frac{1}{2(\tau + 1/2)}\rho v_j + \frac{1}{2(\tau + 1/2)}\rho v_j^2
$$
$$
+ \frac{(\tau - 1/2)}{(\tau + 1/2)}(\bar{f}_4^{j} + \bar{f}_8^{j} + \bar{f}_7^{j}), \tag{3.50}
$$

while in equation (3.49), $(\bar{f}_2^{j+1} + \bar{f}_5^{j+1} + \bar{f}_6^{j+1})$ can be expressed as

$$
(\bar{f}_2^{j+1} + \bar{f}_5^{j+1} + \bar{f}_6^{j+1}) = \frac{\rho}{6(\tau + 1/2)} + \frac{1}{2(\tau + 1/2)}\rho v_j + \frac{1}{2(\tau + 1/2)}\rho v_j^2
$$
$$
+ \frac{(\tau - 1/2)}{(\tau + 1/2)}(\bar{f}_2^{j} + \bar{f}_5^{j} + \bar{f}_6^{j}). \tag{3.51}
$$

Hence equations (3.48), (3.49), (3.50) and (3.51) together give

$$
(\bar{f}_5^{j-1} + \bar{f}_6^{j-1} + \bar{f}_2^{j-1}) - (\bar{f}_7^{j+1} + \bar{f}_8^{j+1} + \bar{f}_4^{j+1}) =
$$
$$
\rho v_{j-1} + \rho v_{j+1} - \frac{1}{(\tau + 1/2)}\rho v_j - \frac{(\tau - 1/2)}{(\tau + 1/2)}\rho v_j. \tag{3.52}
$$

Applying (3.52) into (3.47) gives:

$$
v_{j+1}^2 - v_{j-1}^2 = 2\tau \left(v_{j-1} + v_{j+1} - 2v_j \right). \tag{3.53}
$$

From the definition of the density $\rho = \sum \bar{f}_i^j$ and by applying equations (3.28) into ρ and following the above steps, one can get

$$
v_{j+1}^2 + v_{j-1}^2 - 2v_j^2 = 2\tau \left(v_{j+1} - v_{j-1} \right). \tag{3.54}
$$

Adding equation (3.53) to equation (3.54) yields

$$
v_{j+1} = v_j. \tag{3.55}
$$

then equation (3.55) produces

$$v_j = constant. \tag{3.56}$$

Noting if the boundary condition says $v_j = 0$ then $v_j = 0$ always. Together equations (3.42) and (3.56) yield the second order finite difference form of the incompressible Navier-Stokes equations for channel flow with a constant body force G

$$\nu \frac{\partial^2 u}{\partial y^2} + G = 0. \tag{3.57}$$

So the homogeneous solution of equation (3.42) for unidirectional flow is

$$u_j = \frac{4U_c}{(n-1)^2}(j-1)(n-j) + U_s, \quad j = 1, ..., n-1 \tag{3.58}$$

where the maximum velocity in the centre of the channel is $U_c + U_s$, where

$$U_c = GH^2/8\nu, \tag{3.59}$$

where $H = (n-1)$ is the width of the channel. U_s is slip velocity on the boundary at $j = 0$ and $j = n$ and it depends on which boundary conditions will be used. For half-way bounce-back boundary conditions, there is a slip error at the walls $j = 1$ and $j = n$ which has the following form:

$$U_s = \frac{U_c}{3(n-1)^2}\left(4\tau(4\tau - 5) + 3\right). \tag{3.60}$$

For more details about U_s for bounce-back boundary conditions see [53]. For the moment boundary conditions $U_s = 0$ where the slip error will be eliminated, as will be seen in the next section.

Next, numerical results that confirm the above analysis will be discussed with moment-based boundary conditions and bounce-back method.

3.6 Numerical results for No-slip boundaries

In this section the lattice Boltzmann method will be used to simulate different flows, namely Poiseuille, Couette and lid-cavity flows. In Poiseuille and Couette flows, a comparison will be made between analytical solution of BGK-LBE and the numerical solution of the method. Later, a lid-cavity flow will be simulated and results compared with benchmark data.

3.6.1 Force-driven Poiseuille flow

Poiseuille flow is simulated using the BGK lattice Boltzmann method. The force term calculated from equation (3.59) is $G = 8\nu U_c/H$ and H in these simulations depends on m_y which is the number of the grid points in y direction. Different values of vertical grid points are taken to investigate the accuracy of the lattice Boltzmann method. The number of grid points in x direction will be twice the number of grid points in y direction, where $m_y = (8, 16, 32, 64)$. The relaxation time is calculated as $\tau = 3m_y U_c/Re$ where Re is the centreline Reynolds number $Re = U_c H/\nu$ and the initial density ρ set to be equal to 1. Different implementations of lattice Boltzmann boundary conditions are used. The first one is half-way bounce-back boundary conditions from Section (3.2) on the south and north boundary with periodic boundary conditions from Section (3.1) in the east and west boundaries.

The second case, the moment-based boundary conditions at the wall from Section (3.4) are used with the same periodic conditions. Since the flow is driven by a body force, the moments that depend on $\bar{f}_i$ at the boundary contain the term G. The constraint that should be imposed at the walls in term of $\bar{f}_i$ with a force are

$$
\begin{aligned}
\rho \bar{u}_y &= 0, \\
\rho \bar{u}_x &= \rho u_x - \frac{1}{2}\rho G, \\
\overline{\Pi}_{xx} &= \rho/3 + \rho u_x^2 - \rho G u_x,
\end{aligned}
\tag{3.61}
$$

where u_x is equal to zero because the no-slip condition is applied at the boundary. It should be mentioned that $\Delta x = 1/(m_y)$ for bounce-back boundary conditions and $\Delta x = 1/(m_y - 1)$ for moment boundary conditions. In order to analyse the accuracy of the method with different numbers of grid points, the L_2 relative error was calculated

$$error = \sqrt{\frac{\sum_{i,j}\left(u_x^{lbm} - u_x^{exact}\right)^2}{\sum_{i,j}\left(u_x^{exact}\right)^2}}. \tag{3.62}$$

To reach the steady state measurement we used the criteria

$$|u_{x\max}(t+1) - u_{x\max}(t)| < 10^{-9}. \tag{3.63}$$

To discuss these results, in the first case when the bounce back boundary conditions was implemented there is a slip error in the boundaries represented by U_s from equation (3.60). This error depends on the relaxation time τ [53], which is based on the Reynolds number and the number of grid points. So, an increase in Reynolds number leads to a decrease in the numerical slip. When $Re = 100$ is imposed, the slip error becomes very small. When $Re = 10$, the slip error at the boundaries rises because of the large relaxation time and hence larger U_s. As a result, the numerical error shifts a little from the exact solution, while at $Re = 1$ the numerical slip error increases further and the plot shifted more. When $Re = 0.1$ the numerical slip error is increased and dominates the solution, which reduces the accuracy of the method. In Figure 3.4 an example of our simulation has been inserted where the number of grid points is (128×64) with different values of Reynolds numbers. The structure of half-way bounce-back code is inserted in Appendix A.1

(a) $Re = 100$

(b) $Re = 1$

(c) $Re = 0.1$
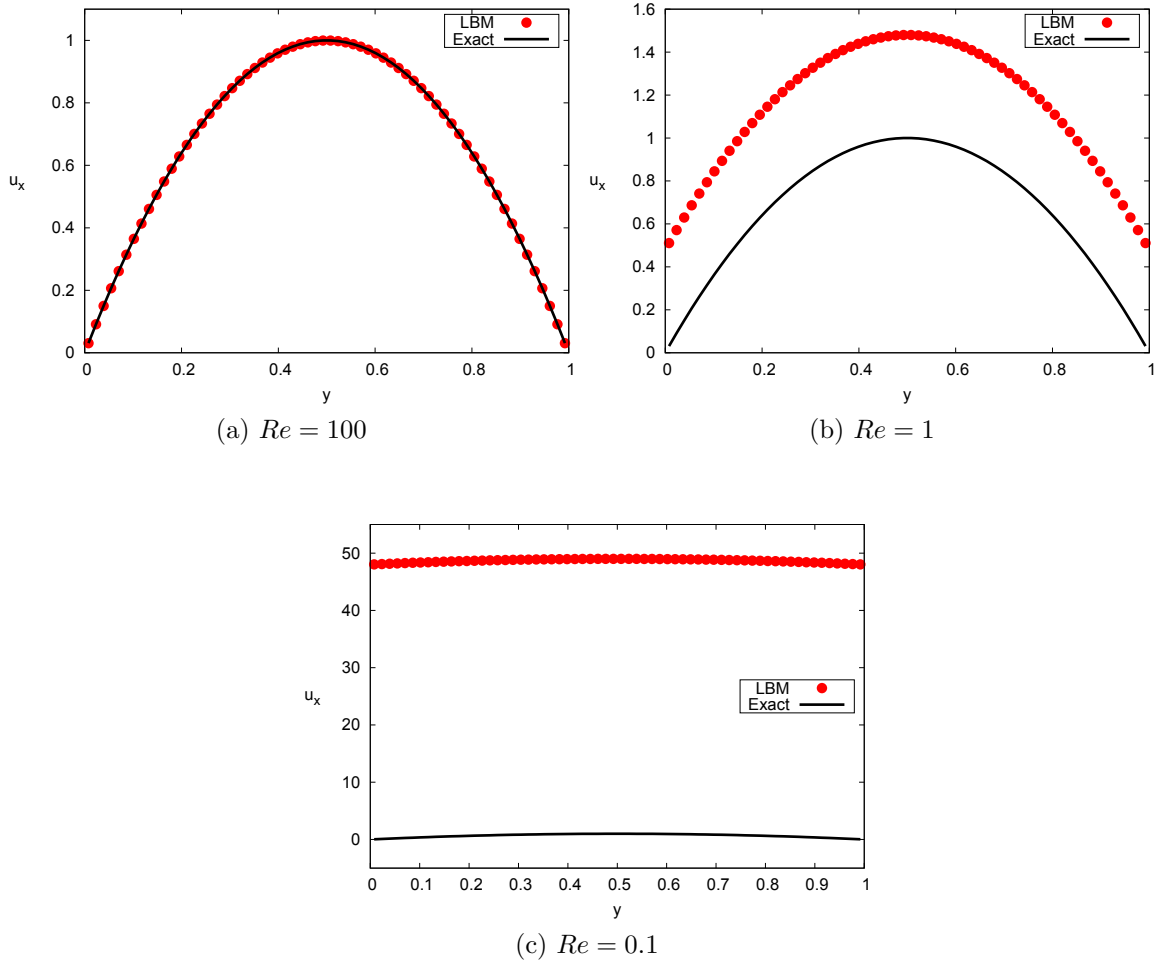
Figure 3.4: Numerical and exact solutions of Poiseuille flow with bounce-back and periodic boundary conditions, $(m_x \times m_y) = 128 \times 64$.

In the second case, when the moment method and periodic boundary conditions are used there is no-slip error since the velocity $U_s = 0$ was imposed on the south and north boundaries. As a result, the exact solution in this case was obtained. In Figure 3.5 the number of grid points is taken (129×65) as an example of this type of boundary conditions.

(a) $Re = 100$

(b) $Re = 1$

(c) $Re = 0.1$
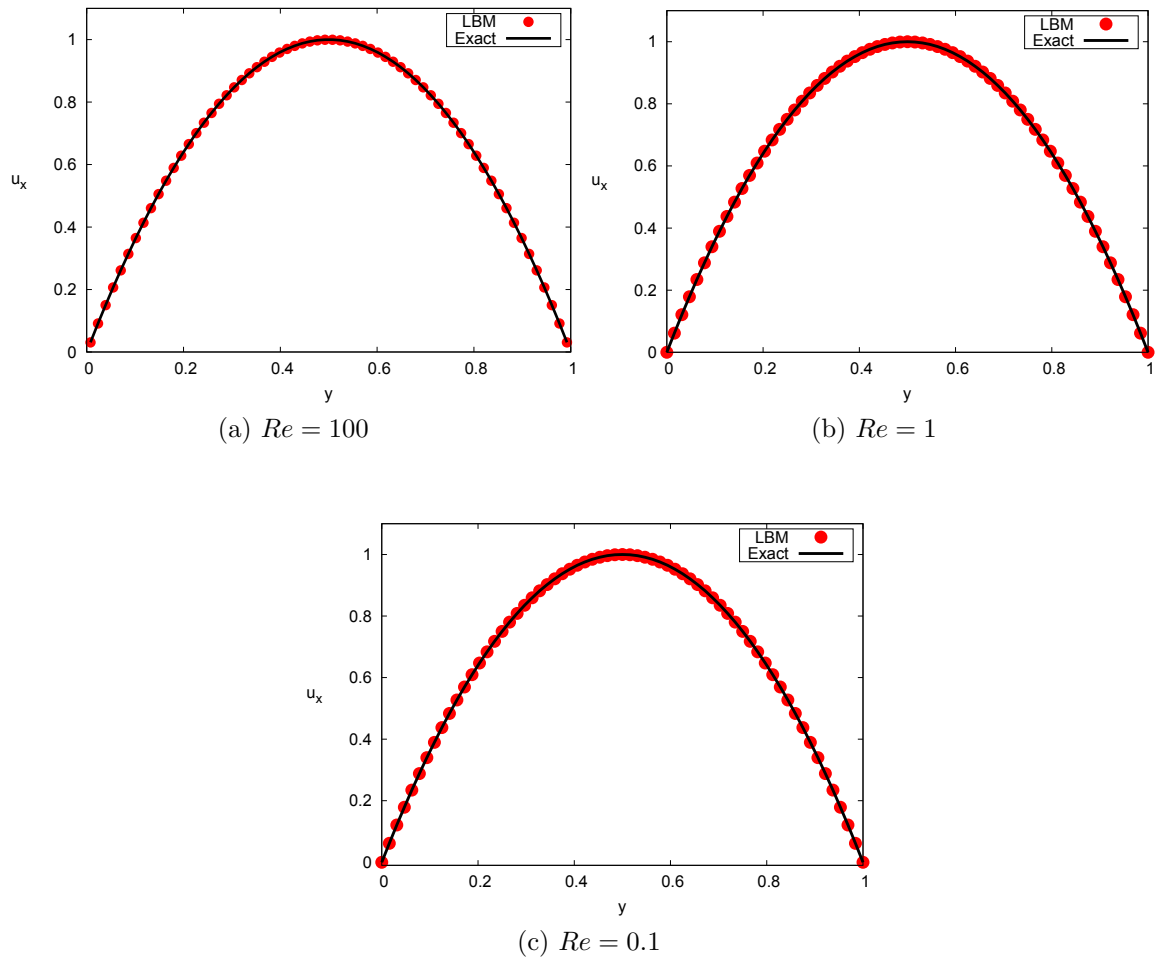
Figure 3.5: Poiseuille flow between two parallel walls simulated by using moment-based method, $(m_x \times m_y) = 128 \times 64$.

Here, small numbers of grid points are chosen, 16×8, at $Re = 1$. Figure 3.6 shows that the numerical solution with bounce-back boundary conditions is affected by the small number of grid points, where the error increased, while the solution with moment boundary conditions has accurate results with the same number of points. Also, the moment method gives the exact solution, if fewer grid points were used at different Reynolds number, for example $m_y = 3$ as in Figure 3.7.

(a) Bounce back
(b) Moment method
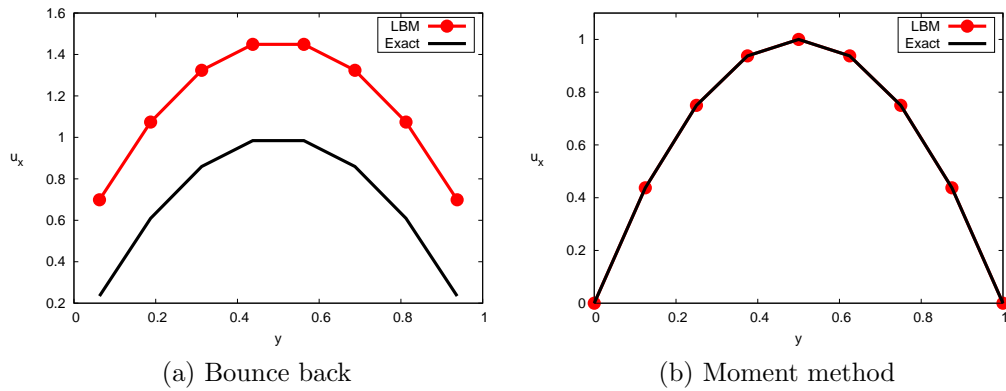
Figure 3.6: Numerical and exact solution of Poiseuille flow at $Re = 1$, $m_y = 8$: (a) Bounce back boundary conditions, (b) Moment boundary conditions.
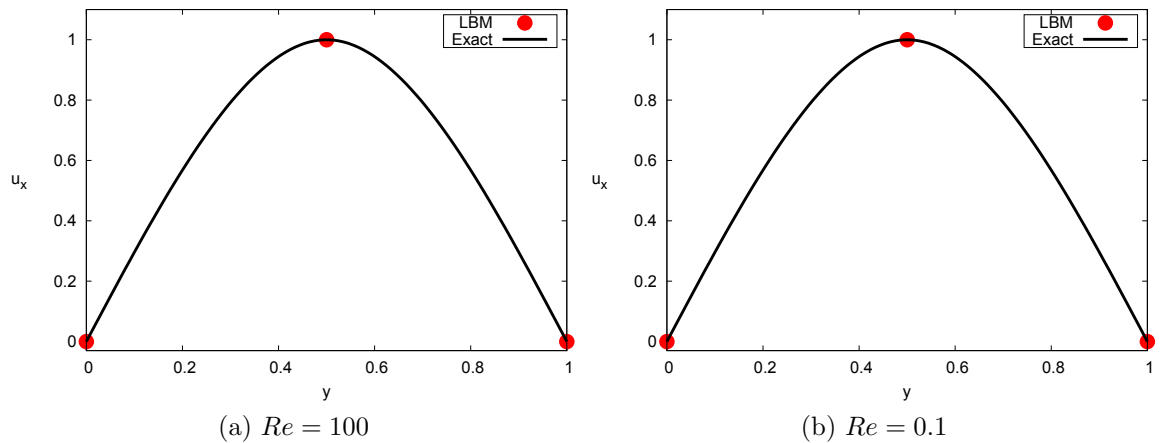
(a) $Re = 100$
(b) $Re = 0.1$

Figure 3.7: Poiseuille flow between two parallel walls simulated by using moment-based method at grid points $m_y = 3$

Nevertheless, the bounce-back boundary conditions and for the same values of Reynolds number, for instance $Re = 100$, when we increased the number of the grid points, the relative error will decrease. It is shown that the half way bounce-back boundary conditions is second-order accurate as expected, see Figure 3.8.
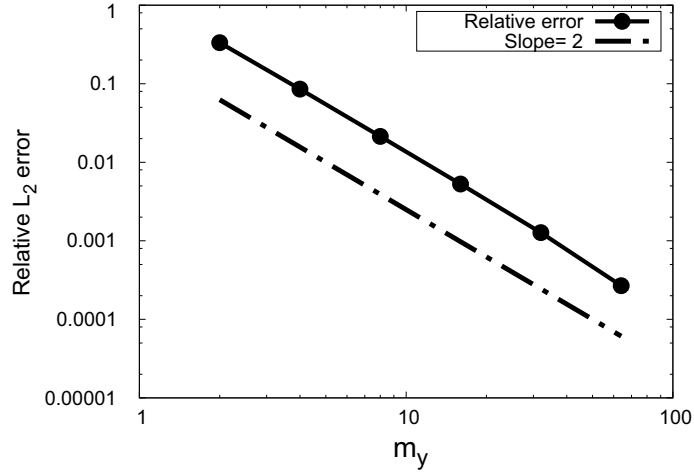
Figure 3.8: Relative error defined in equation (3.62) for half-way bounce-back boundary conditions at $Re = 100$.

3.6.2 Pressure-driven Poiseuille flow

In this flow, the fluid inside the channel is driven by specifying an inlet and outlet pressure. Moment boundary conditions are used at the no-slip solid walls and in the inlet and outlet open boundaries from Section 3.4. Figure 3.9 shows that the pressure at the inlet at $x = 0$ and outlet at $x = m_x$, which is calculated as $P = \rho/3$, presented as $P_{in} = P_0$ and $P_{out} = P_n$, respectively. The pressure in the west boundary $P_{in} = 1$ is bigger than the east one to ensure that the gradient of pressure enforces the flow to move. The gradient of the pressure that acts as a force is $\Delta P = (P_{in} - P_{out})/(m_x - 1)$.
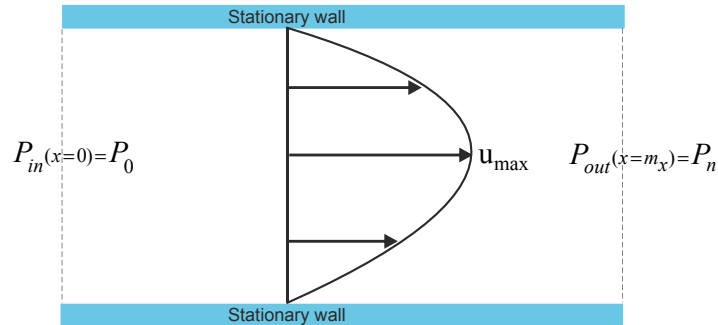
Figure 3.9: Pressure driven Poiseuille flow .

In our simulations the length of the channel is four times its height. The Reynolds number is $Re = 10$, while different numbers of grid points are used m_y=(17, 33, 65,

129) to test the accuracy of the method.

The results of this simulation are very accurate and there is no slip error at the boundary because of moment boundary conditions. By increasing the number of grid points it was noticed that the results are not sensitive to grid points and there is a small relative error. The error that was observed in the simulation is a compressibility error because of the variation in density between the pressure boundaries. As a result, by reducing the Mach number, the error decreases and the incompressibility is third-order accurate, see Figure 3.10
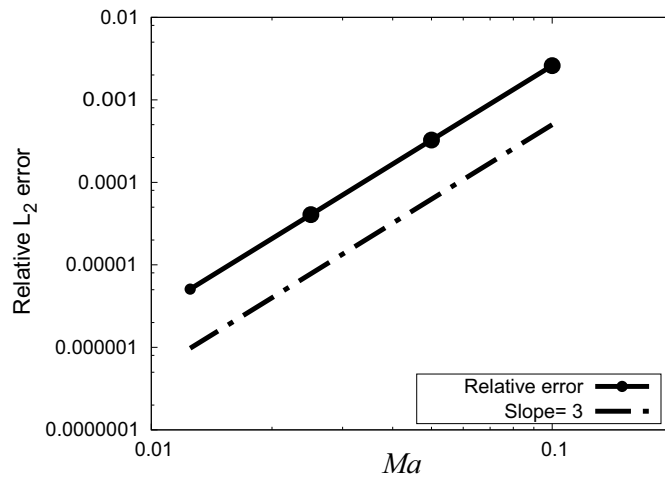
Figure 3.10: Absolute error of the maximum velocity in the centre of the channel with the moment-based boundary condition.

In Figure 3.11 we show the most accurate numerical solution with small Mach number and $Re = 10$ while the number of grid points is (129×33) as an example.
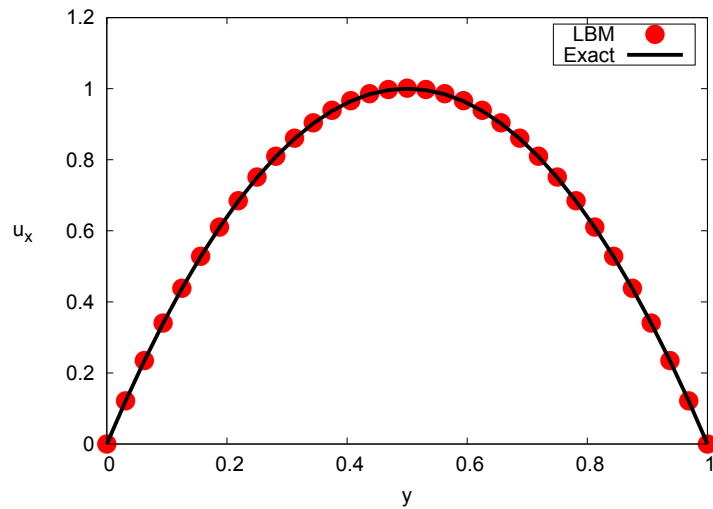
Figure 3.11: Poiseuille flow driven by pressure gradient, $m_x \times m_y = 129 \times 65$.

3.6.3 Couette flow

Using the same strategy as Poiseuille flow, the lattice Boltzmann method is used to simulate Couette flow. This is another simple laminar flow between two parallel plates. The top plate is moving which forces the fluid to move and the bottom one is stationary, this can be seen in Figure 3.12.
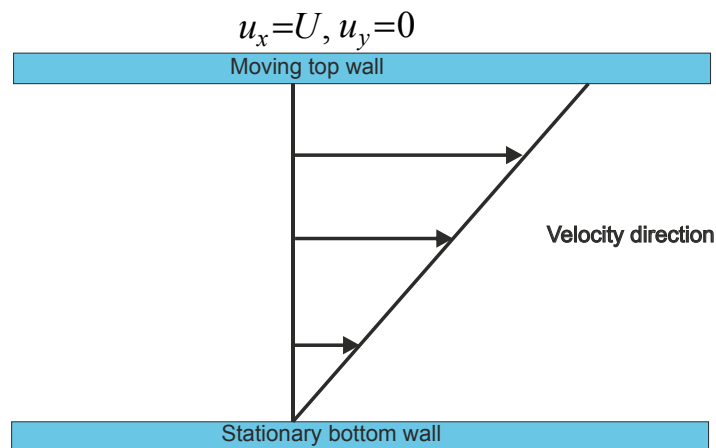
Figure 3.12: Coutte flow.

The boundary conditions that were used to simulate Couette flow are moment boundary conditions. The north boundary is the same as in equation (3.19), but with the moving

top no-slip boundary $u_x = U$, so the following constraints will be used:

$$\rho \bar{u}_y = 0,$$
$$\rho \bar{u}_x = U, \tag{3.64}$$
$$\overline{\Pi}_{xx} = \rho/3 + \rho U^2,$$

where the stress tensor is equal to the equilibrium stress tensor, since the derivative of the velocity in x direction is equal to zero. By solving the above equations, the unknown distribution functions read

$$\bar{f}_4 = \bar{f}_1 + \bar{f}_3 + \bar{f}_2 + 2(\bar{f}_5 + \bar{f}_6) - \frac{\rho}{3} - \rho U^2,$$
$$\bar{f}_7 = \frac{\rho}{6} + \frac{1}{2}\rho U^2 - \frac{1}{2}\rho U - \bar{f}_3 - \bar{f}_6, \tag{3.65}$$
$$\bar{f}_8 = \frac{\rho}{6} + \frac{1}{2}\rho U^2 + \frac{1}{2}\rho U - \bar{f}_1 - \bar{f}_5,$$

where the density is found from the known f_i of the velocity $\rho u_y = 0$ such that

$$\rho = \bar{f}_0 + \bar{f}_1 + \bar{f}_3 + 2(\bar{f}_2 + \bar{f}_5 + \bar{f}_6) - \rho \bar{u}_y. \tag{3.66}$$

For the south wall the velocity $u_x = u_y = 0$ with periodic boundary conditions for the east and west sides. To test the accuracy, the number of grid points is taken to be $(m_x \times m_y) = (17 \times 9)$ first and then $(m_x \times m_y) = (17 \times 3)$. Two values of Reynolds numbers are applied $Re = 100$ and 0.1. The results were compared with the exact solution

$$u(y) = \frac{y \, U_c}{H}, \tag{3.67}$$

where $H = (m_y - 1)$ is the height of the channel.

It was observed that the results with number of grid points $m_x \times m_y = (17 \times 9)$ and different Reynolds number are accurate and give the exact solution, see Figure 3.13. With a small number of grid points (17×3) the accuracy is not affected by the

resolution, as shown in Figure 3.14.

(a) $Re = 100$ (b) $Re = 0.1$
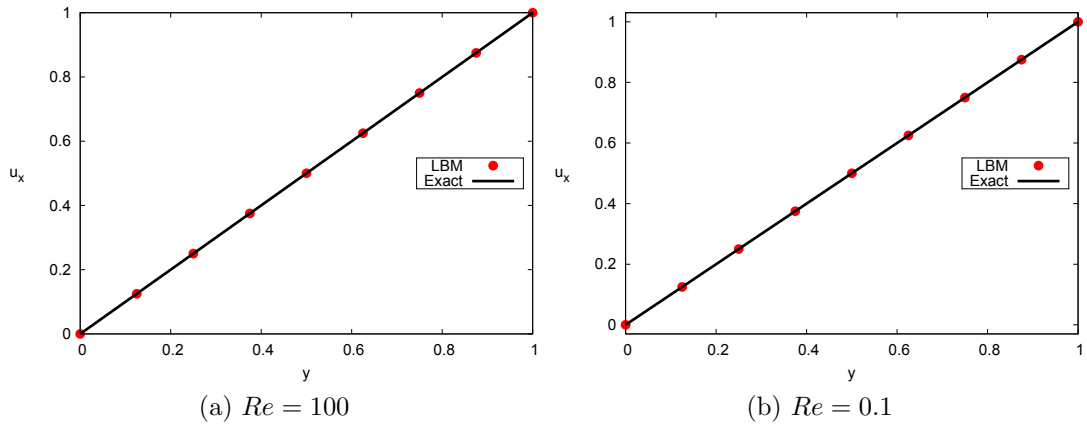
Figure 3.13: Numerical and exact solution Couette flow with moment and periodic boundary conditions when the grid size is (17×9).

(a) $Re = 100$ (b) $Re = 0.1$
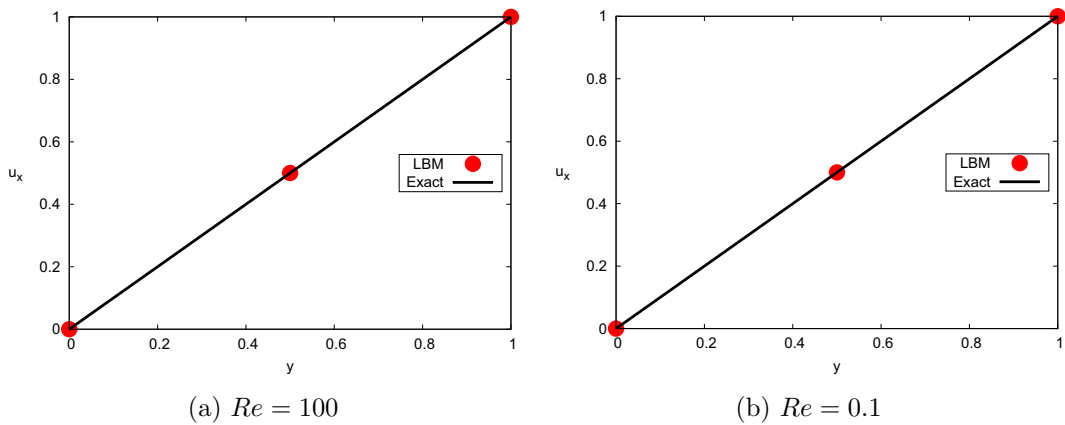
Figure 3.14: Numerical and exact solution Couette flow with moment and periodic boundary conditions when $m_y = 3$.

3.6.4 Lid-driven cavity flow

The third problem that has been investigated to study the accuracy of the moment method by using the lattice Boltzmann method is lid-driven cavity flow. This is the flow in a two-dimensional square cavity filled with an incompressible fluid. The upper lid moves with a constant velocity in the x direction while the other walls are stationary, as shown in Figure 3.15.
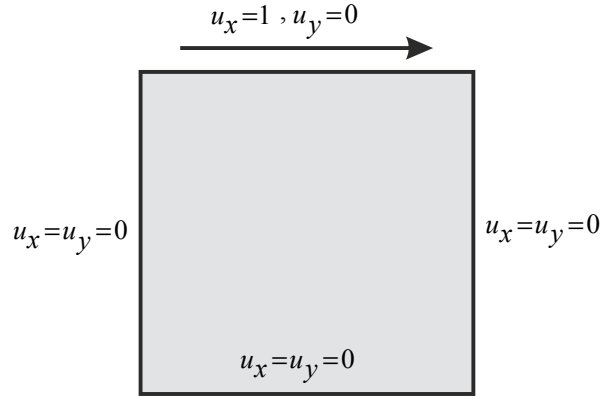
Figure 3.15: Square Lid driven cavity with boundary conditions

3.6.4.1   Problem setup

In the present work, flows at different Reynolds numbers are studied: Re =100, 400, 1000, 3200, 5000 using moment boundary conditions. No-slip and flux conditions $(u_x = u_y = 0)$ are applied to three boundaries. In this type of boundary, the stress tensor $\overline{\overline{\Pi}}_{xx} = \Pi_{xx}^{(0)} = \rho/3 + u_x^2$ is used at the top wall and $\overline{\overline{\Pi}}_{xx} = \Pi_{xx}^{(0)} = \rho/3$ at the other three walls. At the top moving wall the no-slip conditions $(u_x = 1, u_y = 0)$ are applied and the unknown distribution functions are calculated as in equation (3.65). At the corners, the constraints $\overline{\overline{\Pi}}_{xx}$, $\overline{\overline{\Pi}}_{yy}$, $\rho \bar{u}_x$, $\rho \bar{u}_y$ and $\overline{\overline{\Pi}}_{xy} = 0$ are specified.

To examine the accuracy of this method, different grid resolutions are used: (65×65), (129×129), (257×257) and (513×513), and a comparison is made between this method and other methods. The stream function is calculated to test the precision of the method. The stream function ψ is defined to be

$$\psi = \int -u_y dx + u_x dy, \tag{3.68}$$

and the velocity satisfies [106]

$$u_x = \frac{\partial \psi}{\partial y}, u_y = -\frac{\partial \psi}{\partial x}. \tag{3.69}$$

A steady state solution is obtained if the maximum absolute value of the difference between the stream function, at the new time step and the one at the old time step, is

less than 10^{-8}

$$\max_{ij} \left| \psi_{ij}^{(t+1)} - \psi_{ij}^{(t)} \right| < 10^{-8}. \tag{3.70}$$

3.6.4.2 Results and discussion

The biggest challenge that we faced in our simulation is the convergence of the BGK-LBM with moment boundary conditions. For small Re, the results are quite accurate with BGK model; however, it went unstable at moderate Reynolds numbers and often the method did not converge with smaller grid points. For example, our code could not simulate $Re \geq 1000$ on grids (257×257). So, a multiple relaxation time (MRT) from Section (2.6) was used in these cases instead of BGK-LBM for the lattice Boltzmann method. The relaxation times of the ghost moments in the MRT-LBM were set to be $\tau_g = \tau_p = \Delta t/2$. This ensures they decay instantly to equilibrium and is inspired by the MRT scheme proposed by Ladd [67] and discussed by Dellar [28]. Note that in this realisation of MRT the ghost moments do not need to be explicitly included in the code where the hydrodynamics and non-dynamics moments are used to give a complete characterization of LBE. This approach has sometimes been called a "regularized" LBM [70]. The same implementation can be found in the journal article [84].

Tables (3.3), (3.4), (3.5), (3.6) and (3.7) show the results for the maximum and minimum horizontal and vertical velocities. The minimum values of the primary stream function are also inserted in the tables. Moreover, the results were compared with other methods: the finite volume [30, 99], the finite difference [11, 40], the spectral method [9], and LBMs [56, 79], at different Reynolds numbers. Luo *et al.* [79] used a full implementation of the MRT model which linearly transforms the distribution functions where the relaxation rates are given between 0 and 2. Our data in this table was found using (257×257) grid points, the same spatial resolution as the cited LBMs. It is noted that there is excellent agreement between the present work and other methods. In particular, the results are very similar to those obtained by [99], who used a stylised and non-uniform finite volume discretisation and [9] who used a spectral method.

$Re = 100$							
Reference	$y_{(min)}$	$u_{x(min)}$	$x_{(max)}$	$u_{y(max)}$	$x_{(min)}$	$u_{y(min)}$	$\psi_{(min)}$
Present (BGK)	0.4609	-0.21365	0.23828	0.179022	0.8085	-0.2527	-0.103392
Present (MRT)	0.4609	-0.21368	0.23828	0.17903	0.8085	-0.2527	-0.103398
Sahin and Owens [99]	0.4598	-0.21392	0.2354	0.18088	0.8127	-0.2566	-0.103471
Ghia et al. [40]	0.4531	-0.21090	0.2344	0.17527	0.8047	-0.24533	-0.103423
Botella and Peyret [9]	0.4581	-0.21404	0.2370	0.17957	0.8104	-0.25380	-
Bruneau and Jouron [11]	0.4531	-0.2106	0.2344	0.1786	0.8125	-0.2521	-0.1026
Hou et al. [56]	-	-	-	-	-	-	-0.1030
Luo et al. (BGK) [79]	-	-	-	-	-	-	-0.10349
Luo et al.(MRT) [79]	-	-	-	-	-	-	-0.10351

Table 3.3: Comparison of the minimum and maximum values of the velocity u_y along $x = 0.5$ and minimum value of the velocity u_x along $y = 0.5$. The minimum value of the primary stream function ψ obtained from the present work [(BGK-LBM), (MRT-LBM)] and other methods at Re=100 is also shown.

$Re = 400$							
Reference	$y_{(min)}$	$u_{x(min)}$	$x_{(max)}$	$u_{y(max)}$	$x_{(min)}$	$u_{y(min)}$	$\psi_{(min)}$
Present(BGK)	0.2812	-0.32876	0.22656	0.303743	0.8632	-0.45366	-0.114029
Present(MRT)	0.2812	-0.32875	0.22656	0.303732	0.8632	-0.45365	-0.114025
Sahin and Owens [99]	0.2815	-0.32837	0.2253	0.304447	0.8621	-0.456316	-0.113897
Ghia et al. [40]	0.2813	-0.32726	0.2266	0.30203	0.8594	-0.44993	-0.113909
Deng et al. [30]	-	-0.32751	-	0.30271	-	-0.45274	-
Hou et al. [56]	-	-	-	-	-	-	-0.1121
Luo et al. (BGK) [79]	-	-	-	-	-	-	-0.11399
Luo et al.(MRT) [79]	-	-	-	-	-	-	-0.11395

Table 3.4: Comparison of minimum and maximum values of the velocity u_y along $x = 0.5$ and minimum value of the velocity u_x along $y = 0.5$. The minimum value of the primary stream function ψ obtained from the present work [(BGK-LBM), (MRT-LBM)] and other methods at Re=400 is also shown.

$Re = 1000$							
Reference	$y_{(min)}$	$u_{x(min)}$	$x_{(max)}$	$u_{y(max)}$	$x_{(min)}$	$u_{y(min)}$	$\psi_{(min)}$
Present(MRT)	0.17187	-0.388924	0.1562	0.37734	0.9101	-0.52725	-0.11911
Sahin and Owens [99]	0.1727	-0.388103	0.1573	0.37691	0.9087	-0.52844	-0.118800
Ghia et al. [40]	0.1719	-0.38289	0.1563	0.37095	0.9063	-0.51550	-0.117929
Botella and Peyret [9]	0.1717	-0.388569	0.1578	0.37694	0.9092	-0.52707	-0.118936
Bruneau and Jouron [11]	0.1602	-0.3764	0.1523	0.3665	0.9102	-0.5208	-0.1163
Hou et al. [56]	-	-	-	-	-	-	-0.1178
Luo et al.(BGK) [79]	-	-	-	-	-	-	-0.11896
Luo et al.(MRT) [79]	-	-	-	-	-	-	-0.11884

Table 3.5: Comparison of minimum and maximum values of the velocity u_y along $x = 0.5$ and minimum value of the velocity u_x along $y = 0.5$ besides the minimum value of the primary stream function ψ obtained from the present work (MRT-LBM) and other methods at Re=1000 is also shown.

Re = 3200							
Reference	$y_{(min)}$	$u_{x(min)}$	$x_{(max)}$	$u_{y(max)}$	$x_{(min)}$	$u_{y(min)}$	$\psi_{(min)}$
Present(MRT)	0.09375	-0.436873	0.0937	0.434203	0.9492	-0.568876	-0.1222237
Sahin and Owens [99]	0.0921	-0.435402	0.0972	0.432448	0.9491	-0.569145	-0.121628
Ghia *et al.* [40]	0.1016	-0.41933	0.0938	0.42768	0.9453	-0.54053	-0.120377

Table 3.6: Comparison of minimum and maximum values of the velocity u_y along $x = 0.5$ and minimum value of the velocity u_x along $y = 0.5$. The minimum value of the primary stream function ψ obtained from the present work (MRT-LBM) and other methods at Re=3200 is also shown.

Re = 5000							
Reference	$y_{(min)}$	$u_{x(min)}$	$x_{(max)}$	$u_{y(max)}$	$x_{(min)}$	$u_{y(min)}$	$\psi_{(min)}$
Present(MRT)	0.07421	-0.448981	0.07812	0.449503	0.9570	-0.578097	-0.122854
Sahin and Owens [99]	0.0741	-0.447309	0.0799	0.446913	0.9573	-0.576652	-0.122050
Ghia *et al.* [40]	0.0703	-0.43643	0.0781	0.43648	0.9531	-0.55408	-0.118966
Bruneau and Jouron [11]	0.0664	-0.4359	0.0762	0.4259	0.9590	-0.5675	-0.1142
Hou *et al.* [56]	-	-	-	-	-	-	-0.1214

Table 3.7: Comparison of minimum and maximum values of the velocity u_y along $x = 0.5$ and minimum value of the velocity u_x along $y = 0.5$. The minimum value of the primary stream function ψ obtained from the present work (MRT-LBM) and other methods at Re=5000 is also shown.

The relative L_2 error was computed to test the convergence of the algorithm. The error calculation uses results obtained on the finest grid (513×513) as the reference data. Figure 3.16 confirms that the LBM with the moment method is second-order accurate. The results in this figure not only show the expected convergence properties of the LBM, but a comparison with the assumed highly accurate data of [9] and [99] shows excellent agreement, giving confidence to the predictive capabilities of the LBM with moment-based boundary conditions. Furthermore, it was not attempted to optimise the MRT collision operator. The choice of optimal relaxation times is an interesting topic, but a subject for future research.
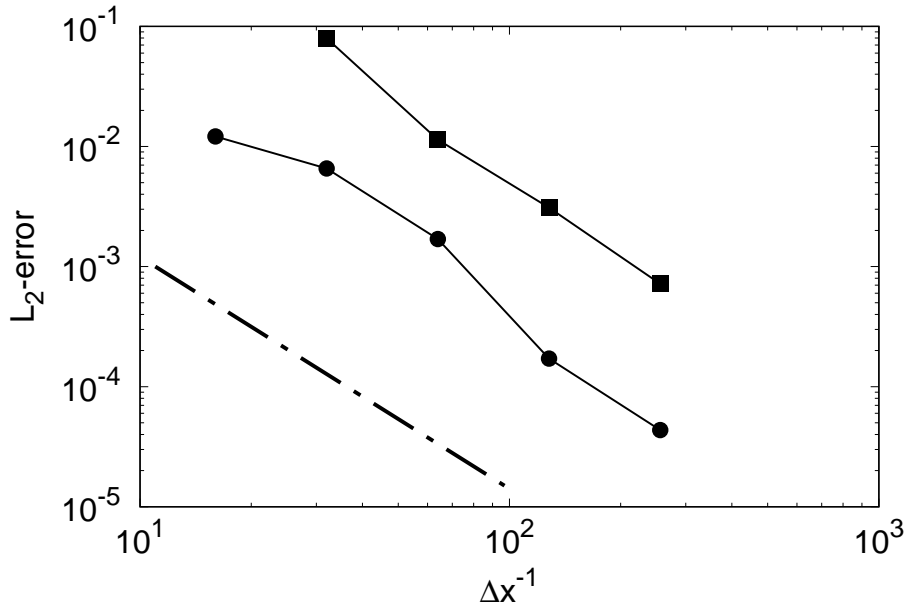
Figure 3.16: Convergence of the minimum primary stream function when Re=100 (filled circle), Re=1000 (filled square) on different grid resolutions. The line of slop 2 (dashed) is also shown. Note that $\Delta x = (m-1)^{-1}$, where mx is the number of grid points in a side of the cavity.

Figures 3.17 and 3.18 make a comparison between the present work and these of [40]. This comparison is for the velocity field along the horizontal and vertical lines respectively, through the centre of the cavity at different grid points over different Reynolds numbers. These figures show the minimum resolution required for stable solutions at a given Reynolds number. This means at grids (17×17) and (65×65) we obtain values at Re=100 until Re=1000. Nevertheless, with more grid points results from Re=100 to Re=5000 were obtained.

Figures 3.17 and 3.18 reveal also that the results become more accurate and closer to those in [40], when the number of grid points is increased. For instance, the results with (17×17) grid points are accurate and have a good agreement with [40] at Re=100. However, the results are inaccurate when the Reynolds number is Re=400, and at Re=10000 there is no convergence with the same number of grid points.

(a) Re= 100

(b) Re= 400

(c) Re= 1000

(d) Re= 3200

(e) Re= 5000
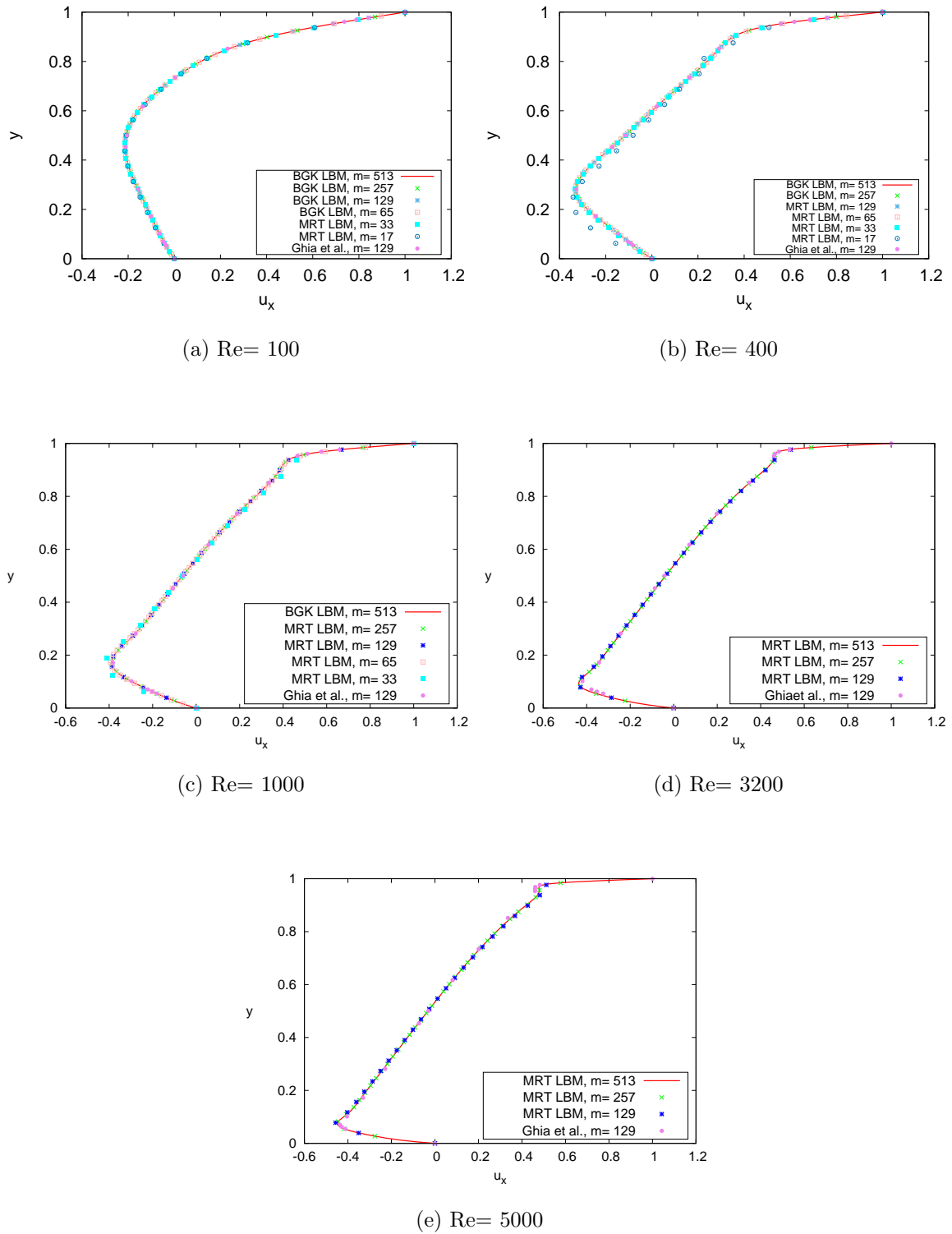
Figure 3.17: A comparison of horizontal velocity u_x along the centre line between the present work and [40] at various Reynolds numbers.

(a) Re= 100

(b) Re= 400

(c) Re= 1000

(d) Re= 3200

(e) Re= 5000
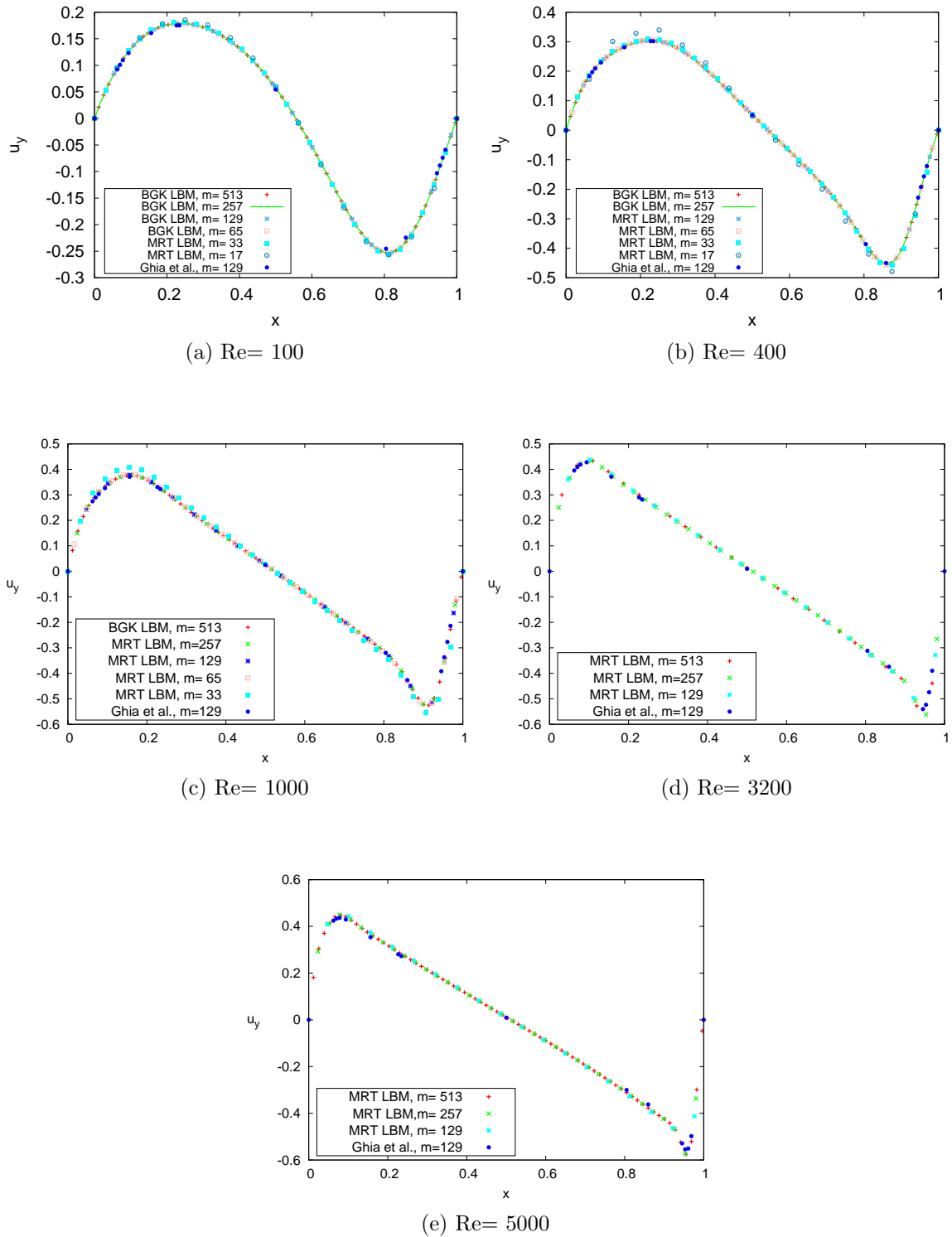
Figure 3.18: A comparison of vertical velocity u_y through the centre line between the present work and [40] at various Reynolds numbers.

Figure 3.19 shows all the results of the computation of streamlines for Reynolds numbers Re=100, 400, 1000, 3200, 5000 when the number of grid points is (257×257) and it clarifies all the expected flow characteristics. For all Reynolds numbers, a primary

vortex near the centre of the cavity is observed. This vortex moves towards the centre of the cavity as the Reynolds number increases. Two secondary vortices appear in the bottom corners which increase in size as the Reynolds number increases. Furthermore, a tertiary vortex in the bottom-right corner for Re=5000 appears as a thin line. When the number of grid points increases, as (513×513), this third vortex becomes more obvious at Re=3200, see Figure 3.20. Note that the results obtained with BGK-LBM and MRT-LBM are similar when the number of the grid points is (257×257) and Re=100 and 400.
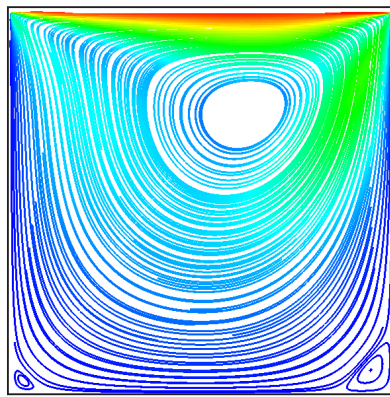
(a) $Re=100$ (b) $Re=400$
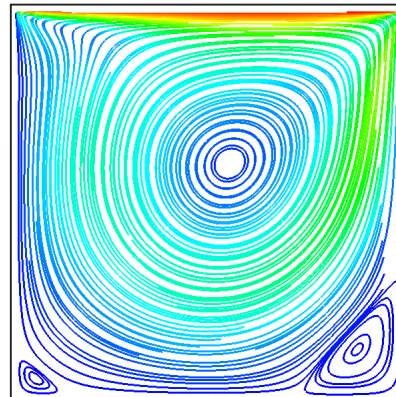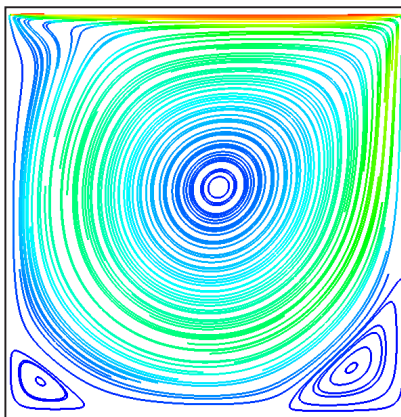
(c) $Re=1000$ (d) $Re=3200$
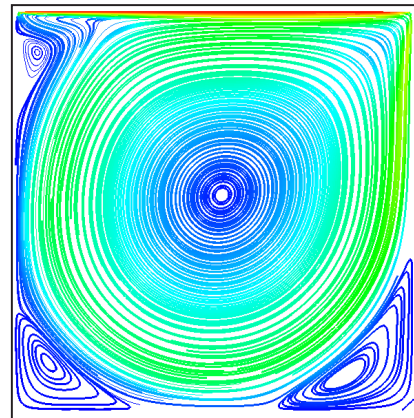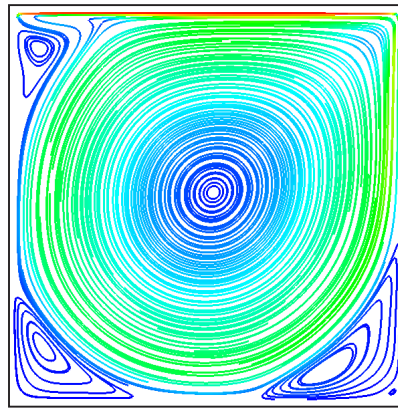
(e) Re=5000

Figure 3.19: Streamlines calculated with 257×257 grid points at different Reynolds numbers: (a) BGK-LBM Re=100, (b) BGK-LBM Re=400, (c) MRT-LBM Re=1000, (d) MRT-LBM Re=3200, (e) MRT-LBM Re=5000.
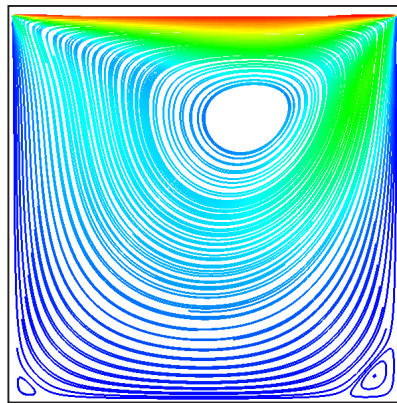
(a) Re=100
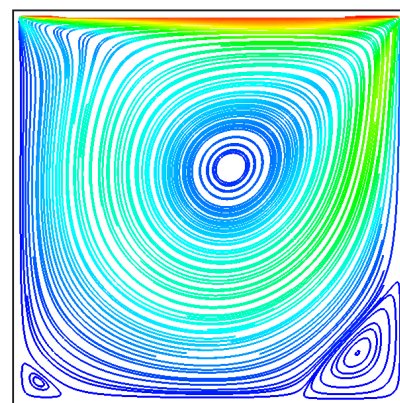
(b) Re=400
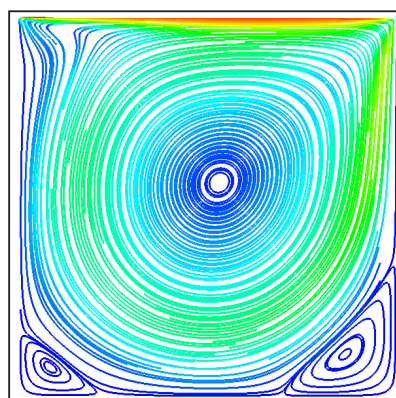
(c) Re=1000
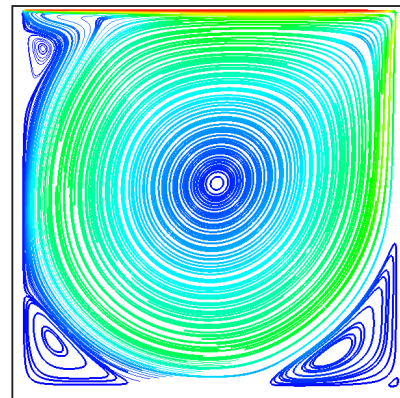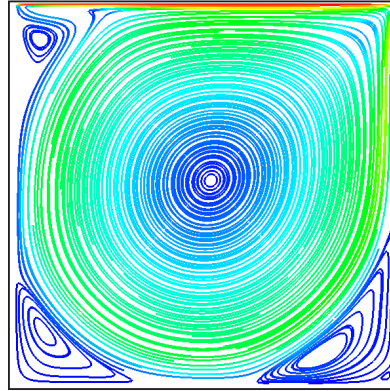
(d) Re=3200

(e) Re=5000

Figure 3.20: Streamlines calculated with 513×513 grid points at different Reynolds numbers: (a) BGK-LBM Re=100, (b) BGK-LBM Re=400, (c) MRT-LBM Re=1000, (d) MRT-LBM Re=3200, (e) MRT-LBM Re=5000.

3.7 Slip boundary conditions

In recent years, the development of micro-electro-mechanical systems has encouraged an increase in research in the field of micro-fluids, such as micro-devices and micro-channel micro-pipes etc. For this kind of problem, the mean free path in a gas can be comparable with the characteristic flow length. Hence the Knudsen number is small so the no-slip condition can not be applied.

The investigation of gaseous flow in micro-electro-mechanical systems has been accomplished in many applications. For example, the micro-Poiseuille problem is one of the simplest applications of the rarefied flow dynamics which is studied analytically, numerically and experimentally [2, 34, 58, 107]. Numerical studies are held by using the lattice Boltzmann method to simulate micro-flow as in [74, 87, 50, 91, 95].

At higher Reynolds numbers, the stress at the boundary increases, which can lead to slippage of the fluid at the boundary, so the flow mimics the slip condition as in turbulent flow [62]. This observation is explained by Galdi and Layton [39]. For that, a significant development of the slip velocity implementation at the boundary will be required.

By applying the slip velocity at the wall, the flow near the wall will be changed

and is influenced by the slip length. The study of slip flow began after an experimental investigation by Kundt and Warburg [65] in a tube of gas. Also it was studied theoretically by Navier [86] who introduced the slip boundary condition. After more than five decades this inspired Maxwell [81] by applying it to gas dynamics problems. Technically the Navier-slip condition assumes that the amount of slip is proportional to the shear rate at the surface. So, Maxwell described the slipping of the flow at the wall by expanding the velocity at the surface by using Taylor expansion

$$u_s - u_w = \tilde{\epsilon}\left(\ell_s \left(\frac{\partial u_s}{\partial n} \right) + \frac{\ell_s^2}{2} \left(\frac{\partial^2 u_s}{\partial n^2} \right) + \dots \right), \qquad (3.71)$$

where u_w is the solid velocity at the wall, u_s is the streamwise velocity, n is the normal direction to the wall and ℓ_s refers to the slip length. The slip length is defined as a distance behind the surface in which the linear extrapolation of the velocity profile is reduced to zero [25, 72]. The combination of $(\partial u_s/\partial n)$ refers to the change of the tangential velocity over the normal direction to the surface. The coefficient $\tilde{\epsilon} = (2 - \epsilon/\epsilon)$ is the streamwise momentum accommodation coefficient and ϵ is the tangential momentum accommodation coefficient. The coefficient $\tilde{\epsilon}$ was introduced by Maxwell [81] in order to transfer all the momentum of the particles when they collide with the wall in the gaseous flows. Following most of the applications, this coefficient was taken equal to 1 and from now we use $\tilde{\epsilon} = 1$. Now truncate equation (3.71) to order one, because the boundary condition to simulate the Navier-Stokes equations is used, and this equation can be an accurate truncation of order one. So, the Navier-Maxwell slip boundary can be written as

$$u_s = \ell_s \frac{\partial u}{\partial n}\bigg|_{wall}. \qquad (3.72)$$

3.7.1 Navier-Maxwell slip for Moment-based boundary conditions

To find the three unknown distribution functions, at the tangential walls for example, the same moments of equation (3.17) are used, but with different conditions. By considering the velocity at the boundary u_x is slipping at the wall, the three constraints of the moments for slip boundary are

$$\rho u_y = 0,$$
$$\rho u_x = \rho u_s, \tag{3.73}$$
$$\Pi_{xx} = \frac{\rho}{3} + \rho u_s^2,$$

where u_s can be found by using the Navier-Maxwell slip of equation (3.72). Note that the viscous term $\tau \Pi_{xx}^{(1)} = -2\mu \partial_x u_x$ in the tangential stress is not zero for the dipole/wall flow with slip, in Chapter 4, but is neglected as it is $O(Ma^2/Re)$. The derivative $(\partial u/\partial n)$ is calculated from the shear stress moment Π_{xy}. From the Chapman-Enskog expansion,

$$\Pi_{xy} \approx \Pi_{xy}^{(0)} + \tau \Pi_{xy}^{(1)},$$
$$= \tau \Pi_{xy}^{(1)}, \tag{3.74}$$

at the wall, since $\Pi_{xy}^{(0)} = \rho u_x u_y = 0$. $\Pi_{xy}^{(1)}$ can be found from equation (2.108) and the assumption of equation (3.72) where $\Pi_{xy}^{(1)} \propto \partial_y u_x$ and $\partial_x u_y = 0$

$$\Pi_{xy}^{(1)} = -\rho c_s^2 \frac{\partial u_x}{\partial y}, \tag{3.75}$$

so

$$\Pi_{xy} = -\mu \frac{\partial u_x}{\partial y}. \tag{3.76}$$

To align with our implementation, the shear stress in terms of $\bar{f}_i$ will be used from equation (2.121) as follows

$$\overline{\Pi}_{xy} = \sum_i \bar{f}_i c_{ix} c_{iy} = \Pi_{xy} + \frac{1}{2\tau}(\Pi_{xy} - \Pi_{xy}^{(0)}). \tag{3.77}$$

At the north wall, in terms of $\bar{f}_i$, the three conditions without the force term are

$$\begin{aligned}
\rho \bar{u}_y &= 0, \\
\rho \bar{u}_x &= \frac{\zeta H}{c_s^2 \rho (2\tau + 1)} \overline{\Pi}_{xy}, \\
\overline{\Pi}_{xx} &= \frac{\rho}{3} + \rho u_s^2,
\end{aligned} \tag{3.78}$$

where $\zeta = \ell_s/H$ is the dimensionless slip length and H is the width. Solving equation(3.78) gives the three unknown distribution functions $\bar{f}_4, \bar{f}_7, \bar{f}_8$ in terms of known ones

$$\begin{aligned}
\bar{f}_4 &= \bar{f}_1 + \bar{f}_2 + \bar{f}_3 + 2(\bar{f}_5 + \bar{f}_6) - \frac{\rho}{3} - \rho u_s^2, \\
\bar{f}_7 &= \frac{\rho}{6} - \bar{f}_3 - \bar{f}_6 + \rho u_s(u_s - 1)/2, \\
\bar{f}_8 &= \frac{\rho}{6} - \bar{f}_1 - \bar{f}_5 + \rho u_s(u_s + 1)/2.
\end{aligned} \tag{3.79}$$

Substituting the distribution functions of equation (3.79) into equation (3.77) gives the shear stress

$$\overline{\Pi}_{xy} = -\rho \bar{u}_s + \bar{f}_1 + \bar{f}_3 + 2(\bar{f}_5 - \bar{f}_6) \tag{3.80}$$

Finally, the slip velocity can be found by applying equation (3.80) into the tangential momentum $\rho \bar{u}_x$ in equation (3.78)

$$u_s = \frac{6\zeta H(\bar{f}_1 - \bar{f}_3 + 2(\bar{f}_5 - \bar{f}_6))}{\rho(2\tau + 1 + 6\zeta H)} \tag{3.81}$$

3.7.2   Numerical simulation of moment slip boundary conditions

Before focusing attention on applying the lattice Boltzmann method for slip boundaries over complex flows, we demonstrate our method's ability to simulate the Poiseuille flow with the Navier-Maxwell condition using moment-based boundary conditions for BGK-LBM. The conditions for the channel flow with force term can be used from equation (3.61), where the velocity u_x at the slip wall can be found from Section 3.7.1 with the existence of the body force such that

$$u_s = \frac{6\zeta H(\bar{f}_1 - \bar{f}_3 + 2(\bar{f}_5 - \bar{f}_6) + \frac{1}{2}\rho G)}{\rho(2\tau + 1 + 6\zeta H)} \tag{3.82}$$

Reis and Dellar [95] specified first-order Navier-Maxwell slip boundaries with the moment method to simulate rarefied open boundary microchannel flow using LBM. For fixed ratio density and various Knudsen numbers their implementation captured the slip flow with second-order accuracy. Here, moment boundary conditions are used with the periodic condition to capture the slip flow for all flow fields. From Section 3.6.1 it has been seen that for small and high Reynolds numbers, the numerical error was eliminated by using moment method; so for slip boundaries, the simulating of the Poiseuille flow for different slip lengths will not be affected by Reynolds number. In Figure 3.21 the result of the tangential velocity u_x is plotted along for a $(m_x \times m_y) = (3 \times 65)$ grid with $Re = 10$ and various slip lengths. Clearly, by increasing the slip length the numerical results depart from the original point (no-slip case) and the velocity profile shifts upwards.
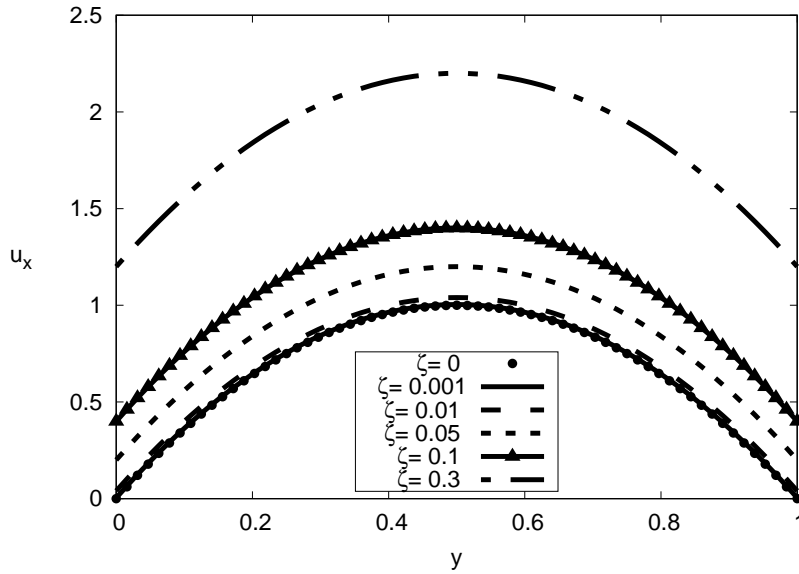
Figure 3.21: Poiseuille flow for Navier-Maxwell slip moment boundary conditions.

3.8   Conclusion

Various boundary conditions were demonstrated to find the unknown functions at the no-slip flat boundaries. Numerical simulations were carried out to assess these boundary conditions and their robustness. The moment-based boundary conditions have been proved to be exact in the simulation of laminar Poiseuille and Couette flows. The moment-based method gave exact results with minimal grid points, $m_y = 3$. A further study was performed to apply moment-based boundary conditions with BGK and MRT-lattice Boltzmann equation for the lid-driven cavity simulation. This work has been published in a journal article [84]. The simulation of the cavity flow using the MRT-LBM with moment boundary conditions is highly accurate. However, the results with BGK-LBM is stable only for small Reynolds numbers, while it is unstable for high Reynolds numbers. This problem does not occur with bounce-back boundary conditions as in [55]. So, to gain excellent results for lattice Boltzmann method for more complicated flows at high Re, it is necessary to use the moment-based boundary conditions with a more accurate model, for example MRT-LBM. Moreover, the moment-based boundary with Navier-slip condition was illustrated and the impact

of the slip length on the behaviour of the flow was shown.

Chapter 4

Dipole wall collision with no-slip boundary conditions

The vortex dipole-wall collision in two dimensional flows is an important problem that has been the subject of numerous recent studies [36, 61]. In this flow two counter-rotating vortices are propelled towards a solid boundary with which they collide. Interactions between dipoles and frictional boundaries are found in a lot of natural phenomena. For example, the effect of the ground on the formulation of secondary vortices when an aeroplane takes off or lands is one of these problems [89]. Another phenomenon is the formulation of large scale vortices in geophysical turbulence at coasts of seas and oceans like the Black Sea and Atlantic Ocean [61] or the coast of Japan. Many laboratory experiments and numerical approximation methods have been used to study the monopole (one vortex) and dipole (two vortices) flows [36]. Orlandi [89] is one of the earliest researchers to study the wall dipole collision numerically and the effect of the flat solid walls on the rotating vortex. Coutsias and Lynove [24] employed Fourier-Chebyshev expansions with a spectral scheme to study the creation of the vortices from the interaction between the no-slip walls and the dipole in a periodic channel. Clercx and Heijst [21] used a Chebyshev pseudospectral method to analyse the dipole-wall collision where the initial trajectory of the dipole is set either perpendicularly to the wall or at an angle of 30° towards one of the no slip walls in a square box. The

authors investigated the dissipation of the energy and how it is related to the growth of the enstrophy in a bounded domain. Clercx and Bruneau [19] gave detailed results of two numerical methods, a finite difference method and a pseudospectral Chebyshev method, to simulate normal and oblique dipole-wall collision in a box. The authors presented authoritative data that can be used as benchmark numerical results. They presented the minimum grid resolutions required by their method to simulate this type of flow accurately. However, presumably due to computational limitations, the maximum Reynolds number achieved in [19] is 5000. Later, Wells *et al.* [111] carried out laboratory and numerical investigations where small scale vorticity in a quasi two dimensional square domain was created within lateral no-slip walls. They explained how the collision between the vortex and the wall created a secondary vortex from boundary layer decay. Kramer [64] in his thesis describes the mechanism of the trajectory for normal dipole wall collisions at high Reynolds numbers by using Chebyshev-τ spectral methods. He gave more details about the small high amplitude vortices that formed from the boundary layer as a result of the collision between the dipole and the boundary. Cieślik *et al.* [18] examined experimentally the interaction between a dipole in a shallow fluid and a side wall in two dimensional simulations then they made a comparison between results of the experiment and three dimension numerical simulation. Using a finite element method, Guzmán *et al.* [47] simulated the dipole collision with a no slip sliding wall where the dipole collided with this wall perpendicularly. The sliding wall moves at a constant speed. This type of collision breaks the symmetry of primary vortices while the collision with a fixed wall maintains the symmetry between them. Also they explained the role of the Reynolds number on the critical speed in their method. Latt and Chopard [71] used a lattice Boltzmann method with bounce-back boundary conditions and a BGK collision operator to simulate this flow. A reasonable agreement with existing benchmark data was shown. However, they only reported results for a Reynolds number of 625.

In this chapter we perform a detailed assessment of moment-based boundary conditions for the lattice Boltzmann equation and use the LBM to numerically study the

wall-dipole collision flow. We use a TRT model with moment-based boundary conditions and study the cases when the dipoles travel towards the wall normally and at angles of 30° and 45°. A thorough assessment and comparison with benchmark data is performed, and an investigation at Reynolds numbers higher than previously reported is conducted. A paper based on this work has been accepted for publication [83].

4.1   Dipole-wall collision

The flow under study is two counter-rotating vortices confined to a square box of size $[-1, 1] \times [-1, 1]$ with no slip boundary conditions on the walls. In accordance with the current literature and to allow for consistent comparisons, the characteristic velocity is given by $U = \frac{1}{4} \int \int |\mathbf{u}|^2 \, dxdy = 1$. The Reynolds number is defined in terms of the half width of the domain H as $Re = UH/\nu$. The vorticity distribution of the individual Gaussian monopoles is given by [13]

$$\omega_0 = \omega_e (1 - (r/r_0)^2) \exp(-(r/r_0)^2), \tag{4.1}$$

where the initial vortex is located in the centre at positions (x_1, y_1) and (x_2, y_2). The velocity can be obtained from the above distribution as

$$
\begin{aligned}
u_{x0} &= -\frac{1}{2} |w_e| \, (y - y_1) \exp\left(-(r_1/r_0)^2\right) + \frac{1}{2} |w_e| \, (y - y_2) \exp\left(-(r_2/r_0)^2\right), \\
u_{y0} &= \frac{1}{2} |w_e| \, (x - x_1) \exp\left(-(r_1/r_0)^2\right) - \frac{1}{2} |w_e| \, (x - x_2) \exp\left(-(r_2/r_0)^2\right),
\end{aligned}
\tag{4.2}
$$

where $r_i = \sqrt{(x - x_i)^2 + (y - y_i)^2}$, $r_0 = 0.1$ is the radius of the monopoles, and w_e the strength of the voriticies.

To test our results the total kinetic energy, $E(t)$, and also the total enstrophy, $\Omega(t)$, are calculated

$$E(t) = \frac{1}{2} \int_{-1}^{1} \int_{1}^{-1} \left|\mathbf{u}^2\right| (\mathbf{x}, t) dxdy, \tag{4.3}$$

$$\Omega(t) = \frac{1}{2} \int_{-1}^{1} \int_{1}^{-1} \left|\omega^2\right| (\mathbf{x}, t) dxdy, \tag{4.4}$$

where $\omega = \partial_x u_y - \partial_y u_x$ is the vorticity.

The initial energy is specified as $E = 2$ which is achieved if the strength of the monopole is fixed to be 299.56. In this work we consider three different problems: one where a dipole collides perpendicular with a solid wall and others where the collision is at an oblique angle of 30° or 45°. The TRT-LBM is used by fixing the parameter $\Lambda = \tau^+ \tau^- = 1/4$. In our simulations we used a range of Reynolds numbers (Re) from 625 to 16,000 for the normal case and 625 to 7500 for the oblique one. Different grid resolutions N_{lb} were employed to test the convergence of the method by monitoring the energy and enstrophy, and the angular momentum in the oblique case only. We consider the results to have converged when

$$\left|E(N_{lb}) - E(N_{lbmax})\right| / E(initial) \leq 0.5\%, \tag{4.5}$$

where $E(N_{lb})$ is the energy evaluated at $t = 2$, $E(N_{lbmax})$ is the energy at the maximum resolution also evaluated at $t = 2$ and $E(initial)$ is the initial value for the kinetic energy.

For both normal and oblique wall collisions, higher Reynolds number simulations require higher resolutions for convergence. In Table 4.1 we include the minimum resolution required by our algorithm to obtain converged solutions. The structure of the code is indicated in Appendix A.2

Re	N_{lb}(normal)	N_{lb}(oblique)30°	N_{lb}(oblique)45°
625	513	513	513
1250	769	769	769
2500	1025	1025	769
5000	3073	4097	1537

Table 4.1: The minimum resolution for convergence LBM.

4.1.1   Normal dipole wall collision

In this case the two monopoles were located at positions $(x_1, y_1) = (0, 0.1)$ and $(x_2, y_2) = (0, -0.1)$, from where they propel themselves towards the east wall directly. In this section we include the results of LBM at $Re=625$ to $Re=5000$ and compare them with the results in [19] and [71]. Figure 4.1 shows the behaviour of the vorticity when the dipole moves towards the no slip boundary at $x = 1$. Our data is taken for $Re = 2500$ with $N_{lb} = 2049$. Most of the vorticity is propelled from the centre of the domain to the right boundary. Around $t = 0.32$ the dipole interacts with the boundary and rebounds from the wall to induce vorticity layers at the boundary where secondary vortices are created. Later, the negative primary vortex detaches from a tertiary thin sheet boundary layer and pairs with positive secondary vortex to form a new dipole then moves towards the same wall to hit it again. The same procedure happens to the positive primary vortex Figure 4.1(d). The thin sheet boundary layer is formed from the gradient of the velocity between the boundary and its nearby region at $t = 0.49$. After $t = 0.6$ a second collision happens and as a result the wall creates more and wilder vortices at the boundary. Then a secondary dipole is separated from the primary dipole and moves towards the west wall, see Figure 4.1(f) which shows the configuration at $t = 1.5$. The two 'horseshoe' shapes that initially surround the primary dipole merge to form a new weak dipole which moves towards the left wall at $x = -1$. This dipole hits the wall at $t = 1$ and creates another weaker dipole. At this wall and similar to the east wall a thin sheet boundary layer appears and creates other weak vortices. Note that the key for the vorticity plots in this figure is similar for all such plots in this chapter.

(a) $t = 0$ (b) $t = 0.2$ (c) $t = 0.32$

(d) t= 0.49   (e) $t = 0.617$ (f) $t = 1.5$
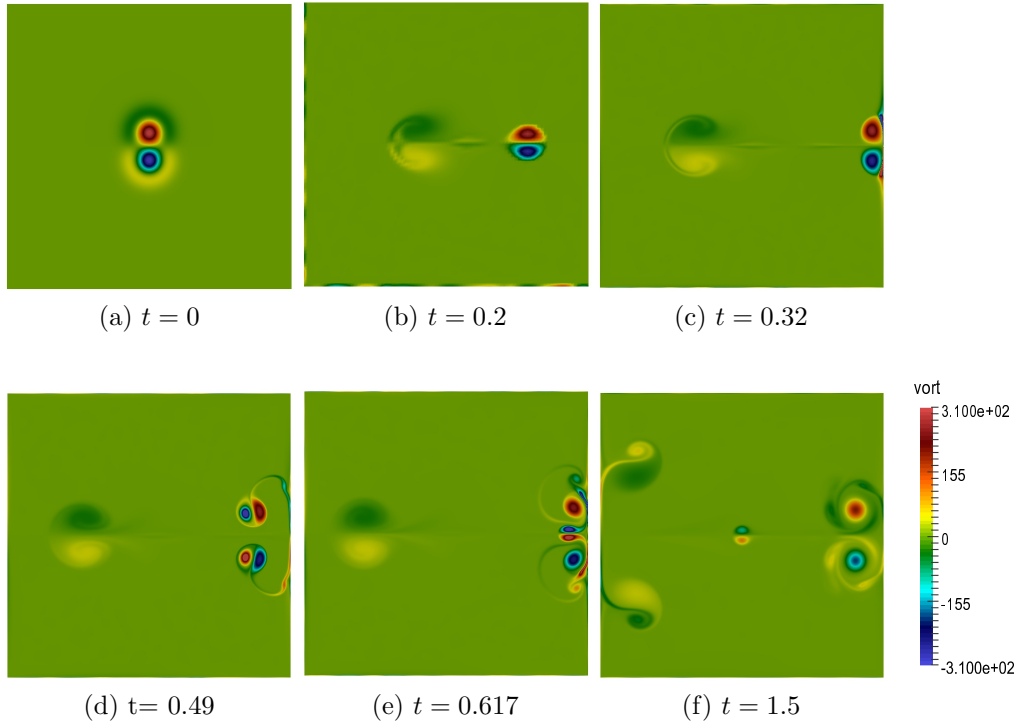
Figure 4.1: Vorticity contours of normal dipole wall collision at Re=2500.

In Figure 4.2 we plot the total kinetic energy $E(t)$ and the total enstrophy $\Omega(t)$ for $Re = 2500$ at different grid resolutions, which demonstrates convergence for $N_{lb} = 1025$. The kinetic energy begins from the initial value $E(0) = 2$ then decreases sharply at $t \approx 0.33$. This sharp dissipation in the energy is due to the first dipole collision with the no-slip wall and corresponds to an increase in the enstrophy at the same time. At the second dipole-wall collision, $t \approx 0.61$, the dissipation of the energy again increases and synchronizes with the second small peak in the enstrophy.

(a) $E(t)$

(b) $\Omega(t)$
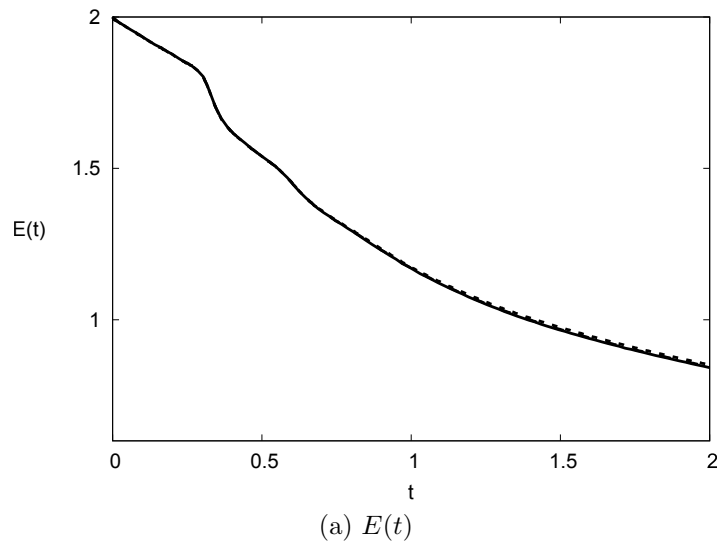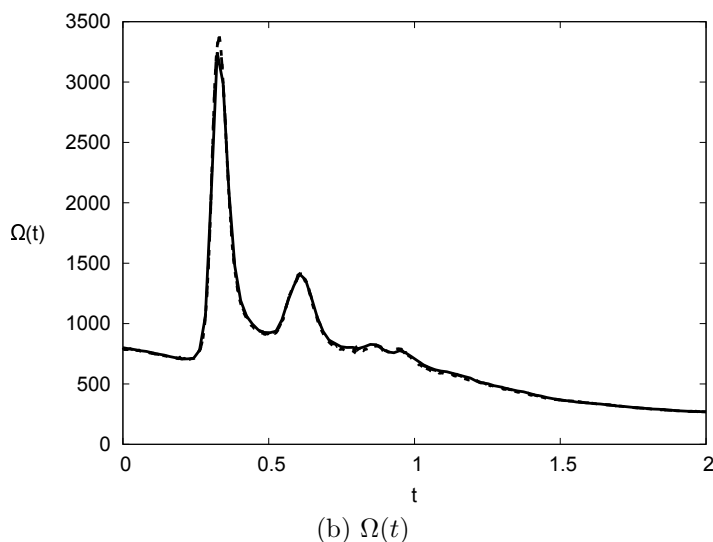
Figure 4.2: The kinetic energy and enstrophy for normal dipole wall collision at $Re = 2500$ and $N_{lb} = 1025$ dotted, 1537 dashed, 2049 line.

In Table 4.2 the first and second local maxima of the enstrophy $\Omega(t)$ as predicted by the TRT-LBM are shown together with the times they appear (denoted t_1 and t_2, respectively). By looking at the results in reference [71] we can see that the value of the first enstrophy peak is close to our result at $Re = 625$ where the first enstrophy peak in this reference is $\Omega_1 = 933.8$ at $t = 0.371$. Also we compare our results with those obtained from a finite difference method (FDM) and of the pseudospectral Chebyshev method (SM) in reference [19]. Flows at different Reynolds numbers are simulated and we have used the same number of grid points as the finite difference method to give a direct comparison between the present work and the work of [19]. Therefore, the resolutions are used here as follows: $Re = 625$ ($N_{lb} = 1025$), $Re = 1250$ ($N_{lb} = 1537$), $Re = 2500$ ($N_{lb} = 2049$) and $Re = 5000$ ($N_{lb} = 3073$).

Re	$t_{1(\text{LBM})}$	Ω_1 (LBM)	$t_{1(\text{FDM})}$	$\Omega_1(\text{FDM})$	t_1 (SM)	Ω_1 (SM)	$t_{2(\text{LBM})}$	Ω_2 (LBM)	$t_{2(\text{FDM})}$	Ω_2 (FDM)	$t_{2(\text{SM})}$	Ω_2 (SM)
625	0.370	931.6	0.371	932.8	0.3711	933.6	0.645	306.2	0.647	305.2	0.6479	305.2
1250	0.343	1884	0.341	1891	0.3414	1899	0.617	727.5	0.616	724.9	0.6162	725.3
2500	0.327	3305	0.328	3270	0.3279	3313	0.617	1413	0.608	1408	0.6089	1418
5000	0.326	5496	0.323	5435	0.3234	5536	0.606	3702	0.605	3667	0.6035	3733

Table 4.2: First and second maximum enstrophy $\Omega(t)$ of the dipole by using TRT-LBM. The results are compared with FDM and SM of [19].

The first and second peaks of the enstrophy at the boundary are attributed to a large generation of the vorticity in the boundary layer. In Figure 4.3 we plot the

vorticity profiles at the boundary $x = 1$ and $-0.6 \leq y \leq 0$ at times $t = 0.4, 0.6, 1$ for $Re = 625, 1250$ and 2500 and we used the same resolution as [19]. The results of the vorticity in our work are in excellent agreement with the results in (Fig. 5) of reference [19]. The vortices at the boundary shows the expected behaviour: the vorticity keeps increasing as the Reynolds number increases. We can notice that the maximum vorticity for $Re = 625$ is highest at $t = 0.4$, soon after the first dipole/wall collision. At $Re = 1250$ and 2500 the maximum vorticity is highest at t = 0.6, around the time of the second collision.
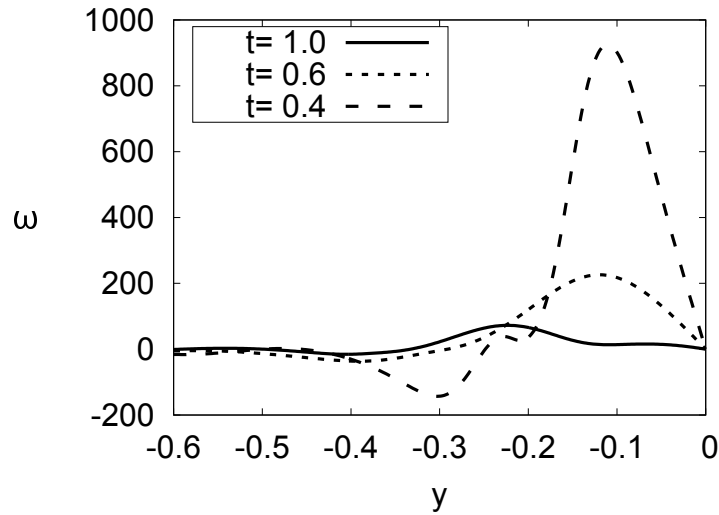
(a) $Re = 625$
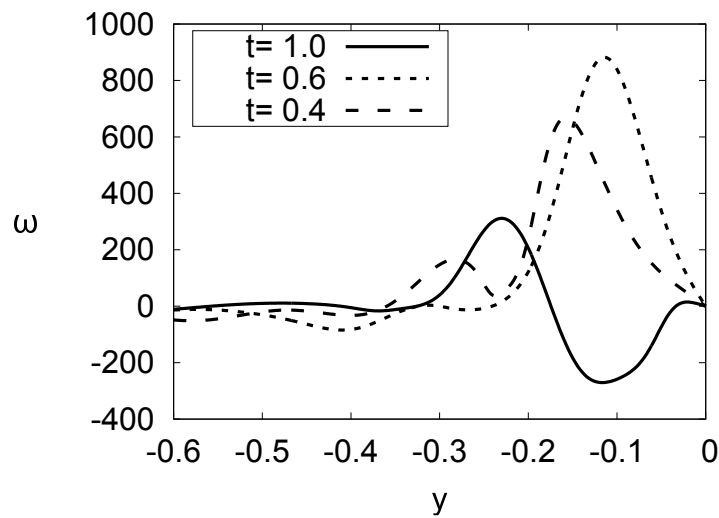
(b) $Re = 1250$

(c) $Re = 2500$
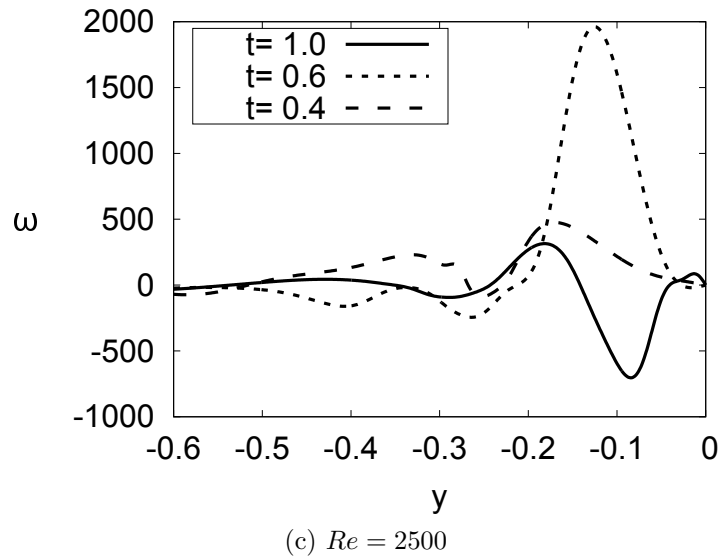
Figure 4.3: The vorticity at the boundary $x = 1$ at time $t = 1$, $t = 0.4$ and $t = 0.6$ at different Reynolds numbers.

To show the effect of the viscosity on the vortices after the dipole collides with the no-slip boundary $x = 1$, vorticity profiles in the domain $(0.3, 1) \times (-0.6, 0.6)$ and $t = 1$ are computed. In Figure 4.4, these profiles are plotted for different Reynolds numbers. We observe the same phenomena as [19]. We can see from these Figures that the flow is symmetric for all Reynolds numbers but the behaviour is different in each snapshot. For $Re = 2500$ we observe the 'rolling mill' effect as a recently-created dipole is ejected away from the right wall- see Figures 4.1 (f) and 4.4(c). This effect can be also observed for $Re = 3200$. At higher Reynolds we get two separate systems that move apart from each other, see Figure 4.4(d).

(a) $Re = 625$ (b) $Re = 1250$ (c) $Re = 2500$ (d) $Re = 5000$
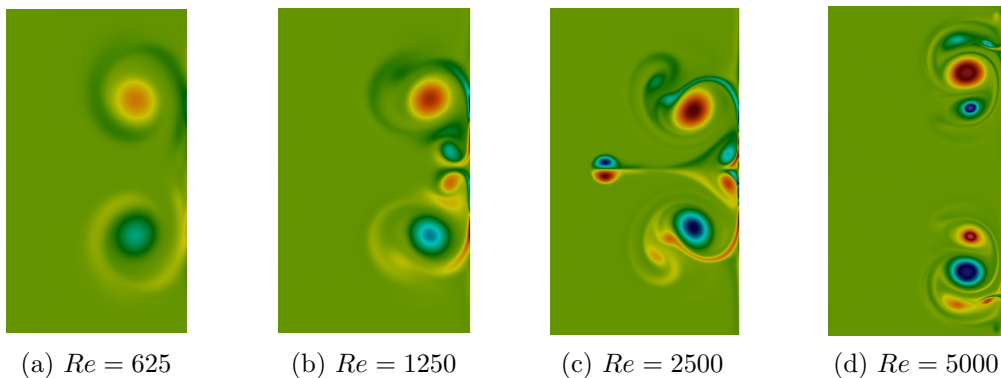
Figure 4.4: Vorticity contours of normal dipole wall collision at $t = 1$. Vorticity profile shown in the subdomain $0.3 \leq x \leq 1, -0.6 \leq y \leq 0.6$.

The maximum values of the primary vortex ω_{max} and its position (x, y) are shown in Table 4.3. The results are compared with the two methods in [19], the finite difference method and the pseudospectral Chebyshev method. The number of grid points used is the same as those used for the finite difference method. In our simulations we observed the results of ω_{max} at different times $t = 0.6, 0.625, 1$ and $t = 1.4$. We can see that the ω_{max} increases with Reynolds number. For each Reynolds number the maximum vorticity decreases in time. The maximum vorticity and its location in our simulations are close to the predictions made by other methods. It should be noted that the vorticity is a primary variable in the formulation of the pseudospectral Chebyshev method in [19] while here it is obtained indirectly by numerically differentiating the predicted velocity field. In addition, in Table 4.4 we present LBM results for the kinetic energy and enstrophy before and after the first and second dipole wall collision and compare them with those in [19].

	current work			Clercx and Bruneau			
Re	t	(x, y)	ω_{max}	$(x, y)_{(FD)}$	$(x, y)_{(SM)}$	$\omega_{max(FD)}$	$\omega_{max(SM)}$
625	0.6	(0.816,0.166)	159.5	-	(0.818,0.165)	-	158.9
	0.625	(0.832,0.166)	155.1	(0.832,0.166)	-	154.2	-
	1.0	(0.804,0.253)	103.1	(0.805,0.254)	(0.805,0.254)	102.6	102.6
	1.4	(0.769,0.306)	71.28	-	(0.769,0.307)	-	71.00
1250	0.6	(0.872,0.148)	219.6	-	(0.874,0.151)	-	219.4
	0.625	(0.884,0.169)	216.5	(0.885,0.174)	-	216.1	-
	1.0	(0.847,0.255)	170.9	(0.848,0.258)	(0.848,0.257)	170.3	170.3
	1.4	(0.808,0.291)	133.2	-	(0.809,0.292)	-	132.7
2500	0.6	(0.894,0.161)	260.9	-	(0.896,0.165)	-	261.9
	0.625	(0.896,0.193)	259.3	(0.896,0.199)	-	260.0	-
	1.0	(0.829,0.219)	231.7	(0.826,0.219)	(0.826,0.217)	231.4	231.4
	1.4	(0.799,0.192)	202.3	-	(0.798,0.195)	-	201.6
5000	0.6	(0.899,0.235)	282.5	-	(0.903,0.244)	-	286.9
	0.625	(0.888,0.272)	283.8	(0.884,0.275)	-	285.9	-
	1.0	(0.818,0.369)	268.2	(0.811,0.367)	(0.811,0.366)	268.6	269.1
	1.4	(0.799,0.192)	202.3	-	(0.798,0.195)	-	201.6

Table 4.3: The maximum vorticity ω_{max} in a normal wall-dipole collision and its location at $t = 0.6, 0.625, 1, 1.4$.

For further investigation and assessment of moment-based conditions we use the

TRT LBM with half-way bounce-back boundary conditions for comparison. There results are shown in Table 4.4 and Table 4.5. We see that the results computed using bounce-back and moment-based conditions are in good agreement. The data set obtained by using moment-based boundary conditions appears to be more accurate than the data set obtained by using bounce-back in the sense that it is in closer agreement with the data set obtained by spectral simulations. This shows that the proposed approach can be a competitive method and gives us confidence to use it to impose physically more complex conditions.

		Lattice Boltzmann method				Clercx and Bruneau			
Re	t	$E(t)_{(MM)}$	$\Omega(t)_{(MM)}$	$E(t)_{(BB)}$	$\Omega(t)_{(BB)}$	$E(t)_{(FD)}$	$E(t)_{(SM)}$	$\Omega(t)_{(FD)}$	$\Omega(t)_{(SM)}$
	0.25	1.501	472.1	1.501	468.9	1.502	1.502	472.7	472.6
625	0.50	1.013	382.6	1.012	378.6	1.013	1.013	380.4	380.6
	0.75	0.767	256.0	0.767	250.1	0.767	0.767	255.0	255.2
	0.25	1.719	613.6	1.719	610.0	1.721	1.720	615.0	615.0
1250	0.50	1.312	612.8	1.311	608.1	1.313	1.313	611.3	611.9
	0.75	1.061	486.2	1.061	477.8	1.061	1.061	484.4	484.7
	0.25	1.848	725.6	1.848	718.5	1.851	1.850	727.8	728.2
2500	0.50	1.540	917.6	1.539	909.2	1.541	1.541	916.6	920.5
	0.75	1.325	809.9	1.325	794.9	1.326	1.326	805.5	808.1
	0.25	1.919	820.3	1.919	808.2	1.923	1.922	822.8	823.1
5000	0.50	1.690	1331	1.689	1317	1.692	1.692	1328	1340
	0.75	1.496	1539	1.495	1455	1.495	1.498	1659	1517

Table 4.4: The values of the energy and the enstrophy at different times 0.25, 0.50, 0.75 which are before, between and after the first two collisions. Here, MM refers to moment method and BB to bounce back.

Re	$t_{1(BB)}$	$\Omega_{1\,(BB)}$	$t_{1(FDM)}$	$\Omega_{1(FDM)}$	$t_{1\,(SM)}$	$\Omega_{1\,(SM)}$	$t_{2(BB)}$	$\Omega_{2\,(BB)}$	$t_{2(FDM)}$	$\Omega_{2\,(FDM)}$	$t_{2(SM)}$	$\Omega_{2\,(SM)}$
625	0.376	853.7	0.371	932.8	0.3711	933.6	0.646	297.5	0.647	305.2	0.6479	305.2
1250	0.344	1752	0.341	1891	0.3414	1899	0.618	705.4	0.616	724.9	0.6162	725.3
2500	0.327	2993	0.328	3270	0.3279	3313	0.617	1352	0.608	1408	0.6089	1418
5000	0.327	4975	0.323	5435	0.3234	5536	0.607	3394	0.605	3667	0.6035	3733

Table 4.5: First and second maximum enstrophy $\Omega(t)$ of the dipole by using TRT-LBM and BB method. The results are compared with FDM and SM of [19].

4.1.1.1 Higher Reynolds numbers

In this section we investigate the behaviour of the flow for $Re = 7500$, 10000 and 16000, (see Figure 4.5) by using the moment-based boundary conditions. For these higher Reynolds numbers the results converged with mesh refinement until $t = 0.6$. In our simulations, the maximum resolution is a grid size of around 4000×4000.

To gauge whether or not this is sufficient, we follow [19] and insist upon having 5 points in the viscous wall boundary layer and estimate the boundary layer thickness as $\delta \approx 1/(4\sqrt{Re})$. For $Re = 10000$, this gives $N_{lb} \approx 4000$ and here we use $N_{lb} = 4097$ and we use this grid size for all Reynolds $Re = 7500, 10000$ and $Re = 16000$. We can see from the figure that results on successive meshes are in successively better agreement. As for lower Reynolds numbers before $t = 0.6$ there are two rapid declines in energy after the first and second wall collisions. Again these correspond with the first and second higher peaks of the enstrophy.
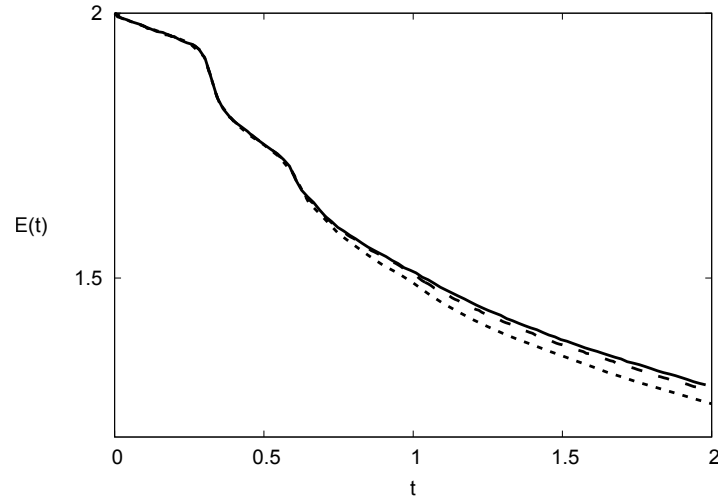
(a) $E(t)$
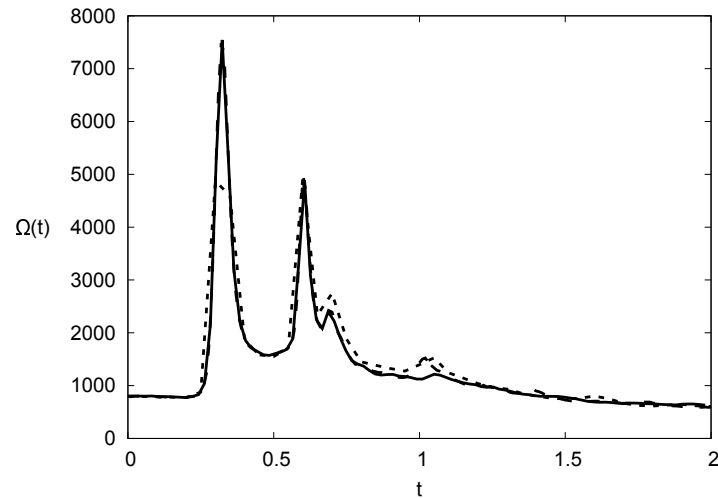
(b) $\Omega(t)$

Figure 4.5: The kinetic energy and enstrophy for normal dipole wall collision at $Re = 7500$ with $N_{lb} = 2049$ (dotted), $N_{lb} = 3073$ (dashed), $N_{lb} = 4097$ (line).

To test the dissipation of the energy at different Reynolds numbers we traced the energy at the time $t = 2$ and different Reynolds numbers. We can notice from Table 4.6 the energy decreases faster for smaller Reynolds number than for larger ones. This is consistent with the values of $E(t)$ at different time steps shown in Table 4.4. The resolutions used are the same as in Tables 4.3 and 4.4.

Re	625	1250	2500	5000	7500	10000	16000
$E(2)$	0.305	0.518	0.841	1.108	1.285	1.359	1.382

Table 4.6: The kinetic energy at $t = 2$.

In Figure 4.6 we make a comparison between high and low Reynolds numbers, $Re = 10000$ and $Re = 625$ as an example. We observe that the number of vortices increases with Reynolds number and the effect of the boundary at the rebound of the dipole makes the number of dipoles at $Re = 10000$ higher than at $Re = 625$. In fact, from Figure 4.4 (a) and Figure 4.6 (a) we can notice that the vortices for $Re = 625$ decrease in strength as time increases. At $Re = 10000$ the space between the upper and lower cores is larger than at the smaller Reynolds number and the space is higher with extra small high value vortices at the corners for $Re = 16000$. This behaviour is more obvious at $Re = 5000$ and higher, see Figure 4.4 (d) and Figure 4.6(b).

(a) $Re = 625$

(b) $Re = 10000$

(c) $Re = 16000$
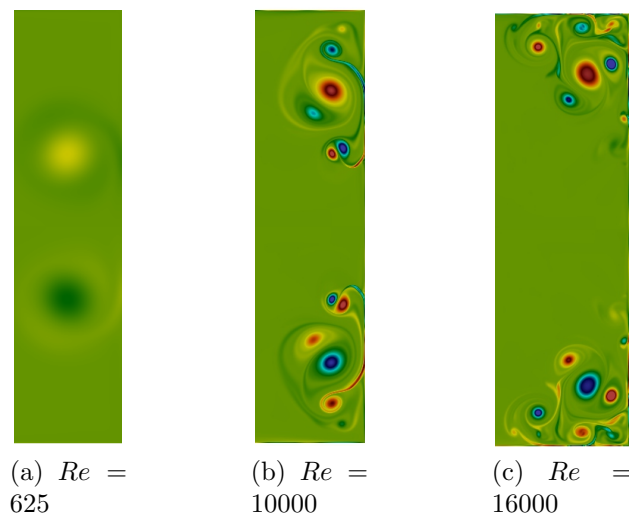
Figure 4.6: Snapshot of vorticity at normal wall dipole collision at $t = 2$ in the subdomain (a,b): $0.5 \leq x \leq 1, -1 \leq y \leq 1$ and (c): $0.4 \leq x \leq 1, -1 \leq y \leq 1$.

As a result of the increased activity at higher Reynolds numbers, there are more enstrophy peaks than at smaller Reynolds numbers. This is owing to the increase in the number of wall-vortex collisions. In Table 4.7 we show the first three maxima in the enstrophy for the three Reynolds numbers. We can notice from Tables 4.2 and 4.7 that the ratio between the first and second enstrophy peaks increases with the Reynolds numbers until flattening off after $Re = 5000$.

Re	t_1	Ω_1(LBM)	t_2	Ω_2 (LBM)	t_3	Ω_3 (LBM)
7500	0.323	7626	0.604	5013	0.685	2418
10000	0.322	9519	0.628	6455	0.721	4479
16000	0.318	12833	0.603	7760	0.65	4105

Table 4.7: First, second and third maxima in enstrophy of the dipole by using TRT-LBM.

For higher Reynolds numbers, tertiary high strength vortices are observed which are created from the wall boundary layer around $t = 0.45$. In Figure 4.7 the upper dipole is plotted (since it is symmetric with the negative ones). These vortices appear as small circles inside the boundary vortex thin sheet for Re=2500 then they become clear for Re=5000. For Re=7500 these vortices move far from the wall then separate from the sheet at the boundary. For Re=10000 a quaternary vortex is formed which merges with the tertiary one, Figure 4.7 (c). This also happens for $Re = 16000$ and is even more evident in that case- see Figure 4.7 (d).

(a) Re= 5000 (b) Re= 7500 (c) $Re = 10000$ (d) $Re = 16000$
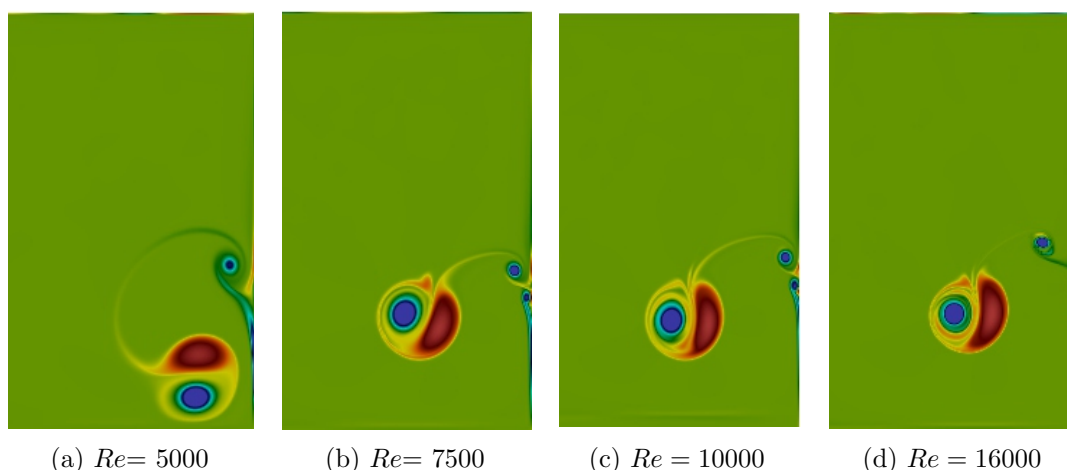
Figure 4.7: Vorticity contours of normal positive dipole wall collision at $t = 0.45$ in the subdomain $0.4 \leq x \leq 1, 0 \leq y \leq 1$.

We computed the maximum vorticity at different times after the second collision but we found qualitatively different behaviour to the flows at smaller Reynolds numbers. For example Table 4.8, at $Re=7500$ we noticed that ω_{max} at $t=0.6$ is equal to 292.7 then at $t=1$ increased to 497.4 before decreasing again. This is similar to the behaviour of ω_{max} at $Re=10000$ and 16000. This behaviour differs from that of ω_{max} in Table 4.3. This is due to the formation of the secondary dipole at the wall after the second collision, as shown in Figure 4.7. For smaller Reynolds numbers this dipole moves towards the wall then merges with the primary vortices. At higher Reynolds numbers, the secondary dipole moves towards the boundary and rotates after the collision. This then creates tertiary and fourth vortices through interaction with the wall. Figure 4.8 shows the generated vortices before, (a, c, e, g), and after, (b, d, f, h), merging with the primary vortices. The behaviour of creating the strong vortices at the boundary is observed also in [64].

Re	t	(x,y)	ω_{max}
7500	0.6	(0.899,0.265)	293.0
	0.625	(0.888,0.307)	292.6
	1.0	(0.808,0.392)	497.4
	1.4	(0.766,0.488)	341.8
10000	0.6	(0.899,0.231)	297.9
	0.625	(0.899,0.274)	294.5
	1.0	(0.839,0.421)	645.0
	1.4	(0.770,0.522)	401.9
16000	0.6	(0.891,0.329)	303.0
	0.625	(0.879,0.359)	303.1
	1.0	(0.878,0.761)	1022
	1.4	(0.805,0.872)	620.3

Table 4.8: The maximum vorticity ω_{max} in a normal wall-dipole collision at $Re=7500$ and 10000, and its location at $t=0.6, 0.625, 1, 1.4$.

(a) $t = 0.55$ (b) $t = 0.63$

$Re= 5000$

(c) $t = 0.64$ (d) $t = 0.74$

$Re= 7500$

(e) $t = 0.66$ (f) $t = 0.8$

$Re= 10000$

(g) $t = 0.62$ (h) $t = 0.74$

$Re= 16000$
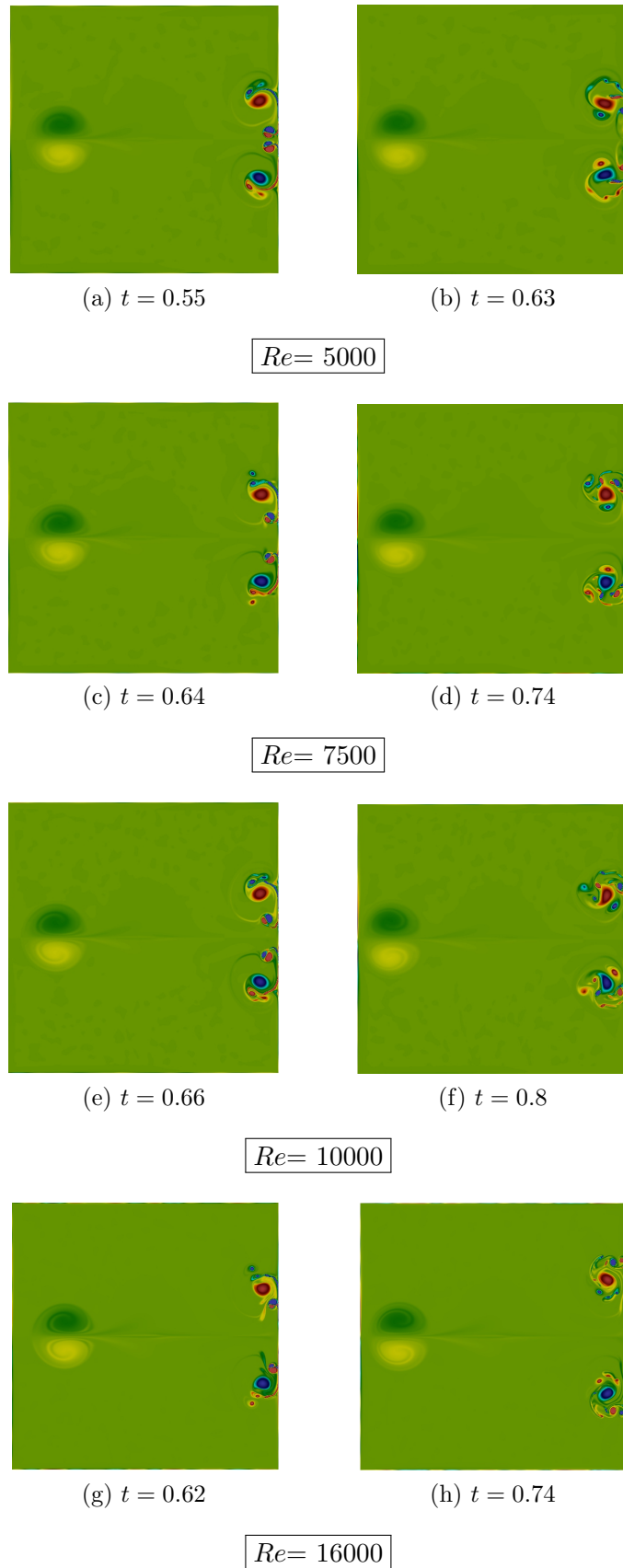
Figure 4.8: Snapshots of the vortices at normal dipole wall collision for $Re= 5000$, 7500, 10000 and 16000.

116

In Figure 4.9 we calculate the relative error for $Re = 625$ with respect to the results with the finest resolution, which in our case is $N_{lb} = 3073$. The L_2-error is computed as $|\varphi(N_{lb}) - \varphi(N_{lbmax})| / \varphi(N_{lbmax})$ where φ is the total kinetic energy or total enstrophy. The convergence of this method is shown to be of second-order.
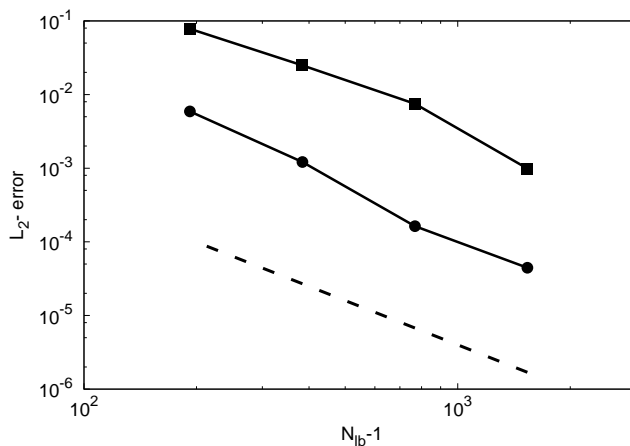
Figure 4.9: L_2-error for the enstrophy (filled square) and total kinetic energy (filled circle): normal collision evaluated for $Re = 625$ at t=0.4. The dashed line is the line of slope 2.

4.1.2 Oblique dipole wall collision

In this case the dipole will release at non-normal incidence. There we use incidence angles of 30° and 45°.

4.1.2.1 Oblique dipole wall collision at angle 30°

We now consider the case of releasing the dipole at an oblique angle and again compare our results with benchmark data. Here, the dipole rolls from the location $(x_1, y_1) = (0.0839, 0.0866)$ and $(x_2, y_2) = (0.1839, -0.0866)$ towards the no-slip wall at $x = 1$ at an angle of 30° to the horizontal. Similar to the previous section, we calculate the total enstrophy and total kinetic energy, from equations (4.4) and (4.3), for different Reynolds numbers and with various grid resolutions.

Vorticity contours are illustrated in Figure 4.10 to show the evolution of the dipole at Re=7500 ($N_{lb} = 3073$). From the figures we can see the behaviour of dipole after the second collision, at $t = 0.6$, is more vigorous and complex than the normal collision

case. Because of the angle of release of the dipole towards the wall, the positive and negative monopoles are not symmetric after the first collision with the boundary. Also, as time progresses the primary and secondary vortices move to the upper wall at $y = 1$. The two horseshoes that surrounded the dipole at the initial time separate from it and move in the opposite direction. After a while the two horseshoe shape vortices create a new, weaker, dipole that interacts with the left corner, which again induces weaker vortices, (see Figure 4.10 (e)) .

(a) $t= 0$ (b) $t= 0.3$ (c) $t= 0.6$

(d) $t= 0.8$ (e) $t= 2$
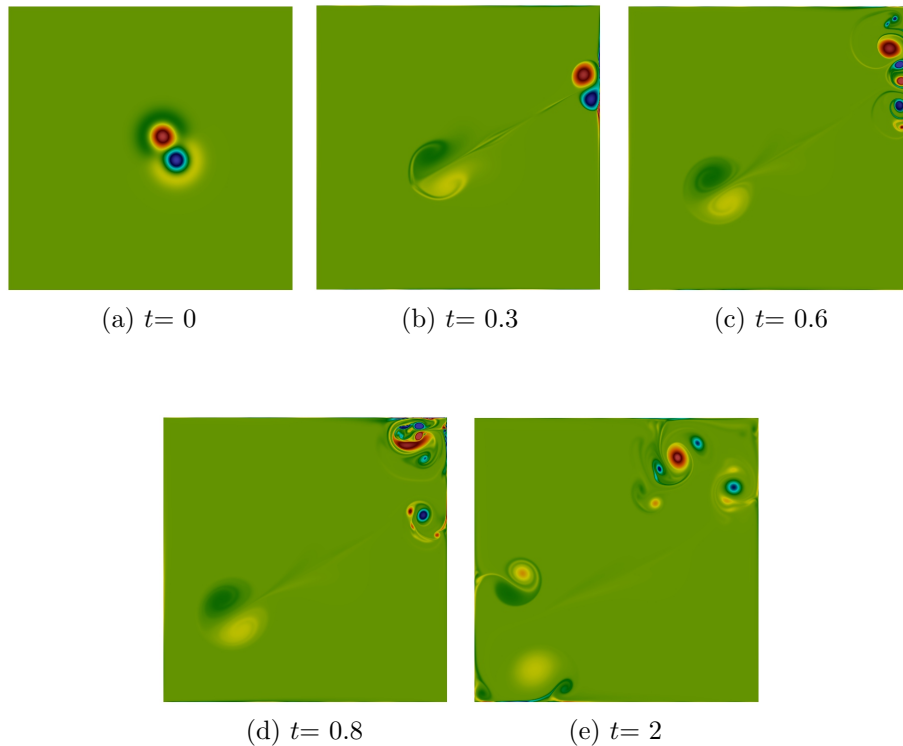
Figure 4.10: Vorticity contours of oblique dipole wall collision at Re= 7500.

Figure 4.11 plots $E(t)$ and $\Omega(t)$ at $Re=2500$ for different resolutions. We observe the convergence of the results at $N_{lb} = 1025$. We note that the energy decays rapidly between $0.32 < t < 0.4$ which is associated with the first peak of the enstrophy. The dissipation of total kinetic energy is less than the dissipation for $Re = 2500$ in the normal case, see Figure 4.2. At higher Reynolds numbers, for example 7500, the energy dissipation is less than that for $Re = 2500$. The first peak of the enstrophy is higher than for $Re = 2500$ and we can see that the number of peaks increases. The profile is less smooth; due to the increase in the number of collisions of additionally

created dipoles with the no-slip wall, see Figure 4.12.

(a) $E(t)$

(b) $\Omega(t)$
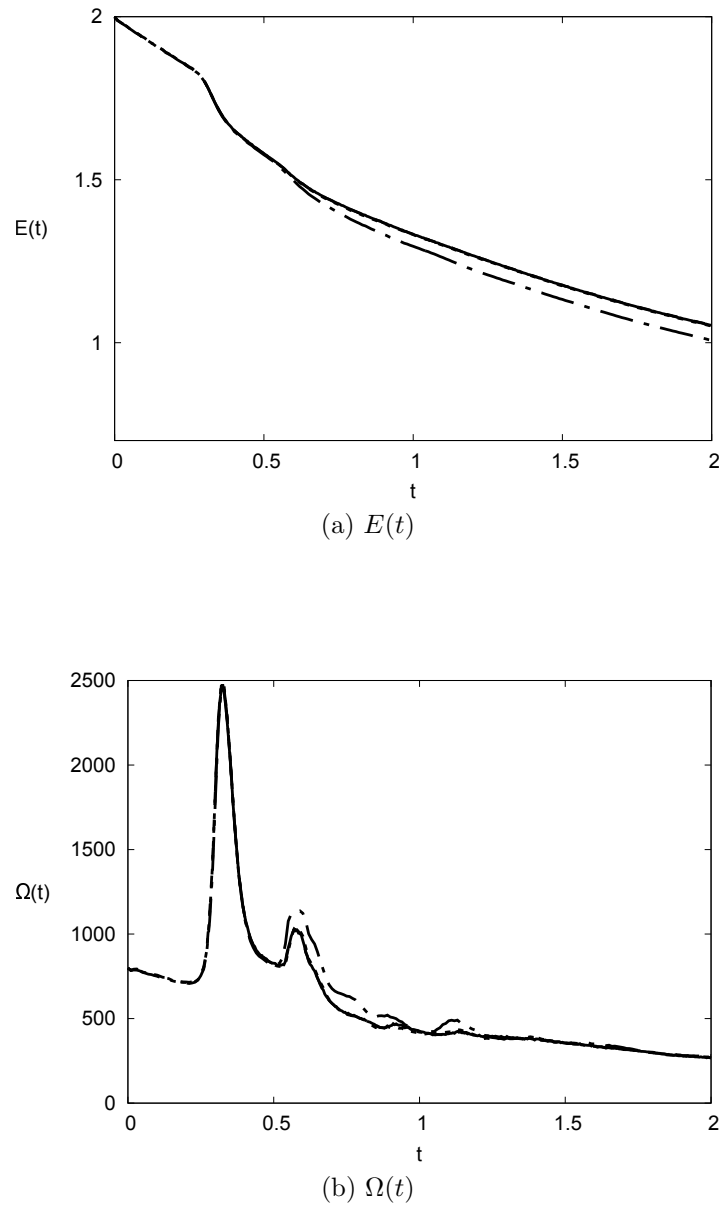
Figure 4.11: The kinetic energy and enstrophy for oblique dipole wall collision at $Re = 2500$ where $N_{lb} = 769$ (dot with dash points), $N_{lb} = 1025$ dotted, 1537 dashed and 2049 solid line.

119

(a) $E(t)$

(b) $\Omega(t)$
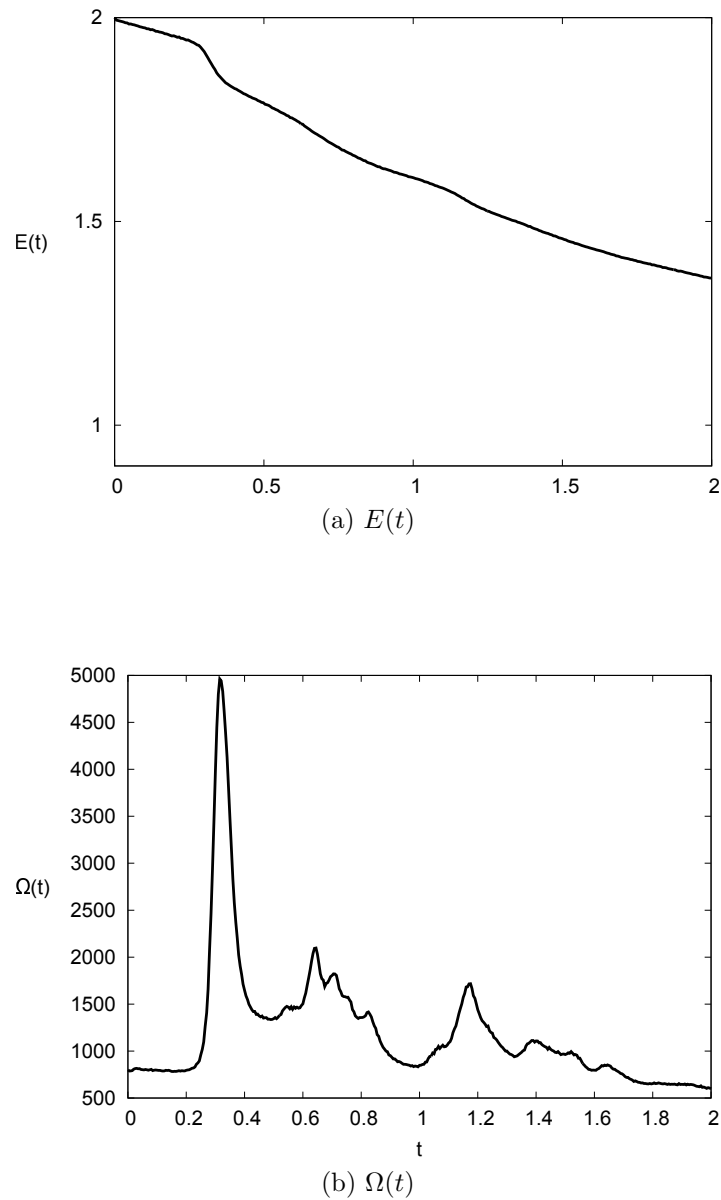
Figure 4.12: The kinetic energy and enstrophy for oblique dipole wall collision at $Re = 7500$, $N_{lb} = 4097$.

Table 4.9 shows the computed energy at various times for a range of Reynolds numbers. As was the case for the normal collision, the energy consistently decreases less quickly at higher Reynolds number than at lower ones.

Re	t	$E(t)$
625	0.3	1.423
	0.5	1.049
	2.0	0.386
1250	0.3	1.659
	0.5	1.353
	2.0	0.675
2500	0.3	1.790
	0.5	1.579
	2.0	1.053
5000	0.3	1.886
	0.5	1.729
	2.0	1.260
7500	0.3	1.916
	0.5	1.789
	2.0	1.360

Table 4.9: The kinetic energy at different times and Reynolds numbers.

The behaviour of the dipole after colliding with the wall for the oblique case is different from the behaviour of the normal case since the symmetry of the dipole will be broken after the collision, as we will see later. So in this problem we will use another important quantity to test the accuracy of the method which is the total angular momentum. The angular momentum of the flow defined with respect to the centre of the square box is:

$$L(t) = \int_{-1}^{1} \int_{-1}^{1} (xu_y(\mathbf{x}, t) - yu_x(\mathbf{x}, t)) dx dy = -\frac{1}{2} \int_{-1}^{1} \int_{-1}^{1} r^2 \omega(\mathbf{x}, t) dx dy. \qquad (4.6)$$

In [19], the angular momentum convergence was a sensitive issue. Here, we examined the convergence of the results for angular momentum at different grid resolutions. As a result, we found that the behaviour of the angular momentum matches the results in [19]. For example, Figure 4.13 shows that the results for $L(t)$ at $Re = 625$ have converged for $N_{lb} = 769$. At $Re = 2500$ convergence is achieved at $N_{lb} = 1537$. For $Re = 7500$ the results have not converged for $N_{lb} = 3073$. Overall, from these figures the angular momentum increases with time also the rate of change of $L(t)$ increases with the Reynolds number. Moreover, the frequencies of the oscillations in the results

become higher with higher Reynolds numbers. This results from the generation of numerous small and high value vortices from the boundary layer.
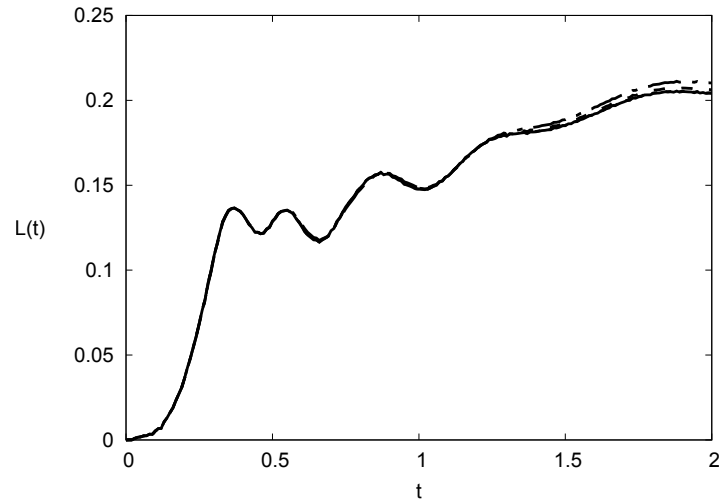
(a) $Re = 625$: $N_{lb} = 513$ (dot with dash points), $N_{lb} = 769$ (dashed), $N_{lb} = 1537$ (dotted) and $N_{lb} = 2049$ (line)
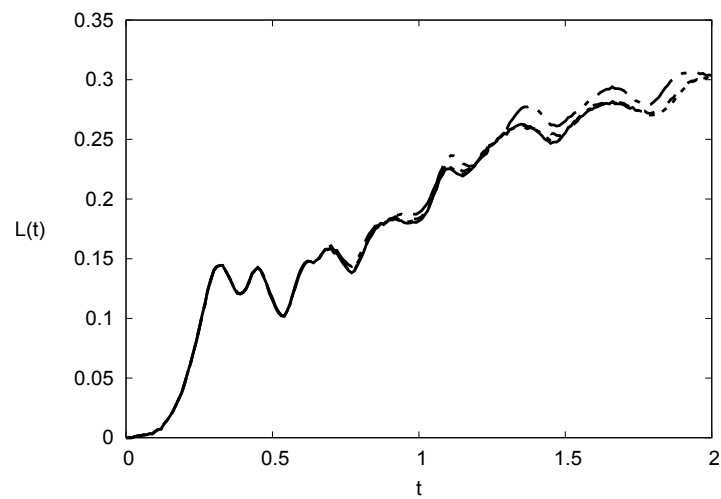
(b) $Re = 2500$: $N_{lb} = 1025$ (dot with dash points), $N_{lb} = 1537$ (dashed) $N_{lb} = 2049$ (dotted) and $N_{lb} = 3073$ (line)
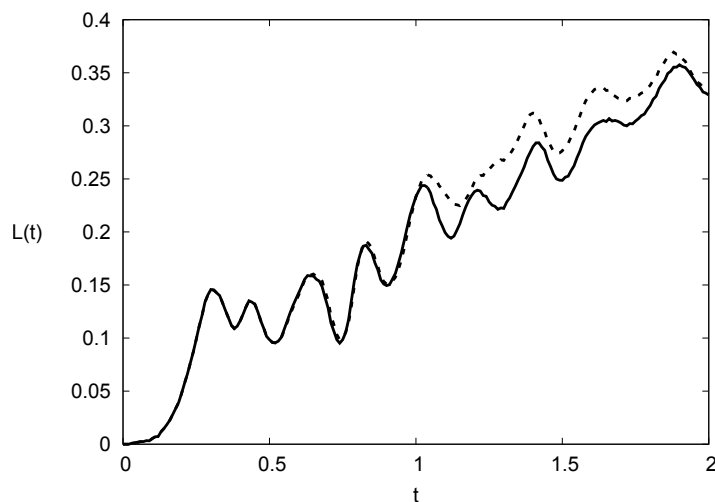
(c) $Re = 7500$: $N_{lb} = 3073$ (dashed) and $N_{lb} = 4097$ (line)

Figure 4.13: The total angular momentum for oblique dipole wall collision at different Reynolds numbers.

Table 4.10 shows the enstrophy $\Omega(t)$ at the first and second dipole collision with the east wall at $x = 1$. We compare our results with data obtained from the finite difference method and the pseudospectral Chebyshev method reported in [19] for different Reynolds numbers. Here we have used the same number of grid points as the finite difference method. The results are in very good agreement with those presented in [19] where the LBM results are closer to the SM than the FDM.

Re	$t_{1(\text{LBM})}$	Ω_1 (LBM)	$t_{1(\text{FDM})}$	Ω_1(FDM)	t_1 (SM)	Ω_1 (SM)	t_2 (LBM)	Ω_2 (LBM)	t_2 (FDM)	Ω_2 (FDM)	t_2(SM)	Ω_2 (SM)
625	0.362	778.3	0.360	766.6	0.359	768.0	0.645	306.2	0.643	304.5	0.6435	304.5
1250	0.333	1485	0.335	1473	0.335	1478	0.582	692.9	0.581	689.4	0.5819	688.8
2500	0.324	2455	0.323	2435	0.323	2447	0.569	1029	0.569	1024	0.5692	1024
5000	0.318	3813	0.317	3769	0.317	3825	0.591	1679	0.591	1707	0.5936	1683
7500	0.320	4966	-	-	-	-	0.65	2008	-	-	-	-

Table 4.10: First and second maximum enstrophy of oblique wall dipole collision using moment method with TRT-LBM. The results are compared with FDM and SM of [19].

Similar to the normal case we applied the half-way bounce-back with TRT-LBM for the purpose of comparison with moment-based conditions. These results are given in Table 4.11 where we once again see that the moment-based approach predicts results in better agreement with spectral simulations than bounce-back.

Re	t_1(BB)	Ω_1 (BB)	t_1(FDM)	Ω_1(FDM)	t_1 (SM)	Ω_1 (SM)	t_2(BB)	Ω_2 (BB)	t_2(FDM)	Ω_2 (FDM)	t_2(SM)	Ω_2 (SM)
625	0.364	722.8	0.360	766.6	0.395	768.0	0.647	295.6	0.6435	304.5	0.6435	304.5
1250	0.333	1385	0.335	1473	0.335	1478	0.583	664.5	0.581	689.4	0.5819	688.8
2500	0.325	2253	0.323	2435	0.323	2447	0.570	979.5	0.569	1024	0.5692	1024
5000	0.319	3480	0.317	3769	0.317	3825	0.591	1628	0.591	1707	0.5936	1683

Table 4.11: First and second maximum enstrophy of Oblique wall dipole collision using bounce-back with TRT-LBM. The results are compared with FDM and SM of [19].

The vorticity ω at the boundary $x = 1$ and $-0.5 \leq y \leq 1$ is plotted in Figure 4.14. In this figure we show the behaviour of the vorticity at different times, including after the first and second collision with the right wall. The data are obtained for $Re = 625, 1250,\ 2500$ and 7500 at time $t = 0.4, 0.6$ and 1. To make a comparison between our results and [19] we used the same resolutions as the finite difference method in that reference. From Figure 4.14 we note, as from [19], that the behaviour of the vorticity at the boundary in the oblique dipole wall collision is more complex than the normal collision case. Similar to the normal case, at $Re = 625$ the maximum vorticity at the wall is highest at t=0.4 whilst at higher Reynolds numbers it is greatest at $t = 0.6$. Also, in each case the highest maximum vorticity is roughly equal in magnitude to the lowest minimum vorticity, as would be the case for the normal collision. Furthermore, additional local maxima appear at later times for higher Re, probably associated with more complex flow patterns due to enhanced vortex creation .
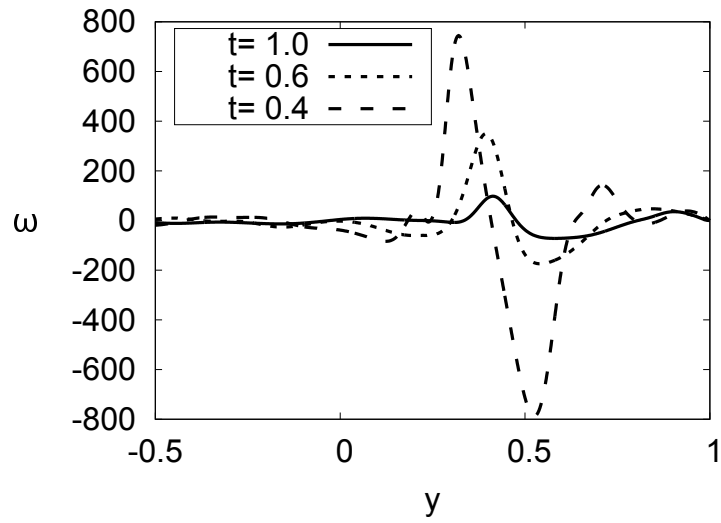
(a) *Re= 625*
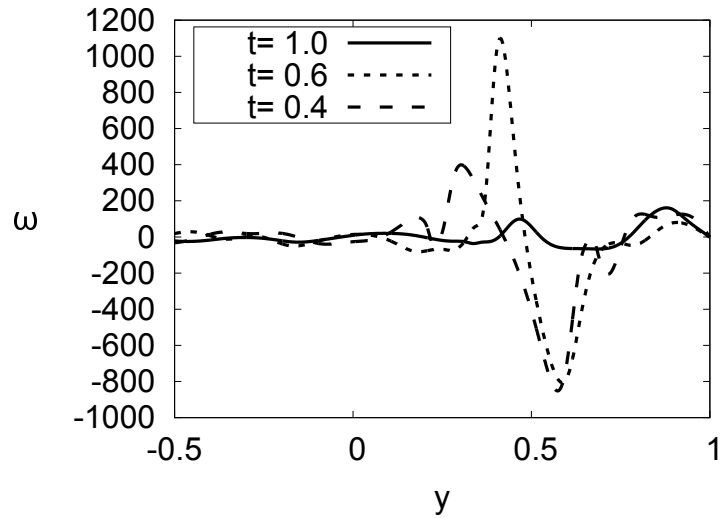
(b) *Re= 1250*
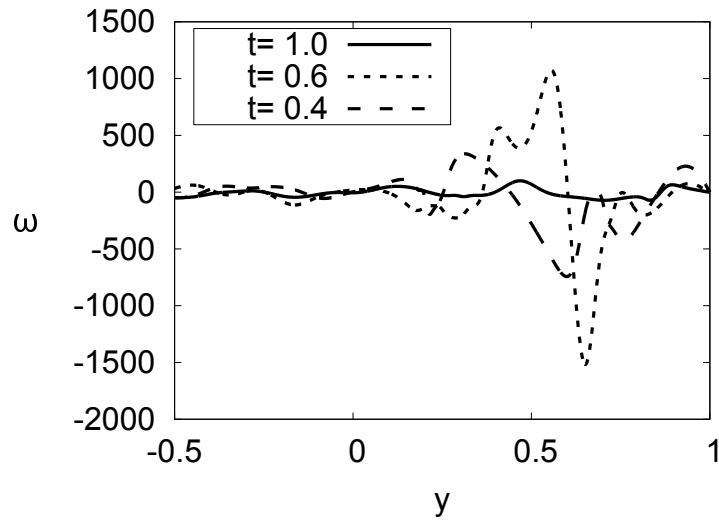
(c) $Re= 2500$
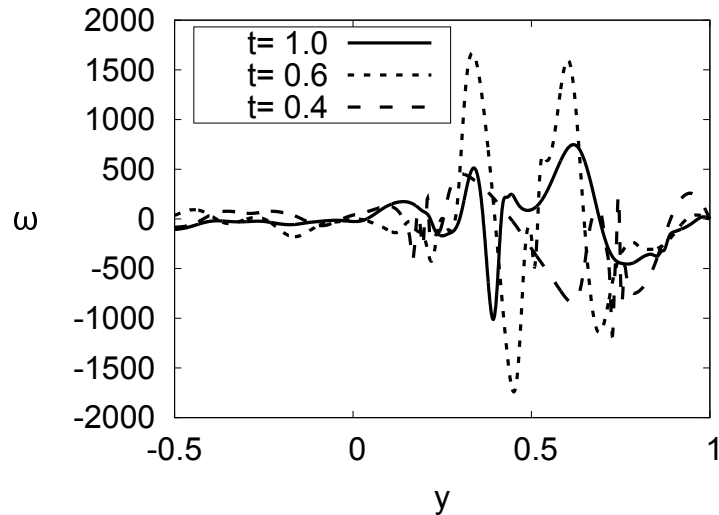
(d) $Re= 7500$

Figure 4.14: The vorticity at the boundary $x = 1$ at time $t = 1$, $t = 0.4$ and $t = 0.6$ at different Reynolds number: (a) N_{lb}=1537, (b) N_{lb}=2049,(c) N_{lb}=3073, (d) N_{lb}=3073 .

After $t = 0.45$ small third vortices start to form from the thin filament sheet that is induced at the boundary for $Re= 5000$ and 7500. Then as time progresses a fourth vortex appears at the positive monopole, Figure 4.15(a, c, e). After $t = 0.6$ the top two vortices unite with others near the top corner and merge with the primary vortex, see Figure 4.15(b, d, f). At smaller Reynolds numbers these vortices are not present at the positive side of the sheet but we can see them clearly on the negative side. We should mention that these small vortices have similar maximum amplitude to the primary dipole.
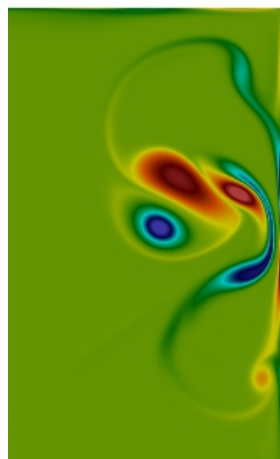
(a) $t = 0.55$
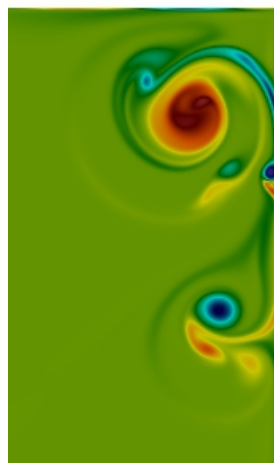
(b) $t = 0.7$

$Re= 2500$

(c) $t = 0.55$

(d) $t = 0.7$

$Re= 5000$

(e) $t = 0.55$ (f) $t = 0.7$
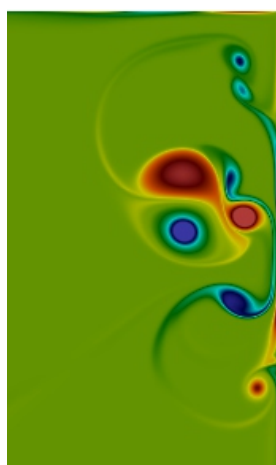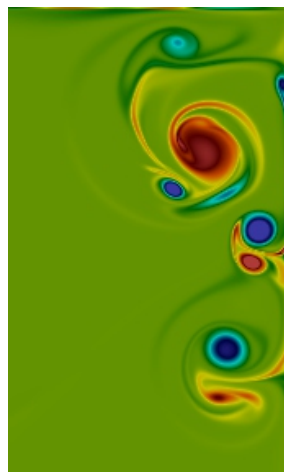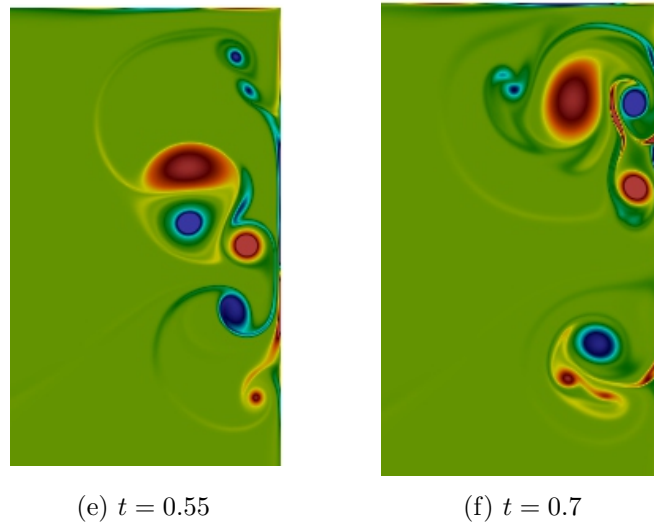
$\boxed{Re= 7500}$

Figure 4.15: Vorticity snapshots of oblique dipole wall collision at $t = 0.55$ and $t = 0.7$ inserted in the first then second row respectively. The subdomain is shown: $0.4 \leq x \leq 1, 0 \leq y \leq 1$.

To better understand the behaviour of the dipole at the boundary after the second collision, in Figure 4.16 we plot vorticity contours for different Reynolds numbers. In this case the most interesting behaviour of the vorticity is at the top-right corner where the dipoles interact with each other after the second collision. In these figures the computations are shown in the domain $0.3 \leq x \leq 1$ and $0 \leq y \leq 1$ at $t = 1$. Here, as the Reynolds number is increased, the vortex collisions near the corner become more energetic creating further vortices. Additional vortices are also created by interactions with the top wall, leading to extremely complex flow patterns.

(a) $Re= 625$ (b) $Re= 1250$ (c) $Re= 2500$

(d) $Re= 5000$ (e) $Re= 7500$
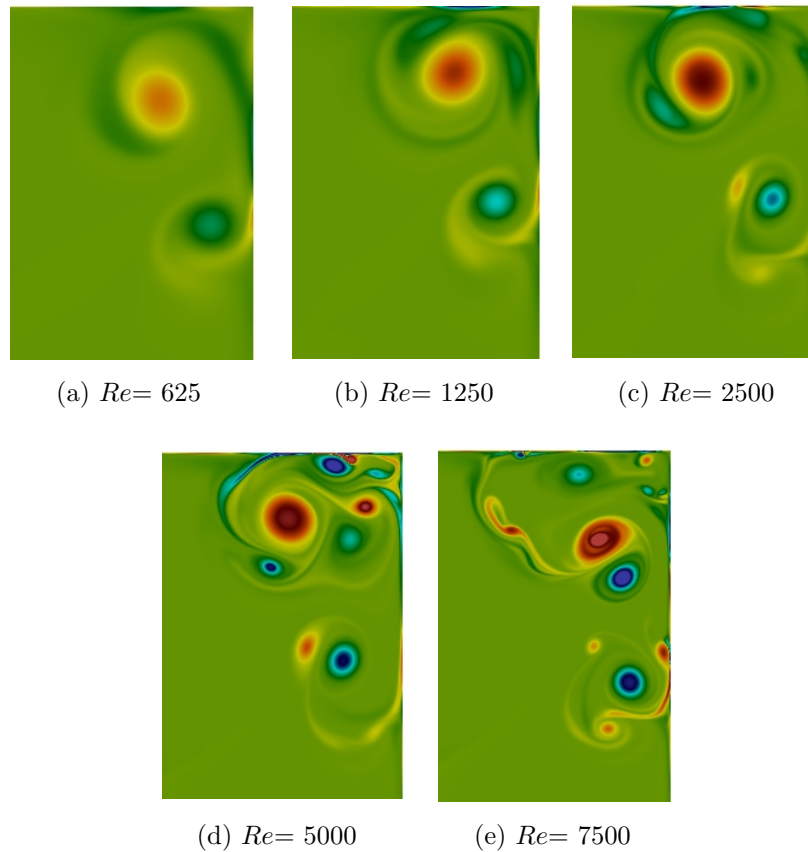
Figure 4.16: Vorticity contours of oblique dipole wall collision at $t = 1$. The vorticity is shown in the domain $0.3 \leq x \leq 1$ and $0 \leq y \leq 1$.

In Tables 4.12 and 4.13 we pick out the maximum and minimum vorticity and the location of these extrema. These data are shown for various Reynolds numbers at different times. We can see in general that the strength of the maximum vortices at each Reynolds number gradually decreases between $t = 0.6$ and $t = 1.8$. However, for $Re = 7500$ small but intense vortices are formed near the top-right corner as the dipole interacts with the corner. These small vortices have a significant impact on the results, causing fluctuations in the maximum vorticity until $t = 1.4$.

Re	t	(x,y)	ω_{max}	$(x,y)_{(FD)}$	$(x,y)_{(SM)}$	$\omega_{max(FD)}$	$\omega_{max(SM)}$
		Current work		Clercx and Bruneau			
625	0.6	(0.740,0.658)	161.9	(0.740,0.659)	(0.740,0.659)	161.40	161.5
	1.2	(0.713,0.770)	94.09	(0.711,0.771)	(0.712,0.772)	93.74	93.80
	1.8	(0.592,0.717)	63.06	(0.591,0.716)	(0.592,0.717)	63.00	63.00
1250	0.6	(0.800,0.606)	220.8	(0.807,0.607)	(0.807,0.607)	220.0	220.0
	1.2	(0.691,0.777)	157.5	(0.691,0.779)	(0.691,0.779)	157.0	157.0
	1.8	(0.553,0.754)	119.9	(0.551,0.754)	(0.550,0.753)	119.6	119.7
2500	0.6	(0.813,0.625)	344.4	(0.900,0.690)	(0.899,0.689)	258.7	258.7
	1.2	(0.613,0.788)	216.7	(0.609,0.789)	(0.608,0.788)	216.6	217.0
	1.8	(0.578,0.685)	192.1	(0.555,0.694)	(0.560,0.691)	191.2	191.6
5000	0.6	(0.789,0.666)	285.4	(0.794,0.680)	(0.797,0.684)	288.0	288.0
	1.2	(0.570,0.732)	261.4	(0.643,0.710)	(0.612,0.712)	264	264
	1.8	(0.618,0.743)	240.6	-	-	-	-
7500	0.6	(0.840,0.704)	293.1	-	-	-	-
	1.2	(0.695,0.856)	493.7	-	-	-	-
	1.8	(0.496,0.757)	359.6	-	-	-	-

Table 4.12: The maximum vorticity ω_{max} at positive vortex in a oblique wall-dipole collision and its location at $t = 0.6, 1.2, 1.8$.

Re	t	(x,y)	ω_{min}	$(x,y)_{(FD)}$	$(x,y)_{(SM)}$	$\omega_{min(FD)}$	$\omega_{min(SM)}$
		current work		Clercx and Bruneau			
625	0.6	(0.897,0.361)	-152.9	(0.898,0.365)	(0.898,0.364)	-151.8	-151.9
	1.2	(0.871,0.434)	-60.33	(0.872,0.435)	(0.872,0.436)	-59.9	-59.9
	1.8	(0.886,0.680)	-29.37	(0.888,0.685)	(0.887,0.685)	-29.2	-29.1
1250	0.6	(0.928,0.383)	-213.4	(0.928,0.381)	(0.928,0.381)	-212.5	-212.7
	1.2	(0.877,0.513)	-108.6	(0.877,0.514)	(0.877,0.513)	-108.3	-108.3
	1.8	(0.811,0.872)	-63.15	(0.811,0.867)	(0.812,0.865)	-63.16	-63.16
2500	0.6	(0.912,0.553)	-341.4	(0.923,0.368)	(0.923,0.368)	-248.2	-248.3
	1.2	(0.906,0.488)	-154.3	(0.906,0.484)	(0.907,0.492)	-155.1	-154.9
	1.8	(0.844,0.763)	-102.9	(0.841,0.746)	(0.841,0.738)	-104.0	-103.7
5000	0.6	(0.893,0.320)	-277.9	(0.892,0.320)	(0.894,0.319)	-278.0	-278.0
	1.2	(0.527,0.599)	-340.0	(0.909,0.470)	-	-224.0	-
	1.8	(0.733,0.812)	-204.1	-	-	-	-
7500	0.6	(0.899,0.588)	-596.8	-	-	-	-
	1.2	(0.850,0.333)	-263.3	-	-	-	-
	1.8	(0.410,0.602)	-232.0	-	-	-	-

Table 4.13: The minimum vorticity ω_{min} at negative vortex in a oblique wall-dipole collision and its location at $t = 0.6, 1.2, 1.8$.

To test the convergence of the oblique dipole wall collision, we calculate the L2-error for the vorticity and the energy at two times. The relative error when $Re = 625$ is

computed with respect to the results with the finest resolution, in our case is $N_{lb} = 3073$. The L2- error is defined as

$$error = \sqrt{\frac{\sum_{i,j} \left(\omega_{ij}\left(N_{lb}\right) - \omega_{ij}\left(N_{lbmax}\right) \right)^2}{\sum_{i,j} \left(\omega_{ij}\left(N_{lbmax}\right) \right)^2}}. \tag{4.7}$$

Since the behaviour of the dipole changes with time, we calculated the error at different times. In Figure 4.17 we plot the errors of $E(t)$ and ω at $t = 0.3$ and $t = 0.5$ for different resolutions. Second-order convergence is shown for TRT-LBM as expected.
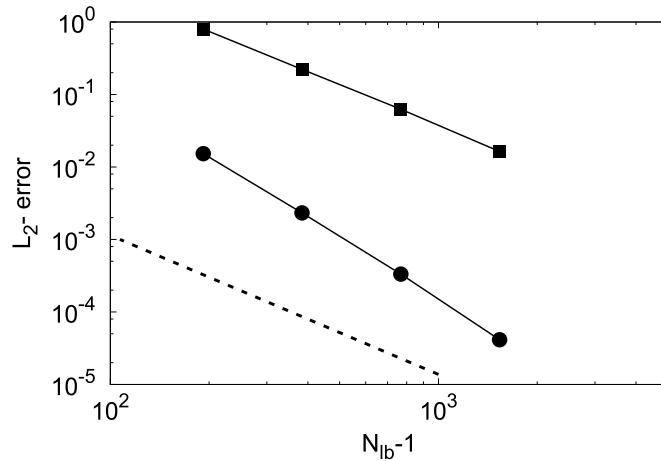
(a) $t = 0.3$
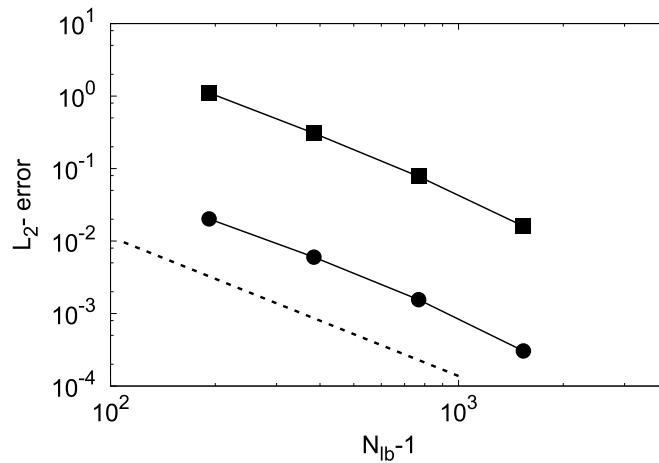
(b) $t = 0.5$

Figure 4.17: The L_2- error for the oblique dipole wall collision for the vorticity (fill square) and the total kinetic energy (fill circle). The error for $Re=625$ at $t=0.3$ (top) and $t=0.5$ (bottom). The line of slope 2 (dashed) is also shown.

4.1.2.2   Oblique dipole wall collision- 45°

Numerous authors have discussed the flow when the dipole collides normally with the wall and at an oblique angle of 30°. In this thesis, and unlike most other works, collisions at an angles of incidence of 45° are also considered. At this angle the dipole moves towards the upper-right corner which causes a distinct phenomenon.

In this case, the dipole releases initially towards the top-right angle at the position (-0.0707,0.0707),(0.0707, -0.0707). First the behaviour of the dipole when it collides with the no-slip wall for $Re = 2500$ is explained. In general, the primary dipole reaches the corner and collides with it around $t = 0.4$ which induces a secondary dipole from the intersecting walls. Thus, two arc vortices surrounding the primary dipole produce a new pair of dipoles which move after the secondary one. This process repeats itself and a new 'rolling-mill ' creates a succession of dipoles. The new pairs of monopoles reflect from the corner and then move towards the bottom-left corner where they collide with the walls to generate a filament sheet of vortices from the boundary layer. Finally, the emanation of the monopoles stops by the dissipation of the primary dipole at the top-right corner. During this process the pairs of additional dipoles lose their strength during their travels. Figure 4.18 shows a sequence of dipoles generated from the initial dipole for $Re = 2500$.

(a) $t = 0.4$

(b) $t = 0.56$

(c) $t = 0.66$

(d) $t = 0.8$

(e) $t = 1.4$

(f) $t = 1.8$
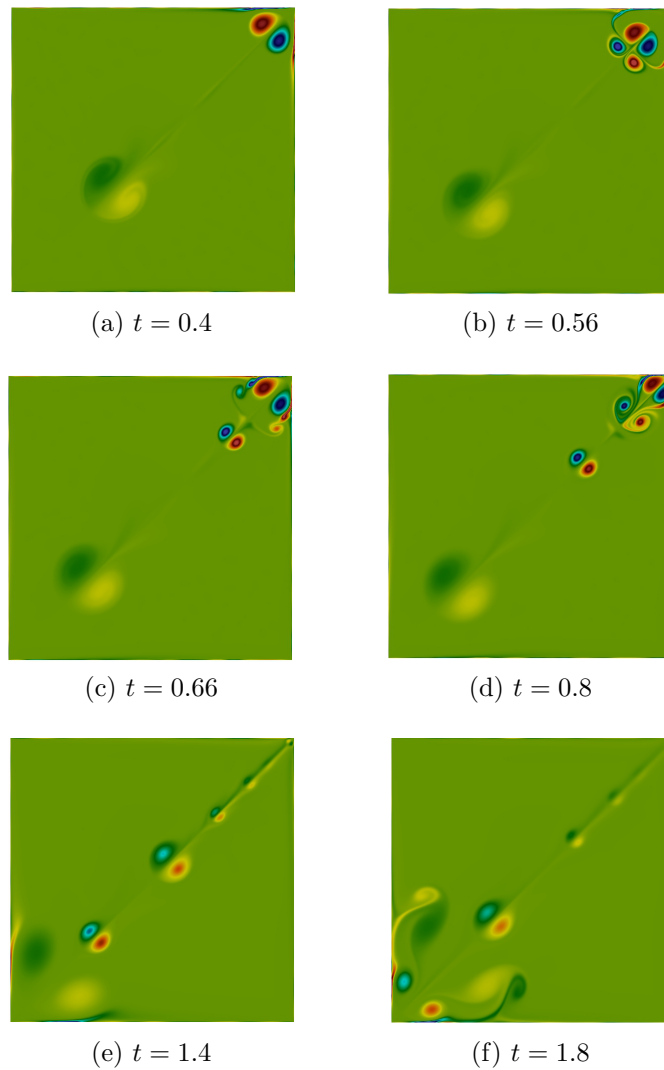
Figure 4.18: Vorticity contours of dipole collision with the no slip wall at an angle of $45°$ for $Re = 2500$.

The general behaviour of the dipole collision with no-slip wall at an angle of $45°$ for other Reynolds numbers is similar to $Re = 2500$ case. The primary dipole loses its strength over time while the secondary dipoles are bounced towards the opposite corner. However, for Reynolds numbers higher than 2500, the secondary dipole is more active on the bottom-left corner which induces small and high magnitude monopoles. The higher the Reynolds numbers, the more frequent is the creation of the dipoles and vortex sheets at this corner. Figure 4.19 compares the generation of the additional dipoles at the bottom-left corner for various Reynolds numbers at $t = 2$.

(a) $Re = 2500$ (b) $Re = 5000$

(c) $Re = 7500$ (d) $Re = 10000$
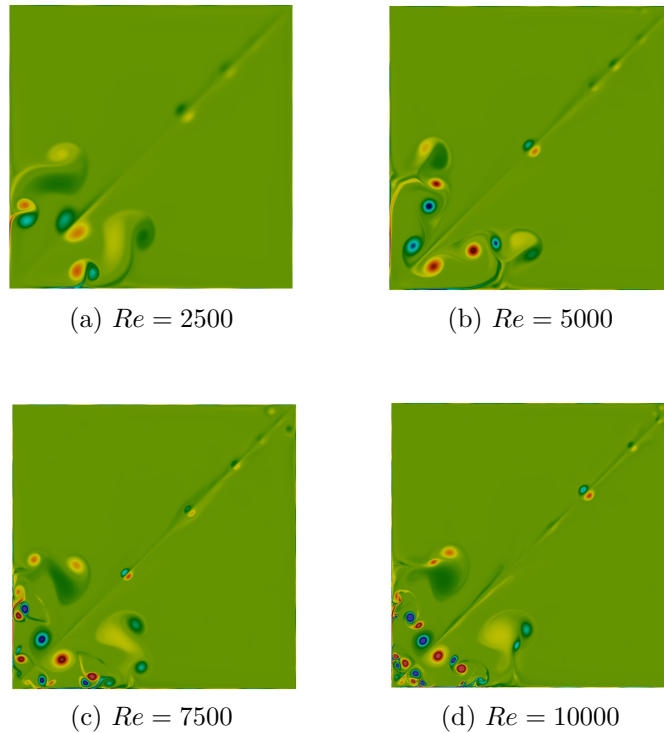
Figure 4.19: Vorticity contours of dipole collision with the no slip wall at an angle of $45°$ at $t = 2$ for various Reynolds numbers.

4.2 Conclusion

In this work we performed a detailed numerical study of complicated flows with no-slip boundaries using moment-based boundary conditions and the TRT-lattice Boltzmann method. We studied the physics of the dipole when it hit the no slip wall at different Reynolds numbers. For normal and oblique wall collisions, the convergence of the total enstrophy and energy were investigated and the convergence of the total angular momentum was also tested for the oblique case at an angle of $30°$. For the Normal dipole wall collision, the angular momentum is zero and that proved the accuracy of our simulation.

At the beginning of this flow, the primary monopoles are released from the two semi circular vortices which propelled towards the right wall. The surrounding shields moved in the opposite direction to create a weaker dipole that hits the left wall to create additional weak vortices. The interaction of the primary dipole with the no-slip right wall created and induced a secondary dipole which interacted with vortices

on the boundary. After the first collision with the wall the symmetry between the two monopoles remained in the normal and diagonal release with an angle of 45°, while it was broken in the oblique collision at 30°. For the three cases, the energy dissipation rate decreased when the Reynolds number increased. As the Reynolds number increased, the ratio between the first and second maxima of the enstrophy increased. The behaviour of the dipole at an incident of 45° shed light on new physics of 'rolling-mill ' phenomenon where the pair of monopoles disappeared during time.

To increase our understanding of dipole wall collisions further we investigated the behaviour of the vortices at the boundary at different times. In the normal case, small and high intensity vortices were created at the wall and merged with the primary vortex for higher Reynolds numbers. For the oblique 30° collision, third and fourth small monopoles were created from the boundary layer wall and become more obvious for higher Reynolds number. Moreover, for both cases we showed the behaviour of the vortices at $x = 1$ for different times and Reynolds numbers and we found that the $\omega(t)$ for Reynolds higher than 625 increased further after the second dipole wall collision. Moreover, the maximum vorticity decreased with respect to time in all cases except for very large Reynolds number which found variations in the results for the oblique case. For the oblique case of 45° collision, by increasing the Reynolds number the additional small and high value monopoles increased and concentrated on the bottom left corner.

The method presented here has been shown to compute solutions that are in very good agreement with benchmark data, including results obtained from spectral method simulations. Also by studying other boundary conditions with this flow, like bounce-back scheme, we proved that the moment-based conditions is a competitive method with other boundary conditions. Releasing the dipole towards the corners which gave a successful simulation increased the confidence that the moment method seems to work well for corners. The LBM with moment based boundary conditions demonstrated second-order accuracy as expected and in agreement with theory, as verified by our convergence studies, and the model discussed here successfully predicted the complex flow in the vicinity of the corners. This increases our confidence in the application

of the LBM with moment-based boundary conditions to flows in confined but regular geometries.

Chapter 5

Dipole wall collision with Navier slip boundary condition

In the last few years, in oceanography and engineering applications, the problem of a vortex rebounding from a slip surface has attracted some attention [61, 110]. Early research on the effect of the free-slip wall on a vortex rebounding from a boundary was conducted by Barker *et al.* [3] and Saffman [98]. In turbulent flows, like in a hurricane and large eddy that rebounds from the ocean, the vortices slip at the boundary, so no-slip conditions are not valid at this kind of flow [39]. This phenomenon is also important in the field of aeroacoustics [76, 26, 57]. For example, the type of the surface, slip or free-slip walls, and the angle of incidence determine the nature of the sound pressure radiated; which could be quadrupolar, octupole or dipole formula [85].

The generation of a sequence of vortices by dipoles colliding with the walls depends on the boundary type. At no-slip walls, numerous additional dipoles are induced after first wall collision, as seen in Chapter 4 . However, in inviscid or slip boundaries, the dynamics of the dipole that rebound from the wall are different. When the Navier-slip condition is applied, the slip length controls the number of vortices that are produced in the boundary layer. At stress-free boundaries there is no generation of vortices at the wall. Carnevale *et al.* [12] carried out numerical and laboratory experiments on dipole collision with no-slip and free-slip walls on flows near the coast. At stress-

free walls, the dipole moves to the edge of the domain without any rebounds from the wall. Sutherland *et al.* [105] used a volume penalisation method to describe the behaviour of the dipole interacting with a slip wall at fixed slip lengths for $Re = 1252$. Compared with the no-slip case, it was shown that when the dipole hits the slip wall, the space between the two monopoles is wider and the number of collisions with the wall is reduced. Sutherland extended the work to demonstrate a collision with an oblique collision in his thesis [104]. The study was expanded to simulate the dipole wall collision in a circular domain.

This chapter follows Sutherland [104] to study the behaviour of the dipole wall collision by using the LBM, then extends the study to include the collision at higher Reynolds numbers. Here, we generalise a dipole incidence with the no-slip walls to include Navier-Maxwell slip condition with moment-based boundary conditions from Section 3.7.1. The Navier slip boundary condition will be applied with increasing slip length until the free-slip boundary is reached. The Two Relaxation Time (TRT) model for the lattice Boltzmann equation is used to simulate the dipole collision with a slip boundary.

First, the normal dipole collision with the slip boundary for moderate and high Reynolds numbers is investigated. The investigation discusses some interesting physics of the flow after the first wall collision. The results of the total kinetic energy and the total enstrophy are normalised in this chapter for the purpose of comparison with [104]. This is followed by studying the effect of the slip length on dipoles which approach from the wall at angles of 30° and 45°. Results are presented here based on the convergence study from the previous chapter, however at big slip lengths and $Re \geq 5000$ the simulations needed less refined grids to converge compared with no-slip, because in this case the velocity gradient is smaller for the slip condition and the simulation does not need highly grid points.

5.1 Normal dipole slip collision

A normal dipole wall collision with slip boundary conditions was implemented. The slip length will be constant in value and independent of Reynolds numbers. The Reynolds numbers are taken between $625 \leq Re \leq 16000$ in the simulations of slip length of at least 0.2. For slip lengths smaller than 0.2 the Reynolds numbers will be taken up to 10000. This is because as the slip length approaches zero, higher grid resolutions are needed for convergence. For $Re > 10000$ and according to the estimation of the boundary layer thickness, more than 4097×4097 grid points are required to gain successful simulation.

5.1.1 Dipole wall collision for various slip lengths

In the case of slip boundaries, the number of the dipole rebounds from the boundary decreases and fewer vortices are generated from the boundary, compared with the no-slip case considered in Chapter 4. The dynamics of the collision with a slip wall is less complicated than the collision with a no-slip boundary, as we will be seen in this chapter. To illustrate the behaviour of the dipole interaction with a slip boundary, the development of vorticity production at the wall for small and large slip lengths for $Re = 2500$ will be discussed. At slip length $\zeta = 0.002$ a dipole collides with the slip wall and is forced to rebound by the impact of the secondary core of vortices similar to the no-slip case. After $t = 0.5$ the secondary monopoles join together at the centre of the wall and create a secondary dipole that sticks to and rotates at the wall, this shown in Figure 5.1 (b). This behaviour differs from the no-slip case where the secondary dipole has the strength to travel further from the wall, see Figure 4.1. A vorticity filament that separates from the boundary layer surrounds the secondary monopoles at around $t = 0.7$. The dipole continues to rotate at the wall until $t = 1.8$; then the primary dipole starts to lose strength. No additional dipoles detach from the boundary layer other than the primary and secondary ones after the second dipole wall collision at $\zeta = 0.002$. Figure 5.1 shows the behaviour of the dipole after it has collided with the

wall at slip length 0.002 and $Re = 2500$. The key for the figures is identical for all vorticity plots in this chapter.

(a) $t = 0.5$ (b) $t = 0.6$ (c) $t = 0.7$

(d) $t = 1$ (e) $t = 1.8$
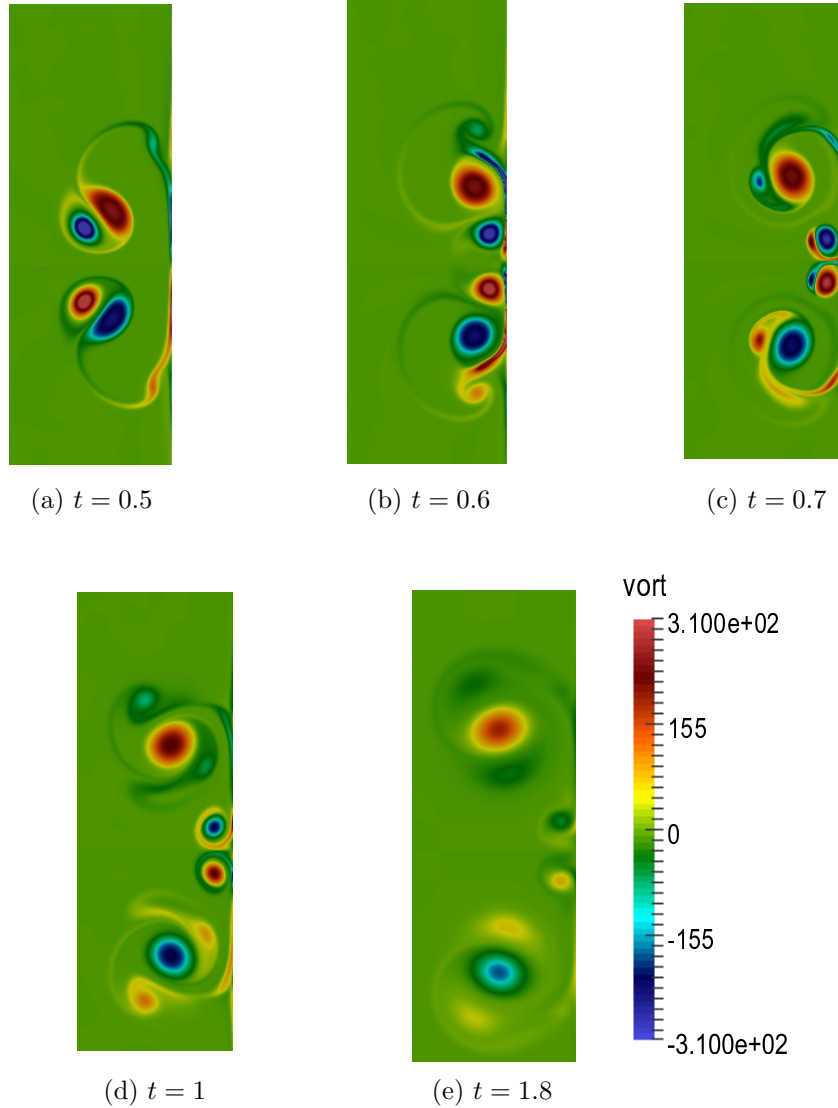
Figure 5.1: Plots of vorticity for normal wall dipole collision at $Re = 2500$ and $\zeta = 0.002$. Contours are shown in the subdomain $0.5 \leq x \leq 1$, $-0.6 \leq y \leq 0.8$ in the vicinity of the collision.

To understand the effect of the large slip length on the behaviour of the dipole, the flow with slip length $\zeta = 0.01$ is studied. Figure 5.2 shows only the top half of the domain, since the normal collision is symmetric about the horizontal centreline. Until the beginning of the second collision at $t = 0.5$, the flow features are similar to those of the collision with a wall of smaller slip length. After the second collision, the pair of dipoles split further, because of the slip effect and the secondary monopoles merge with the primary ones at around $t = 0.6$. Simultaneously, a bundle of vortices starts

to rotate above the primary dipole which is generated from the filament sheet at the boundary. After $t = 1$, these additional vortices lose their strength while the primary dipole retains its strength and continues moving at the slip wall.

(a) $t = 0.5$ (b) $t = 0.6$

(c) $t = 0.7$ (d) $t = 1$
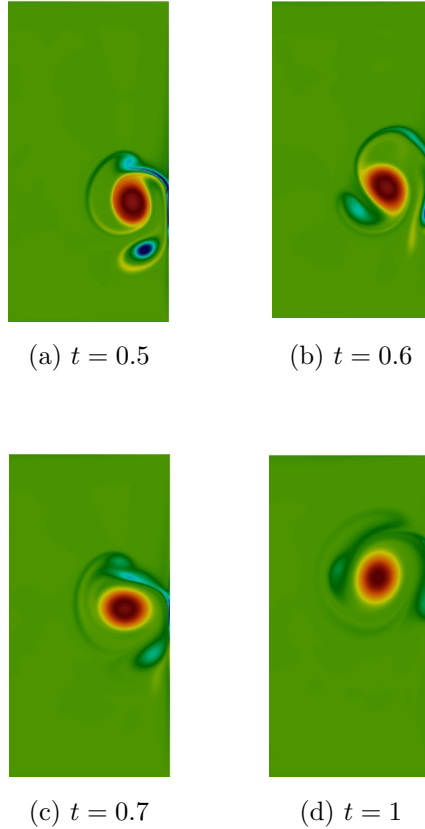
Figure 5.2: Plots of vorticity for normal wall dipole collision for $Re = 2500$ and $\zeta = 0.01$. Contours are shown in the subdomain: $0.5 \leq x \leq 1, 0 \leq y \leq 1$ in the vicinity of the collision.

Figure 5.3 displays the dissipation of total kinetic energy and the total enstrophy at different slip lengths for $Re = 2500$. In general, the plot shows an excellent agreement between the LBM results and the results of [104]. Since the number of vortex wall collisions decrease when the slip length is increased, the dissipation of the energy decreases as the slip length increases and is highest in the no-slip case. For different slip lengths, the dissipation of the energy is the same until around $t = 0.3$ where the first wall collision happens, then it starts to separate according to the slip length. Figure 5.3(b) demonstrates that the maximum enstrophy decreases with increasing slip length and the peaks are highest for the collision with no-slip wall. For the higher values of slip length, as with $\zeta \geq 0.1$, the dissipation of the energy decreases less and the enstrophy

appears as a line without any peaks, since there are no additional collisions with the wall after the first one.
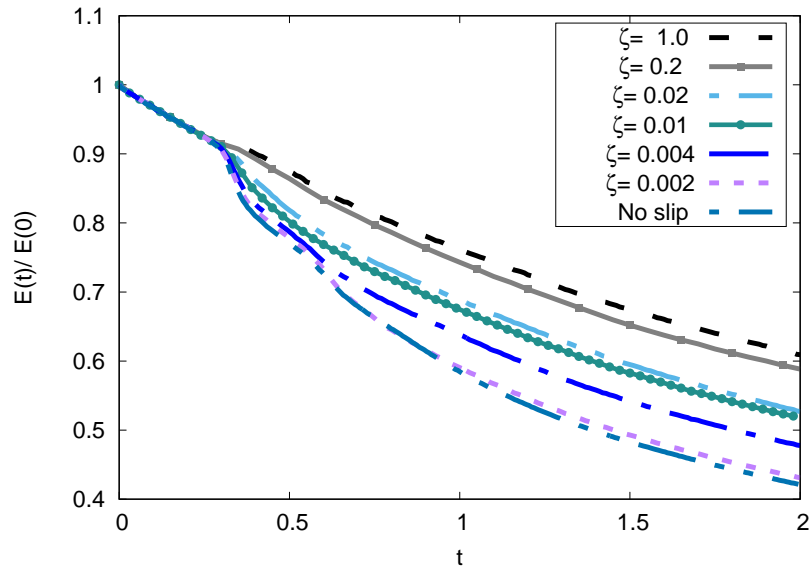
(a) Energy
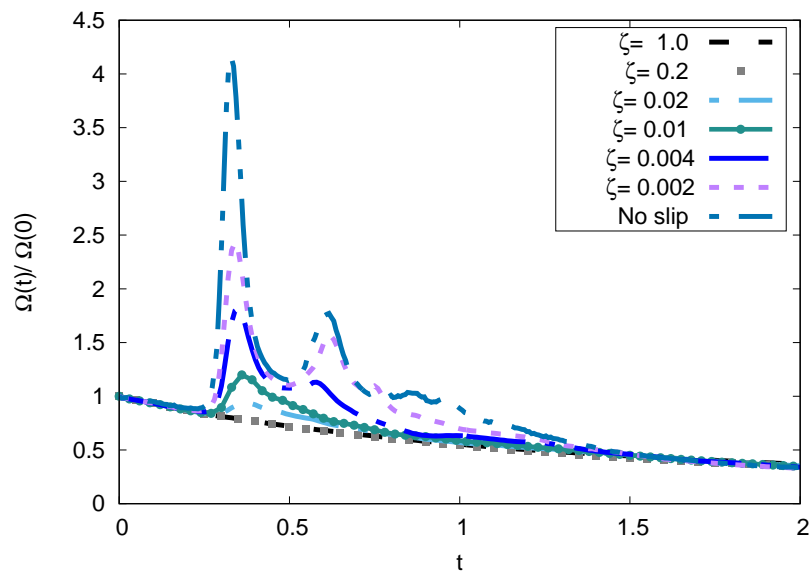
(b) Enstrophy

Figure 5.3: The kinetic energy and total enstrophy for $Re = 2500$ and different slip lengths ζ.

5.1.2 The effect of slip length and Reynolds number on the flow

In this section the roles of the slip length and the Reynolds number are investigated. Figure 5.4 gives a view of how the Reynolds number effects the generation of vortices. The results show the strength of the secondary dipole at two times for a slip length of ζ=0.002. When $Re < 2500$, the secondary monopoles meet at the centre of the wall and create one dipole without any additional monopoles appearing in the boundary layer. However, for $Re \geq 5000$ the small secondary monopoles continuously move with the primary one without losing their strength. At $t = 0.8$ a number of small high magnitude vortices appear at the filament sheet that surrounds the primary monopoles. The number of collisions increases with an increase in Reynolds number. Subsequently, the gap between the two monopoles increases with Reynolds number. The results in Figure 5.4 are given at $t = 0.8$ and $t = 1$ to show the additional vortices at the boundary for different Reynolds numbers. Similar to the collision with the no-slip wall, where Orlandi [89] described the behaviour of the secondary dipole at high Reynolds numbers for no-slip collision, the secondary dipole at the slip boundary is smaller in size and higher in magnitude than was the case for smaller Reynolds numbers. That is because at higher Reynolds numbers, the dissipation of the small secondary vortex is slower. Moreover, increasing the slip length reduces the 'rolling-mill ' effect from the previous chapter especially for high Reynolds numbers since the space between the two primary monopoles is increased. For all Reynolds numbers, there are no further vortices generating from the wall after $t = 1.2$.
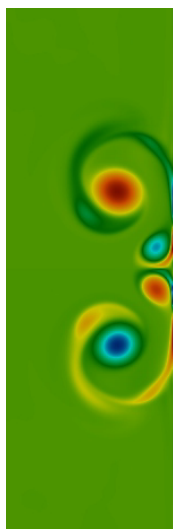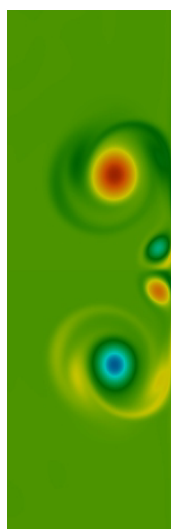
(a) $t = 0.8$ (b) $t = 1$

Re= 1252

(c) $t = 0.8$ (d) $t = 1$

Re= 5000
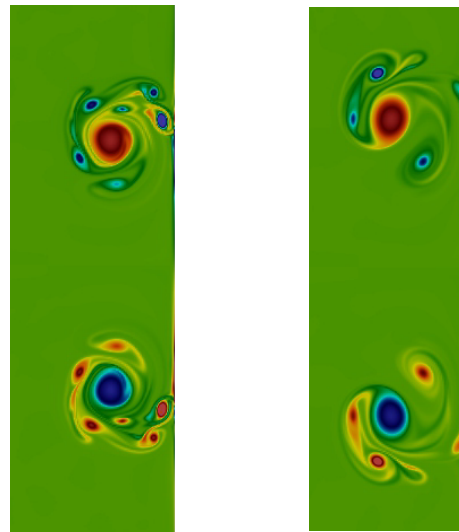
(e) $t = 0.8$ (f) $t = 1$

Re= 7500
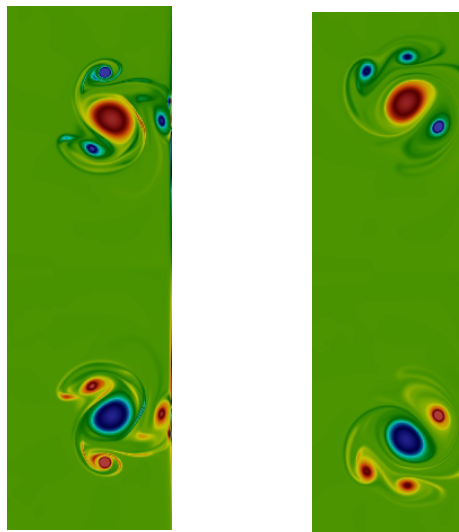
(g) $t = 0.8$ (h) $t = 1$

Re= 10000

Figure 5.4: Plots of vorticity for normal wall dipole collision at $\zeta = 0.002$ and $t = 0.8$ and 1 for various Reynolds numbers. Contours are shown in the subdomain: $0.5 \leq x \leq 1, -0.8 \leq y \leq 0.8$ in the vicinity of the collision.

To demonstrate the effect of Reynolds number on the wall with higher slip lengths, Figure 5.5 shows the influence of slip length $\zeta = 0.01$ on the formulation of vortices at the wall for various Reynolds numbers. As the Reynolds number increases, the space between the two primary monopoles increases until they reach to the top and bottom

walls for $Re \geq 5000$. The times in Figure 5.5 are chosen to show the differences in behaviour at these Reynolds numbers.

In general, for $Re < 2500$ the small secondary monopoles move towards the primary one, then lose their strength over time. At $Re \geq 5000$ the primary monopoles travel far from each other while the secondary small and high amplitude two vorticity cores move towards the center of the wall. For $Re = 7500$ and $Re = 10000$, the two small secondary monopoles that move towards the centre of the wall are wrapped by one high value vortex. For higher slip lengths and higher Reynolds numbers, the dipoles travel to the top and bottom walls.

(a) $t = 0.6$ (b) $t = 1$
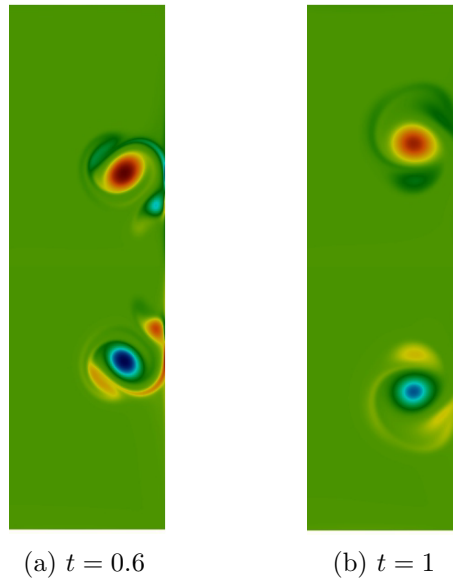
$Re = 1252$

(c) $t = 0.6$ (d) $t = 1$

$Re = 5000$

(e) $t = 0.6$ (f) $t = 1$

$Re = 7500$

(g) $t = 0.6$ (h) $t = 1$

$\boxed{Re = 10000}$
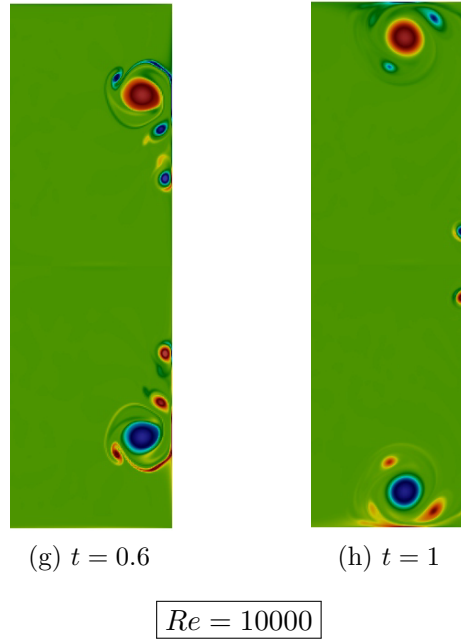
Figure 5.5: Plots of vorticity for normal wall dipole collision at $\zeta = 0.01$ and $t = 0.6, 1$ for various Reynolds numbers. Contours are shown in the subdomain: $0.4 \leq x \leq 1, -1 \leq y \leq 1$ in the vicinity of the collision.

For different slip lengths and similar to the no-slip case, when the Reynolds number was increased, the dissipation of the energy decreased, see Figures 5.3(a) and 5.6(a). The results in Table 5.1 show the impact of the slip and no-slip cases on the dissipation of the kinetic energy for various Reynolds numbers at $t = 2$. The two maximum peaks of the enstrophy increase with higher Reynolds numbers. Also for slip lengths $\zeta > 0$, the enstrophy descends to the same point after $t = 1.2$ for $Re \leq 2500$ and after $t = 1.5$ at higher Reynolds numbers. This change coincides with the lack of vorticity formation at the boundary at this period of time, except for the no-slip conditions where the boundary layer is active and continuously induces more vortices. Moreover, the decay of the enstrophy in the interval $t \in [1.2, 2]$ is faster with larger Reynolds numbers, see Figures 5.3(b) and 5.6(b). In Table 5.2 non-normalized results of the first and second maximum enstrophy are shown for various Reynolds numbers at no-slip and different slip length walls. Except for $\zeta = 0.01$, one peak has appeared as shown in Figure 5.5.
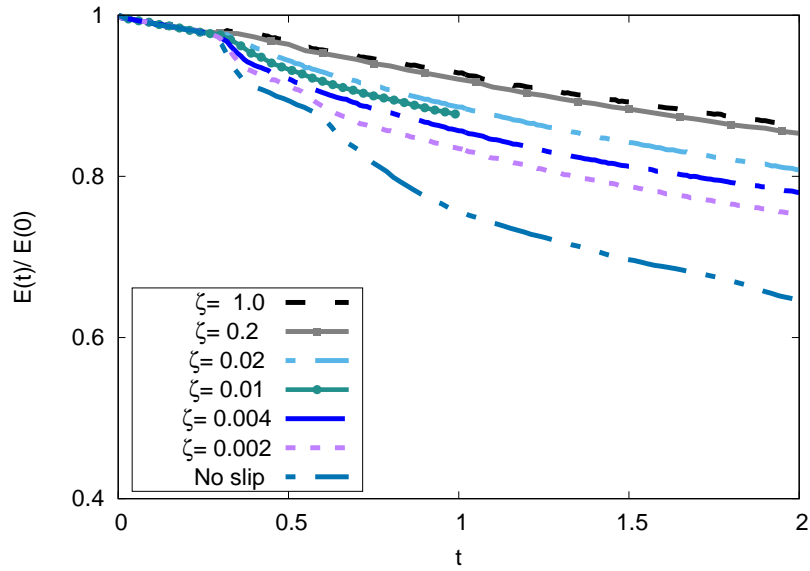
(a) Energy
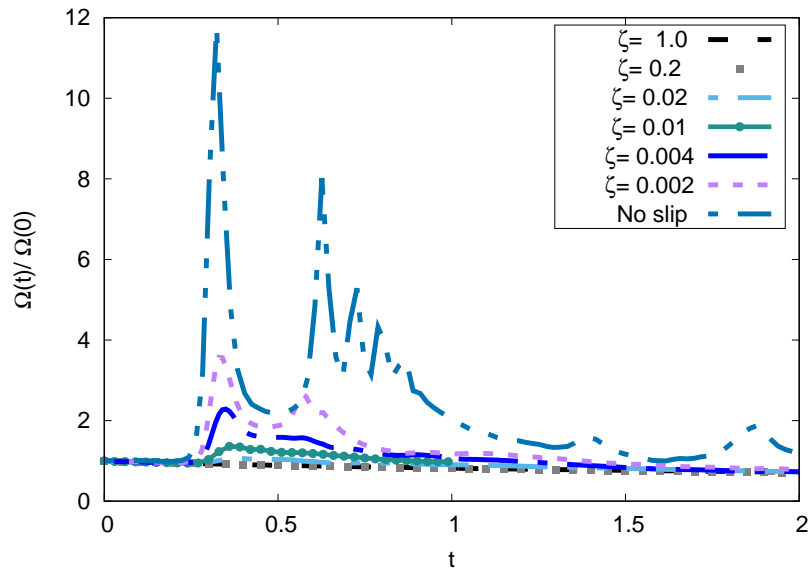
(b) Enstrophy

Figure 5.6: The normalized kinetic energy and total enstrophy for normal wall dipole collision at $Re = 10000$

ζ	$Re = 1252$	$Re = 2500$	$Re = 5000$	$Re = 7500$	$Re = 10000$
0.02	0.344	0.562	0.742	0.76	0.808
0.01	0.333	0.517	0.678	0.753	0.875
0.002	0.272	0.430	0.620	0.699	0.739
0	0.606	0.419	0.554	0.642	0.645

Table 5.1: The kinetic energy at $t = 2$, $E(2)/E(0)$, for normal dipole wall collision for different Reynolds numbers and slip lengths.

Re	ζ	t_1	$\Omega(t_1)$	t_2	$\Omega(t_2)$
	0.01	0.36	952.1	-	-
2500	0.002	0.34	1945	0.64	1153
	No slip	0.327	3305	0.617	1413
	0.01	0.37	1093	-	-
7500	0.002	0.33	2705	0.58	2017
	No slip	0.323	7626	0.604	5013
	0.01	0.37	1109	-	-
10000	0.002	0.33	2897	0.57	2207
	No slip	0.322	9519	0.628	6455

Table 5.2: First and second maximum enstrophy $\Omega(t)$ of the dipole wall collision by using TRT-LBM. Results are given for different slip lengths and Reynolds numbers.

The maximum velocity at the wall is presented for various Reynolds numbers in Figure 5.7. The figure illustrates that the velocity at the wall grows faster with smaller slip lengths. By increasing the Reynolds numbers the dipole is more energetic at the boundary, therefore the maximum velocity at the east wall increases as Reynolds numbers increase.
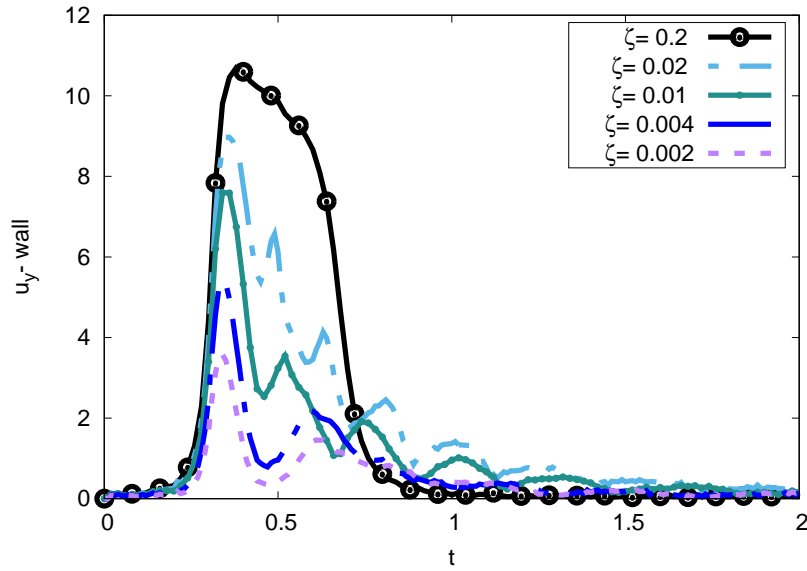
(a) $Re = 1252$
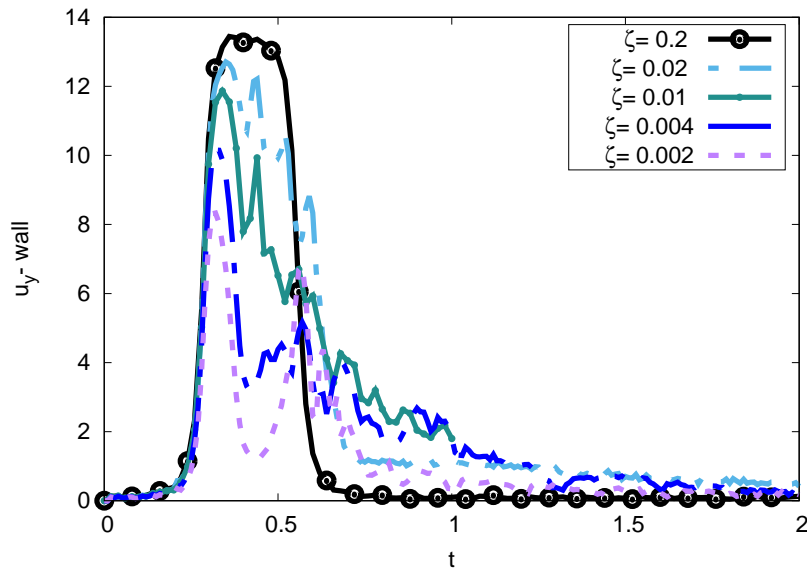
(b) $Re = 10000$

Figure 5.7: The maximum velocity at $x = 1$ with different slip and Re= 1252 and 10000.

5.1.3 Trajectory of the dipole

Kramer [64] made a comparison between the path of a dipole colliding with no-slip and stress-free boundaries at $Re = 1250$. Also the trajectory of a dipole with different slip lengths and stress-free boundaries in a channel for $Re = 1252$ has been studied by Sutherland [104]. Following [104], this section illustrates the trajectory of the maximum vorticity for a dipole colliding with different types of boundaries. The comparison is

given for the path for no-slip, slip and the stress-free walls. Figure 5.8 describes the trajectory of the maximum vorticity of the positive half of the dipole. This figure traces the trajectory of the dipole at $Re = 2500$ and ζ=0.004, 0.002, 0.01 and 0.02. Note that the no-slip is approached as $\zeta \to 0$. Before the first wall collision, the trajectories overlap for different slip lengths for all Reynolds numbers. After the first wall collision the dipole stays close to the wall for a greater distance for higher slip lengths. For smaller slip lengths, as the number of the collisions increases, the rebounds of the dipole from the wall cause the primary vortex to move as a circular trajectory near the wall. For no-slip walls the path of the dipole is very short and the number of circulations is greater.
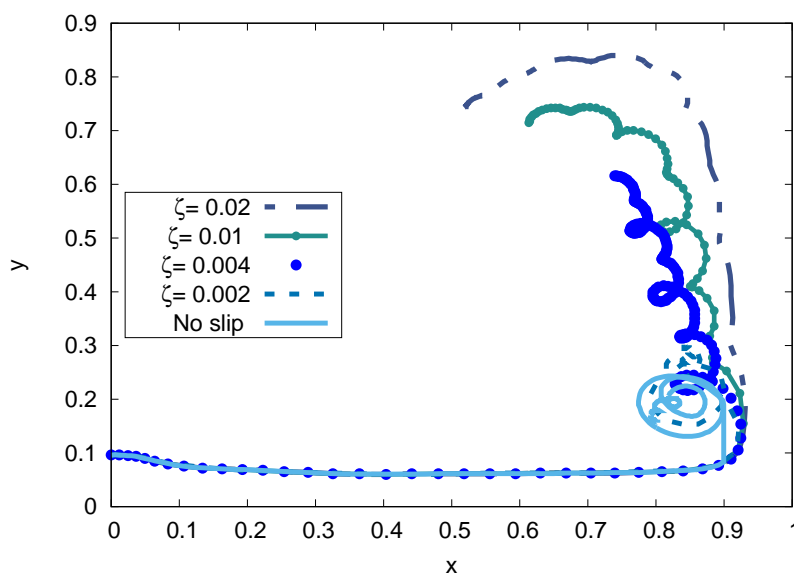
Figure 5.8: Trajectory of the maximum vorticity in the top half of the domain with different slip lengths. The Reynolds number is 2500.

To observe the behaviour of the dipole that collides with a shear stress-free boundary using moment based boundary conditions, different moments should be chosen. The implementation of this case will be given for the east wall as an example. The hydrodynamic condition that was imposed for free-slip wall at the east wall indicates that $\partial u_y/\partial x = 0$. This derivative is embedded within the off-diagonal component of the second-order moment of the LBM, $\Pi_{xy} = \sum_i f_i c_{ix} c_{iy}$. Thus, to impose the free slip condition $\Pi_{xy} = 0$ must be set, since the component of the velocity normal to a wall

and its derivative at the wall are zero.

In Table 3.2 instead of using the moment ρu_y from the second row we will pick Π_{xy} as a second moment. So the conditions will be:

$$\rho u_x = 0; \quad \Pi_{xy} = 0; \quad \Pi_{yy} = \frac{\rho}{3} + \rho u_y^2, \tag{5.1}$$

where $\Pi_{yy} = \Pi_{yy}^{(0)}$ is from the Chapman-Enskog expansion and the free-stress assumption which leads to $\Pi_{yy}^{(1)} = 0$.

Translating these conditions into "barred" moments (see equation (2.117)) and solving for $\bar{f}$ yields the incoming distributions

$$\bar{f}_3 = \bar{f}_1 + \bar{f}_2 + \bar{f}_4 + 2(\bar{f}_5 + \bar{f}_8) - \frac{\rho}{3} - \rho u_y^2,$$

$$\bar{f}_6 = \frac{\rho}{6} - \bar{f}_2/2 - \bar{f}_4/2 - \bar{f}_8 + \rho u_y^2/2, \tag{5.2}$$

$$\bar{f}_7 = \frac{\rho}{6} - \bar{f}_2/2 - \bar{f}_4/2 - \bar{f}_5 + \rho u_y^2/2.$$

The density ρ can be calculated by using the momentum $\rho \bar{u}_x$

$$\rho = -\rho \bar{u}_x + \bar{f}_0 + \bar{f}_2 + \bar{f}_4 + 2(\bar{f}_1 + \bar{f}_5 + 2\bar{f}_8), \tag{5.3}$$

and the momentum $\rho \bar{u}_y$ is obtained from the shear stress $\overline{\overline{\Pi}}_{xy}$

$$\rho \bar{u}_y = -\overline{\overline{\Pi}}_{xy} + \bar{f}_2 - \bar{f}_4 + 2\bar{f}_5 - 2\bar{f}_8. \tag{5.4}$$

Along the stress-free wall, the two primary monopoles separate with the first collision and roll up at the wall . The positive and negative monopoles move with opposite directions without any rebound and do not generate any further vortices at the wall. The walls with slip lengths $\zeta \geq 0.1$ act as a stress-free wall. Figure 5.9 shows the trajectory with slip boundary conditions and slip length $\zeta = 0.2$ matches the trajectory with stress-free walls.
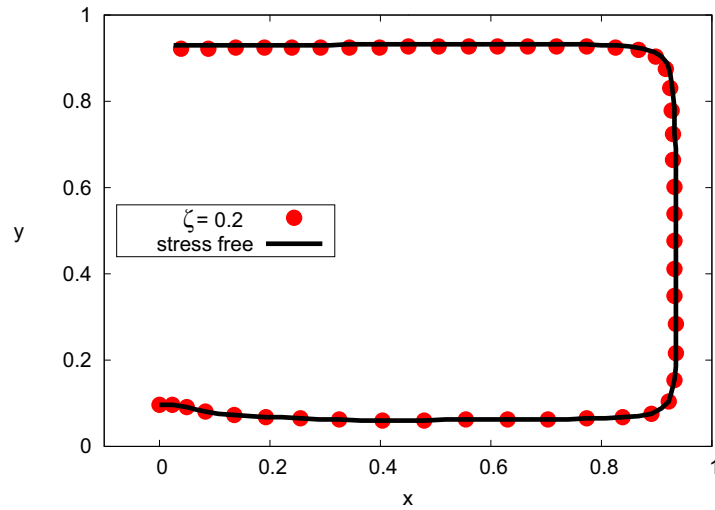
Figure 5.9: Trajectory of the maximum vorticity in the top half in a range of time $t \in [0, 2]$. With $\zeta = 0.2$ and the stress-free condition. The Reynolds number is Re=2500.

5.2 Oblique wall dipole collisions with slip boundaries

In Chapter 4 the behaviour of the dipole when it collides with a no-slip wall at angles of 30° and 45° was explained. From the snapshots, it can be seen that the collision with the no-slip wall at an angle of 30° is more complicated than the normal case. The generation of vortices is more frequent and the symmetry between two monopoles is broken. In this section, a detailed study on the behaviour of dipole collision with various slip lengths with release angle of 30° will be explained. Also the physics of a dipole that collides with a slip wall at an angle of 45° will be discussed. In each case, the influence of the slip length and the Reynolds number on the collision and the formulation of the vortices at the wall is shown.

5.2.1 Dipole slip wall collision at an angle of 30°

Initially, the two counter-rotating vortices of the dipole are located at $(0.0839, 0.0866), (0.1839, -0.0866)$ just like in the no-slip case. Numerical experiments were conducted for dipole wall collisions for various slip lengths. Figure 5.10(a) and (c)

shows there is a small difference in the behaviour of the dipole colliding with no-slip and small slip $\zeta = 0.002$ boundaries at $t = 0.7$ with regard to the generation of vortices near the corner. Except for the no-slip case and at around $t = 1.7$, the negative monopole tends to move towards the upper corner to merge with the positive core, while at $\zeta = 0.002$ it keeps moving at the east wall far from the positive core, see Figure 5.10(b) and (d). For large slip lengths, the two primary monopoles separate further. The secondary negative monopole merges with the positive one after the second collision, while the positive core rotates alone at the wall until it loses its strength over time, see Figure 5.10(e)(f).
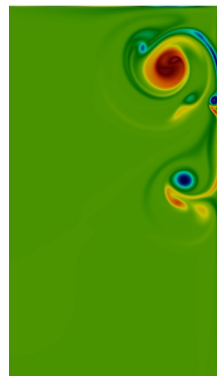
(a) $t = 0.7$ (b) $t = 1.7$

No slip

(c) $t = 0.7$ (d) $t = 1.7$

$\zeta = 0.002$

(e) $t = 0.7$ (f) $t = 1.7$

$\boxed{\zeta = 0.01}$
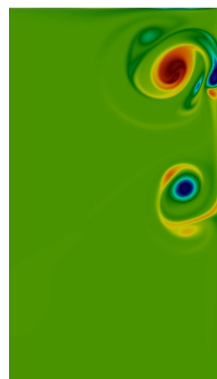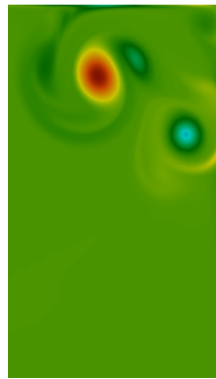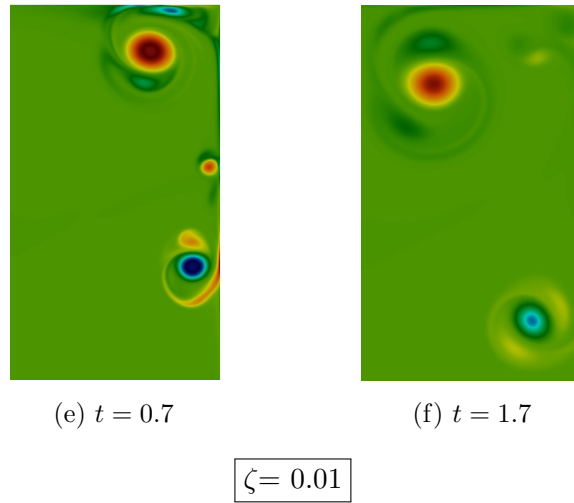
Figure 5.10: Vorticity plots for oblique wall dipole collision at angle of $30°$ for no slip, slip $\zeta = 0.002$, 0.01 at $t = 0.7, 1.7$ and $Re = 2500$. Contours are shown in the subdomain: $0.2 \leq x \leq 1, -0.4 \leq y \leq 1$ in the vicinity of the collision.

By looking at the general behaviour of the total energy, enstrophy and the maximum velocity at the wall, the differences between each slip and no-slip boundary can be observed. Figures 5.11 and 5.12 show that the dissipation of the energy, the rise of the enstrophy peaks and the maximum velocity at the wall behave differently in these flows. The ratio of the energy dissipation is greater and the peaks of the enstrophy are higher with collisions normal to the wall compared with the collision at $30°$.
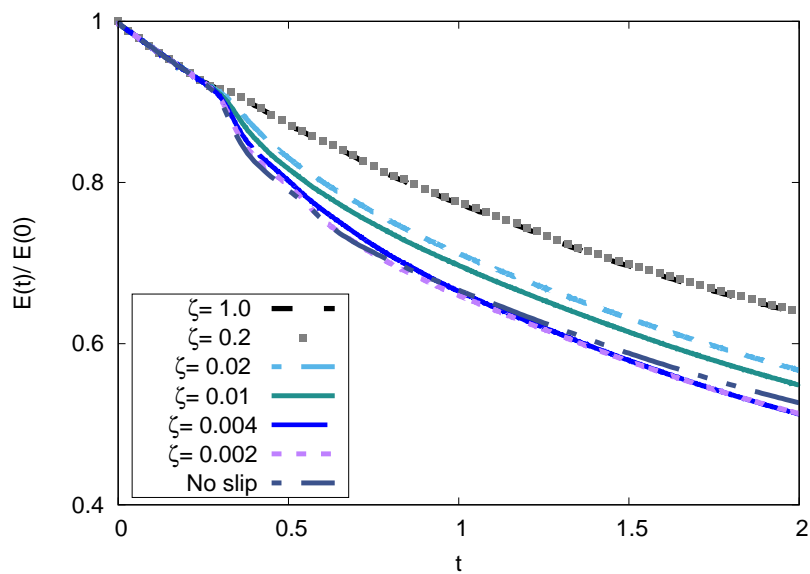
(a) Energy
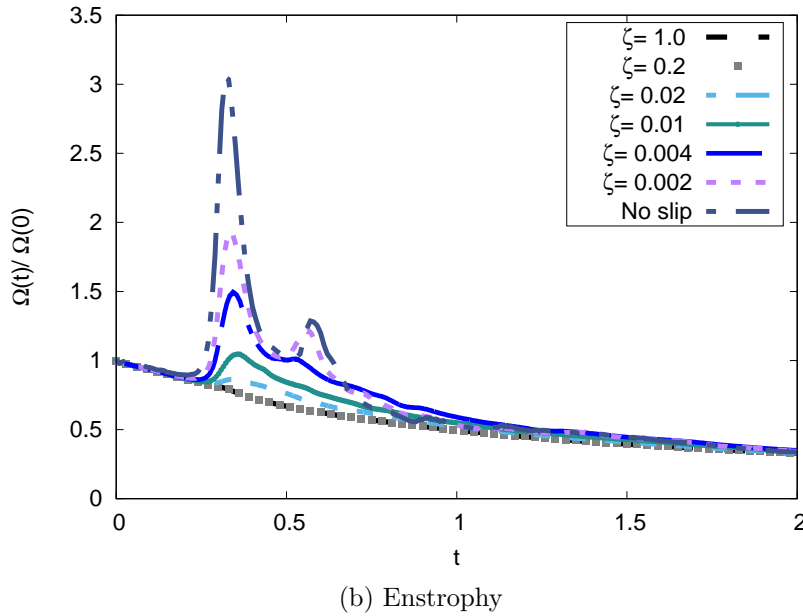
(b) Enstrophy

Figure 5.11: The total kinetic energy and total enstrophy at $Re = 2500$ for oblique dipole wall collision at and angle of $30°$ for different slip lengths.
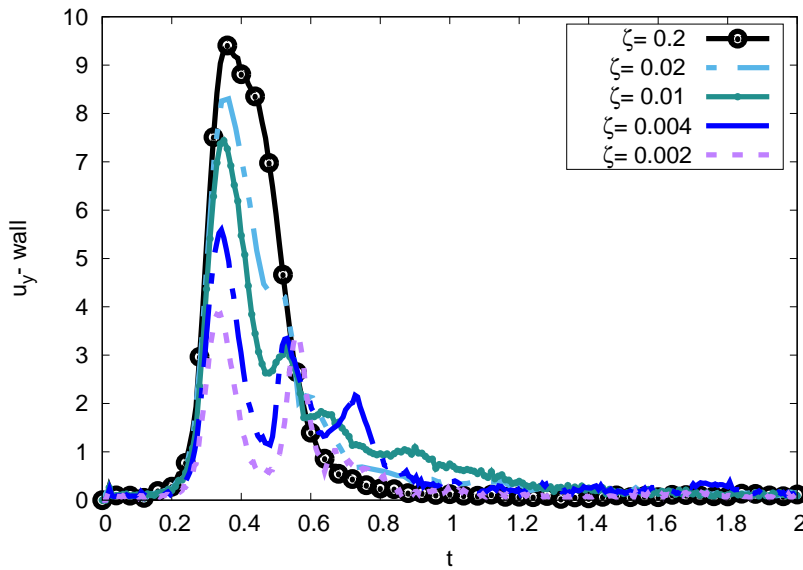
Figure 5.12: The maximum velocity at $x = 1$ with different slip lengths for $Re = 2500$.

Figure 5.13 illustrates the effect of the Reynolds numbers on the vortex boundary interaction for $\zeta = 0.002$. For Reynolds numbers higher than 2500, additional vorticity cores are generated from the positive monopole, see Figure 5.13 (a) and (c). As time progresses, the secondary dipole loses its strength more slowly with higher Reynolds numbers. Moreover, at $t = 1$, the small and high value negative monopole keeps

rotating around the positive monopole for $Re = 7500$. The positive core of vorticity also preserves its strength and moves towards the nearest corner. However, for $Re = 5000$ the secondary positive core loses its intensity over time, while the negative one behaves similarly to the monopole for $Re = 7500$, see Figure 5.14. Figure 5.15 shows that for $Re = 5000$ and $Re = 7500$ at larger slip lengths, the boundary layer creates more vortices from the negative primary monopole than those in the collision. However, after $t = 0.7$ and for different Reynolds numbers, the tertiary vortices start to lose their strength, while the space between the positive and negative cores increases with the increasing Reynolds numbers.

(a) $t = 0.6$ (b) $t = 1$

Re= 5000

(c) $t = 0.6$ (d) $t = 1$
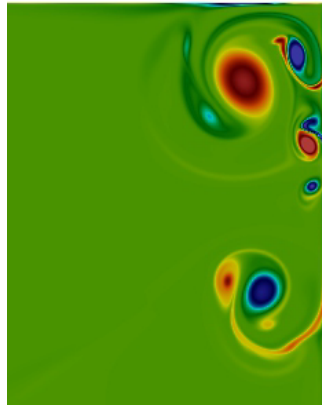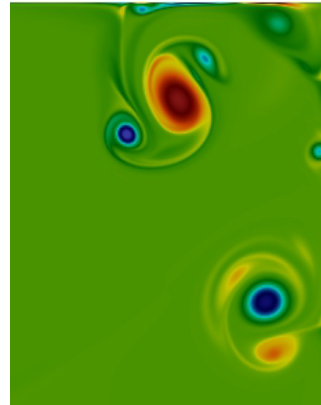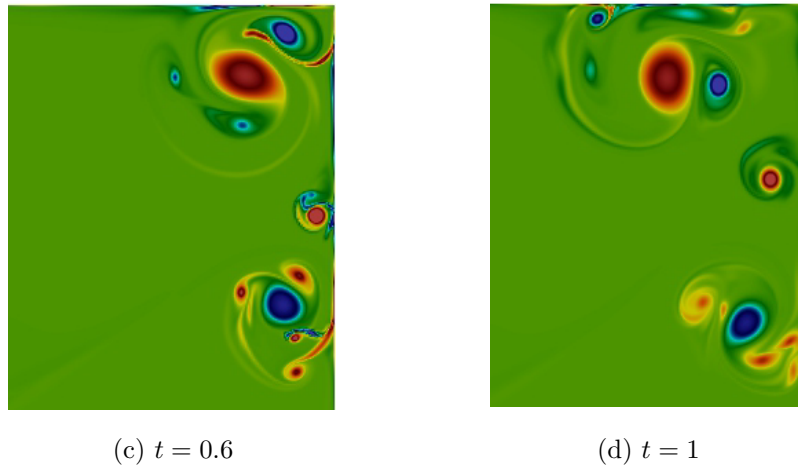
Re= 7500

Figure 5.13: Vorticity fields of dipole wall collision at an angle of $30°$ at $\zeta = 0.002$ and $t = 0.6, 1$ for Reynolds numbers 5000 and 7500. Contours are shown in the subdomain: $0.2 \leq x \leq 1, 0 \leq y \leq 1$ in the vicinity of the collision.

(a) $Re = 5000$ (b) $Re = 7500$
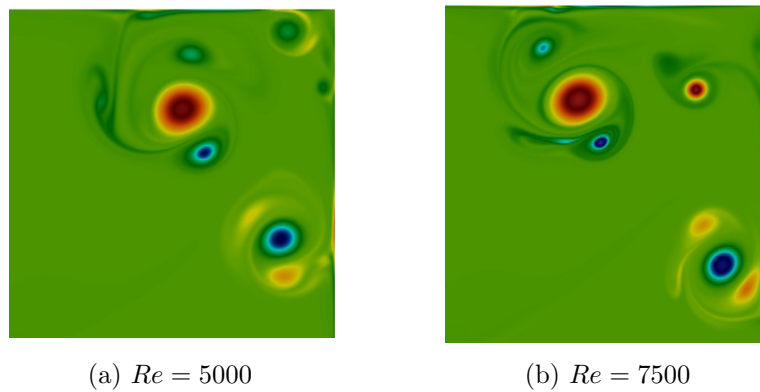
Figure 5.14: Vorticity fields of dipole wall collision at an angle of $30°$ at $\zeta = 0.002$ and $t = 1.5$ for Reynolds numbers 5000 and 7500. Contours are shown in the subdomain: $0 \leq x \leq 1, 0 \leq y \leq 1$ in the vicinity of the collision.

(a) $Re = 5000$ (b) $Re = 7500$
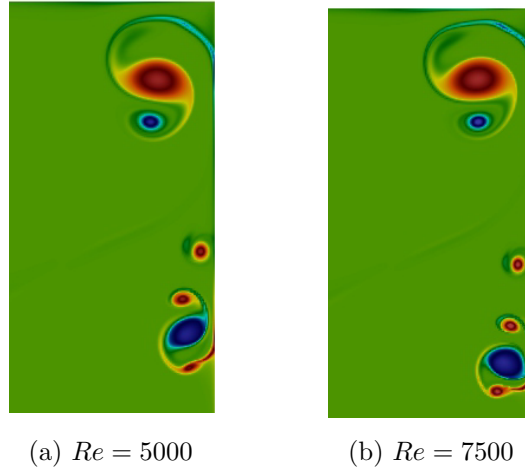
Figure 5.15: Vorticity fields of dipole wall collision at an angle of 30° at $\zeta = 0.01$ and $t = 0.5$ for Reynolds numbers 5000 and 7500. Contours are shown in the subdomain: $0.4 \leq x \leq 1, -0.2 \leq y \leq 1$ in the vicinity of the collision.

To obtain all the information about the dipole wall collision at an angle of 30° for various slip lengths, the total angular momentum is plotted for $Re = 2500$ and $Re = 7500$ in Figure 5.16. The plots illustrate that before the first wall interaction, the angular momentum is independent of slip length. After collision, the results of angular momentum is highly sensitive to slip length. The fluctuation of the angular momentum decreases for large slip lengths, especially $\zeta \geq 0.1$. By tracing the vorticity contours for these two slip lengths, the two high and low peaks of $L(t)$ can be explained. During the movement of the dipole along the slip wall and when the dipole reaches the corners, the angular momentum has sudden jumps. The high peaks of the angular momentum represent the results when the negative monopole reaches the bottom corners, while the minimum jumps describe the arrival of the positive monopole at the upper corners. Chapter 4 compares the recurrence of the oscillations in the results of the angular momentum for a dipole colliding with no-slip wall at different Reynolds numbers which increases with the Reynolds number. Here, the oscillation of the angular momentum is slightly effected by increasing the Reynolds number at a slip boundary.
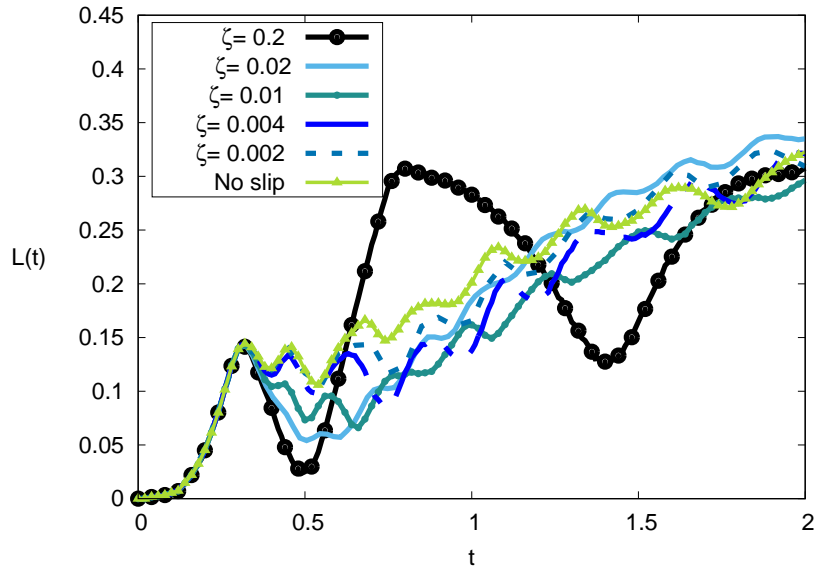
(a) $Re = 2500$
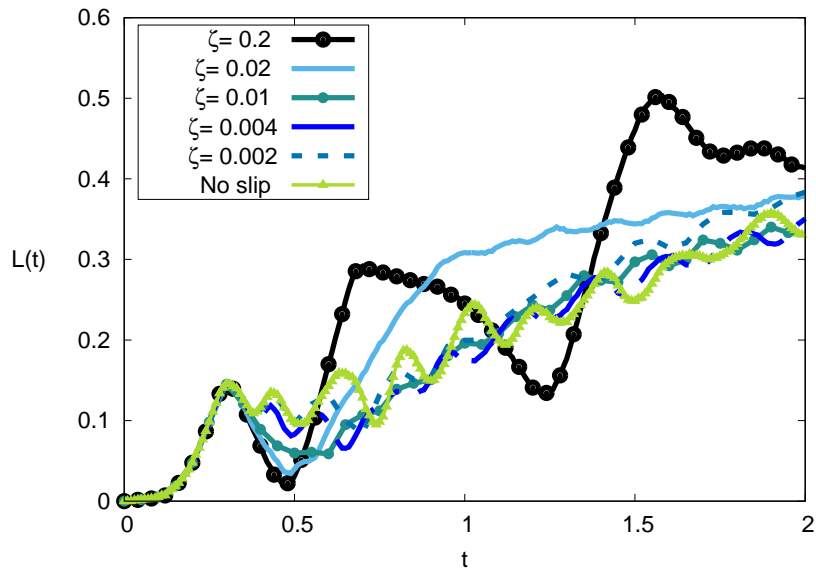
(b) $Re = 7500$

Figure 5.16: The total angular momentum at $Re = 2500$ and $Re = 7500$ for oblique wall dipole collision at and angle of 30° and different slip lengths.

5.2.2 Dipole slip wall collision at an angle of $45°$

In the collision at an angle of 45° with the Navier slip boundary, the dissipation of the primary dipole differs from the one in the collision with the no-slip wall. Figure 5.17 displays a comparison between a dipole which collides with slip and no-slip boundaries

for $Re = 2500$. The data is presented at $t = 0.8$ and $t = 1$. For $\zeta = 0.002$ and 0.004, the primary dipole loses its strength more slowly than the collision with no-slip wall. Also the number of emitted dipoles decreases as slip length increases. At higher slip lengths of $\zeta = 0.02$ and 0.01, the primary dipole does not lose its strength after collision, but the positive and negative monopoles move to the upper and right boundaries, respectively. As the slip length increases, the primary monopoles are able to move further from the corner. Each vortex induces only a secondary monopole which moves further from the primary one towards the corner. After $t = 1$, the two small secondary monopoles combine as one dipole at the corner, see Figures 5.17 (f) and (h). At $\zeta = 0.02$, they start to lose their strength when they reach the corner. At $\zeta \geq 0.2$, and similar to the normal and oblique at an angle of $30°$ collisions the primary dipole separates as two monopoles and moves along the walls without any further actions, since the walls act as stress-free boundaries.
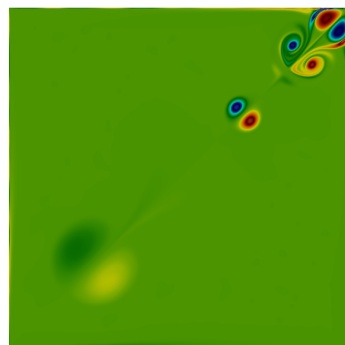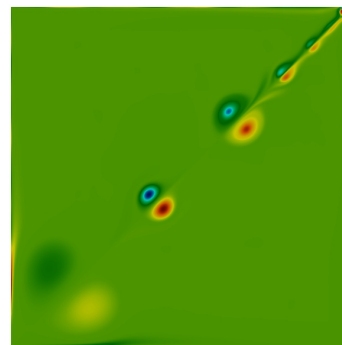
(a) $t = 0.8$ (b) $t = 1.2$

No-slip

(c) $t = 0.8$ (d) $t = 1.2$

$\zeta = 0.002$

162

(e) $t = 0.8$ (f) $t = 1.2$

$\zeta = 0.01$

(g) $t = 0.8$ (h) $t = 1.2$
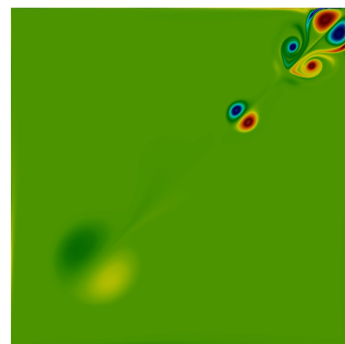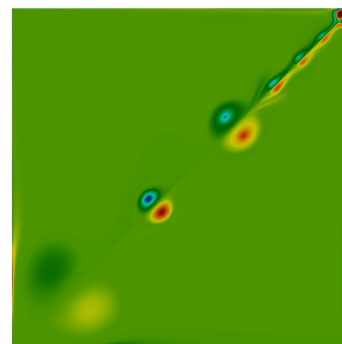
$\zeta = 0.02$
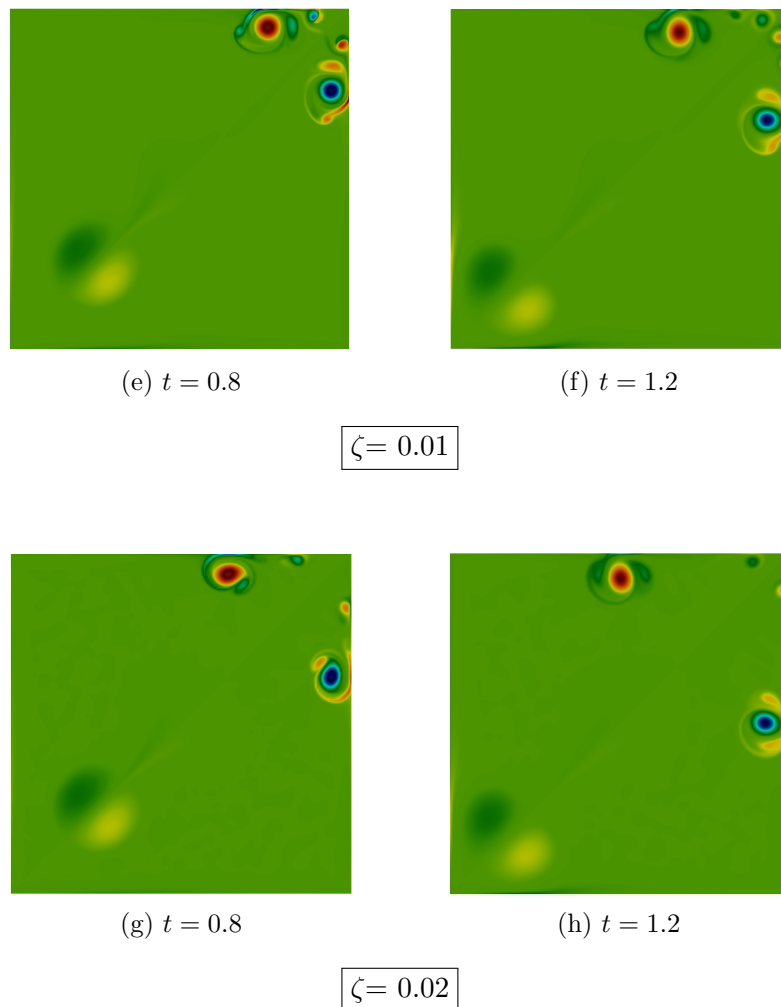
Figure 5.17: Vorticity fields of dipole wall collision at an angle of $45°$ at no-slip and slip $\zeta = 0.002, 0.004, 0.01, 0.02$ at $t = 0.8, 1.2$ for $Re = 2500$.

Figure 5.18 shows the total kinetic energy and the total enstrophy for dipole wall collisions at $45°$. The dissipation of the energy behaves in an unexpected manner. Here, the dissipation of the energy for $\zeta = 0.002$ is lower than that for no-slip collisions and it is even lower for $\zeta = 0.004$ after $t = 1.0$. That coincides with the enstrophy growth for $\zeta = 0.004$ and 0.002 at $t = 1$.

(a) Energy
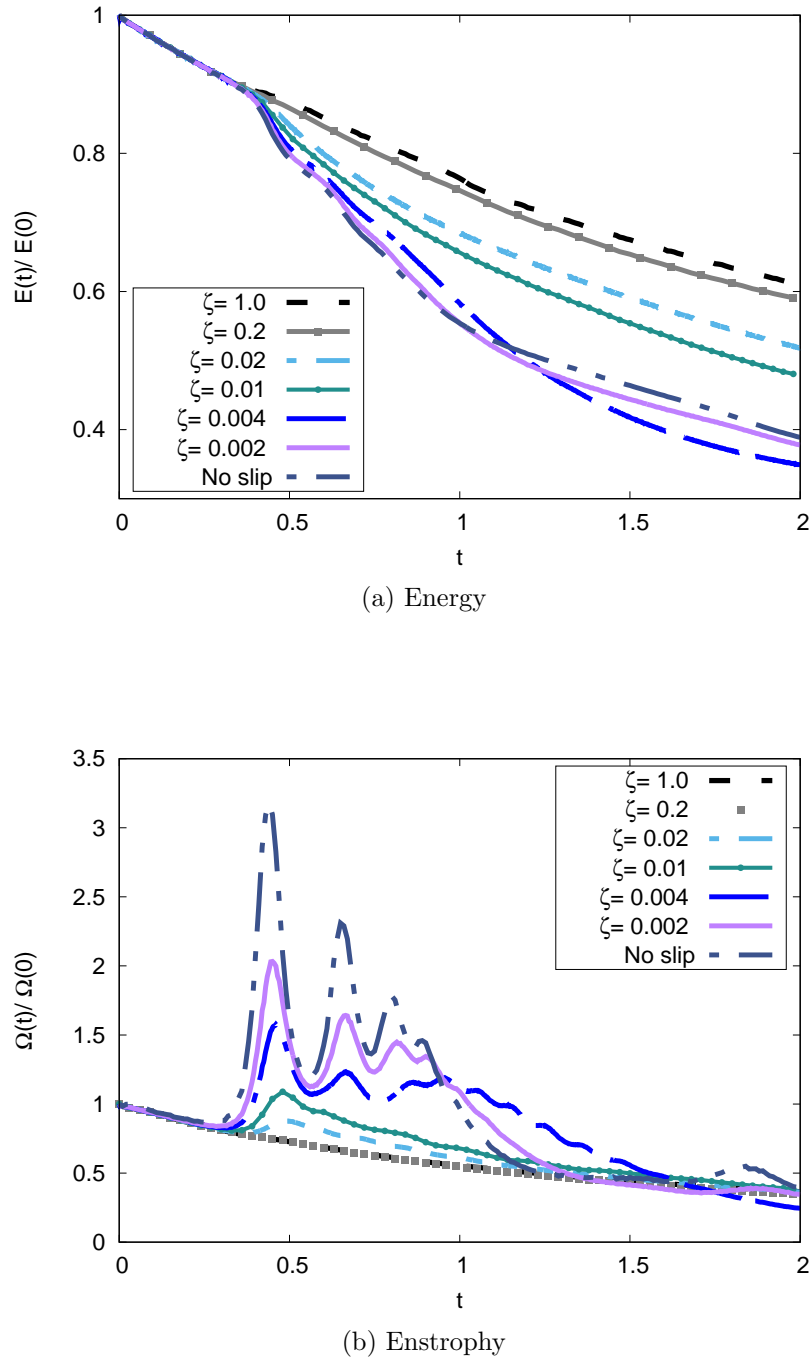
(b) Enstrophy

Figure 5.18: The normalized total kinetic energy and total enstrophy at $Re = 2500$ for oblique at an angle of $45°$ case different slip lengths.

For slip length 0.002, the main feature to be noticed is when the secondary dipole hits the opposite corner at $t = 2$. Figure 5.19 shows that the number of additional cores of vorticity at the bottom-left corner increases with higher Reynolds numbers. Additionally, the number of the emission dipoles from the primary one rises with Reynolds number. For $\zeta = 0.004$, by increasing the Reynolds numbers the roll up of the dipole

at the corner increases. This induces more small dipoles at the corner. For $Re = 5000$, the secondary dipole sticks and rolls up at the corner until its strength reduces at $t = 1$. Meanwhile, what is left from the secondary dipole is an arc of sheets of vortices that surrounds the primary dipole, see Figure 5.20.

(a) $Re = 2500$

(b) $Re = 5000$

(c) $Re = 7500$

(d) $Re = 10000$
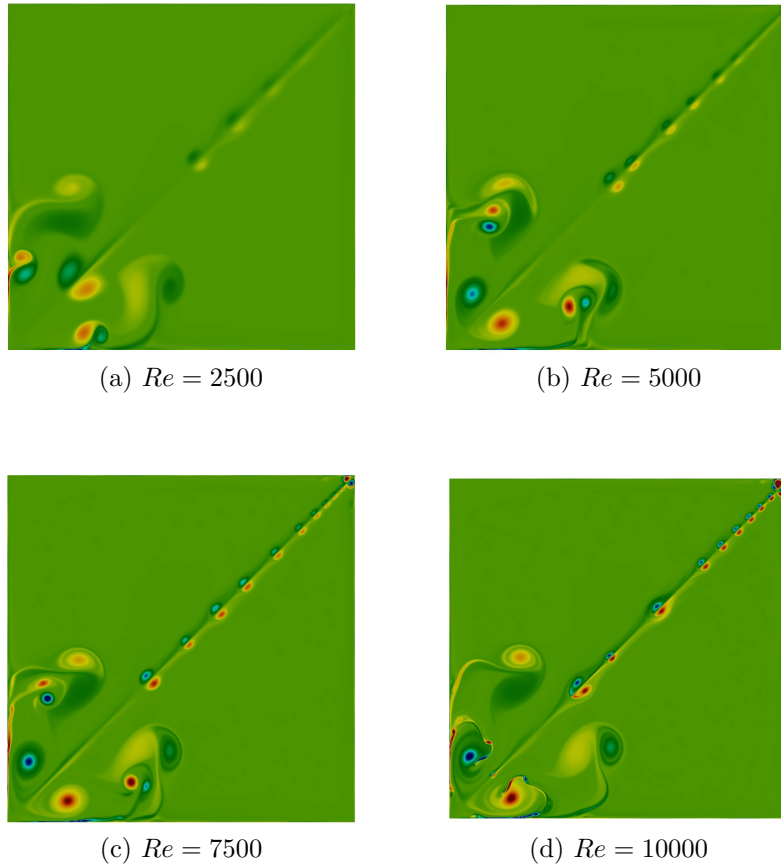
Figure 5.19: Vorticity fields of dipole wall collision at an angle of $45°$ for slip length $\zeta=0.002$ at $t = 2$. The Reynolds numbers are $Re = 2500, 5000, 7500$ and 10000.

(a) $t = 0.7$

(b) $t = 0.8$

(c) $t = 0.9$ (d) $t = 1.5$
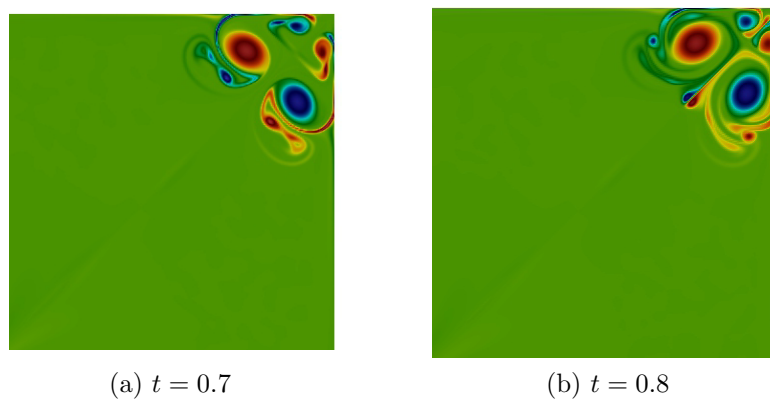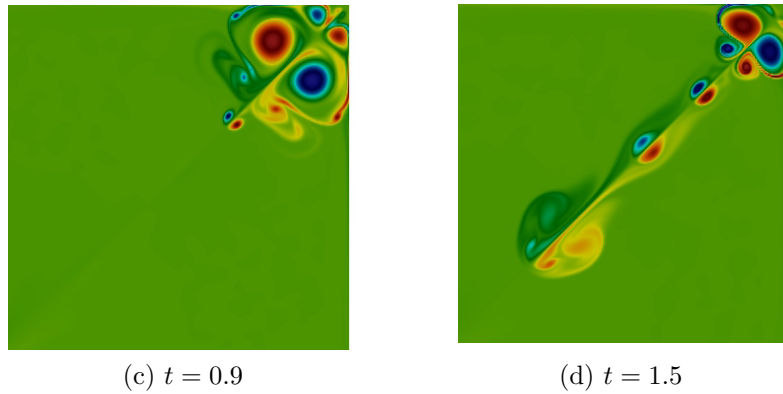
Figure 5.20: Vorticity fields of dipole collision for the slip $\zeta = 0.004$ wall at an angle of 45° for $Re = 5000$. Contours are shown in the subdomain: $-0.2 \leq x \leq 1, -0.2 \leq y \leq 1$ in the vicinity of the collision.

Figure 5.21 shows that the mechanism of the dipole after collision with the corner for $Re = 7500$ differs from other cases since the dipoles do not detach from the boundary to the opposite direction. Instead, the secondary dipole stimulates a number of small dipoles from the corner that rotate with each other near the corner. At the same time, vorticity filament sheets detach from the slip walls which surround the dipoles near the linked walls. The primary two monopoles tumble down on the top and right walls, respectively which generates numerous small and high strength monopoles that surround the primary dipole. However, for $Re = 10000$, the vortices at the corner cluster in an orderly manner to produce more dipoles at the corner. The secondary dipole manages to travel alone to the opposite direction leaving the primary dipole to move at the walls, see Figure 5.22. In the last two cases, the primary dipole only slowly loses its strength over time.

(a) $t = 0.7$

(b) $t = 0.9$

(c) $t = 1$

(d) $t = 1.8$
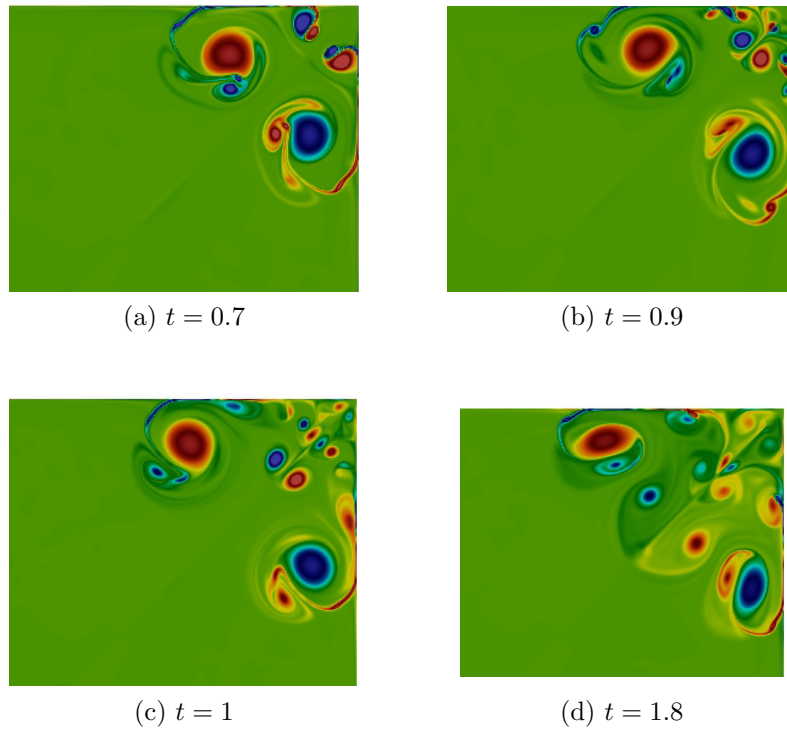
Figure 5.21: Vorticity of dipole collision with the slip ζ=0.004 wall at an angle of 45° for $Re = 7500$. Contours are shown in the subdomain: $0 \leq x \leq 1, 0.2 \leq y \leq 1$ in the vicinity of the collision.

(a) $t = 0.7$

(b) $t = 0.9$

(c) $t = 1$

(d) $t = 1.8$
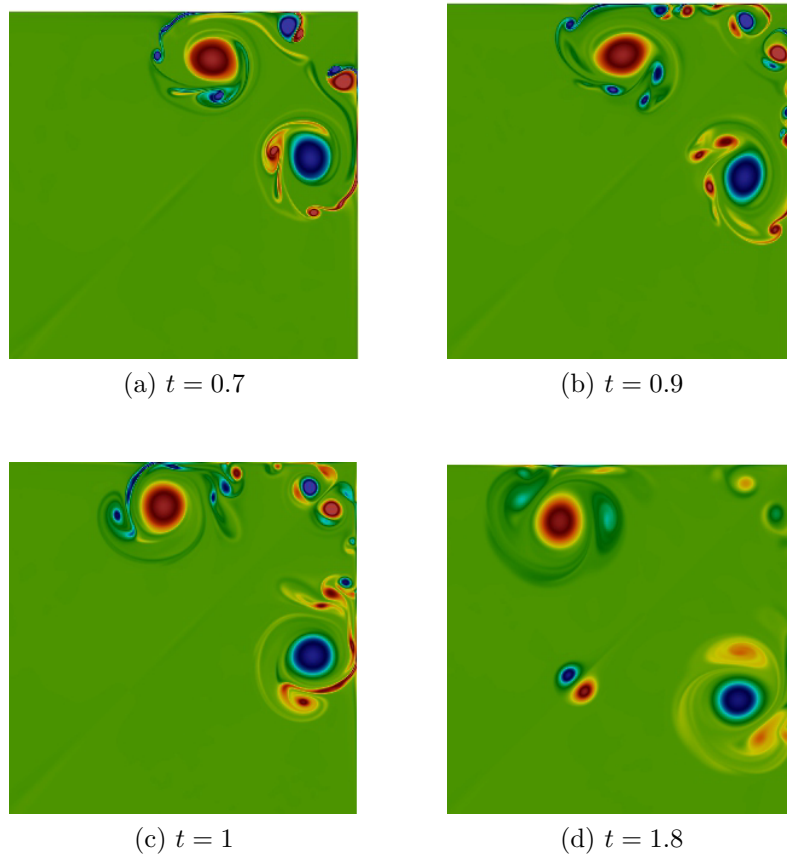
Figure 5.22: Vorticity of dipole collision with the slip ζ=0.004 wall at an angle of 45° for $Re = 10000$. Contours are shown in the subdomain: $0 \leq x \leq 1, 0 \leq y \leq 1$ in the vicinity of the collision.

Table 5.3 summarises the values of the kinetic energy at $t = 2$ to clarify the dissipation of the energy behaviour for different Reynolds numbers and slip lengths for an incidence angle of 45°. Firstly, similar to other angles of collision, the dissipation of the kinetic energy decreases by increasing Reynolds numbers for different slip lengths and no-slip collisions. Secondly, in contrast to other angles of collision, the decay of the kinetic energy in the no-slip case is slower than for small slip lengths, $\zeta = 0.002$ and 0.004, at $t \geq 1.2$ for small Reynolds numbers. This confirms the results in Figure 5.18. By increasing the Reynolds number, the dissipation rate becomes regular and similar to the ones with normal collision and at an angle of 30°, where the energy dissipates faster for no-slip collisions. Figure 5.23 illustrates the dissipation of the kinetic energy and the persistence of the enstrophy for $Re = 10000$ and various slip lengths. For this Reynolds number the decay of the kinetic energy and the enstrophy after $t = 1$ differs from the cases with smaller Reynolds numbers, especially for $\zeta = 0.002$ and 0.004, (see Figure 5.18).
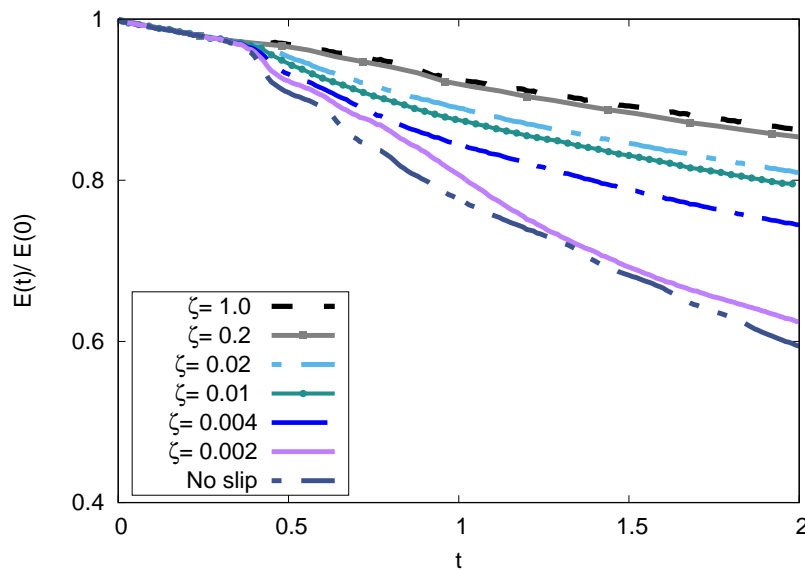
(a) Energy
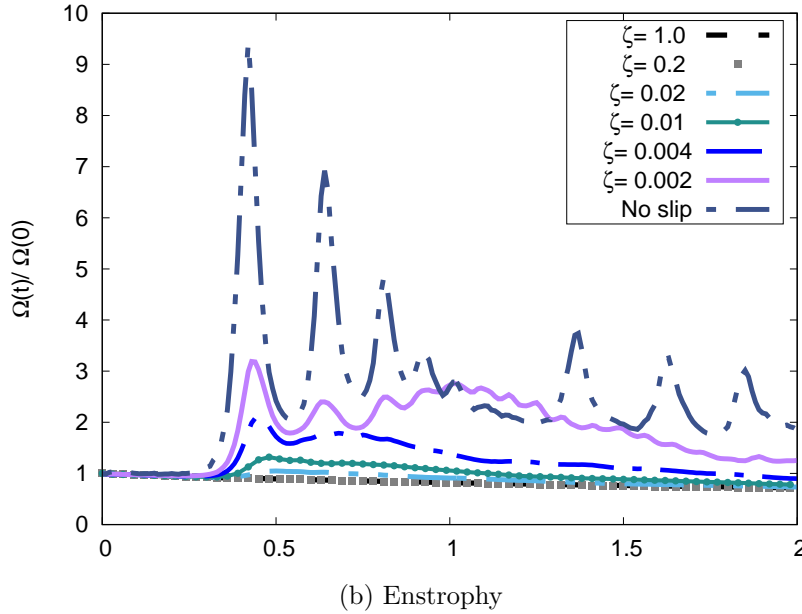
(b) Enstrophy

Figure 5.23: The total kinetic energy and total enstrophy at $Re = 10000$ for oblique at an angle of $45°$ and different slip lengths.

| ζ	$Re = 1252$	$Re = 2500$	$Re = 5000$	$Re = 7500$	$Re = 10000$
0.02	0.324	0.518	0.690	0.766	0.809
0.01	0.274	0.477	0.661	0.744	0.793
0.002	0.253	0.377	0.504	0.576	0.624
No slip	0.260	0.388	0.519	0.577	0.594

Table 5.3: The kinetic energy at $t = 2$, $E(2)$, for dipole wall colliding at an angle of $45°$ for different Reynolds numbers and slip length.

5.3   Conclusion

The dipole wall collision with slip boundaries has been studied in this chapter. The effect of the slip lengths, Reynolds numbers and the angle of the collision on this flow were investigated. The moment-based boundary conditions with the Navier slip condition were applied to simulate this flow.

In this research, the trajectory of the flow at normal collision for various slip lengths was tracked. The route of the dipole is longer with higher slip lengths and shear-free boundaries while, in small and no-slip cases the dipole moved in a circular shape for a small distance after collision. Secondly, as the slip length increased, the generation of cores of vorticity at the boundary decreased. The maximum enstrophy decreased by

169

increasing the slip length which coincided with the reduction of the energy dissipation when a higher slip length was applied. For the collision at an angle of 30°, the oscillation of the angular momentum decreased with higher slip lengths except for two higher jumps when the two monopoles reach the corners of the box.

The behaviour of the dipole at $\zeta \geq 0.1$ is identical to the free-shear boundary where the two cores of monopoles moved along the wall without any further action. The kinetic energy and the enstrophy results matched the results of Sutherland $et\ al$ [105] for $Re = 1252$. For the normal case, at higher slip lengths and Reynolds numbers when the space between the two monopoles has increased, the secondary small dipole moved towards the centre of the collided wall to create a small dipole. At a collision angle of 45°, the emanation of the dipole towards the opposite direction stopped and number of the dipoles that were created from at the top corner decreased. Similar to the normal case, by increasing the slip length two secondary monopoles separated from the primary one and created a dipole at the top-right corner. However, at large Reynolds numbers the boundary layer created numerous vortices for ζ=0.004 which gathered to form dipoles for $Re = 10000$.

Chapter 6

The dissipation of the kinetic energy for dipole wall collision flow

Previous chapters illustrated that the sudden decrease of the kinetic energy with the increase of the total enstrophy are the main features that distinguish the dipole wall collision flow. So, to increase our understanding of this feature and how these quantities relate to each other, a study is carried out to further investigate the energy dissipation and enstrophy growth scales. Farge *et al.* [35] and Sutherland *et al.* [104] used a volume penalisation method to study the energy dissipation rate for dipole wall collision at different slip lengths. Farge *et al.* [35] showed that as the viscosity tends to zero the energy will dissipate to non zero limits in the dipole wall collision. Similar to them, Sutherland [104] studied the dissipation of the kinetic energy and the growth of the enstrophy in an open channel domain for various slip lengths, comparing the results with those in [35]. Sutherland *et al.* [104] showed that the penalisation method needed a higher number of grid points to simulate the boundary layer to generate more vortices at the boundary. They also showed that in order to get coherent energy dissipation in the limit of vanishing viscosity, a fixed square resolution should be applied.

This chapter will investigate the scale of the dissipation of the energy and the growth of enstrophy for dipole wall collisions by using the LBM with slip and no-slip boundaries. The results will be shown for three cases: the dipole collides with the wall

normally, and non-normal incidents at an angle of 30° and 45°. The behaviour will be compared with the results of [104].

6.1 The relation between the dissipation of the kinetic energy and the enstrophy

The decay of the energy after the first collision in a bounded domain can be explained by finding the relation between the dissipation of the total kinetic energy and the production of the vortices at the boundary. So the argument starts from the incompressible Navier-Stokes equations

$$\frac{\partial \mathbf{u}}{\partial t} + \mathbf{u} \cdot \nabla \mathbf{u} = -\frac{1}{\rho} \nabla P + \nu \nabla^2 \mathbf{u},$$
$$\nabla \cdot \mathbf{u} = 0. \tag{6.1}$$

Using the standard relation

$$\nabla^2 \mathbf{u} = \nabla (\overset{0}{\cancel{\nabla \cdot \mathbf{u}}}) - \nabla \times \left(\nabla \times \mathbf{u} \right), \tag{6.2}$$

then multiplying the momentum equation by $\mathbf{u}$ gives,

$$\rho \mathbf{u} \cdot \frac{\partial \mathbf{u}}{\partial t} + \rho \mathbf{u} \cdot \left(\mathbf{u} \cdot \nabla \mathbf{u} \right) = -\mathbf{u} \cdot \nabla P - \mu \mathbf{u} \cdot \left(\nabla \times \left(\nabla \times \mathbf{u} \right) \right). \tag{6.3}$$

The first term of equation (6.3) represents the dissipation of the kinetic energy per unit volume and by assuming the constant ρ we get

$$\rho \mathbf{u} \cdot \frac{\partial \mathbf{u}}{\partial t} = \frac{1}{2} \frac{\partial}{\partial t} (\rho |\mathbf{u}|^2) = \frac{\partial E_v}{\partial t}, \tag{6.4}$$

Chapter 6. The dissipation of the kinetic energy for dipole wall collision flow

where E_v is the energy per unit volume.

Since $\mathbf{u} \cdot \nabla \mathbf{u} = \frac{1}{2} \nabla |\mathbf{u}|^2 + (\nabla \times \mathbf{u}) \times \mathbf{u}$,

$$\mathbf{u} \cdot (\mathbf{u} \cdot \nabla \mathbf{u}) = \frac{1}{2} \mathbf{u} \cdot \nabla |\mathbf{u}|^2 + \mathbf{u} \cdot ((\nabla \times \mathbf{u}) \times \mathbf{u}). \tag{6.5}$$

Furthermore,

$$\nabla \cdot \left(|\mathbf{u}|^2 \, \mathbf{u} \right) = \mathbf{u} \cdot \nabla \left(|\mathbf{u}|^2 \right) + |\mathbf{u}|^2 \cancel{\nabla \cdot \mathbf{u}}^{\,0} \tag{6.6}$$

The pressure term can be written as

$$\nabla \cdot \left(P\mathbf{u} \right) = P\cancel{\nabla \cdot \mathbf{u}}^{\,0} + \nabla P \cdot \mathbf{u}, \tag{6.7}$$

The fourth term of equation (6.3) can be rewritten as follows

$$\mathbf{u} \cdot \left(\nabla \times \left(\nabla \times \mathbf{u} \right) \right) = \nabla \cdot \left(\left(\nabla \times \mathbf{u} \right) \times \mathbf{u} \right) + |\nabla \times \mathbf{u}|^2. \tag{6.8}$$

Substituting equations (6.4), (6.6), (6.7) and (6.8) into equation (6.3) gives

$$\frac{\partial E_v}{\partial t} + \nabla \cdot \left((P + E_v)\rho\mathbf{u} + \mu(\boldsymbol{\omega} \times \mathbf{u}) \right) = -\mu \, |\boldsymbol{\omega}|^2, \tag{6.9}$$

where $\boldsymbol{\omega} = \nabla \times \mathbf{u}$ is the vorticity of the flow.

In order to find the total kinetic energy and total enstrophy, both sides of equation (6.9) are integrated over domain V

$$\int_V \left(\frac{\partial E_v}{\partial t} + \nabla \cdot \left((P + E_v)\mathbf{u} + \mu(\boldsymbol{\omega} \times \mathbf{u}) \right) \right) dV = -\mu \int_V |\boldsymbol{\omega}|^2 dV. \tag{6.10}$$

The first term of the left side of equation (6.10) represents the dissipation of the total kinetic energy

$$\int_V \frac{\partial E_v}{\partial t} dV = \frac{dE}{dt}, \tag{6.11}$$

173

while the integration of the right side gives the total enstrophy part

$$-\mu \int_V |\boldsymbol{\omega}|^2 dV = -2\mu\Omega. \tag{6.12}$$

What remains is the integration of the second part of equation (6.10). Therefore, using the divergence theorem $\int_V \nabla \cdot \mathbf{A} dV = \int_S (\mathbf{A} \cdot \mathbf{n}) dS$ where $\int_S$ is the integration on the boundary and $\mathbf{n}$ is unit normal on it, gives

$$\int_V \nabla \cdot \left((P + E_v)\mathbf{u} + \mu(\omega \times \mathbf{u}) \right) dV = \int_S \left(\left((P + E_v)\mathbf{u} + \mu(\omega \times \mathbf{u}) \right) \cdot \mathbf{n} \right) dS \tag{6.13}$$

The results of equations (6.11), (6.12) and (6.13) yield the evaluation of the decay of the total kinetic energy and its relation with the total enstrophy and the velocity for viscous and slip boundaries

$$\frac{dE}{dt} = -2\mu\Omega - \mu \int_S (\omega \times \mathbf{u}) \cdot \mathbf{n} dS, \tag{6.14}$$

where the dimensionless version of equation (6.14) can be written as

$$\frac{d\tilde{E}}{dt} = -\frac{2}{Re}\tilde{\Omega} - \frac{1}{Re} \int_{\tilde{S}} (\tilde{\omega} \times \tilde{\mathbf{u}}) \cdot \mathbf{n} d\tilde{S}, \tag{6.15}$$

where the overbar indicates a dimensionless quantity. In the following, overbars are omitted for clarity.

The second term on the right-hand side of the above equation depends on the relation between the velocity and the vorticity at the boundary. In fact, equation (6.15) can explain the increase of the kinetic energy dissipation when the slip length is decreased as in Figure 5.3(a). By decreasing the slip length, the boundary layer induced more vortices than at higher slip length. Therefore, the enstrophy with the third term of equation (6.15) increases, which leads to a more rapid dissipation of the kinetic energy.

For no-slip boundaries, the last term of equation (6.15) vanishes and the non dimensional relation between the kinetic energy and the enstrophy for viscous flow with

no-slip boundaries becomes

$$\frac{d\tilde{E}}{dt} = -\frac{2}{Re}\tilde{\Omega}. \tag{6.16}$$

To test the validity of equation (6.15), we plot the values for each side of this equation over time intervals $\delta t = 0.1$. Figure 6.1 ($Re = 2500$, $\zeta = 0.01$ for normal collision) shows that this does not give smooth results and the dissipation in particular is subject to random variations. However, evaluating over much smaller time intervals $\delta t = 0.0001$ shows that these noisy random variations are due to high frequency oscillations, which are adequately resolved with a time interval of 0.0001, see Figure 6.2. This phenomenon is observed for every Re, ζ and at every angle of incidence. The oscillations were also grid-independent at the highest resolutions used. The oscillations can be eliminated using a double-smoothing process as follows:

$$\frac{dE_i^*}{dt} = \frac{E_{i-49} - E_{i-50}}{\delta t} + \frac{E_{i-47} - E_{i-48}}{\delta t} + \ldots + \frac{E_{i+50} - E_{i+49}}{\delta t}, \tag{6.17}$$

so the intermediate average step will be

$$\frac{dE_i^*}{dt} = \frac{E_{i+50} - E_{i-50}}{100\delta t}. \tag{6.18}$$

The average dissipation over 100 step is then

$$\frac{dE_i}{dt} = \frac{1}{100\delta t} \sum_{j=i-50}^{i+50} \frac{dE_j^*}{dt}. \tag{6.19}$$

Figure 6.3 shows that the doubly-smoothed results satisfy equation (6.15) reasonably well for $Re = 2500$, $\zeta = 0.01$, normal collision.

Figure 6.1: The relationship between the energy dissipation and the enstrophy in equation (6.15) for dipole wall collision for $Re = 2500$ at $\zeta = 0.01$ using $\delta t = 0.1$. The left side of the equation (red line), the right side (circle line).

Figure 6.2: The relationship between the energy dissipation and the enstrophy in equation (6.15) for dipole wall collision at $\zeta = 0.01$ for $Re = 2500$ using $\delta t = 0.0001$. The right side of the equation (line), the left side (circle line).
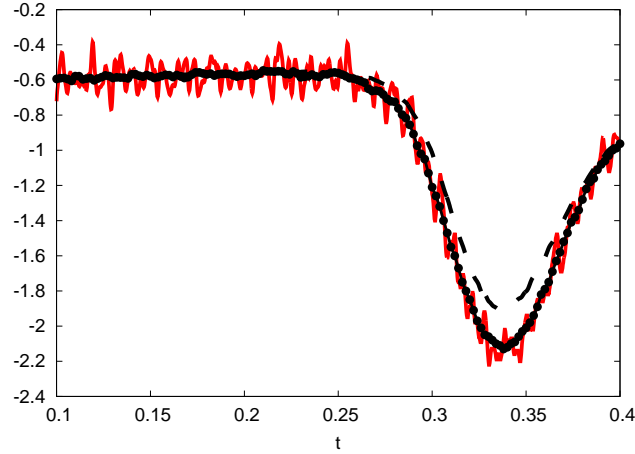
Figure 6.3: The left side of equation (6.15) for dipole wall collision at $\zeta = 0.01$ for $Re = 2500$ using $\delta t = 0.0001$. The left side of the equation is smoothed (red line), the double smooth process (line with circle) and the right side of equation (6.15) (dashed).

A possible cause for these oscillations is a compressibility effect. The analysis leading to equation (6.15) is based upon the assumption that the flow is incompressible $\nabla \cdot \mathbf{u} = 0$. Lattice Boltzmann method simulations are weakly-compressible but compressibility effects can be made smaller by reducing the Mach number in the simulations. Here, we reduce the mean velocity $u_{lb} = \frac{1}{(m-1)^2} \int_0^m \int_0^m |\mathbf{u}|^2 \, dx dy$ at the beginning of the simulation. That means reducing the Mach number from $Ma = 0.01\sqrt{3}$ to $0.001\sqrt{3}$. Reducing the Mach number and using the mean average dissipation over 100 time steps results in a smooth curve and excellent agreement between the two sides of equation (6.15), as shown in Figure 6.4. This figure illustrates the role of the last term in equation (6.15) for $Re = 2500$ and $Ma = 0.001\sqrt{3}$, especially after the first dipole wall collision. The kinetic energy and the enstrophy which are the focus of previous chapters are not significantly affected by random variations. Thus reducing the Mach number as above does not affect the results obtained in previous chapters.
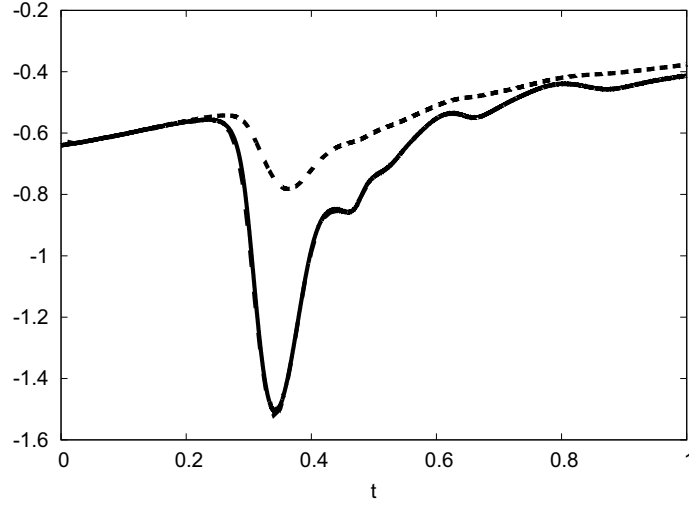
Figure 6.4: The relationship between the energy dissipation and the enstrophy in equation (6.15) for dipole wall collision at $\zeta = 0.004$ for $Re = 2500$ and $Ma = 0.001\sqrt{3}$. The left side of the equation (dashed), the right side (line) and the right side of equation (6.16) (dotted).

To show the effect of the Reynolds number and slip length on this relation, the ratio between the right-hand side of equation (6.15) and equation (6.16) is calculated as follows

$$\vartheta = \frac{max\left|-2\mu\Omega - \mu\int_S (\omega \times \mathbf{u}) \cdot \mathbf{n}dS\right|}{max\left|-\frac{2}{Re}\Omega\right|}. \tag{6.20}$$

Table 6.1 and Table 6.2 show that the ratio increases with increasing Reynolds numbers for a given angle of incidence. The results in the table indicate that when ζ become large, the ratio decreases and then will be close to unity. This is because the boundary layer is not present and there are no additional vortices at the wall for the shear stress-free boundaries that come from the higher slip lengths, so the effect of enstrophy in equation (6.15) is weak. As a result, the right side of equations (6.15) and equation (6.16) are equal. Figure 6.5 demonstrates the results for higher slip length $\zeta = 2$ and $Re = 2500$, as an example. The ratio reaches maximum value between $\zeta = 0.004$ and 0.02 and depends upon Reynolds number and angle of incidence. As expected as $\zeta \longrightarrow 0$, the ratio will approach to unity where the Navier boundary condition reduces to the no-slip case.

ζ	$Re = 625$	Re=1250	$Re = 2500$	$Re = 5000$
0.0005	1.061	1.105	1.187	1.275
0.002	1.201	1.377	1.550	1.750
0.004	1.343	1.575	1.622	2.165
0.01	1.524	1.779	2.041	2.224
0.02	1.545	1.737	1.903	2.061
0.1	1.162	1.275	1.307	1.317

Table 6.1: The ratio in equation (6.20) for normal dipole wall collision for different
Reynolds numbers and slip lengths.

ζ	$Re = 625$	Re=1250	$Re = 2500$	$Re = 5000$
0.0005	1.052	1.095	1.158	1.255
0.002	1.177	1.304	1.467	1.696
0.004	1.279	1.457	1.661	1.905
0.01	1.408	1.620	1.798	2.004
0.02	1.374	1.576	1.689	1.790
0.1	1.126	1.191	1.216	1.220

Table 6.2: The ratio in equation (6.20) for 30° dipole wall collision for different Reynolds
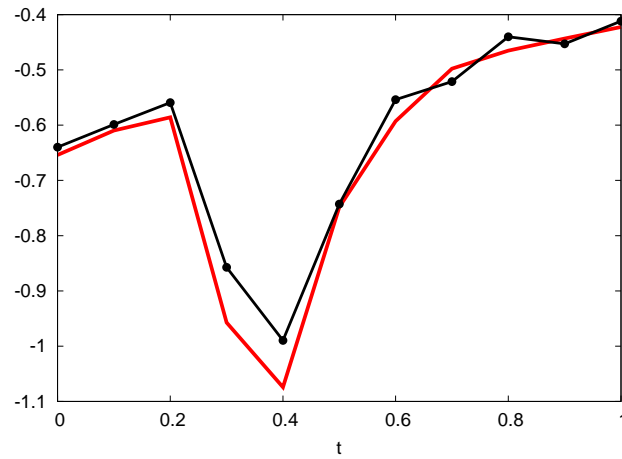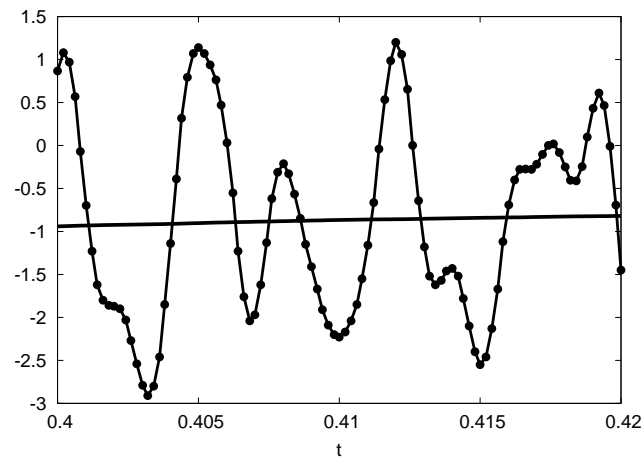numbers and slip lengths.
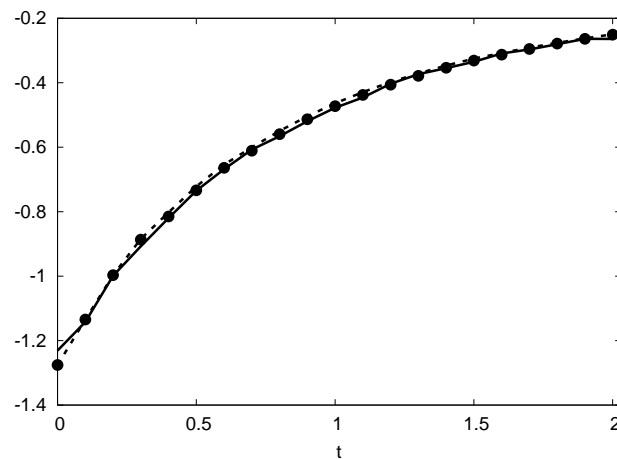
Figure 6.5: The relationship between the energy dissipation and the enstrophy in equation
(6.15) for dipole wall collision and $\zeta = 2$ for $Re = 1252$ and $Ma = 0.001\sqrt{3}$. The left side of
the equation (line), the right side (circle) and the right side of equation (6.16) (dotted) .

6.2 Scaling relations of boundary layer vorticity

Many authors studied the dissipation of energy for no-slip and slip boundaries for dipole wall collisions. Clercx and Heijst [21] studied the scaling of dissipation of the energy and the increase of the maximum enstrophy and the palinstrophy for no-slip unbounded and bounded domains. So, in a range of Reynolds numbers less than or equal to 128000, the investigation satisfied the relationship of equation (6.16). For both normal and oblique collisions, the increase of the maximum enstrophy with Reynolds number is $\Omega_{max} \propto Re^{0.8}$ for Reynolds numbers less than 20000. For Reynolds numbers greater than or equal to 20000, the scaling is $\Omega_{max} \propto Re^{0.5}$. Oscillating plates as a boundary layer for no-slip boundaries are simulated by Keetels *et al.* [63] to study the enstrophy and palinstrophy $P(t)$ peak scales. Keetels *et al.* [63] found that the enstrophy is approximately proportional to $Re^{0.75}$ and $P(t) \propto Re^{2.25}$ for Reynolds numbers less than 20000. For Reynolds numbers equal or greater than 20000 the scaling is $\Omega(t) \propto Re^{0.5}$ and and $P(t) \propto Re^{1.5}$.

For slip and free-slip boundaries, Farge *et al.* [35] investigated the kinetic energy dissipation and enstrophy for various slip lengths for $Re \leq 7880$. Farge *et al.* [35] demonstrate that there is less dissipation in the energy as the Reynolds number increases. Following Farge *et al.* [35], Sutherland [104] applied the no-slip and slip boundary conditions to seek the energy dissipation structure. In their work they used the same slip lengths as [35]. For no-slip and slip with slip length $\zeta = 4/Re$ cases, the Prandtl theory is satisfied with a slope equal to -0.43. For a slip length equal to 0.003 this theory was satisfied with a slope equal to -0.53 ± 0.05. Clercx and Heijst [22] summarise and review the most recent dipole wall collision numerical investigations. This article concentrates on the scaling of the dissipation of the energy in the vanishing viscosity limit.

This thesis studies the dissipation of the energy by using the TRT-LBM with moment-based boundary conditions and extends the study of [104, 35] to include other angles of incidence to find the scale of the energy dissipation and enstrophy growth.

The investigations include the no-slip and and slip lengths $\zeta = 0.004, 4/Re$. The choice of the small slip 0.004 and slip equal to $4/Re$ is taken for the purpose of comparison since it is used in [104, 35] to show the effect of Reynolds number on the slip length. Also with the first dipole wall collision, the scaling of the maximum enstrophy $\Omega(t)_{max}$ for no-slip and different slip lengths boundaries will be demonstrated.

The examination of the dissipation of the kinetic energy for dipole wall collisions will consider three regimes. Taking Figure 5.3, as an example, the dissipation of the energy increases rapidly around $t = 0.3$ where the dipole reaches the wall while the dissipation is stable before $t = 0.3$. So the first regime is located before the first dipole wall collision. In that regime and according to equation (6.15) the enstrophy is changing slowly and the effect of the boundary is negligible. In this regime from equation (6.15), the scale of the energy dissipation satisfies the following:

$$E(t_2) - E(t_1) \propto Re^{-1}. \tag{6.21}$$

The second regime is located when the dipole approaches the wall and the effect of the vortices starts to appear on the boundary to generate a boundary layer. As noted from Chapter 1, the boundary layer thickness is proportional to $Re^{-1/2}$. Hence Prandtl theory states that in the boundary layer the dissipation of the energy scales with a fractional power of Re such that

$$E(t_2) - E(t_1) \propto Re^{-1/2}. \tag{6.22}$$

In the third regime, the generation of the vortices is reduced at the boundary. For different slip lengths, the total enstrophy collapses onto one line without any peaks. Therefore, the scaling of the dissipation of the total energy and the enstrophy that will be investigated is based on equation (6.16).
.

6.3 Energy dissipation for normal case

As mentioned previously, there are three regimes used to identify the energy dissipation of the dipole. For all regimes, the energy dissipation as a function of Reynolds number is taken in a range of $Re = 625$ to 10000. The first regime is identified as the period before the dipole wall collision. The average dissipation is evaluated in the range of time $t \in [0, 0.2]$ for different slip lengths, see Figure 5.6, where the energy dissipation for different slip lengths collapses onto one line in this time interval. The energy dissipation scales as Re^{-1} for all slip and no-slip boundary conditions, as shown in Figure 6.6. The dissipation of the energy rate and the growth of the enstrophy will be divided by $\Delta(t) = (t_2 - t_1)$.
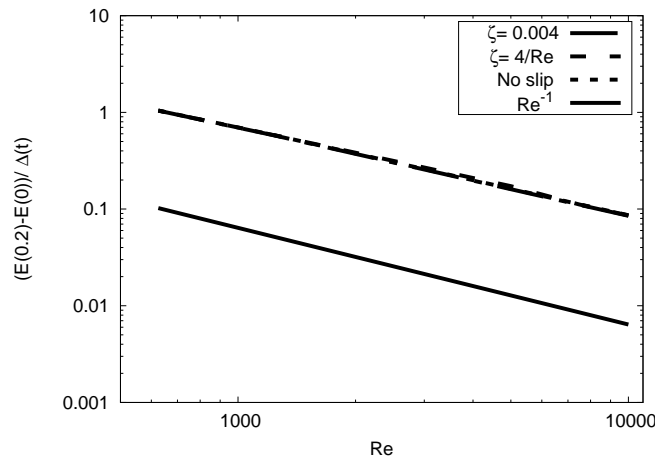
Figure 6.6: Energy dissipation for normal case in the free-viscosity regime, $t \in [0, 0.2]$. The dissipation of the energy for slip lengths: ζ=0.004 (dashed), $\zeta = 4/Re$ (dashed and dotted) and no-slip (dotted) are shown. The slop of Re^{-1} (line) is also given.

In the second regime, the dipole approaches the wall where Prandtl theory will be tested. Farge *et al.* [35] used their vorticity calculations to find the time where the Prandtl theory is verified. Also to ensure the interval chosen satisfies the Prandtl's theory, the growth of the enstrophy in the same time interval was investigated. The same procedure is followed up by Sutherland *et al.* [105]. Sutherland *et al.* [104] described the method to find the time interval where Prandtl's theory is valid. Thus the search begins by looking at the vorticity plots to find the time where the dipole collides with the wall. Then the energy dissipation is studied at each time interval after

the boundary layer appears and before it detaches from the wall and moves towards the domain where equation (6.22) is not broken. By studying the vorticity contour plots and testing the time interval, the energy dissipation that satisfies Prandtl's theory is found. Our method showed accurate results and captured the findings of Sutherland *et al.* [104]. For ζ=0.004 the boundary layer starts to appear at $t = 0.23$, so the choice for t_1 starts from 0.23, while t_2 will be taken when the boundary layer starts to separate from the wall to the fluid regime after $t = 0.47$. Figure 6.7 shows the dissipation rate of energy and the rate growth of enstrophy for closed intervals where Prandtl's theory is verified. Thus the dissipation rate of energy decay $\Delta E/\Delta t \propto Re^{\gamma}$ where γ is equal to 0.5 and the growth rate of the enstrophy use $\Delta \Omega/\Delta t$ is proportional to Re for higher Reynolds numbers, as in Figure 6.7.
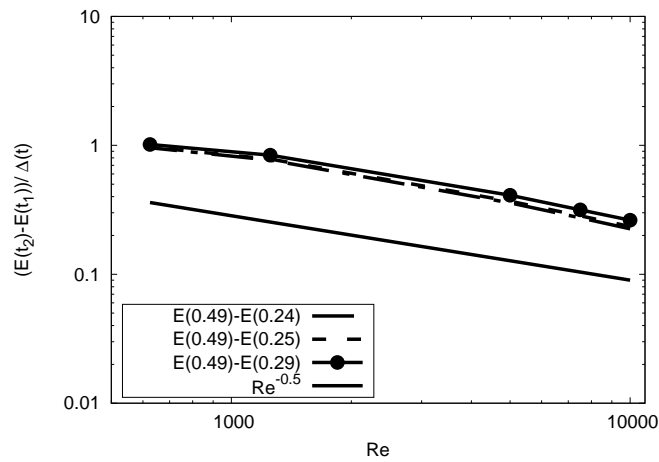
(a) Energy dissipation
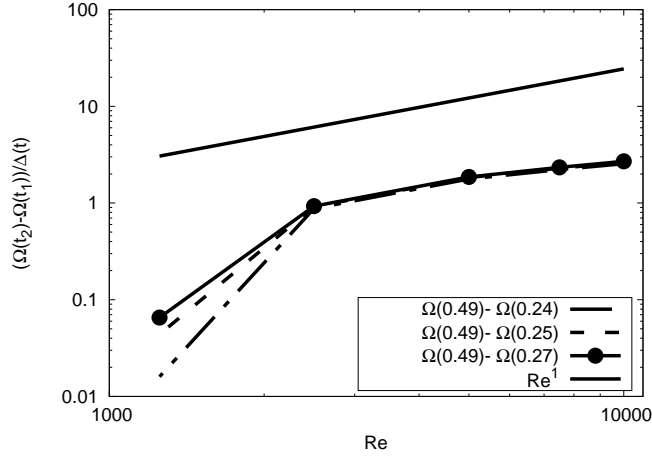
(b) Enstrophy growth

Figure 6.7:   Energy dissipation and enstrophy growth at ζ=0.004 for normal wall collision

Figures 6.8 and 6.9 present the dissipation of energy and growth of enstrophy scales for no-slip wall and a wall with a Navier-slip boundary condition with slip length $\zeta = 4/Re$. From the vorticity contours, the generation of a boundary layer appears earlier than for ζ=0.004. In these cases the boundary layer starts to appear around $t = 0.2$. It was observed that the energy dissipation scale for these cases is proportional to $Re^{-\gamma}$ where $\gamma = 0.5$ for $Re \geq 1252$ and $\gamma = 0.43$ for $Re < 1252$. These results coincide with the growth of enstrophy differences such that $\Delta\Omega \propto Re$. Thus, following [104], $\Delta\Omega$ is satisfying Prandtl's boundary layer theory. However, the enstrophy growth for LBM for $\zeta = 0.004, 4/Re$ and the no-slip case gave the same range of slope for higher Reynolds numbers where the enstrophy grows linearly with Re.
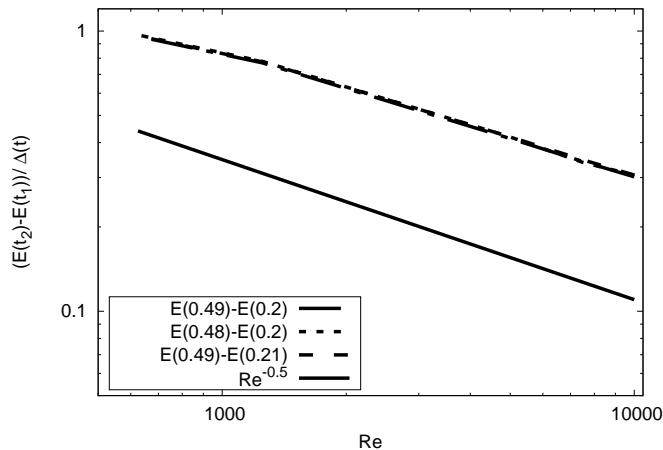
(a) Energy dissipation

(b) Enstrophy growth

Figure 6.8: Energy dissipation and enstrophy growth for no-slip for normal dipole wall collision.
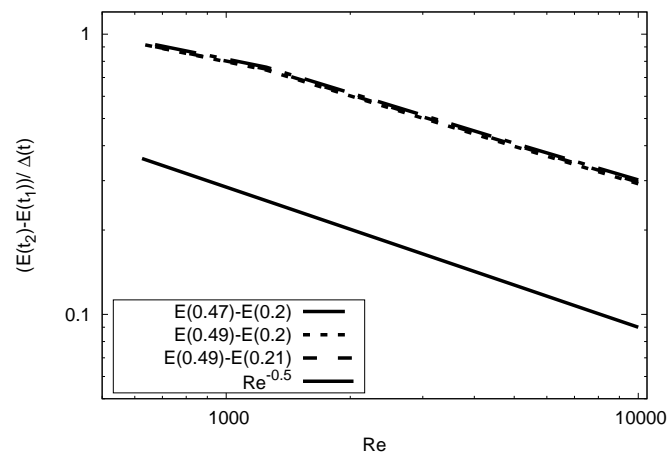
(a) Energy dissipation

(b) Enstrophy growth

Figure 6.9: Energy dissipation and enstrophy growth at $\zeta = 4/Re$ for normal dipole wall collision.

The third regime is identified as the time interval in which the boundary layer is less active and the generation of vortices at the boundary is reduced. This regime is identified as the range at $t \in [1.5, 2]$ for various slip lengths. In Figure 6.10 the dissipation of energy during this interval and the total enstrophy at $t = 2$ are plotted for various Reynolds numbers. The energy dissipation rate is independent of slip length and it is approximately proportional to $Re^{-0.5}$.

(a) Energy dissipation
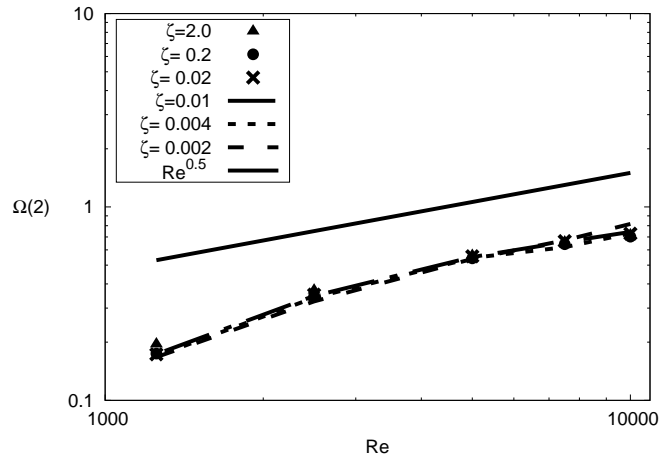
(b) Enstrophy

Figure 6.10: Energy dissipation for $t \in [1.5, 2]$ and enstrophy at $t = 2$ at different slip length for normal dipole wall collision.

Similar to [21], the scaling behaviour of the maximum enstrophy is now examined. It was found that $\Omega_{max}(t) \propto Re^{0.8}$ for no-slip dipole wall collision. For various slip lengths it was observed that the maximum enstrophy scale decreases when the slip length is increased, see Figure 6.11(a). Since there are no peaks at very high slip lengths, the maximum enstrophy value of this quantity after the first dipole incident with the boundary is taken. The energy dissipation is shown in Figure 6.11(b) for the same time interval where the maximum enstrophy appears. It is remarkable that the dissipation rate decreases by increasing the slip length. Figure 6.11 shows that differences in ζ influence the maximum enstrophy much more strongly than the dissipation rate. The discrepancy is due to the extra wall term in equation (6.15).

(a) Maximum enstrophy

(b) Energy dissipation

Figure 6.11: The maximum enstrophy and the dissipation of the energy in the same period of time for no-slip and slip normal dipole wall collision.

6.4 Energy dissipation for oblique-$30°$ dipole wall collision case

To complete our investigation of energy dissipation structure for dipole wall collision, Prandtl's boundary layer theory is applied to an oblique case. The same procedure that was used in Section 6.3 was followed where there are three regimes to test for this case. For an oblique case at an angle of $30°$ the dipole reaches the wall at approximately the same time as for a normal case. The interval used is the same as for the normal collision,

since the negative monopole reaches the wall around $t = 0.3$ where the boundary layer appears at the same time as for the normal case, see Figure 4.10 (b). Figure 6.12 plots the dissipation of the energy and the growth of the enstrophy rates near the wall for $\zeta = 0.004, 4/Re$ and no-slip cases for $t \in [0.21, 0.48]$ (again as for normal case, these results were not sensitive to the time range interval). The energy dissipation and enstrophy growth are consist with Prandtl's theory in this regime.
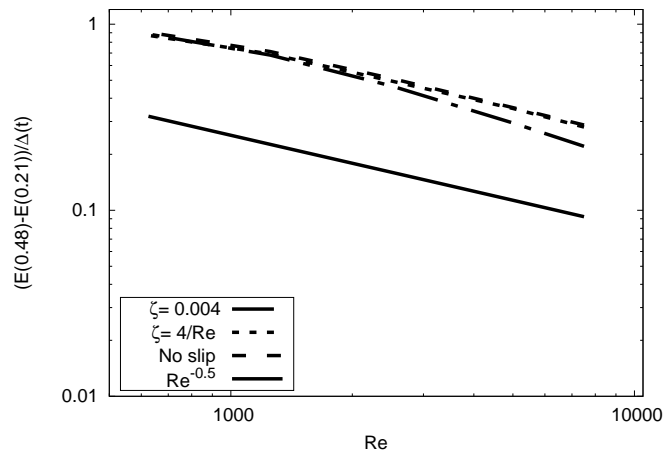
(a) Energy dissipation
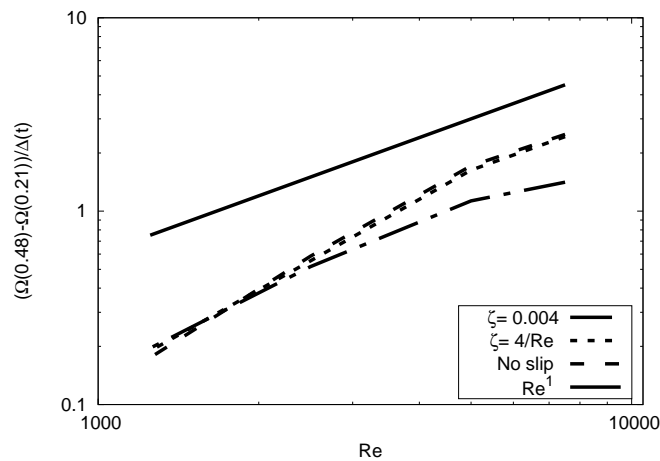
(b) Enstrophy growth

Figure 6.12: Energy dissipation and enstrophy growth for for oblique-30° dipole wall collision

6.5 Energy dissipation for oblique-$45°$ dipole wall collision case

The next test studies the dissipation of the energy for the dipole wall collision at an angle of $45°$. Note again there are three regimes to identify the energy dissipation rate. Since the distance that the dipole travels to reach the wall is higher at this angle, the time interval for the second regime is different from the previous cases. For the first regime $t \in [0, 0.23]$ where the dipole travels towards the wall, the dissipation rates for $\zeta = 0.004, 4/Re$ and no-slip cases are plotted in Figure 6.13.
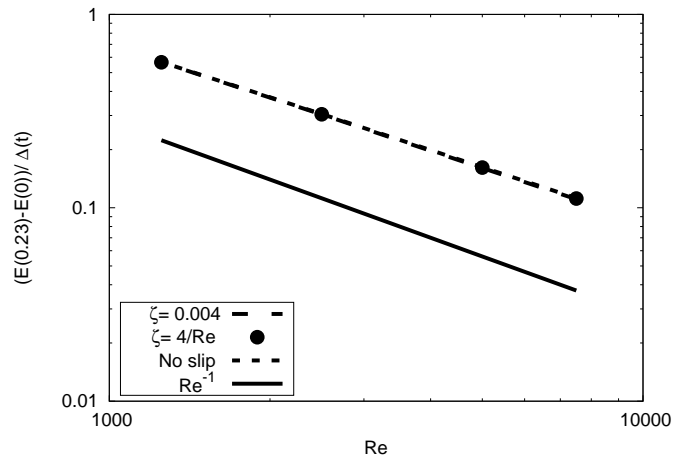
Figure 6.13: Energy dissipation for oblique case at an angle $45°$ for the free viscosity regime. The dissipation of the energy is shown for slip lengths $\zeta = 0.004$ (dashed), $\zeta = 4/Re$ (dashed and dotted) and the no-slip boundary (dotted). The slope of Re^{-1} (line) is given..

The same procedure as before was followed to identify the range of collision time intervals for the second regime where Prandt's theory holds. For various slip lengths and no-slip cases, the results are consistent with boundary layer theory in the range of the collision time intervals. Since the distance that the dipole travels to reach the corner is longer, the time interval for the second regime is different. For higher Reynolds numbers, the decay of the energy gives the slope -0.5. The enstrophy growth is linear for higher Reynolds numbers. The maximum enstrophy was evaluated and similar results as for the normal case and the findings of Clercx and Heijsk [21] were found. As was the case for the normal collision, the maximum enstrophy slope decreases from

$\gamma = 0.8$ for a no-slip case to $\gamma = 0.1$ for $\zeta = 0.2$ and 2 where $\Omega_{max}(t) \propto Re^{\gamma}$, see Figure 6.11.
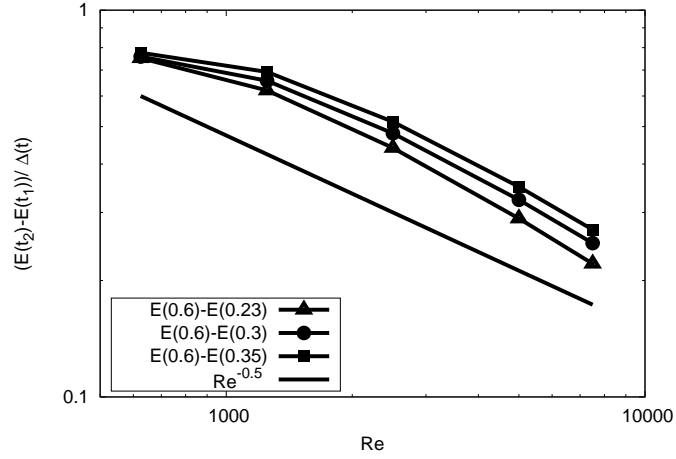
(a) Energy dissipation
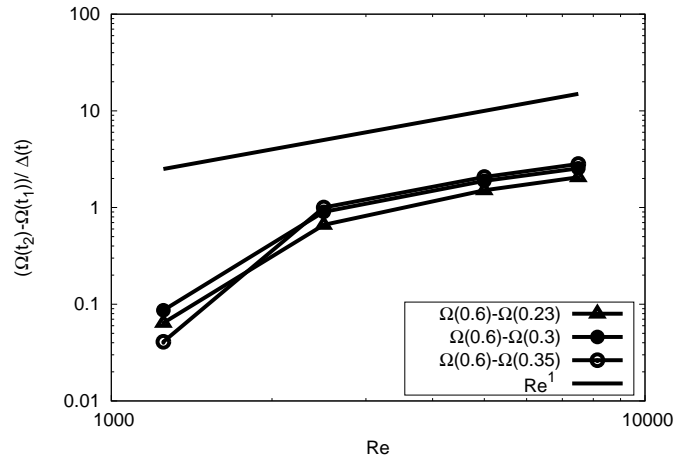
(b) Enstrophy growth

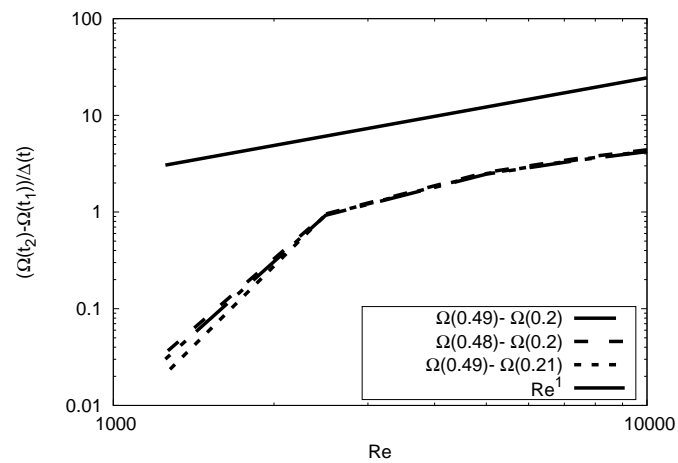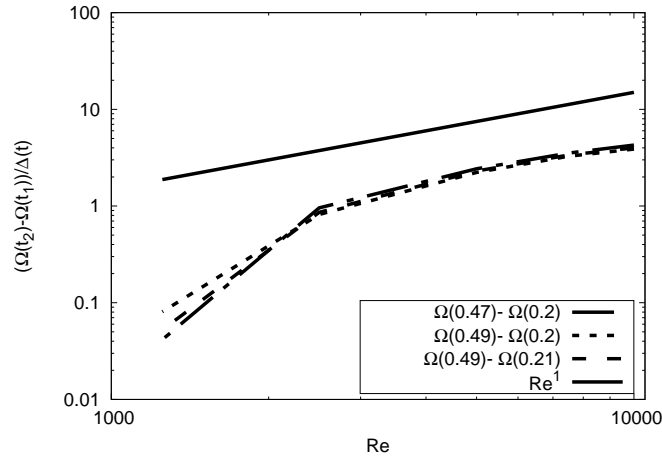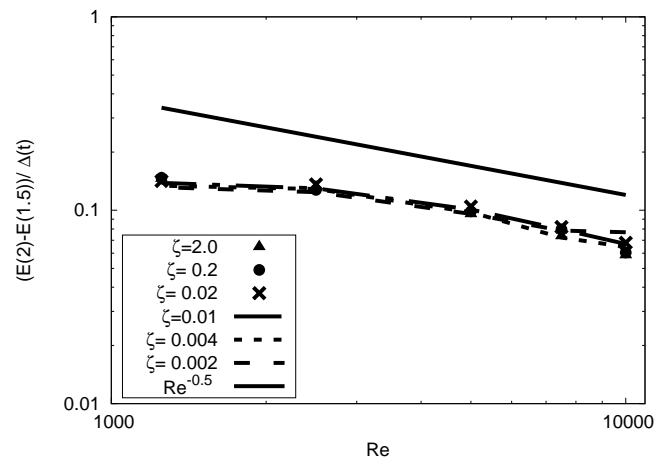Figure 6.14: Energy dissipation and enstrophy growth scales at $\zeta = 0.004$ for oblique-45° dipole wall collision.
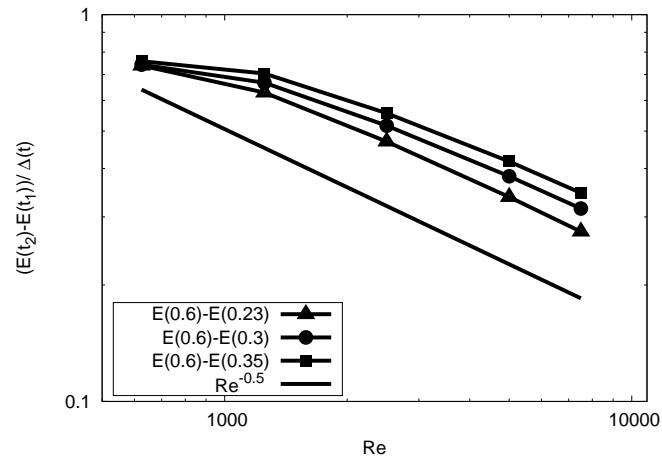
(a) Energy dissipation
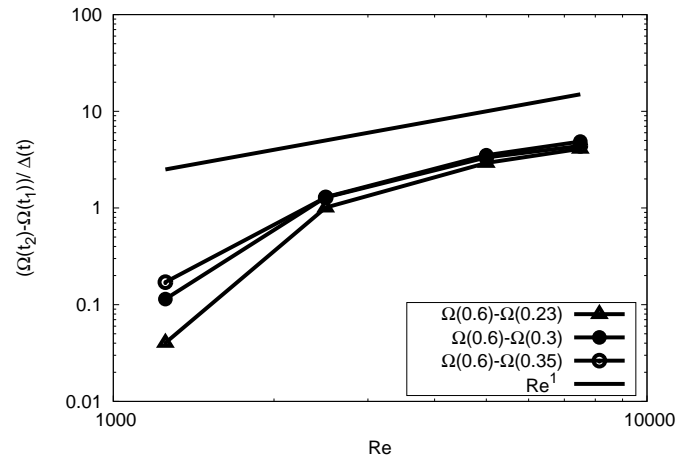
(b) Enstrophy growth

Figure 6.15: Energy dissipation and enstrophy growth scales at $\zeta = 4/Re$ for oblique-45° dipole wall collision
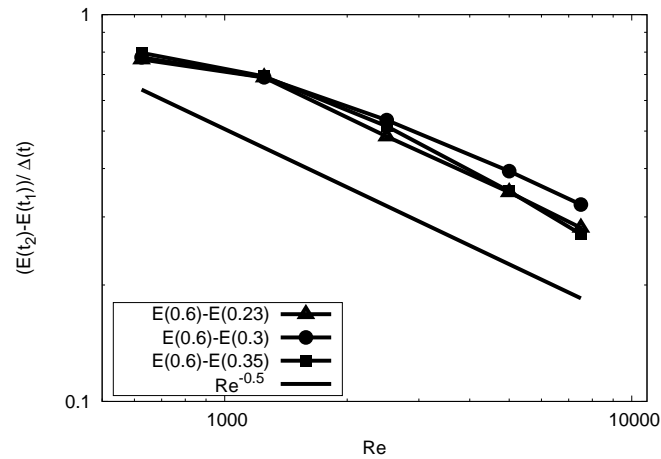
(a) Energy dissipation
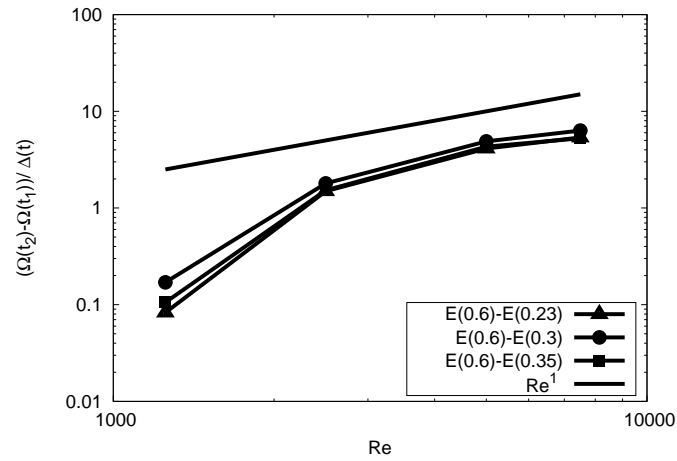
(b) Enstrophy growth

Figure 6.16: Energy dissipation and enstrophy growth at no-slip for oblique-45° dipole wall collision.

For this case, the third regime was identified as the previous $t \in [1.5, 2]$. For the no-slip, $\zeta = 0.002$ and $\zeta = 0.004$ boundaries the dipole is still active and continues to generate small dipoles at boundaries until the primary dipole disappears, see Figures 5.18 and 5.23. As a result, the enstrophy is still fluctuating in time for these slip lengths, thus it is not appropriate to evaluate average values over this period. Figure 6.17 shows the dissipation of the energy for $t \in [1.5, 2]$ with the enstrophy at $t = 2$ for slip lengths $\zeta = 2$, 0.2, 0.02 and 0.01.
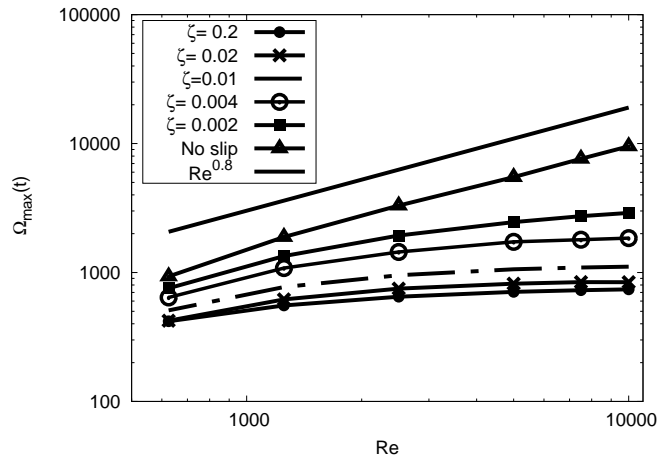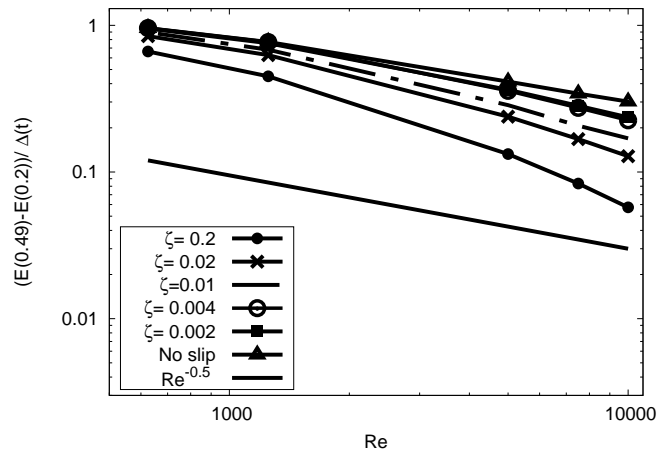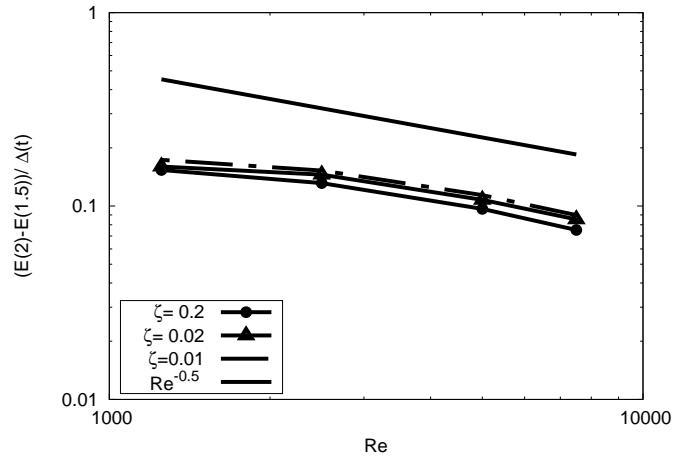
(a) Energy dissipation
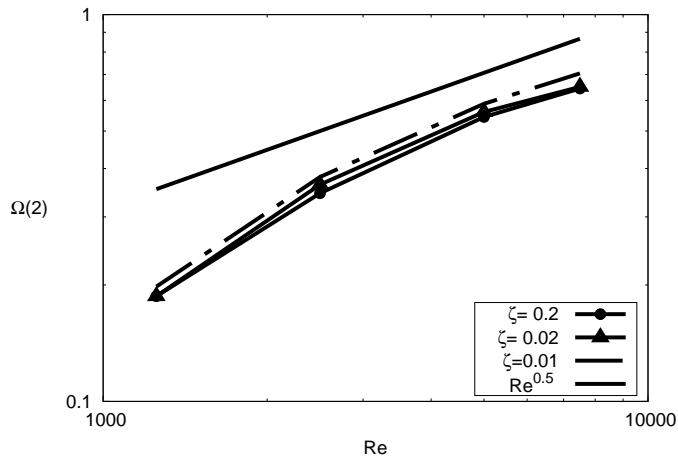
(b) Enstrophy

Figure 6.17: Energy dissipation for $t \in [1.5, 2]$ and enstrophy at $t = 2$ scales at different slip lengths for oblique-45° dipole wall collision.

6.6 Conclusion

The relationship between the dissipation of the kinetic energy and the growth of the enstrophy was examined in this chapter. Conventionally, the dissipation rate is directly proportional to the enstrophy; however, it has been shown here that the presence of wall slip creates additional dissipation. This relation was found theoretically and confirmed numerically by using the LBM. The extra dissipation is due to contributions from $\boldsymbol{\omega} \times \mathbf{u}$ at slip boundaries. This effect vanishes completely for both no-slip ($\mathbf{u} = 0$) and free-slip ($\omega = 0$) boundaries and has maximum influence for finite values of slip

length, since the formation of vortices at the wall is reduced. The analysis showed that the dissipation of the energy fluctuated probably due to compressibility effects. By reducing the compressibility effect which is represented by the Mach number and taking the moving average over 100 time steps, the oscillation of the dissipation of the energy in equation (6.15) was eliminated. So, from this relation we can measure the quality of the computational results. The numerical study was performed for intermediate and higher Reynolds numbers, fixed slip length and $\zeta \propto Re^{-1}$. Following previous studies, the dissipation of the energy scales was investigated for the normal dipole wall collision then we extend the study to various dipole release angles. The study includes three regimes. For different angles of incidence, the first stage the dissipation of the energy is proportional to Re^{-1}. In the second regime, where the boundary layer effects are dominate, energy dissipation is consistent with the Prandtl theory for which $\frac{dE}{dt} \propto Re^{-0.5}$ and $\Delta\Omega(t) \propto Re$. The last stage is when the boundary layer production is reduced, then the dissipation of the energy was proportional to $Re^{-0.5}$ and enstrophy $\propto Re^{0.5}$. In all cases, the maximum enstrophy scaled $Re^{0.8}$ while, it decreased significantly with the increasing slip length.

Chapter 7

Analysis of the stress field computed by the lattice Boltzmann equation

As pointed out in the previous chapters, moment-based boundary conditions for both slip and no-slip are second-order accurate for simple and complex flows. Although the simulations that were carried out showed that this scheme has a simple and accurate framework for the lattice Boltzmann method, it nevertheless has its shortcomings. For example, the results of BGK model are, like other on-grid methods, unstable in two-dimensional flows at high Reynolds numbers and coarse resolutions like in the cavity flow. The reasons why are still not clear. Reis [94] focussed his attention on one problem in the Poiseuille flow for the no-slip boundary conditions. The investigation showed that the tangential stress of the LBM does not vanish at a solid boundary, which is contrary to the stress of the Navier-Stokes equations. It appears that the LBM stress includes a non-vanishing Burnett contribution that comes from truncating the Chapman-Enskog expansion at $O(Kn^2)$. Moreover, the tangential stress develops spurious oscillations at the boundary if the boundary conditions do not take into consideration the Burnett term, and they may also have an affect on the bulk flow. To solve this problem, Reis [94] solved the equations governing the LBM stress field analytically in planar channel

flow and proposed a consistent boundary condition implementation that depends on the deviatoric stress

$$\boldsymbol{\Gamma} = \boldsymbol{\Pi}^0 - \boldsymbol{\Pi}. \tag{7.1}$$

By applying the new conditions, the spurious oscillations are eliminated at the boundary.

Since this thesis involves an investigation of slip and no-slip boundaries, this chapter reviews the investigation of a no-slip case of [94] and gives a detailed study of the three components of the deviatoric stress. Then based on the same procedure an attempt is made to extend the method to include the Navier-slip condition with the moment-based approach. Finally, to avoid the spurious oscillations for the slip conditions, new constraint at the boundary which depends on the stress will be found for two models of lattice Boltzmann equation.

7.1 The evaluation of the deviatoric stress Γ

The density ρ, momentum $\rho\mathbf{u}$ and the stress $\boldsymbol{\Pi}$ can be found for LBM by analysing its moments with respect to the particle velocity. To establish this, the three hydrodynamic moment equations from the discrete Boltzmann equations (2.83), (2.84) and (2.85) are used, but instead of using the Chapman-Enskog expansion to find the solution for long timescales, the methodology that was proposed by using Maxwells equations [59]. In the kinetic theory, the moments of the particle velocity distribution function can be written in the frame moving with the flow, that is they can be expressed with respect to the peculiar velocity. This velocity is defined as the difference between the local fluid velocity and the particle velocity such that $\boldsymbol{\xi}_i = \mathbf{c}_i - \mathbf{u}$. By using the definition of the third moment of the peculiar velocity $\boldsymbol{\xi}_i$ one can get

$$\phi_{\alpha\beta\gamma} = \sum f_i \xi_{i\alpha} \xi_{i\beta} \xi_{i\gamma},$$

$$
\begin{aligned}
&= \sum f_i(c_{i\alpha} - u_\alpha)(c_{i\beta} - u_\beta)(c_{i\gamma} - u_\gamma), \\
&= \sum f_i c_{i\alpha} c_{i\beta} c_{i\gamma} - \sum f_i c_{i\alpha} c_{i\beta} u_\gamma - \sum f_i c_{i\alpha} c_{i\gamma} u_\beta \\
&+ \sum f_i c_{i\alpha} u_\beta u_\gamma - \sum f_i c_{i\beta} c_{i\gamma} u_\alpha + \sum f_i c_{i\beta} u_\alpha u_\gamma \\
&+ \sum f_i c_{i\gamma} u_\alpha u_\beta - \sum f_i u_\alpha u_\beta u_\gamma,
\end{aligned}
\tag{7.2}
$$

Using the definitions $Q_{\alpha\beta\gamma} = \sum f_i c_{i\alpha} c_{i\beta} c_{i\gamma}$ and $\Pi_{\alpha\beta} = \sum f_i c_{i\alpha} c_{i\beta}$ to simplify equation (7.2) and truncating the expression at $O(u_\alpha u_\beta u_\gamma)$ yields

$$
\phi_{\alpha\beta\gamma} = Q_{\alpha\beta\gamma} - \Pi_{\alpha\beta} u_\gamma - \Pi_{\alpha\gamma} u_\beta - \Pi_{\beta\gamma} u_\alpha + O(\rho u_\alpha u_\beta u_\gamma),
\tag{7.3}
$$

then by reformulating the last equation for the deviatoric stress of (7.1) we have

$$
Q_{\alpha\beta\gamma} = \phi_{\alpha\beta\gamma} + u_\alpha(\rho c_s^2 \delta_{\beta\gamma} - \Gamma_{\beta\gamma}) + u_\beta(\rho c_s^2 \delta_{\alpha\gamma} - \Gamma_{\alpha\gamma}) + u_\gamma(\rho c_s^2 \delta_{\alpha\beta} - \Gamma_{\alpha\beta}),
\tag{7.4}
$$

By using equations (7.4) and (7.1), the left side of equation (2.85) can be found to be

$$
\partial_t \Pi_{\alpha\beta} + \partial_\gamma Q_{\alpha\beta\gamma} = \partial_t(\Pi_{\alpha\beta}^{(0)} - \Gamma_{\alpha\beta}) + \partial_\gamma \bigg(\phi_{\alpha\beta\gamma} + u_\alpha(\rho c_s^2 \delta_{\beta\gamma} - \Gamma_{\beta\gamma}) + u_\beta(\rho c_s^2 \delta_{\alpha\gamma} - \Gamma_{\alpha\gamma})
$$
$$
+ u_\gamma(\rho c_s^2 \delta_{\alpha\beta} - \Gamma_{\alpha\beta}) \bigg).
\tag{7.5}
$$

The temporal derivative of the equilibrium stress can be found by using equation (2.104)

$$
\begin{aligned}
\partial_t \Pi_{\alpha\beta}^{(0)} &= \partial_t(\rho c_s^2 \delta_{\alpha\beta} + \rho u_\alpha u_\beta), \\
&= -c_s^2 \delta_{\alpha\beta} \partial_\gamma \rho u_\gamma - u_\alpha \partial_\gamma \Pi_{\beta\gamma} - u_\beta \partial_\gamma \Pi_{\alpha\gamma} + u_\alpha u_\beta \partial_\gamma \rho u_\gamma + u_\alpha F_\beta + u_\beta F_\alpha,
\end{aligned}
\tag{7.6}
$$

which leads to,

$$
\partial_t \Pi_{\alpha\beta}^0 = -c_s^2 \delta_{\alpha\beta} \partial_\gamma \rho u_\gamma - u_\alpha \partial_\gamma(\Pi_{\beta\gamma}^0 - \Gamma_{\beta\gamma}) - u_\beta \partial_\gamma(\Pi_{\alpha\gamma}^0 - \Gamma_{\alpha\gamma}) + u_\alpha F_\beta + u_\beta F_\alpha +
$$
$$
u_\alpha u_\beta \partial_\gamma \rho u_\gamma.
\tag{7.7}
$$

The equation of the deviatoric stress can be found by applying equation (7.7) into equation (7.5) then substituting the result into equation (2.97)

$$\Gamma_{\alpha\beta} + \tau\left(\partial_t\Gamma_{\alpha\beta} + u_\gamma\partial_\gamma\Gamma_{\alpha\beta} + \Gamma_{\alpha\gamma}\partial_\gamma u_\beta + \Gamma_{\beta\gamma}\partial_\gamma u_\alpha - \partial_\gamma\phi_{\alpha\beta\gamma}\right) = \mu(\partial_\beta u_\alpha + \partial_\alpha u_\beta). \tag{7.8}$$

The third-order moment $\phi_{\alpha\beta\gamma} \approx \phi_{\alpha\beta\gamma}^{(0)}$ as long as its relaxation time is short. Note that if the stress were Newtonian, the term in the brackets on the left-hand side would be absent. Therefore, the three components of the stress in equation (7.8) for the time independent, unidirectional, channel flow where $\mathbf{u} = (u(y), 0)$ are

$$\Gamma_{xx} + 2\tau\Gamma_{xy}\frac{\partial u}{\partial y} = 0, \tag{7.9}$$

$$\Gamma_{yy} = 0, \tag{7.10}$$

$$\Gamma_{xy} - \mu\frac{\partial u}{\partial y} = 0. \tag{7.11}$$

Equation (7.11) is the Newtonian shear stress and equation (7.10) is the normal component of the Newtonian stress in this flow. However, the tangential component of the stress, equation (7.9), does not vanish, as would be the case in the Navier-Stokes equations in unidirectional channel flow. In fact, the stress is typical of the stress of the Burnett equation for the Poiseuille flow which can be found by truncating the Chapman-Enskog expansion of the continuous Boltzmann equation at $O(\tau^2)$.

7.2 The components of the stress tensor for channel flow

A recurrence relation for the LBM in planar channel flows was found in Chapter 2 and solved analytically for the velocity profile. Reis [94] used the same procedure to find the three components of the stress tensor $\mathbf{\Gamma}$ then used them to find consistent boundary conditions for the LBM stress. Here, the solution of the recurrence equation for the

three components of the stress tensor are presented in detail. Since the algorithm is formulated in terms of $\bar{f}_i$, then one must be aware of the relationship between $\mathbf{\Gamma}$ and $\overline{\overline{\Pi}}$

$$\mathbf{\Gamma} = \mathbf{\Pi}^0 - \mathbf{\Pi} = \frac{\left(2\tau(\mathbf{\Pi}^{(0)} - \overline{\overline{\Pi}}) - \tau(\mathbf{Fu} + \mathbf{uF})\right)}{(2\tau + 1)}, \tag{7.12}$$

where $\mathbf{F} = (\rho G, 0)$ is the force term in the unidirectional flow.

Firstly, the shear stress tensor can be found in terms of the recurrence relations of $\bar{f}_i^j$ in equation (3.28) as

$$
\begin{aligned}
\overline{\Pi}_{xy}^j &= \sum \bar{f}_i c_{ix} c_{iy} = (\bar{f}_5^j - \bar{f}_6^j + \bar{f}_7^j + \bar{f}_8^j) \\
&= \frac{\rho}{2(\tau + 1/2)}(u_{j+1}v_{j+1} + u_{j-1}v_{j-1}) + \frac{\tau\rho G}{2(\tau + 1/2)}(v_{j+1} + v_{j-1}) \\
&\quad + \frac{\rho}{6(\tau + 1/2)}(u_{j-1} - u_{j+1}) + \frac{(\tau - 1/2)}{(\tau + 1/2)}(\bar{f}_5^{j-1} - \bar{f}_6^{j-1} + \bar{f}_7^{j+1} - \bar{f}_8^{j+1}).
\end{aligned} \tag{7.13}
$$

By equation (3.56) $v_j = 0$ in plane channel flow, so equation (7.13) becomes

$$\overline{\Pi}_{xy}^j = \frac{\rho}{6(\tau + 1/2)}(u_{j-1} - u_{j+1}) + \frac{(\tau - 1/2)}{(\tau + 1/2)}(\bar{f}_5^{j-1} - \bar{f}_6^{j-1} + \bar{f}_7^{j+1} - \bar{f}_8^{j+1}). \tag{7.14}$$

Equations (3.36), (3.37), (3.38) and (3.39) are used to eliminate the distribution functions with indices $(j + 1)$ and $(j - 1)$ in favour of $\bar{f}_j$

$$\overline{\Pi}_{xy}^j = \frac{\rho\tau}{3(\tau + 1/2)}(\bar{u}_{j-1} - \bar{u}_{j+1}) + \frac{(\tau - 1/2)^2}{(\tau + 1/2)^2}\overline{\Pi}_{xy}^j, \tag{7.15}$$

so

$$\overline{\Pi}_{xy}^j = -\frac{\rho(\tau + 1/2)}{6}(\bar{u}_{j+1} - \bar{u}_{j-1}). \tag{7.16}$$

For Poiseuille flow $\overline{\Pi}_{xy}^{(0)} = 0$, so by applying equation (7.16) into equation (7.12) one can get

$$\Gamma_{xy}^{j} = \overline{\Pi}_{xy}^{0} - \overline{\Pi}_{xy}^{j} = \frac{1}{2}\mu(\bar{u}_{j+1} - \bar{u}_{j-1}), \tag{7.17}$$

where $\mu = \rho\tau/3$. This coincides with the second-order approximation to $\Gamma_{xy}^{j} = \mu(\partial u/\partial y)$.

For channel flow and since the flow is moving in the tangential direction only, zero normal momentum flux should be proven. Similar to the previous steps we have

$$\overline{\Pi}_{yy}^{j} = \sum \bar{f}_i c_{iy} c_{iy} = \bar{f}_2^{j} + \bar{f}_4^{j} + \bar{f}_5^{j} + \bar{f}_6^{j} + \bar{f}_7^{j} + \bar{f}_8^{j} \tag{7.18}$$

Inserting equations (3.45) and (3.46) into equation (7.18) yields

$$\overline{\Pi}_{yy}^{j} = \frac{\rho}{3(\tau + 1/2)} + \frac{(\tau - 1/2)}{(\tau + 1/2)}(\bar{f}_2^{j-1} + \bar{f}_5^{j-1} + \bar{f}_6^{j-1} + \bar{f}_4^{j+1} + \bar{f}_7^{j+1} + \bar{f}_8^{j+1}) \tag{7.19}$$

To eliminate $\bar{f}_i^{\mp j}$, equations (3.48),(3.49),(3.50) and (3.51) are combined then applied into equation (7.19). The vertical velocity is $\bar{v}_j = 0$, therefore

$$\overline{\Pi}_{yy}^{j} = \frac{\rho}{3(\tau + 1/2)} + \frac{(\tau - 1/2)}{(\tau + 1/2)}\left(\frac{\rho}{3(\tau + 1/2)} + \frac{(\tau - 1/2)}{(\tau + 1/2)}\overline{\Pi}_{yy}^{j}\right), \tag{7.20}$$

so the normal momentum tensor is

$$\overline{\Pi}_{yy}^{j} = \rho/3. \tag{7.21}$$

Using the transformation in equation (7.12) gives the normal deviatoric stress

$$\Gamma_{yy}^{j} = 0, \tag{7.22}$$

which is consistent with the assumption of the unidirectional channel flow.

The next step will be finding the tangential deviatoric stress, starting with the

tangential momentum flux

$$\overline{\Pi}^j_{xx} = \sum \bar{f}_i c_{ix} c_{ix} = \bar{f}^j_1 + \bar{f}^j_3 + \bar{f}^j_5 + \bar{f}^j_6 + \bar{f}^j_7 + \bar{f}^j_8. \tag{7.23}$$

Applying the recurrence relation of equations (3.28b), (3.28d), (3.28f), (3.28g), (3.28h) and (3.28i) to equation (7.23) and $v_j = 0$ gives

$$\begin{aligned}
\overline{\Pi}^j_{xx} &= \frac{2}{9} \frac{(\tau + 1)}{(\tau + 1/2)} \rho + \frac{2}{3} \rho u^2_j + \frac{\rho}{6(\tau + 1/2)} (u^2_{j-1} + u^2_{j+1}) \\
&+ \frac{\rho \tau G}{3(\tau + 1/2)} (u_{j+1} + u_{j-1}) + \frac{4}{3} \tau \rho G u_j + \frac{(\tau - 1/2)}{(\tau + 1/2)} \\
&(\bar{f}^{j-1}_5 + \bar{f}^{j-1}_6 + \bar{f}^{j+1}_7 + \bar{f}^{j+1}_8).
\end{aligned} \tag{7.24}$$

To express $\overline{\Pi}^j_{xx}$ in terms of the velocities, the $\bar{f}^{j\pm1}_i$ should be eliminated from the last equation. Firstly, introduce $F_* = F^{j+1} + F^{j-1}$ where $F^{j-1} = \bar{f}^{j-1}_5 + \bar{f}^{j-1}_6$ and $F^{j+1} = \bar{f}^{j+1}_7 + \bar{f}^{j+1}_8$. To find F^{j-1}, the tangential momentum of grid $(j-1)$ is applied as follows

$$F^{j-1} = \overline{\Pi}^{j-1}_{xx} - (\bar{f}^{j-1}_1 + \bar{f}^{j-1}_3 + \bar{f}^{j-1}_5 + \bar{f}^{j-1}_6 + \bar{f}^{j-1}_7 + \bar{f}^{j-1}_8). \tag{7.25}$$

Apply the recurrence relations of $\bar{f}_i$ and replacing (j) with $(j-1)$ yields

$$\begin{aligned}
F^{j-1} &= \overline{\Pi}^{j-1}_{xx} - \bigg(\frac{4}{3} \tau \rho G u_{j-1} + \frac{1}{3(\tau + 1/2)} \tau \rho G u_j - \frac{\rho}{6(\tau + 1/2)} v_j \\
&+ \frac{2}{3} \rho u^2_{j-1} - \frac{1}{3} \rho v^2_{j-1} + \frac{\rho}{6(\tau + 1/2)} u^2_j + \frac{\rho}{6(\tau + 1/2)} v^2_j \\
&\frac{\rho}{18(\tau + 1/2)} + \frac{2\rho}{9} + \frac{(\tau - 1/2)}{(\tau + 1/2)} (\bar{f}^j_7 + \bar{f}^j_8) \bigg).
\end{aligned} \tag{7.26}$$

Now the tangential momentum of index $(j+1)$ is applied as follows:

$$F^{j+1} = \overline{\Pi}^{j+1}_{xx} - (\bar{f}^{j+1}_1 + \bar{f}^{j+1}_3 + \bar{f}^{j+1}_5 + \bar{f}^{j+1}_6 + \bar{f}^{j+1}_7 + \bar{f}^{j+1}_8). \tag{7.27}$$

Apply the recurrence relations of $\bar{f}_i$, replacing (j) with $(j+1)$ to produce

$$
\begin{aligned}
F^{j+1} = \overline{\Pi}_{xx}^{j+1} - \Bigg(&\frac{4}{3}\tau\rho G u_{j+1} + \frac{1}{3(\tau+1/2)}\tau\rho G u_j + \frac{\rho}{6(\tau+1/2)}v_j \\
&+ \frac{2}{3}\rho u_{j+1}^2 - \frac{1}{3}\rho v_{j+1}^2 + \frac{\rho}{6(\tau+1/2)}u_j^2 + \frac{\rho}{6(\tau+1/2)}v_j^2 \\
&\frac{\rho}{18(\tau+1/2)} + \frac{2\rho}{9} + \frac{(\tau-1/2)}{(\tau+1/2)}(\bar{f}_5^j + \bar{f}_6^j)\Bigg).
\end{aligned}
\tag{7.28}
$$

Combine equation (7.26) and equation (7.28) to give

$$
\begin{aligned}
F_* =&\overline{\Pi}_{xx}^{j+1} + \overline{\Pi}_{xx}^{j-1} - \frac{4}{3}\tau\rho G u_{j-1} - \frac{2}{3}\rho u_{j-1}^2 - \frac{1}{3}\rho v_{j-1}^2 - \frac{2}{3(\tau+1/2)}\tau\rho G u_j \\
&- \frac{\rho}{3(\tau+1/2)}u_j^2 - \frac{\rho}{3(\tau+1/2)}v_j^2 - \frac{4}{3}\tau\rho G u_{j+1} - \frac{2}{3}\rho u_{j+1}^2 + \frac{1}{3}\rho v_{j+1}^2 \\
&- \frac{\rho}{9(\tau+1/2)} - \frac{4\rho}{9} - \frac{(\tau-1/2)}{(\tau+1/2)}(\bar{f}_5^j + \bar{f}_6^j + \bar{f}_7^j + \bar{f}_8^j).
\end{aligned}
\tag{7.29}
$$

The last term of equation (7.29) can be found easily from equation (7.23) where

$$
\bar{f}_5^j + \bar{f}_6^j + \bar{f}_7^j + \bar{f}_8^j = \overline{\Pi}^j - \Bigg(\frac{\rho}{9}(6u_j^2 - 3v_j^2) + \frac{4\tau\rho G}{3}u_j + \frac{2\rho}{9}\Bigg).
\tag{7.30}
$$

After applying equation (7.30) to equation (7.29) and setting $v_j = 0$ then multiplying it by $(\tau-1/2)/(\tau+1/2)$, adding the result into equation (7.24) to get

$$
\begin{aligned}
\overline{\Pi}_{xx}^j =& \frac{(\tau-1/2)}{(\tau+1/2)}\overline{\Pi}_{xx}^{j+1} - \frac{(\tau-1/2)^2}{(\tau+1/2)^2}\overline{\Pi}_{xx}^j + \frac{(\tau-1/2)}{(\tau+1/2)}\overline{\Pi}_{xx}^{j-1} + \frac{(3-4\tau)}{3(\tau+1/2)}\rho\tau G\Bigg(\frac{\rho}{3(\tau+1/2)} \\
&(u_{j+1} + u_{j-1}) + \frac{\rho(3-4\tau)}{6(\tau+1/2)}(u_{j-1}^2 + u_{j+1}^2) + \frac{2}{3}\rho u_j^2 - \frac{(\tau-1/2)}{(\tau+1/2)}\Bigg(\frac{\rho}{3(\tau+1/2)} - \frac{2\rho}{3} \\
&\frac{(\tau-1/2)}{(\tau+1/2)}\Bigg)u_j^2 - \frac{(\tau-1/2)}{(\tau+1/2)}\Bigg(\frac{2}{3(\tau+1/2)} - \frac{4}{3}\frac{(\tau-1/2)}{(\tau+1/2)} + \frac{4}{3}\Bigg)\tau\rho G u_j + \frac{\rho}{3(\tau+1/2)^2},
\end{aligned}
\tag{7.31}
$$

where v_j and $v_{j\mp1}$ have vanished because of equations (3.53), (3.54) and (3.56). By inserting equation (7.12) into equation (7.31), the solution will be found in terms of

Γ^j_{xx} instead of $\overline{\overline{\Pi}}^j_{xx}$. Therefore, equation (7.31) can be expressed as

$$\Gamma^j_{xx} - (\tau^2 - 1/4)\left(\Gamma^{j-1}_{xx} - 2\Gamma^j_{xx} + \Gamma^{j+1}_{xx}\right) = -\frac{1}{3}\rho\tau^2(u^2_{j-1} - 2u^2_j + u^2_{j+1})$$
$$- \frac{1}{2}\tau\rho G(u_{j-1} + 2u_j + u_{j+1}) + \frac{4}{3}\tau^3\rho G(u_{j-1} - 2u_j + u_{j+1}). \tag{7.32}$$

To solve equation (7.32) in terms of Γ_{xx}, the complementary and the particular solution of this equation should be calculated. Reis [94] gives a detailed explanation on how to find the solution of equation (7.32). In this article, the complementary solution was found by assuming $\Gamma^{j(comp)} = A\lambda^j + B\lambda^{-j}$ where $\lambda = (\tau - 1/2)/(\tau + 1/2)$. Thus, by finding the values of A and B on the boundary, the homogeneous solution is

$$\Gamma^{j(comp)}_{xx} = -\left(\frac{\Gamma^{wall}}{(\lambda^n + \lambda)}\right)\lambda + \frac{\Gamma^{wall}}{(\lambda^n + \lambda)}\lambda^{-j}. \tag{7.33}$$

By substituting the second-order particular form into equation (7.32) and applying the analytical solution of u_j the particular solution can be found that

$$\Gamma^{j(part)}_{xx} = \rho G^2\left(-6j^2 + 6j(n+1) - 3n - \frac{3}{2}n^2 - 16\tau^2 + \frac{3}{2}\right)$$
$$= -2\mu\tau\left(\frac{u_{j+1} - u_{j-1}}{2}\right)^2 - \rho G^2(16\tau^2 - 3). \tag{7.34}$$

Finally adding the complementary solution and particular solution together and setting Γ^{wall}_{xx} equal $\Gamma^{j(part)}_{xx}$ which depends on the location of the wall, yields

$$\Gamma^j_{xx} = -\frac{\Gamma^{wall}_{xx}}{(\lambda^n + \lambda)}(\lambda^j + \lambda^{n+1-j}) - 2\mu\tau\left(\frac{u_{j+1} - u_{j-1}}{2}\right)^2 - \rho G^2(16\tau^2 - 3) \tag{7.35}$$

7.2.1 The boundary conditions for the stress Γ

We now seek solutions of LBE with boundary conditions that are consistent with the deviatoric stress from the previous section. Using equation (7.12) yields the tangential

momentum at the boundary

$$\overline{\Pi}_{xx} = \frac{\rho}{3} + \rho u_s^2 - \rho G u_s - (1 + \frac{1}{2\tau})\Gamma_{xx}, \tag{7.36}$$

where u_s is the slip velocity, while the shear momentum will be

$$\overline{\Pi}_{xy} = -\left(1 + \frac{1}{2\tau}\right)\Gamma_{xy}. \tag{7.37}$$

The relation between the tangential stress and the deviatoric stress can be found by using equations (7.9), (7.11) and (7.12):

$$\overline{\Pi}_{xx} = \frac{\rho}{3} + \rho u_s^2 - \rho G u_s - \left(\frac{2\tau + 1}{\mu}\right)\Gamma_{xy}^2. \tag{7.38}$$

Substituting the relation (7.37) into equation (7.38) leads to

$$\overline{\Pi}_{xx} = \frac{\rho}{3} + \rho u_s^2 - \rho G u_s + \frac{6\tau}{\rho(\tau + 1/2)}\overline{\Pi}_{xy}^2. \tag{7.39}$$

Taking the north boundary as an example and from Table 3.1, the three linearly independent conditions are

$$\begin{aligned}
\rho \overline{u}_y &= 0, \\
\rho \overline{u}_x &= \rho u_s - \frac{1}{2}\rho G, \\
\overline{\Pi}_{xx} &= \frac{\rho}{3} + \rho u_s^2 - \rho G u_s + \frac{6\tau}{\rho(\tau + 1/2)}\overline{\Pi}_{xy}^2.
\end{aligned} \tag{7.40}$$

The conditions of equation (7.40) give the three unknown distribution functions for slip north boundary

$$
\begin{aligned}
\bar{f}_4 &= \bar{f}_1 + \bar{f}_3 + \bar{f}_2 + 2(\bar{f}_5 + \bar{f}_6) - \frac{\rho}{3} - \rho u_s^2 + \rho G u_s, \\
&\quad - \frac{6\tau}{\rho(\tau + 1/2)}\overline{\overline{\Pi}}_{xy}^2, \\
\bar{f}_7 &= \frac{\rho}{6} - \bar{f}_3 - \bar{f}_6 + \rho u_s(u_s - 1)/2 + \rho G(1/2 - u_s)/2 \\
&\quad + \frac{3\tau}{\rho(\tau + 1/2)}\overline{\overline{\Pi}}_{xy}^2, \\
\bar{f}_8 &= \frac{\rho}{6} - \bar{f}_1 - \bar{f}_5 + \rho u_s(u_s + 1)/2 - \rho G(1/2 + u_s)/2 \\
&\quad + \frac{3\tau}{\rho(\tau + 1/2)}\overline{\overline{\Pi}}_{xy}^2,
\end{aligned}
\tag{7.41}
$$

where $\overline{\overline{\Pi}}_{xy}$ can be found from the tangential momentum ρu_x at the boundary

$$
\overline{\overline{\Pi}}_{xy} = 2f_5 - 2f_6 + \frac{\rho G}{2} - \rho u_s.
\tag{7.42}
$$

The velocity at the slip wall is proportional to (du/dy) and it is controlled by a slip length ζ

$$
u_s = \zeta \frac{\partial u}{\partial y}\bigg|_{wall},
\tag{7.43}
$$

where the derivative in equation (7.43) can be obtained locally from the shear stress $\overline{\overline{\Pi}}_{xy}$ in equation (7.42), see equation (3.76). Therefore, the velocity at the wall is found to be similar to that obtained from the procedure in Section 3.7.1.

7.2.2 Numerical simulation of the deviatoric stress

In the case of the Navier slip condition with the moment-based method, from Section 3.7.1, and similar to the no-slip implementation in [94], Γ_{xx} produces an oscillation at the slip boundary. This feeds into the flow and causes fluctuations in the stress than can spread across the whole domain. Figure 7.1 plots the tangential stress for

$Re = 100$, $m_y = 33$ and $\zeta = 0.1$. In this figure a comparison between the analytical solution of equation (7.35), partial differential equation solution of equation (7.9) and lattice Boltzmann solution (7.12) is made. The lattice Boltzmann prediction and the analytical solution match and the spurious oscillations are clear. By increasing the resolution, the fluctuation in the bulk flow decreases, but it remains near the boundary, regardless of the number of grid points. The same observation holds for both small and large slip lengths, $\zeta = 0.01$ and $\zeta = 1$, as an example.

To eliminate the oscillations near the boundary, the stress boundary condition with slip boundary conditions from Section 7.2.1 was applied using the same parameters that were previously utilised. Results plotted in Figure (7.2) show that the fluctuation near the boundary disappears and the three solutions give a parabolic shape for Γ_{xx}. Some of the simulations were at lower Reynolds numbers, so we increase the relaxation time in order to calculate the stress Γ_{xx} accurately in the channel flow which reduces the Knudsen number Kn, as ($Kn \propto Ma/Re$). This gives a slower relaxation rate which breaks the hypothesis of Section 7.2. So the numerical simulation gives improper results with the absence of oscillation at the boundary, see Figure 7.3. The parameters in this Figure are taken to be $Re = 100$ and $Re = 0.1$ with $Ma = 0.01\sqrt{3}$ and the grid size is $m_y = 33$.
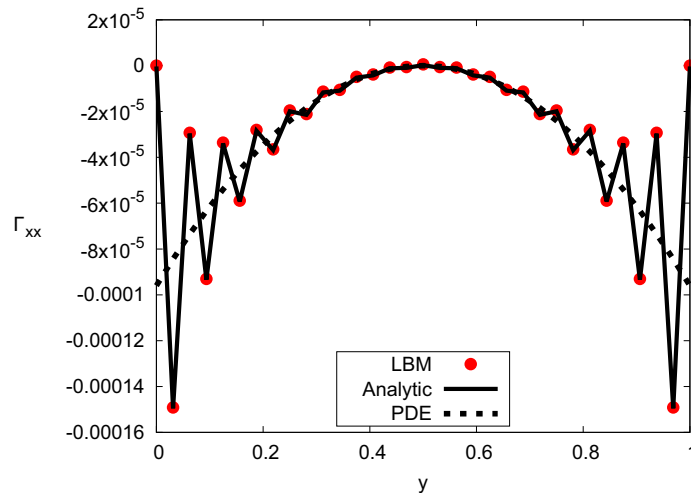
(a) $m_y = 33$
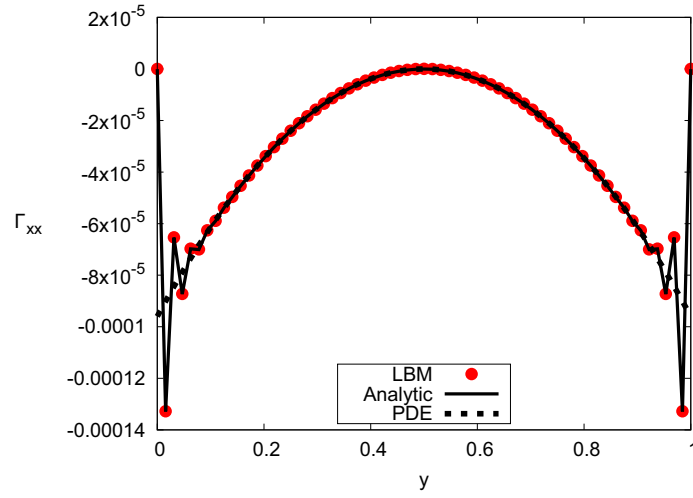
(b) $m_y = 65$

Figure 7.1: Tangential deviatoric stress for Poiseuille flow using Navier slip moment-based boundary conditions. The results are plotted for $Re = 100$, $Ma = 0.1\sqrt{3}$ and ζ=0.1.
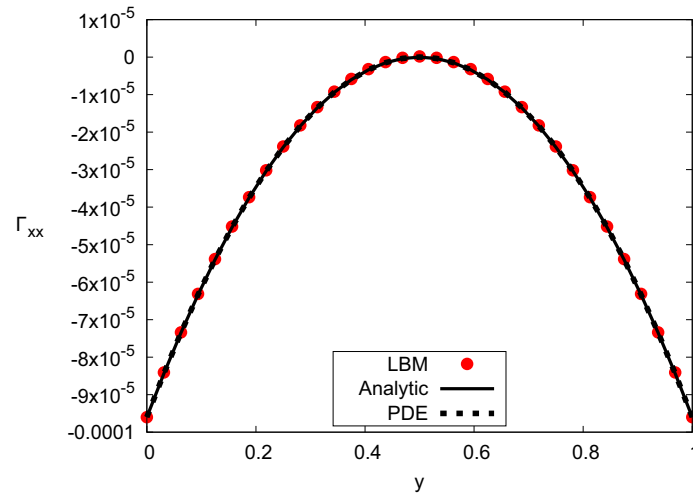
Figure 7.2: Poiseuille flow for stress slip moment boundary conditions. The results are plotted for $Re = 100$, $Ma = 0.1\sqrt{3}$ and ζ=0.1.

(a) $Re = 100$ (b) $Re = 0.1$
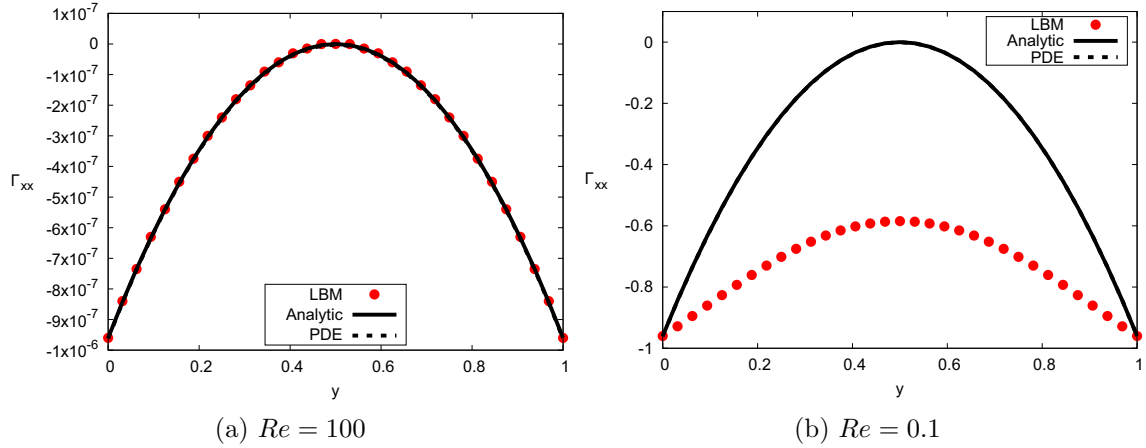
Figure 7.3: Tangential deviatoric stress for Poiseuille flow using stress slip moment boundary conditions. The results are plotted for $\zeta = 0.1$ and $Ma = 0.01\sqrt{3}$.

7.3   The tangential stress with the TRT-model

The analysis in the previous sections was based on the assumption that the relaxation time τ is short, therefore $\mathbf{Q}$ relaxes to its equilibrium very quickly. However, this may not be the case in some flows such as low Reynolds numbers flows.

Moreover in the BGK model, only when $\tau = 1/2$, the recurrence of the stress in the left- side of equation (7.32) will disappear. This means the stress does not depend on the stress at neighbouring nodes $\Gamma^{j\mp1}$ and can be written in an explicit scheme and the recusance minimizes to Γ^j. However, with the TRT-LBM model the stress is based on the product of two different relaxation times. So, there is a freedom to choose the viscosity and we can still find the other relaxation time by choosing the product equal to 1/4. This leads to numerical stability and confirms the good choice of the parameter Λ in the TRT model where the solution depends on explicit expression for Γ^j. The only non locality can be found in the velocity components with the nearest nodes.

7.3.1 The deviatoric stress with two relaxation times

The TRT-DBE which relaxes the odd and even order moments at different rates can be written as

$$\partial_t f_i + \boldsymbol{\xi}_i \cdot \nabla f_k = -\frac{1}{\tau^+}\left(\frac{1}{2}(f_i + f_{\tilde{i}}) - f_i^{(0+)}\right) - \frac{1}{\tau^-}\left(\frac{1}{2}(f_i - f_{\tilde{i}}) - f_k^{(0-)}\right), \qquad (7.44)$$

where τ^+ is the relaxation time for even moments and τ^- is the relaxation time for odd moments. The equilibrium function is split into its even and odd constituents, $f_i^{(0+)}$ and $f_i^{(0-)}$, respectively [33].

The PDE equation (7.44) can be discretised in a similar way to the BGK equation from Section 2.5.4 to obtain the TRT-LBE

$$\bar{f}_k(\mathbf{x} + \boldsymbol{\xi}_k \Delta t, t + \Delta t) = \bar{f}_k(\mathbf{x}, t) - \frac{\Delta t}{(\tau^+ + \Delta t/2)}\left[\frac{1}{2}(\bar{f}_k(\mathbf{x}, t) + \bar{f}_{\tilde{k}}(\mathbf{x}, t)) - f_k^{(0+)}(\mathbf{x}, t)\right]$$
$$- \frac{\Delta t}{(\tau^- + \Delta t/2)}\left[\frac{1}{2}(\bar{f}_k(\mathbf{x}, t) + \bar{f}_{\tilde{k}}(\mathbf{x}, t)) - f_k^{(0-)}(\mathbf{x}, t)\right].$$
$$(7.45)$$

The BGK LBM is recovered from equation (7.45) when $\tau^+ = \tau^-$.

The evolution equation of the deviatoric stress for two relaxation times can be derived in the same way as the BGK model and writing the relaxation time $\tau = \tau^+$. The term $(\partial_\gamma \phi_{\alpha\beta\gamma})$ in equation (7.8) is not vanishing as in the BGK model, in the evaluation of the stresses Γ_{xx} and Γ_{xy}. This is because in the TRT model, the analysis depends on two relaxation times such that $\tau^- \gg \tau^+$. However, the BGK model depends on one relaxation time and this can give a slow relaxation rate which gives an incorrect solution as seen before. To calculate the shear stress Γ_{xy}, it should be understood that the third-order moment in equation (7.8), $\partial_y \phi_{xyy} = (2/3)\partial_{yy}\Gamma_{xy}$, is equal to zero, since the second derivative of the deviatoric shear stress vanishes for this kind of flow. Therefore, the shear stress is computed similarly to the BGK model with τ replaced by τ^+.

Now the tangential component of the stress can be written as

$$\Gamma_{xx} = -2\tau^+\mu(\partial_y u_x)^2 + \tau^+\partial_y\phi_{xxy}, \tag{7.46}$$

where the third-order moment ϕ_{xxy} is calculated as follows

$$\phi_{xxy} = \sum f_i\xi_{ix}\xi_{ix}\xi_{iy},$$
$$= \sum f_i(c_{ix} - u_x)(c_{ix} - u_x)(c_{iy} - u_y). \tag{7.47}$$

Simplifying this equation then applying equation (7.1) gives

$$\phi_{xxy} = Q_{xxy} + 2u_x\Gamma_{xy}, \tag{7.48}$$

and by using the relation $\Psi_y = 6Q_{yxx} - 2\rho u_y$ in equation (2.131) where Ψ_y can be found by choosing the y-component of equation (2.129) such that

$$\Psi_y = -4\tau^-\rho u_x\partial_y u_x + 2\tau^{-2}\mu\partial_{yyy}u_x. \tag{7.49}$$

Inserting equation (7.49) into equation (7.48) and neglecting $O((\tau^-)^2\tau^+)$, yields

$$\phi_{xxy} = \frac{-2}{3}\tau^-\rho u_x\partial_y u_x + 2u_x\Gamma_{xy}$$
$$= \frac{2}{3}\rho(\tau^+ - \tau^-)u_x\partial_y u_x. \tag{7.50}$$

According to equation (7.50), the tangential stress of equation (7.46) will be

$$\Gamma_{xx} = -2\tau^+\mu(\partial_y u_x)^2 - \partial_y\left(\frac{2}{3}\rho\tau^+(\tau^+ - \tau^-)u_x\partial_y u_x\right), \tag{7.51}$$

which leads to the tangential stress at slip boundaries

$$\Gamma_{xx} = \frac{2}{3}\rho\tau^+(\tau^+ - \tau^-)u_x\partial_{yy}u_x - \frac{2}{3}\rho\Lambda(\partial_y u_x)^2. \tag{7.52}$$

7.3.2 The analytic solution with TRT-LBM and moment boundary conditions

If the same procedure that was done with the BGK model is followed the same evaluation of the stress Γ_{xx} as equation (7.32) is obtained. The only difference is by exchanging τ^2 by Λ and τ by τ^+. So the general evaluation of the tangential stress for TRT-LBE reads

$$\Gamma_{xx}^j - (\Lambda - 1/4)\left(\Gamma_{xx}^{j-1} - 2\Gamma_{xx}^j + \Gamma_{xx}^{j+1}\right) = -\frac{1}{3}\rho\Lambda(u_{j-1}^2 - 2u_j^2 + u_{j+1}^2)$$

$$-\frac{1}{2}\tau^+\rho G(u_{j-1} + 2u_j + u_{j+1}) + \frac{4}{3}\Lambda\tau^+\rho G(u_{j-1} - 2u_j + u_{j+1}). \tag{7.53}$$

This equation is easy to solve for Γ_{xx} if the recurrence relation of the stress is eliminated by sitting $\Lambda = 1/4$.

To find the numerical solution of the TRT-LBM, conditions need to be imposed that are compatible with the tangential stress. By using equation (7.52) and following the same procedure as in Section 7.2.1, $\overline{\overline{\Pi}}_{xx}$ can be found at a slip wall

$$\overline{\overline{\Pi}}_{xx} = \frac{\rho}{3} + \rho u_s^2 - \rho u_s G + \frac{2}{3}\rho(\tau + 1/2)(\tau^+ - \tau^-)u_s\partial_{yy}u_s$$

$$+ \frac{6\tau^-}{(\tau + 1/2)}\overline{\Pi}_{xy}^2 \tag{7.54}$$

The three unknown functions at a north boundary are calculated by imposing the following three following constraints

$$\rho\overline{u}_y = 0,$$

$$\rho\overline{u}_x = \rho u_s - \frac{1}{2}\rho G, \tag{7.55}$$

$$\overline{\overline{\Pi}}_{xx} = \frac{\rho}{3} + \rho u_s^2 - \rho u_s G + \frac{2}{3}\rho(\tau + 1/2)(\tau^+ - \tau^-)u_s\partial_{yy}u_s.$$

So, the three $\bar{f}_i$ are

$$\bar{f}_4 = \bar{f}_1 + \bar{f}_3 + \bar{f}_2 + 2(\bar{f}_5 + \bar{f}_6) - \frac{\rho}{3} - \rho u_s^2 + \rho G u_s,$$

$$- \frac{2}{3}\rho(\tau + 1/2)(\tau^+ - \tau^-)u_s\partial_{yy}u_s - \frac{6\tau}{\rho(\tau + 1/2)}\overline{\Pi}_{xy}^2,$$

$$\bar{f}_7 = \frac{\rho}{6} - \bar{f}_3 - \bar{f}_6 + \rho u_s(u_s - 1)/2 + \rho G(1/2 - u_s)/2$$

$$+ \frac{1}{3}\rho(\tau^+ + 1/2)(\tau^+ - \tau^-)u_s\partial_{yy}u_s + \frac{3\tau}{\rho(\tau + 1/2)}\overline{\Pi}_{xy}^2, \qquad (7.56)$$

$$\bar{f}_8 = \frac{\rho}{6} - \bar{f}_1 - \bar{f}_5 + \rho u_s(u_s + 1)/2 - \rho G(1/2 + u_s)/2$$

$$+ \frac{1}{3}\rho(\tau^+ + 1/2)(\tau^+ - \tau^-)u_s\partial_{yy}u_s + \frac{3\tau}{\rho(\tau + 1/2)}\overline{\Pi}_{xy}^2,$$

where $\overline{\Pi}_{xy}^2$ and u_s at the slip boundary can be calculated from equation (7.42) and equation (3.81), respectively. The second derivative of u_s in the above equations can be found easily from the analytical solution of equation (3.58) where $\partial_{yy}u_s = \partial_{yy}u_x = (-3/\tau)G$.

Figure 7.4 displays a developed fully parabolic solution for the tangential deviatoric stress for channel flow. The parameters were taken to be $Re = 100$, $Ma = 0.01\sqrt{3}$, the grid points is $m_y = 33$ while the slip length is equal to $\zeta = 0.001$. Similar parameters are used for the flow with $Re = 0.1$. It demonstrates also the matching of the results between the analytical solution of equation (7.53) at $\Lambda = 1/4$, the PDE solution of equation (7.52) and numerical lattice Boltzmann predictions for the TRT slip conditions of equation (7.56). The spurious fluctuations have been eliminated. The effect of the slip length on the results is also studied. For various slip lengths the behaviour of the flow differs from the one with the BGK model. At higher slip lengths, the results of the tangential stress drifts up for $Re = 100$ and drifts down for $Re = 0.1$. This change in the behaviour happens because of the first term in the right side of equation (7.52). This term includes two different relaxation times so it shifted the results from its original point. This behaviour was not observed with the BGK model, because in the tangential stress the relaxation times are equal so this term is not included.

(a) $Re = 100$ (b) $Re = 0.1$
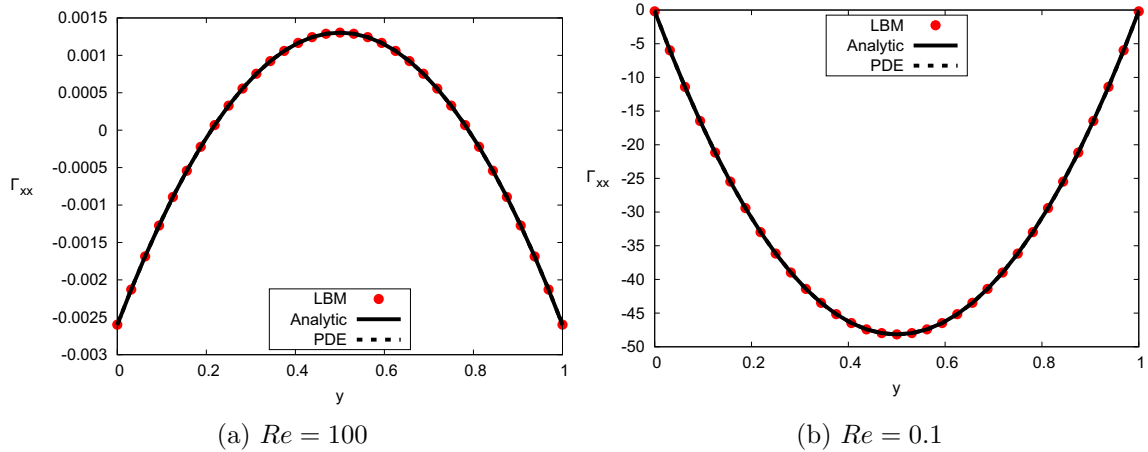
Figure 7.4: Tangential deviatoric stress for the Poiseuille flow by using the TRT-stress slip moment boundary conditions. The results are plotted for ζ=0.001 and $Ma = 0.01\sqrt{3}$.

(a) $Re = 100$ (b) $Re = 0.1$
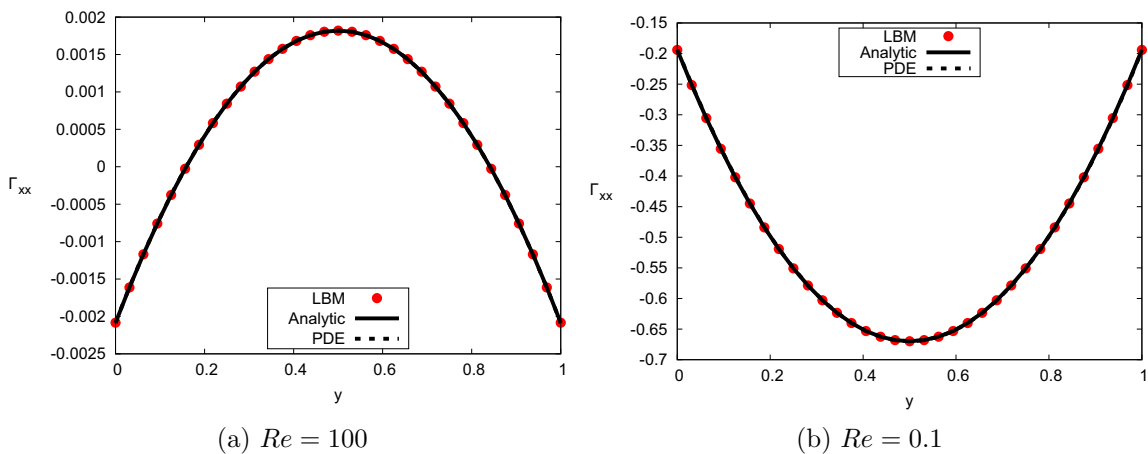
Figure 7.5: Tangential deviatoric stress for the Poiseuille flow by using the TRT-stress slip moment boundary conditions. The results are plotted for ζ=0.1 and $Ma = 0.01\sqrt{3}$.

7.4   Conclusion

In this chapter the stress field obtained using the BGK and the TRT lattice Boltzmann models with moment slip boundary conditions was analysed. Similar to the no-slip study of Reis [94], the tangential stress for unidirectional channel flow does not equal zero as is the case in the Navier-Stokes equations. Instead, it emulated the non-zero stress $\Gamma_{xx} = -2\mu\tau(\acute{u})^2$ of Burnett type at $O(Kn^2)$. The inconsistency between the equations we are solving and the conditions we are imposing caused spurious oscillations. To remove this oscillations, boundary conditions that depend on devi-

atoric stress are introduced. This condition reduced the oscillations of the stress at the boundary particularly at higher resolutions. However, at small Reynolds numbers hence large relaxation time our argument will not be valid and gave improper numerical solution. Alternatively, slip moment boundary conditions that are based on the model with $\Lambda = 1/4$ gave the correct numerical solution. With this model and contrary to the BGK model the slip length ζ has the effect of shifting the results of the tangential stress upwards and downwards for $Re = 100$ and $Re = 0.1$ respectively.

Chapter 8

General conclusions and future work

8.1 Conclusions

In this thesis different numerical implementations based on the lattice Boltzmann method were studied by using the moment-based boundary conditions method for slip and no-slip boundaries. These numerical studies have yielded promising and accurate results.

This work was started by introducing some basic fluid flow concepts and historical background of the LBM. Then another approach which was based on kinetic theory was used to derive the BGK-LBE. From the DBE, the macroscopic Navier-Stokes equations were recovered by using the Chapman-Enskog expansion. In this thesis the stability of the method was increased by using MRT model. Here, the method of Dellar [28] was followed.

Different boundary conditions were presented. For flat walls, the moment-based boundary conditions were used at the beginning of this thesis to eliminate the drawback of the half-way bounce-back boundary conditions. Moment method depends on the moments that are used to recover the Navier-Stokes equations. A detailed study of finding the analytical solution of the LBE was shown for the Poiseuille flow. Some

numerical simulations with moment based boundary conditions were carried out for simple flows like Poiseuille and Coutte flows with moment-based boundary conditions. By specifying the velocity at the wall to be zero for no-slip case, an exact solution was found for these two flows in horizontally infinite domains. By applying the moment method with open vertical boundaries for channel flow, third-order accuracy in Ma was obtained.

Another problem which was investigated was the lid-driven cavity. In this flow, larger Reynolds numbers were applied to test the accuracy of the no-slip moment boundary conditions. The BGK model was stable for moderate Reynolds numbers; however, the simulations were unsuccessful with small relaxation times and fewer grid points. To overcome this, the MRT-LBM model was used. In this model, the relaxation time of the momentum flux was set by the Reynolds number while the ghost moment relaxation times were set to be $\Delta t/2$ to guarantee the stability of the method. The method gave excellent results - an agreement for the velocity components and the minimum values of the primary stream functions with the benchmark results that were used for comparison. Moreover, second-order precision was obtained for the method that was implemented.

The investigation was extended to include the dipole wall collision flow. In this two-dimensional flow, the interaction between the wall and the two cores of vorticity were studied extensively. The TRT-LBM model with moment-based boundary conditions was shown to be accurate with good stability properties. In the first set of studies, the dipole was released normally towards a no-slip wall, and then in the next sets at angles of 30° and 45°. After the first dipole wall collision, the boundary induced small and high value vortices which increased by increasing the Reynolds numbers. The incidence with the wall at an angle of 30° was more interesting than the normal case since the two primary monopoles were not symmetric. This made the vortices that were created at the wall more vigorous. However, the behaviour of the dipole that collided with the corner at an angle of 45° was completely different. That was because after the first collision the corner induced additional dipoles which decayed over time. The success

of the simulation towards the corner increased the confidence in the choice of moments for the boundary conditions at corners.

The interaction between the dipole and the boundary increased the dissipation of the energy and the growth of the enstrophy. The results of these quantities were compared with benchmark data of the finite difference method and of the pseudospectral Chebyshev method in [19]. A very good agreement was obtained between these results and the other numerical data. Moreover, moment-based boundary conditions results were in better agreement than the bounce-back method with the benchmark data.

Also achieved in this thesis was another cornerstone study which was modifying the moment-based boundary conditions to include the Navier-slip condition. This method was used to study the dipole-wall collision problem with slippage on the walls. The effect of different amounts of slip, as governed by the slip length, was studied. By increasing the slip length, the generation of vortices at the wall, the dissipation of the energy and the maximum of the enstrophy were decreased. The trajectory of the dipole was shorter for smaller slip lengths and it matched the path of the dipole at shear-free stress wall at much larger slip lengths.

The relation between the dissipation of the energy rate and the enstrophy was examined and contrasted with theoretical predictions. It was shown that the normal relationship between dissipation and enstrophy is modified in the presence of wall slip. The findings indicated that by increasing the Reynolds numbers, the dissipation of the energy decreased while it was increased by increasing the enstrophy. This observation confirms the results in this thesis. Moreover, this relation showed some fluctuation in the dissipation of the energy results for longer timesteps which was eliminated by reducing the Mach number and taking a moving average every 100 time steps.

The dissipation of the energy for dipole wall collision can be divided into three regimes. In the absence of the viscosity, the dissipation was proportional to Re^{-1} while it was proportional to $Re^{-0.5}$ near the boundary where the Prandtl theory was satisfied. In the region where the generating of the vortices was reduced at the wall, the dissipation was proportional to $Re^{-0.5}$ and the enstrophy growth was to $Re^{-0.5}$.

Moreover, the maximum enstrophy scale reduced when the slip length was raised.

Finally the stress field was studied for planner channel flow. The study of Reis [94] was extended in this thesis to include the moment method with slip boundaries. As a result, spurious oscillations were found near the boundary and they were eliminated by using conditions that are consistent with the deviatoric stress. Nevertheless, at lower Reynolds numbers some assumptions were broken and incorrect numerical solutions were found. Instead, stress boundary conditions for a TRT-LBM model were applied and gave the correct solution. In this case and contrary to the BGK model, by increasing the slip length the results are shifted because in the tangential stress the relaxation times are not equal.

8.2   Future work

The numerical results obtained in this thesis confirm the accuracy of the lattice Boltzmann method with moment-based boundary conditions. Therefore, from this approach the following possible future work can be included:

Extend the numerical model to three dimensional problems space [17] for no-slip and slip boundaries. The result of the interaction between the vortex and the wall is an example of what can be seen in fluid turbulence [44]. By applying higher Reynolds numbers for no-slip boundaries, one can investigate other real problems such as in turbulent flows and analysing the stability of the method which can be examined [23, 20]. Also in the same field of study one can investigate the dissipation of the energy in the limit of vanishing viscosity. For the last two cases, the parallelisation of the code is required.

Since the moment-based boundary conditions proved its efficiency in the simulations of flat walls, one can test the application of the moment-based method with curved geometries [104].

Appendix A

flowcharts of LBM simulation

In order to explain the general procedure of the algorithm for lattice Boltzmann method with moment based boundary conditions and bounce back method, flowcharts of these methods are inserted in the appendix.

A.1 LBM with half-way bounce-back boundary conditions

In this simulation, the half-way bounce-back boundary conditions are applied before the streaming step. This is because the half-way bounce-back will happen at two time steps. Figure A.1 shows the flowchart of bounce-back with LBM.
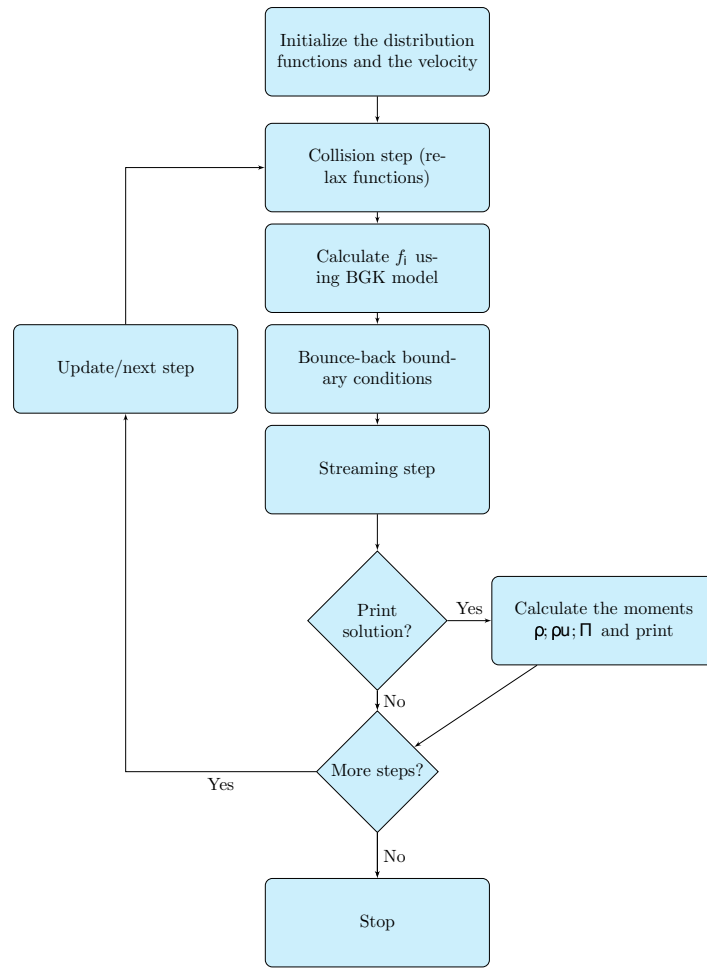
Figure A.1: The LBM flowchart with half-way bounce-back method.

A.2 LBM with moment based boundary conditions

By using Fortran code, the LBM with moment-base boundary conditions is used to simulate the dipole-wall collision flow. The main logical steps of our procedure can be demonstrated by a flowchart that is shown in Figure A.2 . In the initial step we set $\rho = 1$, and u_x, u_y are calculated by using equation(4.2). The probability distribution functions are initialized by using equation (2.78) where $\bar{f}_i = \bar{f}_i^{(0)}$. In the collision step, the moments relax to their equilibrium, equation (2.132), by using two relaxation times. Then the distribution functions are updated by using equation (2.135). By applying the streaming step, the distribution functions propagate to the nearest node; however at the boundary three unknown functions are located. To find the unknown

distribution functions at the boundary we used the moment-based boundary conditions
from Section(3.4). The above steps are repeated until the time condition is fulfilled .
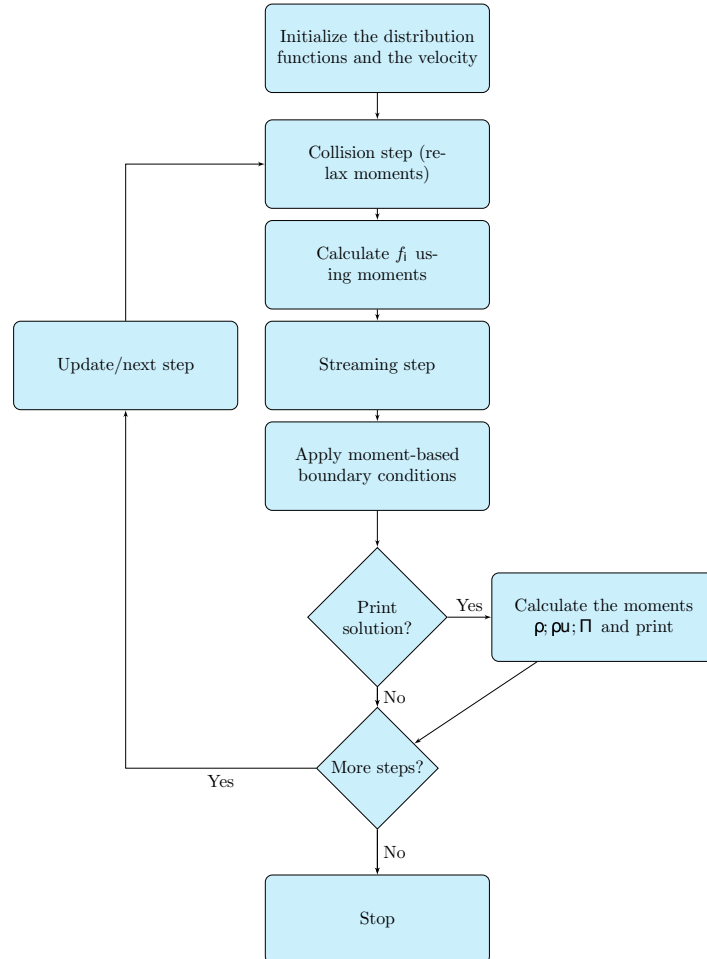
Figure A.2: The LBM flowchart with Moment method.

Bibliography

[1] R. Allen and T. Reis. Moment-based boundary conditions for lattice Boltzmann simulations of natural convection in cavities. *Prog. Comp. Fluid Dyn.: An Int. J.*, 16(4):216–231, 2016.

[2] E. B. Arkilic, M. A. Schmidt, and K. S. Breuer. Gaseous slip flow in long microchannels. *J. Micro syst.*, 6(2):167–178, 1997.

[3] S. J. Barker and S. C. Crow. The motion of two-dimensional vortex pairs in a ground effect. *J. Fluid Mech.*, 82(4):659–671, 1977.

[4] S. Bennett. *A lattice Boltzmann model for diffusion of binary gas mixtures*. PhD thesis, University of Cambridge, 2010.

[5] S. Bennett, P. Asinari, and P.J. Dellar. A lattice Boltzmann model for diffusion of binary gas mixtures that includes diffusion slip. *Int. J. Numer. Meth. Fluids*, 69:171–189, 2012.

[6] R. Benzi, S. Succi, and M. Vergassola. Turbulence modelling by nonhydrodynamic variables. *Europhys. Lett.*, 13:727, 1990.

[7] P. L. Bhatnagar, E. P. Gross, and M. Krook. A model for collision processes in gases. i. small amplitude processes in charged and neutral one-component systems. *Phys. Rev.*, 94(3):511, 1954.

[8] L. Boltzmann. Vorlesungen über gasstheorie, vol. 2 (ja barth, leipzig, 1896-1898) english translation by h. brush, lectures on gas theory, 1964.

Bibliography

[9] O. Botella and R. Peyret. Benchmark spectral results on the lid-driven cavity flow. *Comput. Fluids*, 27:421–433, 1998.

[10] M. Bouzidi, M. Firdaouss, and P. Lallemand. Momentum transfer of a Boltzmann-lattice fluid with boundaries. *Phys. Fluids*, 13(11):3452–3459, 2001.

[11] C.H. Bruneau and C. Jouron. An efficient scheme for solving steady incompressible Navier-Stokes equations. *J. Comput. Phys.*, 89:389–413, 1990.

[12] G.F. Carnevale, O.U. Velasco Fuentes, and P. Orlandi. Inviscid dipole-vortex rebound from a wall or coast. *J. Fluid Mech.*, 351:75–103, 1997.

[13] X.J. Carton and J.C. McWilliams. Barotropic and baroclinic instabilities of axisymmetric vortices in a quasigeostrophic model. In *Elsevier oceanography series*, volume 50, pages 225–244. Elsevier, 1989.

[14] C. Cercignani. The Boltzmann equation. In *The Boltzmann Equation and Its Applications*, pages 40–103. Springer-Verlag, New York, 1988.

[15] S. Chapman and Th. G. Cowling. *The mathematical theory of non-uniform gases: an account of the kinetic theory of viscosity, thermal conduction and diffusion in gases.* (Cambridge Univ Press, Cambridge, England, 1970.

[16] S. Chen, H. Chen, D. Martnez, and W. Matthaeus. Lattice Boltzmann model for simulation of magnetohydrodynamics. *Phys. Rev. Lett.*, 67:3776, 1991.

[17] Sh. Chen, Z. Wang, X. Shan, and G. D. Doolen. Lattice Boltzmann computational fluid dynamics in three dimensions. *J. Stat. Phys.*, 68(3-4):379–400, 1992.

[18] A.R. Cieślik, R.A.D. Akkermans, L.P.J. Kamp, H.J.H. Clercx, and G.J.F. Van Heijst. Dipole-wall collision in a shallow fluid. *Eur. J. Mech. B/Fluids*, 28:397–404, 2009.

[19] H.J.H. Clercx and C.-H. Bruneau. The normal and oblique collision of a dipole with a no-slip boundary. *Comput. Fluids*, 35:245–279, 2006.

Bibliography

[20] H.J.H. Clercx, S.R. Maassen, and G.J.F. Van Heijst. Spontaneous spin-up during the decay of 2d turbulence in a square container with rigid boundaries. *Phys. Rev. Lett.*, 80(23):5129, 1998.

[21] H.J.H. Clercx and G.J.F. van Heijst. Dissipation of kinetic energy in two-dimensional bounded flows. *Phys. Rev. E*, 65:066305, 2002.

[22] H.J.H Clercx and G.J.F. van Heijst. Dissipation of coherent structures in confined two-dimensional turbulence. *Phys. Fluids*, 29(11):111103, 2017.

[23] H.J.H. Clercx, G.J.F. Van Heijst, D. Molenaar, and M.G. Wells. No-slip walls as vorticity sources in two-dimensional bounded turbulence. *Dyn. Atmos. Oceans*, 40(1-2):3–21, 2005.

[24] E.A. Coutsias and J.-P. Lynov. Fundamental interactions of vortical structures with boundary layers in two-dimensional flows. *Physica D*, 51:482–497, 1991.

[25] V.S.J. Craig, C. Neto, and D. R.M. Williams. Shear-dependent boundary slip in an aqueous Newtonian liquid. *Phys. Rev. Lett.*, 87(5):054504, 2001.

[26] N. Curle. The influence of solid boundaries upon aerodynamic sound. *Proc. R. Soc. Lond. A*, 231(1187):505–514, 1955.

[27] A. W. Date. *Introduction to computational fluid dynamics*. Cambridge University Press, UK, 2005.

[28] P.J. Dellar. Nonhydrodynamic modes and a priori construction of shallow water lattice Boltzmann equations. *Phys. Rev. E*, 65:036309, 2002.

[29] P.J. Dellar. Incompressible limits of lattice Boltzmann equations using multiple relaxation times. *J. Comput. Phys.*, 190:351–370, 2003.

[30] G. Deng, J. Piquet, P. Queutey, and M. Visonneau. Incompressible flow calculations with a consistent physical interpolation finite volume approach. *Comput. Fluids*, 23:1029–1047, 1994.

Bibliography

[31] M. Deville and T.B Gatski. *Mathematical modeling for complex fluids and flows.* Springer Science & Business Media, 2012.

[32] D. d'Humiéres. Generalized lattice Boltzmann equations. *Prog. Astronaut. Aeronaut.*, pages 450–458, 1992.

[33] D. D'Humiéres and I. Ginzburg. Viscosity independent numerical errors for lattice Boltzmann models: from recurrence equations tomagic collision numbers. *Comput. Math. Appl.*, 58:823–840, 2009.

[34] N. Dongari, A. Agrawal, and A. Agrawal. Analytical solution of gaseous slip flow in long microchannels. *Int. J. Heat Mass Tran.*, 50(17-18):3411–3421, 2007.

[35] M. Farge, K. Schneider, et al. Energy dissipating structures produced by walls in two-dimensional flows at vanishing viscosity. *Phys. Rev. Lett.*, 106(18):184502, 2011.

[36] K. N. Fedorov and A. I. Ginzburg. *The near-surface layer of the ocean.* VSP Utrecht, Netherlands, 1992.

[37] P. A. Fishwick. *Handbook of dynamic system modeling.* CRC Press, New York, 2007.

[38] U. Frisch, B. Hasslacher, and Y. Pomeau. Lattice-gas automata for the Navier-Stokes equation. *Phys. Rev. Lett.*, 56:1505–1508, 1986.

[39] G. P. Galdi and W. J. Layton. Approximation of the larger eddies in fluid motions ii: A model for space-filtered flow. *Mathematical Models and Methods in Applied Sciences*, 10(03):343–350, 2000.

[40] U. Ghia, K.N. Ghia, and C.T. Shin. High-resolutions for incompressible flow using the Navier-Stokes equations and a multigrid method. *J. Comput. Phys.*, 48:387–411, 1982.

[41] I. Ginzbourg and P.M. Adler. Boundary flow condition analysis for the three-dimensional lattice Boltzmann model. *J. Phys. II. France*, 4:191–214, 1994.

[42] I. Ginzburg. Equilibrium-type and link-type lattice Boltzmann models for generic advection and anisotropic-dispersion equation. *Adv. Water Resour.*, 28:1171–1195, 2005.

[43] I. Ginzburg and D. d'Humiéres. Multireflection boundary conditions for lattice Boltzmann models. *Phys. Rev. E*, 68:066614, 2003.

[44] G. J. Goni, S. L. Garzoli, A. J. Roubicek, D. B. Olson, and O. B. Brown. Agulhas ring dynamics from topex/poseidon satellite altimeter data. *J. Mar. Res.*, 55(5):861–883, 1997.

[45] H. Grad. Note on n-dimensional Hermite polynomials. *Commun. Pure Appl. Maths.*, 2:325–330, 1949.

[46] Z. Guo and C. Shu. *Lattice Boltzmann method and its applications in engineering*. World Scientific, Company Incorporated, 2013.

[47] J.E.V. Guzmán, L.P.J. Kamp, and G.J.F. Van Heijst. Vortex dipole collision with a sliding wall. *Fluid Dyn. Res.*, 45:045501, 2013.

[48] A. Hantsch, T. Reis, and U. Gross. Moment method boundary conditions for multiphase lattice Boltzmann simulations with partially-wetted walls. *J. Comput. Multiphase Flows*, 7:1–14, 2015.

[49] J. Hardy, O. De Pazzis, and Y. Pomeau. Molecular dynamics of a classical lattice gas: Transport properties and time correlation functions. *Phys. Rev. A*, 13:1949, 1976.

[50] Q. He and X-P. Wang. Numerical study of the effect of navier slip on the driven cavity flow. *ZAMM Z. Angew. Math. Mech*, 89(10):857–868, 2009.

[51] X. He and L.S. Luo. A priori derivation of the lattice Boltzmann equation. *Phys. Rev. E*, 55:R6333, 1997.

[52] X. He, X. Shan, and G.D. Doolen. Discrete Boltzmann equation model for non-ideal gases. *Phys. Rev. E*, 57:R13, 1998.

[53] X.Y. He, Q.S. Zou, L.S. Luo, and M. Dembo. Analytic solutions of simple flows and analysis of nonslip boundary conditions for the lattice Boltzmann BGK model. *J. Stat. Phys.*, 87:115–136, 1997.

[54] F. Higuera and J. Jimenez. Boltzmann approach to lattice gas simulations. *Europhys. Lett.*, 9:663, 1989.

[55] S. Hou, Q. Zou, G.D. Chen, S.and Doolen, and A. C. Cogley. Simulation of cavity flow by the lattice Boltzmann method. *J. Comput. Phys.*, 118:329–347, 1995.

[56] S. Hou, Q. Zou, S. Chen, G. D. Doolen, and A. C. Cogley. Simulation of cavity flow by the lattice Boltzmann method. *J. Comp. Phys.*, 118(2)(2):329 –347, 1995.

[57] M.S. Howe. *Theory of vortex sound*, volume 33. Cambridge University Press, UK, 2003.

[58] Sh-Sh. Hsieh, H-H. Tsai, Ch-Y. Lin, Ch-F. Huang, and Ch-M. Chien. Gas flow in a long microchannel. *Int. J. Heat Mass Transf*, 47(17-18):3877–3887, 2004.

[59] E. Ikenberry and C. Truesdell. On the pressures and the flux of energy in a gas according to maxwell's kinetic theory, i. *J. Rational Mech. Anal*, 5(1):1–54, 1956.

[60] T. Inamuro, M. Yoshino, H. Inoue, R. Mizuno, and F. Ogino. A lattice Boltzmann method for a binary miscible fluid mixture and its application to a heat-transfer problem. *J. Comp. Phys*, 179:201–215, 2002.

[61] B.M. Jamart and J.C.J. Nihoul. *Mesoscale/Synoptic Coherent Structures in Geophysical Turbulence*, volume 50. Elsevier, New York,, 1989.

Bibliography

[62] V. John and A. Liakos. Time-dependent flow across a step: the slip with friction boundary condition. *Int. J. Numer. Meth. Fluids*, 50(6):713–731, 2006.

[63] G.H. Keetels, W. Kramer, H.J.H Clercx, and G.J.F. van Heijst. On the Reynolds number scaling of vorticity production at no-slip walls during vortex-wall collisions. *Theoretical and comput. Fluid Dyn*, 25(5):293–300, 2011.

[64] W. Kramer. *Dispersion of tracers in two-dimensional bounded turbulence.* PhD thesis, Eindhoven University of Technology, Eindhoven, Netherlands, 2007.

[65] A Kundt and E Warburg. Ix. on friction and heat-conduction in rarefied gases. *The London, Edinburgh, and Dublin Philosophical Magazine and J. Science*, 50(328):53–62, 1875.

[66] P. K Kundu, I. Cohen, and D. Dowling. *Fluid Mechanics.* Academic Press, 1992.

[67] A.J.C. Ladd. Numerical simulations of particulate suspensions via a discretized Boltzmann equation. part 1. theoretical foundation. *J. Fluid Mech.*, 271:285–309, 1994.

[68] P. Lallemand and L.S. Luo. Theory of the lattice Boltzmann method: Dispersion, dissipation, isotropy, Galilean invariance, and stability. *Phys. Rev. E*, 61:6546, 2000.

[69] J. Latt. Choice of units in lattice Boltzmann simulations. *Freely available online at http://lbmethod. org/_media/howtos: lbunits. pdf*, 2008.

[70] J. Latt and B. Chopard. Lattice Boltzmann method with regularized pre-collision distribution functions. *Comput. Fluid.*, 72:165–168, 2006.

[71] J. Latt and B. Chopard. A benchmark case for lattice Boltzmann: turbulent dipole-wall collision. *Int. J. Mod. Phys. C*, 18:619–626, 2007.

[72] E. Lauga and H.A. Stone. Effective slip in pressure-driven stokes flow. *J. Fluid Mech.*, 489:55–77, 2003.

[73] B. Lautrup. *Physics of continuous matter: exotic and everyday phenomena in the macroscopic world.* CRC press, 2004.

[74] T. Lee and Ch.-L. Lin. Rarefaction and compressibility effects of the lattice-Boltzmann-equation method in a gas microchannel. *Phys. Rev. E*, 71(4):046706, 2005.

[75] S.K. Lele. Compact finite difference schemes with spectral-like resolution. *J. Comput. Phys.*, 103:16–42, 1992.

[76] M.J. Lighthill. On sound generated aerodynamically. *Phil. Trans. R. Soc. A*, 564:1952, 1954.

[77] L.S. Luo. *Lattice-gas automata and lattice Boltzmann equations for two-dimensional hydrodynamics.* PhD thesis, Georgiargia Institute of Technology, 1993.

[78] L.S. Luo. The lattice-gas and lattice Boltzmann methods: past, present, and future. 2000.

[79] L.S. Luo, W. Liao, X. Chen, Y. Peng, W. Zhang, et al. Numerics of the lattice Boltzmann method: Effects of collision models on the lattice Boltzmann simulations. *Phys. Rev. E*, 83(5):056710, 2011.

[80] N. S. Martys, X. Shan, and H. Chen. Evaluation of the external force term in the discrete Boltzmann equation. *Phys. Rev. E*, 58(5):6855, 1998.

[81] James Clerk Maxwell. Scientific papers. *C. Maxwell*, 1879.

[82] G. R. McNamara and G. Zanetti. Use of the Boltzmann equation to simulate lattice-gas automata. *Phys. Rev. Lett.*, 61:2332, 1988.

[83] S. Mohammed, D. Graham, and T. Reis. Assessing moment-based boundary conditions for the lattice Boltzmann equation: A study of dipole-wall collisions. *Comput. Fluids.*, 2018.

[84] S. Mohammed and T. Reis. Using the lid-driven cavity flow to validate moment-based boundary conditions for the lattice Boltzmann equation. *Arch. Mech. Eng.*, 64(1):57–74, 2017.

[85] Y. Nakashima and O. Inoue. Sound generation by a vortex ring collision with a wall. *Phys. Fluids*, 20(12):126104, 2008.

[86] C.L.M.H. Navier. Mémoire sur les lois du mouvement des fluides. *Mém. Acad. Sci. Inst. F.*, 6(1823):389–440, 1823.

[87] X. Nie, G. D. Doolen, and S. Chen. Lattice-Boltzmann simulations of fluid flows in mems. *J. Stat. Phys.*, 107(1-2):279–289, 2002.

[88] D.R. Noble, S. Chen, G. Georgiadis, and R. O. Buckius. A consistent hydro-dynamic boundary condition for the lattice Boltzmann method. *Phys. Fluids*, 7(1):203–209, 1995.

[89] P. Orlandi. Vortex dipole rebound from a wall. *Phys. Fluids A: Fluid Dynamics (1989-1993)*, 2:1429–1436, 1990.

[90] A. R. Paterson. *A first course in fluid dynamics*. Cambridge university press, UK, 1983.

[91] A. Perumal, G. V.S. Kumar, and A. K. Dass. Application of lattice Boltzmann method to flows in microgeometries. *CFD lett*, 2(2):75–84, 2010.

[92] L. Prandtl. Über flussigkeitsbewegung bei sehr kleiner reibung. *Verhandl. III, Internat. Math.-Kong., Heidelberg, Teubner, Leipzig, 1904*, pages 484–491, 1904.

[93] Y. H. Qian. Lattice gas and lattice kinetic theory applied to the Navier-Stokes equations. *Doktorarbeit, Universite Pierre et Marie Curie, Paris*, 1990.

[94] T. Reis. On the lattice Boltzmann deviatoric stress: Analysis, boundary conditions, and relaxation times. *to be submitted to IMA J. Num. Analn*, (2018).

[95] T. Reis and P.J. Dellar. Moment-based formulation of Navier–Maxwell slip boundary conditions for lattice Boltzmann simulations of rarefied flows in microchannels. *Phys Fluids*, 2012.

[96] T. Reis and T.N. Phillips. Alternative approach to the solution of the dispersion relation for a generalized lattice Boltzmann equation. *Phys. Rev. E*, 77(2):026702, 2008.

[97] D. H. Rothman and S. Zaleski. *Lattice-gas cellular automata: simple models of complex hydrodynamics*, volume 5. Cambridge University Press, UK, 2004.

[98] P.G. Saffman. The approach of a vortex pair to a plane surface in inviscid fluid. *J. Fluid Mech.*, 92(3):497–503, 1979.

[99] M. Sahin and R.G. Owens. A novel fully implicit finite volume method applied to the lid-driven cavity problem part i: High Reynolds number flow calculations. *Int. J. Numer. Meth. Fluids*, 42:57–77, 2003.

[100] H. Schlichting et al. *Boundary-layer theory*. Springer, New York, 1974.

[101] H. Schlichting and K. Gersten. *Boundary-layer theory*. Springer, Berlin, 2016.

[102] X. Shan, X.F. Yuan, and H. Chen. Kinetic theory representation of hydrodynamics: a way beyond the Navier–Stokes equation. *J. Fluid Mech.*, 550:413–441, 2006.

[103] S. Succi. *The lattice Boltzmann equation for fluid dynamics and beyond*. Oxford University Press, uk, 2001.

[104] D. Sutherland. *Numerical study of vortex generation in bounded flows with no-slip and partial slip boundary conditions*. PhD thesis, 2014.

[105] D. Sutherland, C. Macaskill, and D.G. Dritschel. The effect of slip length on vortex rebound from a rigid boundary. *Phys. Fluids (1994-present)*, 25:093104, 2013.

Bibliography

[106] J. R. Toro and S. Pedraza. *Flow evolution mechanisms of lid-driven cavities.* INTECH Open Access Publisher, 2011.

[107] D. C. Tretheway, X Liu, and C. D. Meinhart. Analysis of slip flow in microchannels. In *Proceedings of 11th International Symposium on Applications of Laser Techniques to Fluid Mechanics, Lisbon*, pages 8–11. Citeseer, 2002.

[108] F.J. Uribe and A.L. Garcia. Burnett description for plane Poiseuille flow. *Phys. Rev. E*, 60(4):4063, 1999.

[109] E. Viggen. The lattice Boltzmann method with applications in acoustics. *Master's Thesis, NTNU Trondheim, Norway*, 2009.

[110] T. von Larcher and P. D. Williams. *Modeling Atmospheric and Oceanic Flows: Insights from Laboratory Experiments and Numerical Simulations*, volume 205. John Wiley & Sons, Hoboken, New Jersey, 2014.

[111] M.G. Wells, H.J.H. Clercx, and G.J.F. Van Heijst. Vortices in oscillating spin-up. *J. Fluid Mech.*, 573:339–369, 2007.

[112] D.A. Wolf-Gladrow. *Lattice-gas cellular automata and lattice Boltzmann models: An Introduction.* Springer Science & Business Media, 2000.

[113] Q. Zou and X. He. On pressure and velocity boundary conditions for the lattice Boltzmann BGK model. *Phys. Fluids.*, 9:1591–1598, 1997.